Oliver Kastner

First Principles Modelling of Shape Memory Alloys

Molecular Dynamics Simulations



Springer Series in Materials Science

Volume 163

Series Editors

Zhiming M. Wang, Fayetteville, AR, USA Chennupati Jagadish, Canberra, ACT, Australia Robert Hull, Charlottesville, VA, USA Richard M. Osgood, New York, NY, USA Jürgen Parisi, Oldenburg, Germany

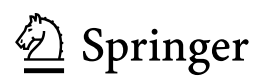
For further volumes: http://www.springer.com/series/856

The Springer Series in Materials Science covers the complete spectrum of materials physics, including fundamental principles, physical properties, materials theory and design. Recognizing the increasing importance of materials science in future device technologies, the book titles in this series reflect the state-of-the-art in understanding and controlling the structure and properties of all important classes of materials.

Oliver Kastner

First Principles Modelling of Shape Memory Alloys

Molecular Dynamics Simulations



Oliver Kastner Faculty of Mechanical Engineering Institute for Materials Ruhr University Bochum 44780 Bochum Germany

ISSN 0933-033X ISBN 978-3-642-28618-6 ISBN 978-3-642-28619-3 (eBook) DOI 10.1007/978-3-642-28619-3 Springer Heidelberg New York Dordrecht London

Library of Congress Control Number: 2012937646

© Springer-Verlag Berlin Heidelberg 2012

This work is subject to copyright. All rights are reserved by the Publisher, whether the whole or part of the material is concerned, specifically the rights of translation, reprinting, reuse of illustrations, recitation, broadcasting, reproduction on microfilms or in any other physical way, and transmission or information storage and retrieval, electronic adaptation, computer software, or by similar or dissimilar methodology now known or hereafter developed. Exempted from this legal reservation are brief excerpts in connection with reviews or scholarly analysis or material supplied specifically for the purpose of being entered and executed on a computer system, for exclusive use by the purchaser of the work. Duplication of this publication or parts thereof is permitted only under the provisions of the Copyright Law of the Publisher's location, in its current version, and permission for use must always be obtained from Springer. Permissions for use may be obtained through RightsLink at the Copyright Clearance Center. Violations are liable to prosecution under the respective Copyright Law.

The use of general descriptive names, registered names, trademarks, service marks, etc. in this publication does not imply, even in the absence of a specific statement, that such names are exempt from the relevant protective laws and regulations and therefore free for general use.

While the advice and information in this book are believed to be true and accurate at the date of publication, neither the authors nor the editors nor the publisher can accept any legal responsibility for any errors or omissions that may be made. The publisher makes no warranty, express or implied, with respect to the material contained herein.

Printed on acid-free paper

Springer is part of Springer Science+Business Media (www.springer.com)



Preface

The fascinating properties of shape memory alloys have inspired engineers ever since their discovery some 60 years ago. The reason for their attractiveness lies in the fact that these materials combine both functional and structural properties. They share their processing techniques with metals, can be cast or sintered into any shape and they can be rolled, cut, milled and welded. They are progressively ductile and are electrically and thermally conductive. Thus, their physical properties admit structural functionality. What makes them special is the fact that all these properties strongly depend on temperature. One consequence of this dependency yields the characteristic shape-memory effect: shape memory alloys can recover processed reference configurations after significant plastic deformations simply upon a change of temperature, thus adding functional abilities to structural elements. The epithet *smart material* was swiftly coined.

This work deals with a theoretical investigation of this class of alloys at the atomic scale. Here, we are concerned with length and timescales some orders of magnitudes below typical current engineering applications. One might object that these scales were not within the realm of an engineering faculty, where the majority of work deals with the design of useful technical applications. A 3-fold reply might be given to this objection: based on the historical context, with regard to the subjects contents and due to the need for interdisciplinary research work.

Historically, material sciences emerged at the intersection of engineering demands and scholastic nature sciences. Even before the theory of the atomic structure of matter was gradually formulated in the nineteenth century, natural philosophers like Descartes speculated about a microscopic conception of matter. However, techniques first needed to be developed before experimental evidence was obtained.

Milestones in the development of the materials sciences were set by the engineers, Osmond and Martens, who brilliantly advanced the microstructural characterisation of steel. Since their days, all improvements in microscopy directly

viii Preface

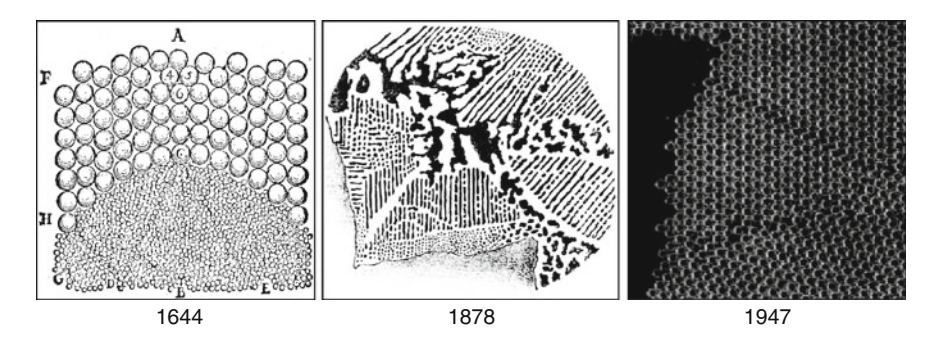


Fig. 1 Approaches to the microstructure. 1644: Descartes speculates about the particulate character of matter [1]. 1878: Martens draws micrographic images of etched steel [2]. 1947: Bragg and Nye model close-packed lattices by bubble rafts on soap suds [3].

affected the understanding of materials; from light microscopy down to the atomic level by transmission electron microscopy. However, microscopy today can still not reveal how the observed structures evolve dynamically. Here, molecular dynamics (MD) simulations may assist with regard to this: From first principles— Newton's Equations of Motion—we can dynamically simulate nucleation and growth of microstructural forming processes in solids on a computer. Hence, lattice transformations can be observed and analysed in situ rather than post mortem. In MD, some macroscopic variables can be controlled (temperature, applied load, etc.) during which the reaction of the test system is studied. Owing to this similarity to "real-world" laboratory experiments, the term "MD simulations experiments" is frequently used. Nota bene, even a method such as this has an analogous precursor: In 1947, Bragg and Nye investigated bubble rafts on soap suds as a dynamic model for domain structures and dislocations in close-packed lattices. Their intuitive images soon became part of the textbook literature. The bubble model also teaches us that a comprehensive model must not necessarily be complicated if it only represents the fundamental physics correctly. In this case, even simple models may contribute new insights into the subject matter under investigation and widen the scientific horizon.

In general, applications currently demand miniaturised designs. This tendency has, during the last two decades, already borne a new branch of engineering, the so-called nanoscale technology. Here, applications are particularly restricted by their weight and size, therefore a combination of the structural and functional features make shape memory alloys attractive as actuators or propulsion elements. Thin film applications processed, for example, by sputter deposition techniques, truly range in nanoscale dimensions and thus, in principle, become accessible to atomistic modelling. Also, atomistic methods can serve to determine local or boundary conditions for continuum-scale models. The necessary mathematical

Preface

techniques needed to bridge the gap between the atomic up to the continuum scale have already been developed (coarse-graining methods) and have been applied to, for example, cracktip simulations.

The last item concerns the need for interdisciplinary research work. Contemporary solid-state physics focuses on the subatomic structure of metals, hence addressing length and timescales far below the atomic level. Here, for example, ab-initio calculations based on quantum mechanics improve our understanding of the energetic states which determine the cohesive forces between atoms in lattices. With the increasing availability of computational resources, these methods quickly became more popular and readily spawned a lively research community. In principle, such methods can be used to derive the interaction potentials needed by the MD method. Therefore, MD again represents a scale bridging technique which is able to link subatomic modelling to the mesoscopic microstructural calculations under consideration in materials sciences. It is prudent to maintain this link: in order to further interdisciplinary research as well as to share results and discoveries between the disciplines. From a broader perspective, this topic also addresses didactic issues.

With this background in mind, the reader is now warmly welcome to share some endeavours towards a better understanding of shape memory alloys on the atomic level. The core of this work deals with a two-dimensional (2D) Lennard-Jones model, which will be proven to represent a reliable model system for martensite/austenite transformations. We present MD simulations of martensitic phase transformations, studying post-transformation microstructures and motile austenite-martensite interfaces. The material model exhibits full thermo-mechanical coupling and is thus capable of related material behaviour such as pseudoplasticity/elasticity and the shape memory effect. Even in 2D, rich transformation morphologies can be studied which exhibit striking similarities to real materials.

Among the observed phenomena, we discuss the nucleation and show the propagation of motile transformation fronts, martensitic plate growth, the twinning process, the formation/accommodation of martensitic domain structures, the generation of transformation-related lattice defects and their influence on the transformation processes. The evolution of defect structures is investigated by means of simulations of cyclic transformation/reverse transformation processes. During transformations, lattice defects are generated which affect subsequent transformations and vary the potential energy landscape of the sample. Some of the defects persist through the transformation, providing nucleation centres for subsequent cycles. Such defects may provide a memory of previous structures, and thereby may be the basis of a reversible shape memory effect.

Much effort was spent in describing the simulations as complete as possible using words and figures. For technical reasons, some colour figures are converted into greyscale in the printable version of this book. The respective colour figures are available in the online version. In addition to these, we have attached videos

x Preface

which afford an intuitive understanding of the processes discussed. These videos are available online at www.olli-kastner.de/pub/md.

Acknowledgments

The work presented here evolved over a 4 year period at the Department of Materials Science, Institute for Materials of the Ruhr-University Bochum, Germany. My thanks are due to the Director of this chair, Gunther Eggeler who, in 2005, gave me the marvellous opportunity to participate in his research group on shape memory materials. A substantial basis for my work was certainly Gunther Eggerler's generous and remarkable technical support. Moreover, and even more importantly from the perspective of an un-established postdoctoral fellow, was his intellectual backing and his complete trust in the ongoing research activities. All this provided the creative and autonomous research conditions I very much appreciated.

At ESOMAT 2006, I received the opportunity to communicate some preliminary results of my research model to Graeme Ackland who, by that time, was already an internationally honoured scientist in this field. Luckily, the model convinced him and we started a collaboration which frequently took me to his department at the University of Edinburgh. The present work gained much persuasiveness and conciseness by Graeme Ackland's experience, extraordinary knowledge and intellectual brilliance. I thankfully appreciate his contributions.

The work also improved thanks to continuous considerations by many colleagues in the course of seminars and conferences, by visiting guests and during peer reviews. Special thanks are due to Wolf Weiss (Weierstrass Institute for Applied Maths, Berlin/Germany), Roni Shneck (Ben Gurion University of the Negev, Beer-Sheva/Israel), Stefan Seelecke (Universität Saarbrücken/Germany), Yonzhong Huo (Fudan University, Shanghai/China) and to my colleagues at the Ruhr-University Bochum.

The contents of this book were accepted as Habilitation theses by the Faculty of Mechanical engineering of Ruhr-University Bochum/Germany. Many persons—known and unkown—paid attention to it during the course of the Habilitation procedure. Many thanks to all of them.

My work was funded by the German Research Foundation (DFG) under contract KA 2304/1-1,2, KA 2304/2-1 and within the framework of the DFG Collaborative Research Centre SFB 459 (sub-project A11). The European Union funded through HPC Europa programme contracts 728, 1026 and 1257. Computational resources were provided by the NIC at Germany's national supercomputing centre in Jülich [4] and by the EPCC at the University of Edinburgh, Scotland [5].

References

- 1. R. Descartes, In *Oeuvres de Descartes*, edited by C. Adam et al. (L. Cerf, Paris, 1897–1913)
- 2. A. Martens, Über die mikroskopische Untersuchung des Eisens. Zeitschrift des Vereines Deutscher Ingenieure, 22, 11–18 (1878)
- 3. L. Bragg, J.F. Nye, A dynamical model of a crystal structure. Proc. Roy. Soc. A. 190, 474–481 (1947)
- 4. John von Neumann Institute for Computing (NIC). Internet resource.http://www.fz-juelich.de/nic
- 5. Edinburgh Parallel Computing Centre (EPCC). Internet resource.http://www.epcc.ed.ac.uk

Contents

1	Prep	paratio	ns											
	1.1	An In	troduction to Shape Memory Alloys											
		1.1.1	Thermo-Mechanical Phenomena											
		1.1.2	Martensitic Transformations											
		1.1.3	Microstructures											
		1.1.4	Scales											
	1.2 Crystallographic Theory													
	1.3	-	nodynamics											
		1.3.1	Phase Stability Criterion											
		1.3.2	Nucleation and Hysteresis											
		1.3.3	Dynamics of Atomic Assemblies											
		1.3.4	Statistical Thermodynamics											
	1.4 Engineering Models of SMA													
	Refe													
2	The Method of Molecular Dynamics Simulations													
	2.1	Intera	ction Models											
	erics													
		2.2.1	Accuracy Issues											
		2.2.2	Integration Schemes											
		2.2.3	Non-Dimensionalisation											
		2 2 4												
		2.2.4	Thermostats											
		2.2.4												
			Periodic Boundary Conditions											
		2.2.5	Periodic Boundary Conditions											
		2.2.5 2.2.6	Periodic Boundary Conditions											
	2.3	2.2.5 2.2.6 2.2.7 2.2.8	Periodic Boundary Conditions											

xiv Contents

3			Material	59									
	3.1		Model Material	59									
	3.2		e and Perfect Single Crystals	64									
		3.2.1	Harmonic Limit: Linearised Equations of Motion	64									
		3.2.2	Phase Stability of 2D Lattices	67									
		3.2.3	Entropic Stabilisation of Austenite	71									
	3.3		Illographic Theory	74									
	3.4	Therm	no-Mechanical Properties	74									
		3.4.1	Individual Crystallites	74									
		3.4.2	Chains of Crystallites	77									
	Refe	erences		84									
4	Latt	tice Tra	nnsformations in 2D Crystals	87									
	4.1		erature-Induced Transformations	87									
		4.1.1	Strip-Shaped Rectangles	88									
		4.1.2	Quad-Shaped Rectangles	90									
		4.1.3	Substrate Layers	98									
	4.2	Transf	Formation Dynamics and Microstructure	100									
	4.3		ation of Martensite	102									
		4.3.1	Simulation Setup	104									
		4.3.2	Simulation Result	105									
		4.3.3	Nucleation Centres	108									
		4.3.4	Frequency Analysis	110									
		4.3.5	Phase Space Analysis	118									
		4.3.6	Entropic Nucleation Barrier	120									
	4.4		e Testing in the Pseudo-Elastic Regime	121									
		4.4.1	Simulation Procedure	121									
		4.4.2	Load Control Mode	123									
		4.4.3	Displacement Control Mode	129									
	4.5 Tensile Testing in the Pseudo-Plastic Regime												
	4.6		formation Cycles	134 137									
	7.0	4.6.1	Procedure	137									
		4.6.2	Reverse Transformation of the 160,000-Atom Quad	139									
		4.6.3	Cyclic Transformation Processes	139									
	4.7		resis and Functional Fatigue	145									
	4.7	4.7.1	Thermodynamic Hysteresis	145									
		4.7.1		143									
			Functional Fatigue.	146									
	ъ с	4.7.3	Predicted and Observed Hysteresis										
	Kefe	erences		148									
5			nnsformations in 3D Crystals	151									
	5.1		ennard–Jones Crystals	151									
		5.1.1	Model Material	151									
		5.1.2	Procedure	153									
		5.1.3	Results	154									

Contents xv

	5.2	Zircon	ium C	rysta	١												 		157
		5.2.1	Mode	el													 		157
		5.2.2	Simu	lation	ı Pı	oc	ed	ure	e								 		159
		5.2.3	Resu	lts													 		160
	5.3	Conclu	usions														 		162
	Refe	erences															 		162
6	Con	clusion	s																165
	Refe	erence.															 		168
Inc	dex .																 		169

Chapter 1 **Preparations**

This chapter reviews the fundamental material properties of shape memory alloys and thereby sets up the physical situation our modelling is referring to. Laboratory observations reveal scale-specific characteristics the modelling must reflect. Therefore, shape memory alloys are a prime example of cross-scale modelling. We briefly explain the respective modelling approaches to place the method of molecular dynamics simulations into the scope of the scientific frame work.

1.1 An Introduction to Shape Memory Alloys

1.1.1 Thermo-Mechanical Phenomena

If a material has the ability to recover a large, remaining deformation by undergoing a change in temperature, it is called a shape memory material. This behaviour is observed for different materials, metallic as well as non-metallic. This work is concerned with the memory effect in shape memory alloys (SMA). It was first observed in Au_{47.5}Cd by Chang and Read [1] in 1951. Subsequent to this, it was reported for several other alloys, such as Ti–Ni (1963) [2, 3], In-Ti (1953) [4], Cu–Zn (1956) [5–7] and Cu-Al-Ni (1957) [8]. Such alloys characteristically exhibit a strong-temperature dependent stress/strain relation.

Figure 1.1 shows process diagrams which illustrate the thermo-mechanical properties of the specific SMA nickel-titanium. (a)–(c) shows three load–strain isotherms, measured for the temperatures $T_1 < T_2 < T_3$. All curves exhibit significant yielding deformation if the sample is loaded beyond its yield point $P_{\rm crit}$. These points depend on the temperature, $P_{\rm crit}(T_1) < P_{\rm crit}(T_2) < P_{\rm crit}(T_3)$. Upon unloading, the material's response differs, again depending on the temperature: at higher temperatures, T_2 or T_3 , the deformation recovers at almost constant recovery loads $P'_{\rm crit}$, while at lower temperatures T_1 no recovery is observed. Rather, the completely unloaded sample exhibits the remaining deformation ε' . Below, as well as above the T-specific yield

1

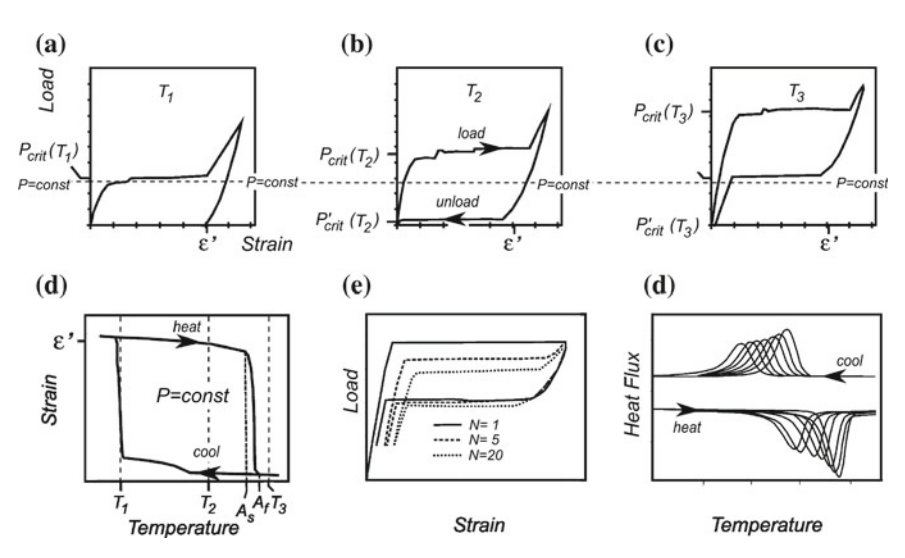


Fig. 1.1 Macroscopic phenomena with SMA. \mathbf{a} - \mathbf{c} Three load–strain isotherms of a NiTi wire. \mathbf{d} The corresponding strain-temperature relation for load P = const. (Courtesy of Musolff [9]). \mathbf{e} Tensile cycling of a pristine NiTi specimen. \mathbf{f} Thermal cycling in a DSC device, where phase transformations are indicated by deviations from the base line signals. The upper array of curves refers to austenite/martensite transformations during cooling and the lower one to reverse processes during heating. (Courtesy of Wagner and Frenzel [10])

and recovery loads, the sample is elastic within certain ranges. The high temperature load–strain response is called pseudo-elastic and that at low temperature is called pseudo-plastic.

The strain-temperature diagram of Fig. 1.1d may be derived from a set of load-strain isotherms by evaluation at a selected constant load. It is obtained from the load-strain curves in (a)–(c) for the constant load P = const. indicated. The strain-temperature diagram (d) may be used to explain the the shape memory effect (SME): subject to the tensile load P, the sample is pseudo-plastically deformed at low temperature T_1 to the strain ε' . The sample recovers shape if heated beyond the critical temperature $T = A_f$ in Fig. 1.1d. At high temperatures T_3 , the sample is only slightly strained, corresponding to the applied load remaining constant during the heating, and this strain may be further recovered elastically, if the sample is unload at this temperature (not shown). This observation conveys the impression that the alloy "remembered" its reference shape, thus suggesting the material's name.

Unfortunately—from an engineer's viewpoint—the process diagrams of SMAs exhibit hysteresis. In general, the width of the hysteresis loops depend on the specific alloy under consideration and on the processing of the sample. Loading direction also has an impact on the hysteresis behaviour, especially in single-crystalline samples. Some materials may exhibit vanishing hysteresis with $P_{\rm crit}(T) \approx P'_{\rm crit}(T)$. However, the situation can become even worse: the material's hysteresis appears to depend on the history of the processes performed on it. Transformation loads and

transformation temperatures change during cyclic mechanical or thermal loading. This effect is augmented for pristine materials following casting/heat treatment, but it also affects their long-term service properties. Material scientists subsume such behaviour under the terminology *functional fatigue* [11–14] because of its detrimental effect on material reliability in technical applications. Figure 1.1 illustrates this property during (e) mechanical cycling (20 load cycles) and (f) thermal cycling, as observed with a NiTi sample.

1.1.2 Martensitic Transformations

The SME is based on a special class of solid-solid phase transformations called *martensitic transformations* (MT). These occur in crystalline materials between two fundamental lattice structures called austenite and martensite [15–18]. Austenite forms highly symmetric unit cells which are stable at high temperature. During a MT, the austenitic lattice undergoes a shear and or a shear/shuffle type of transformation and forms martensite which has a lesser degree of symmetry. Variants of martensite exist, basically because there are different deformation modes of the austenitic lattice. Martensite is stable at low temperature, such that lattice transformations may be induced by lowering the temperature below certain transformation temperatures (temperature induced MT). At high temperatures, where austenite is stable, MT may be also induced by applying external loads.

The investigation of MT has a long tradition. It can be traced back to early observations in the 19th century of *martensitic microstructures* in steel—the eponym is Adolf Martens — and has produced a vast literature. An internet inquiry yields a total of 11,488 hits on the Boolean keyword combination ("martensitic transformation" or "martensitic microstructure") and "shape memory" for the period 1955-2008 [41]. Figure 1.2 depicts this research activity. Notwithstanding this, a final definition of MT which is accepted by all scientists on the field is still overdue. Vivid discussions on this topic are documented in the literature. As late as 1995, the International Conference on Martensitic Transformations (ICOMAT) included a panel discussion, where P.C. Clapp presented a review of past definitions under the provocative title "How would we recognise a martensitic transformation if it bumped into us on a dark & austy night?" His own "irreducible" conjecture was: "A martensitic transformation involves a cooperative motion of atoms across an interface causing a shape change and sound" [42]. The constituents of other definitions were

- MT is diffusion-less and entails a cooperative movement of atoms, leading to a change in shape of the entire body,
- during MT, nearest atomic neighbours remain nearest neighbours,
- MT involves growth processes,
- MT exhibits undistorted, straight interfaces between the parent and the product phase,

¹ The diagram also nicely reveals an inflationary increase in publications in the internet age.

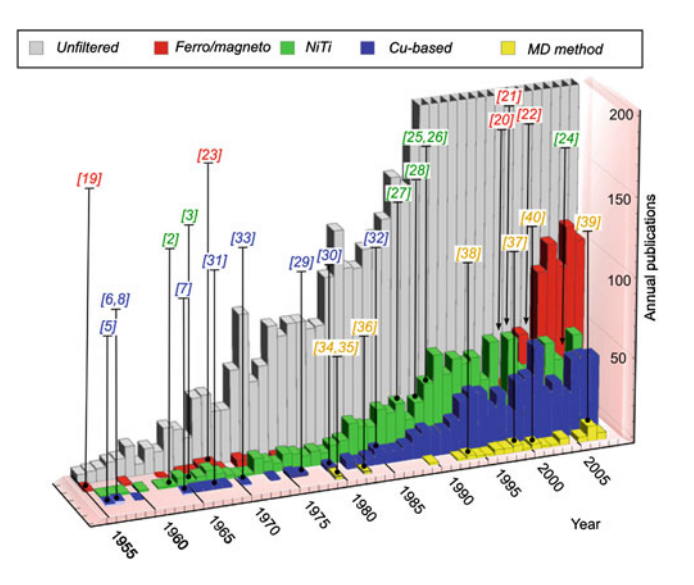


Fig. 1.2 Research activity on shape memory alloys and martensitic transformations 1955–2008. Internet database queries for publications with Boolean keyword combinations of ("martensitic transformation" or "martensitic microstructure") and "shape memory" in the title (grey, cut-off above 200 hits/year). Additional filter settings with respect to specific materials, yield the coloured columns. The labels [5...40] reference pioneering and most cited works. Note only 46 works match a combinatorial query with respect to ("molecular dynamics" or "atomistic methods").

 MT includes orientation relationships between principle directions of the lattices involved.

Olson's definition summarises most of these constituents and is generally accepted today: MT is a shear dominant, lattice distortive, diffusion-less transformation occurring by nucleation and growth [43].

1.1.3 Microstructures

A twinned microstructure is a characteristic of martensite. Twins are martensite variants which are crystallographically compatible along their interface and energetically equivalent. The formation dynamics are complex and yield characteristic, twinned domain structures. Figures 1.3, 1.4 and 1.5 show examples from the centimetre down to the nano scale of lengths.

The martensitic morphology is distinctively recognised in copper based SMA. Figure 1.3 shows observations with a CuNiAl single crystal. On the centimetre scale (a,b), martensite forms wedge-shaped domains by nucleation and growth. If the sample is polished in the austenitic phase, the wedges produce tangible surface textures: the flanks of the wedges in (b) are slightly tilted such that they protrude from the plane

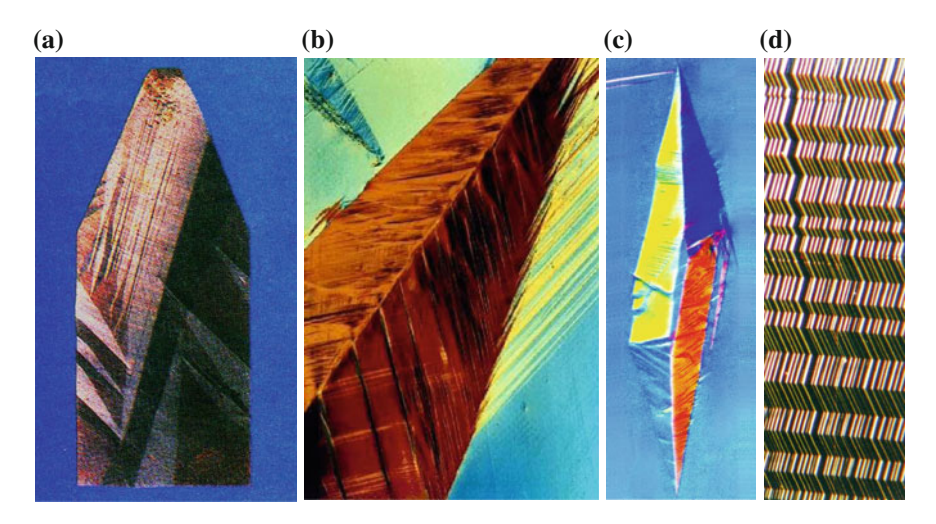


Fig. 1.3 Martensite in a CuNiAl single crystal plate. a Temperature-induced wedge-shaped martensitic domains. Centimetre-scale. b Low magnification $(16.5\times)$ of a single wedge (orange). c Four-sided nucleus of compatible variants which belong to the same plate group. Magnification $100\times$. d Regular stacks of twins. Magnification $200\times$ [44]

by a small angle. The angle is not arbitrary, rather it is dictated by the crystallographic compatibility condition between parent and product phases. Their interface, called the habit plane, is macroscopically sharp and planar. Fiducial scratches, tagged on a sample in the parent phase, remain piecewise linear in the product phase. A similar compatibility relation holds between martensite twin variants. Compatible variants form *plate groups*. Fig. 1.3 (c) shows a martensite nucleus that consists of four variants belonging to the same plate group. Twinned structures are produced during self-accommodation processes while martensite is formed. The product exhibits a lamellar structure of regularly stacked, alternating twin variants. These can be observed by optical microscopy at the sub-millimetre scale in Cu-based alloys, Fig. 1.3(d), but are also reflected on much smaller scales, see below.

Figure 1.4 illustrates how martensite wedges are macroscopically formed in a CuNiAl single crystal, showing a series of snapshots obtained from a differential image correlation (DIC) study. The material is the same as in Fig. 1.3. DIC traces the evolution of surface deformations by means of a computer-aided analysis of digital images taken continuesly during the process. For this purpose, the sample needs to be coated with a tracer paint. Using stereographic projection, the method yields all components of the transformation surface strains. Figure 1.4a shows the MT nucleation at a singular point at the plate edge. It forms a wedge by a growth process into the bulk material (b)–(c). Eventually, more nuclei appear at other loci and grow, producing a diverse martensite structure (d). The final product (not shown) is similar to the one of Fig. 1.3a.

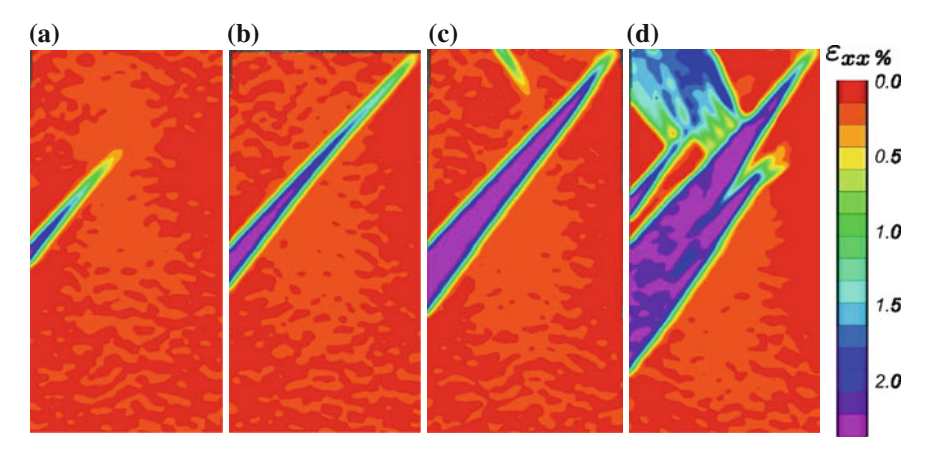


Fig. 1.4 Four consecutive snapshots during a DIC observation of the nucleation and growth of martensite wedges in an austenitic CuNiAl single crystal plate. Plate dimensions $50 \times 25 \times 3$ mm. Colours code the transformation strains ε_{xx} with respect to the austenitic reference configuration (red/orange). Martensite plates exhibit almost homogeneous strains (purple). Note the significant strain gradient field around the wedges. Ref. [45] with courtesy of Musolff for providing the sample (Video available online)

Transmission electron microscopy (TEM) reveals the structure of martensite down to the atomic length scale. Figure 1.5 presents images of various materials from the micro- to the nanometric scale. NiTi (a, c) has a comparatively small-sized domain structure. The two images in (a) and (c), show the characteristic twin lamella of martensite in this alloy. In the case of (c), the martensitic self-accommodation process has produced the typical herringbone structure within a small grain. The lamellar morphology is more pronounced in (b) which depicts a TEM image of NiTiFe. The use of high resolution (HR) TEM enables morphologies to be studied even down to the atomic scale, Fig. 1.5d. Here, white dots locate the positions of individual atoms in a NiAl lattice—or rather, the positions of atomic columns oriented in the viewing direction. This image beautifully confirms that locally, MT produces homogeneous deformations within individual lamellae, where the lattice is regular. Thus, the structure must have been produced by regimented atomic movements during the transformation, which inspired the phrase military transformation. For this particular example, the lamella widths range between 10 and 20 unit cells. Across the interfaces of the adjacent lamellae, the strain field is discontinues.

1.1.4 Scales

Materials sciences experimentally and theoretically address the properties of materials across a range of length- and times scales. The technical evolution of microscopy and the coming of computational sciences have emphasised this general approach

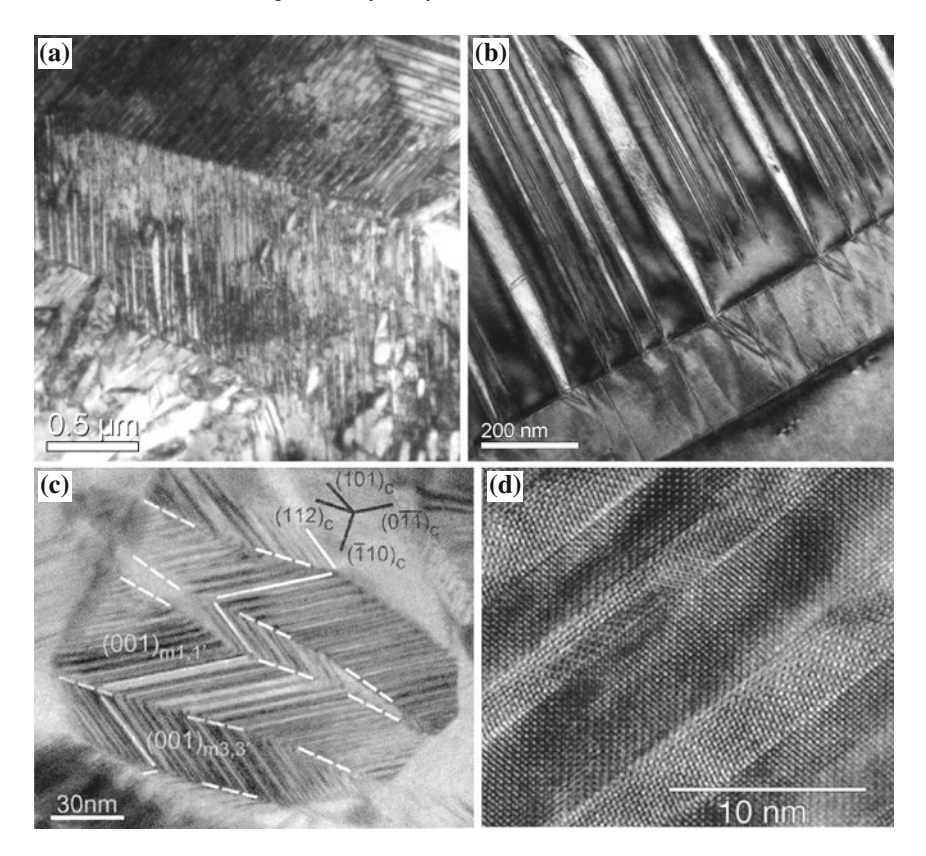


Fig. 1.5 TEM and HR-TEM images of martensite in various SMAs, micro- to nanometre length scale. **a** NiTi, **b** NiTiFe (both images courtesy Ch. Somsen [46]). **c** NiTi [47]. **d** NiAl courtesy D. Schryvers [48]

during the past decade. Shape memory alloy research may well be viewed as a prime example of this. Macroscopic observables are temperature, load and strain. Experiments exhibt a characteristic coupling of these quantities, effectively rationalised by thermodynamics. On the other hand, microscopy unveils complex details of these lattice transformations at the atomic length scale: product lattices are constituted by (locally homogeneous) transformation strains, governed by coherency constraints to be met along planar phase interfaces. These constraints are met during accomodation processes, forming destinct microstructures. High-resolution transmission electron microscopy is capable of resolving these with atomic detail post-mortem, however, the formation *dynamics* remains experimentally unresolved at this scale level. To understand the dynamics on the atomic scale, we are to rely on theoretical approaches. Here, the micro scale variables are positions and velocities of discrete atoms. These quantities are governed by equations of motion. Still, thermodynamics rules stability, but in this case the stability criterion is determined by atomic vibrations and interaction forces. The forces, however, cannot be measured directly.

In this situation, the sub-atomic scale gains importance, as binding forces between atoms are dependent of the distributions of charged sub-atomic particles, electrons and protons.

Against the background of this complexity, it is easy to see that the physics of shape memory alloys indeed poses a multi-scale problem. The significant time and length scales may be roughly divided into the four categories sub-micro-meso-macro. Each scale employs characteristic times and lengths.

The sub-microscopic level concerns the electronic structure of atomic cores and the related electron distributions. These are investigated by means of ab initio models and quantum mechanics. On the microscopic level, atoms are considered as masspoints in the mathematical sense. Based on semi-emperical interaction-functions given, formations of lattice structures can be investigated by molecular dynamics simulations and, statically, by relaxation methods. Characteristic times and lengths are the period of an atomic oscillation (≈ 1 fs) and a lattice constant (≈ 1 Å), respectively. Processes accessible by these methods range up to nano seconds and micro metres. The mesoscopic scale level is somewhat ambiguously positioned between micro and macro and concerns characteristic microstructural entities having the capability of influencing the macroscopic material properties as ensembles. Examples are martensite lamellae, precipitates, inclusions, dislocations, grains and domains. Mesoscopic entities have characteristic lengths from nanometres up to micrometres. The characteristic time may be defined with respect to the speed of sound. Mesoscale processes are accessible by both atomistic and continuum methods ("micro-mechanics"), thus opening up the opportunity of transferring information between these two modelling techniques.

Above the mesoscopic level, matter is considered to be macroscopically continuous and the classical continuum theories of mechanics and thermodynamics are applied. A typical numerical tool used for computing the continuum-level field equations is the finite element method (FEM).

While each scale incorporates complex theories and sophisticated mathematical toolsets of own rank, additional challenges arise from the need of bridging information between the scale, since different, scale-specific sets of variables are used. For example, atomic interaction forces on the micro scale depend on charge distributions resolved on the submicro-scale. These, however, are not represented on the micro scale. Similarly, constitutive equations are required as function of the thermo-mechanical field variables on the macro-scale, whereas the microscale concerns velocities and positions of atoms. Bridging between the scales is a classical problem and has been tackled since long. Cauchy, for example, derived the elasticity tensor of a monatomic solid in 1890 based on assumptions on the atomic interactions. His work has yielded restrictive relations on the number of independent elastic constants [49] which, however, were later experimentally disproved. These *Cauchy relations* are therefore today regarded as a negative test for the reliability of an atomic interaction model.² Another, most important classical scale-bridging method was contributed

² Note in 1915, Born was able to prove the Cauchy relations do not apply in the case of nested, many-species lattices owing to the contributions from interactions between the sublattices [50].

within the framework of statistical thermodynamics by Maxwell and Boltzmann. Boltzmann's statistical interpretation of the entropy for an ideal gas was quickly extrapolated to condensed matter; his approach still represents the only theoretical method of rationalising entropy and all related thermodynamic quantities from first principles. For this reason his famous formula $S = k \log W$ ranges among the most important equations of all physics [51].

1.2 Crystallographic Theory

The crystallographic theory of martensite [15, 16, 18, 52–56] relies on two phenomenological macroscopic observations: First, austenite-martensite phase boundaries appear as invariant *habit planes*, which are sharp, non-rotated and undistorted. Second, linear fiducial scratches remain piecewise linear after the transformation. From these two observations it can be concluded that, macroscopically, the deformation gradient **F** may be expressed by

$$\mathbf{F} = \mathbf{I} + \mathbf{d} \otimes \mathbf{p} \tag{1.1}$$

(**p**—normal to the habit plane, **d**—arbitrary vector, **I**—identity matrix). Microscopically, the deformation gradient can be represented by a combination of the Bain transformation $\mathbf{B}(\eta_1, \eta_2, \eta_3)$, simple shear $\mathbf{P}(s)$ and rotations $\mathbf{R}(\alpha, \beta, \gamma)$,

$$\mathbf{F} = \mathbf{RPB}.\tag{1.2}$$

The Bain transformation incorporates changes in the lattice parameters (η_1, η_2, η_3) during the transformation. This is illustrated in Fig. 1.6. The lattice parameters can, in principle, be measured by X-ray methods and thus are taken as given in this theory. The shear is indicated by a scalar shear parameter s and the rotation by the three Eulerian angles (α, β, γ) . Both shear and rotation are required to compatibly "fit" the product to the parent along a habit plane.

Equations (1.1) and (1.2) establish a nine-dimensional algebraic system for determining the components of \mathbf{d} and \mathbf{p} ; the rotations and the shear as functions of the Bain parameters ($|\mathbf{p}|=1$ serves as implicit condition). This system is non-linear, thus multiple solutions exist which indicate martensite variants. Among these variants, not all pairings are compatible such that martensite twins form. Twins are formed by pairs of compatible variants \mathbf{F} and $\tilde{\mathbf{F}}$ that obey the twinning condition

$$\mathbf{F} - \tilde{\mathbf{F}} = \mathbf{a} \otimes \mathbf{m} \tag{1.3}$$

along their interface (**m**—normal to that interface, **a**—arbitrary vector). This condition holds if one of the two following conditions is satisfied: either the deformation

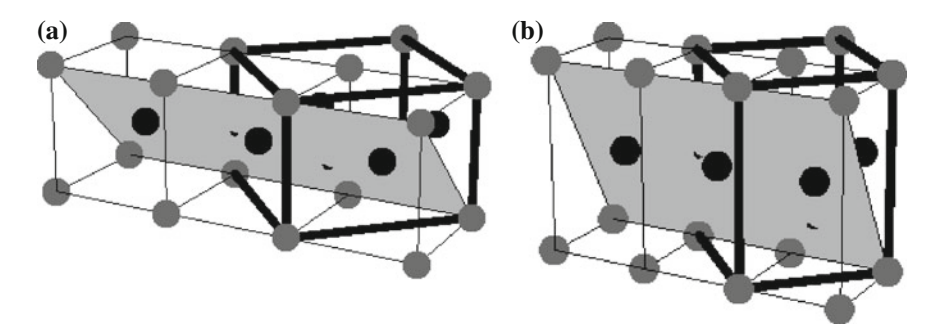


Fig. 1.6 Bain transformation of a body-centred-cubic (bcc) lattice. The cubic parent lattice (**a**) may be alternatively described by primitive bcc unit cells (thin lines) or by face-centred-tetragonal (fct) unit cells (bold lines). The Bain transformation stretches the fct lattice homogeneously along one cell axis and compresses it along the other two, thus producing a deformed fct cell in the product lattice (**b**), while the bcc parent cells deform into bct product cells. The Bain parameters (η_1 , η_2 , η_3) indicate the ratios of the fct unit cell edge lengths in the two structures. During this process, the plane (011)_{bcc} is slightly rotated so as to become the product plane (011)_{bct} which is close-packed

vectors d and \tilde{d} or the habit plane normals p and \tilde{p} of the variant pair concerned are parallel.

Kinematic compatible martensites:
$$\mathbf{d} \parallel \tilde{\mathbf{d}} \vee \mathbf{p} \parallel \tilde{\mathbf{p}}$$
. (1.4)

To model the lamellar microstructure of martensite, energetic arguments were introduced. The concept by James and Ball [57] follows the idea that the microstructure may be represented by a sequence of piecewise homogeneous deformations $y^i(x)$ which obey the crystallographic conditions. The microstructure is determined by minimising the total free energy F in a domain Ω ,

$$F = \int_{\Omega} f(\mathbf{F}(y^{i})) dx + \sigma A(i) \to \min!, \tag{1.5}$$

where the specific free energy f is represented by the elastic strain energy of the sequence. The term $\sigma A(i)$ represents the interface energy between martensitic vari-

³ Proof following I. Müller in three steps:

^{1.} Suppose $\mathbf{d} \parallel \tilde{\mathbf{d}}$, that is $\tilde{\mathbf{d}} = \alpha \mathbf{d}$, where α is a real scalar. Hence $\mathbf{F} - \tilde{\mathbf{F}} = \mathbf{d} \otimes (\mathbf{p} - \alpha \tilde{\mathbf{p}})$ and we conclude that the condition (1.3) holds for $\mathbf{a} = \mathbf{d}$ and $\mathbf{m} = \mathbf{p} - \alpha \tilde{\mathbf{p}}$.

^{2.} Suppose $\mathbf{p} \| \tilde{\mathbf{p}}$, that is $\tilde{\mathbf{p}} = \beta \mathbf{p}$, where β is a real scalar. Hence $\mathbf{F} - \tilde{\mathbf{F}} = (\mathbf{d} - \beta \tilde{\mathbf{d}}) \otimes \mathbf{p}$ and we conclude that the condition (1.3) holds for $\mathbf{a} = \mathbf{d} - \beta \tilde{\mathbf{d}}$ and $\mathbf{m} = \mathbf{p}$

^{3.} Now suppose that the two vectors \mathbf{p} and $\tilde{\mathbf{p}}$ are not parallel, $\mathbf{p} \not\parallel \tilde{\mathbf{p}}$. Thus the normal vector \mathbf{m} may be represented as a linear combination of \mathbf{p} and $\tilde{\mathbf{p}}$, $\mathbf{m} = \alpha \, \mathbf{p} + \beta \, \tilde{\mathbf{p}}$, where α , β are real scalars. It follows from (1.3) that $\mathbf{d} \otimes \mathbf{p} - \tilde{\mathbf{d}} \otimes \tilde{\mathbf{p}} = \mathbf{a} \otimes (\alpha \, \mathbf{p} + \beta \, \tilde{\mathbf{p}})$, or, after re-arranging $(\mathbf{d} - \alpha \, \mathbf{a}) \otimes \mathbf{p} = (\tilde{\mathbf{d}} - \beta \, \mathbf{a}) \otimes \tilde{\mathbf{p}}$. This condition implies the vectors \mathbf{d} and $\tilde{\mathbf{d}}$ must be parallel in this case, since $\mathbf{d} = \alpha \, \mathbf{a}$ and $\tilde{\mathbf{d}} = \beta \, \mathbf{a}$ are the only choices which meet the condition (1.3). With this result, we may now return to 1, which concludes the proof of the statement (1.4).

ants and it scales proportionally with the number of interfaces. *Without* the interface term, the variational Eq. (1.5) yields an unrealistic, infinitely fine microstructure, while finite-sized microstructures are generated if the interface energy is taken into consideration: The strain energy term in Eq. (1.5) delimits only a few interfaces while the interface term represses many interfaces. Thus when both terms are present, their effects mediated each other and they yield a finite-sized microstructure. A related variational model considers smooth energy functions and the interface energies are modelled as proportional to the square of the second derivative y''(x) [58–64]. Yet another related concept considers homogeneous phase mixtures and introduces phase field variables controlled by a set of Langevin type equations [65, 66]. Here again, strain gradients represent interface energies.

Kinetic aspects of phase transformations in solids were investigated separately by continuum methods [67–69], however, such work focuses on the thermodynamics of transformation shocks in one-dimensional settings whereby the microstructural detail is lost.

1.3 Thermodynamics

1.3.1 Phase Stability Criterion

The stability of a physical system is a subject of thermodynamics. If a system is exposed to non-equlibrium conditions, transport processes result which adjust the system variables. Such processes are described by the thermodynamic field theory. Continuum-scale field variables are defined, typically the fields of (partial) density, the motion related variables (partial) velocity and strain and temperature. These quantities must obey the local balance laws of (partial) mass, (partial) momentum and energy in all regular material points, and their respective jump conditions at singular surfaces. These balance equations incorporate a range of additional physical quantities called the "constitutive" equantions— caloric and thermal equations of state, heat flux and diffusion flux, etc.—which must be determined as functions of the field variables in order to constitute a closed mathematical system of equations. Experiments reveal these functions exhibit material-specific depencies of the field variables and their determination is subject of the thermodynamic materials theory. Thermodynamics axiomatically sets up an important constraint on the constitutive equantions, called the "entropy principle". This principle is constituted by the entropy balance, which represents an inequality: Entropy is not conserved during a thermodynamic process, rather than it experiences production which is non-negative by any experience [70].

Therefore, the entropy principle defines the "direction" of relaxation processes into equilibrium states, which are characterised by the phase equilibrium, the mechanical equilibrium and the thermal equilibrium. To see this we focus attention to the integral balance equations of mass, energy and entropy which we specify for the

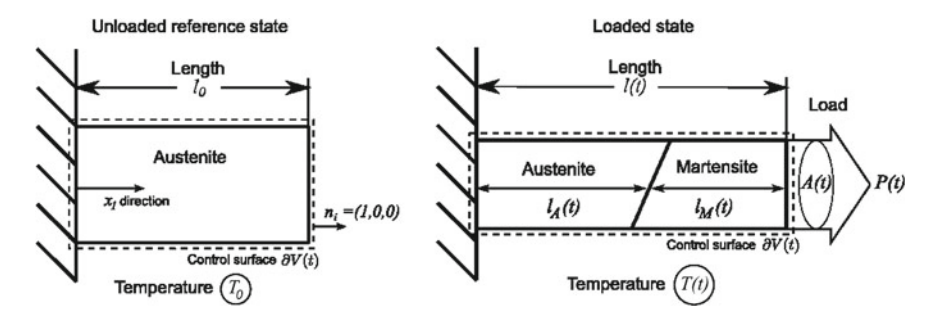


Fig. 1.7 Sketch on the phase stability criterion. A uni-axially applied load P affects the current length l(t) effecting work at a rate $P^{dl/dt}$ across the control surface

situation of a specimen under axial tensile load, cf. Fig. 1.7, in order to derive and investigate these thermodynamic equilibrium criteria. For details we refer to textbooks [71]; our presentation of the matter further benefits from the studies of [72–75].

The balance equations for mass, energy and entropy of the specimen under axial tensile load of Fig. 1.7 read

$$\frac{\mathrm{d}m}{\mathrm{d}t} = 0 \quad \to \quad m_M(t) = m - m_A(t),\tag{1.6}$$

$$\frac{\mathrm{d}m}{\mathrm{d}t} = 0 \quad \to \quad m_M(t) = m - m_A(t), \tag{1.6}$$

$$\frac{\mathrm{d}(U + K)}{\mathrm{d}t} = \dot{Q} + \oint\limits_{\partial V(t)} t_{ij} v_i n_j \, dA, \tag{1.7}$$

$$\frac{\mathrm{d}S}{\mathrm{d}t} \ge \frac{\dot{Q}}{T}.\tag{1.8}$$

We consider a specimen of mass m which may decompose into generic phases austenite (A) and martensite (M). The partial masses are m_A and m_M . The total mass is conserved, Eq. $(1.6)_1$, hence these partial masses are related, Eq. $(1.6)_2$.

The energy balance (1.7) states the change of the total energy—the sum of the internal energy U and the kinetic energy K—results from heat exchange Q with the ambience and from external working. Here we neglect working effected by body forces like gravitation or external magnetic fields in order to focus on the effect of tensional forces acting across the control surface $\partial V(t)$. These are represented by Cauchy stress t_{ij} acting on surface elements dA at the local velocities v_i These surface elements are oriented by normal vectors n_i .

The surface integral on the right-hand side of Eq. (1.7) may be simplified to a tangible expression employing some assumptions: As of Fig. 1.7, tensions are only acting across the surface segments to the left and right of the tensile specimen. To the left, it is rigidly fixed and the surface velocities are locally zero, $v_i = 0$. To the righthand side—the loading side—the velocity of the surface is $v_i = (dl(t)/dt, 0, 0)$ and only axial tensions are applied, which are effected by a nominal force P(t). Here, the surface has the size A(t) and the normal vector is $n_i = (1, 0, 0)$. Hence the axial

surface stress component reads $t_{11} = P(t)/A(t)$. In this simple situation the surface integral in Eq. (1.7) reduces to

$$\oint_{\partial V(t)} t_{ij} v_i n_j dA = \int_{A(t)} \begin{pmatrix} \frac{\mathrm{d}l(t)}{\mathrm{d}t} \\ 0 \\ 0 \end{pmatrix}^T \begin{pmatrix} \frac{P(t)}{A(t)} & 0 & 0 \\ 0 & 0 & 0 \\ 0 & 0 & 0 \end{pmatrix} \begin{pmatrix} 1 \\ 0 \\ 0 \end{pmatrix} dA = P(t) \frac{\mathrm{d}l}{\mathrm{d}t}.$$
(1.9)

We consider slow processes, where the changes of the kinetic energy K may be neglected. Further we assume the heat exchange \dot{Q} with the ambience occurs at a homogeneous surface temperature T. The entropy S of the specimen according to Eq. (1.8) then changes due to the heat exchanged at that temperature and by a—here not further specified—entropy production rate, which is non-negative. By eliminating the heat flux from Eqs. (1.7) and (1.8), and applying a Legendre Transformation, the stability criterion is furnished:

$$\frac{\mathrm{d}}{\mathrm{d}t}\left(U - TS - Pl\right) \le -S\frac{\mathrm{d}T}{\mathrm{d}t} - l\frac{\mathrm{d}P}{\mathrm{d}t}.\tag{1.10}$$

This criterion states for fixed external load P and fixed surface temperature T, the rate of the Gibbs free enthalpy $G \equiv U - TS - Pl$ is negative such that it eventually becomes minimal at equilibrium. This minimum-condition is a direct consequence of the entropy inequality.

A few re-arrangements are useful. Conventionally, the absolute axial length l(t) of the specimen is substituted by the strain $\varepsilon=(l-l_0)/l_0$, where $l_0(T_0,P=0)$ denotes a reference length. In the framework of SMA, the reference state is typically unloaded austenite at a reference temperature T_0 , where this phase is stable. In this state the loading surface has the area A_0 and $\rho_0=m(l_0/A_0)$ denotes the mass density in the reference state. The phase specific strains are ε_A and ε_M . These are defined for austenite and martensite with $l=l_A$ and $l=l_M$, respectively.

The Cauchy stress t_{ij} in Eq. (1.7) refers to the current area A(t). Alternatively, we may relate the applied forces P(t) to the reference area A_0 and define the (first) Piola–Kirchhoff stress component $\sigma = P/A_0$.

Finally, we may introduce mass-specific quatities of energy and entropy, u = U/m and s = S/m. The phase-specific equivalents of these quantities are $u_{A,M} = U_{A,M}/m_{A,M}$ and $s_{A,M} = S_{A,M}/m_{A,M}$, respectively. Empoying these definitions, the mass specific total free enthalpy reads $g = u - Ts - \sigma \varepsilon/\rho_0$. The mass-specific free enthalpies are defined as $g_A = u_A - Ts_A - \sigma \varepsilon_A/\rho_0$ for the austenite and $g_M = u_M - Ts_M - \sigma \varepsilon_M/\rho_0$ for the martensite, respectively.

According to Eq. (1.10) has the total free enthaply a minimum at equilibrium. Employing all the new quantities defined above, a global equilibrium state hence is characterised by the condition

$$\frac{\mathrm{d}}{\mathrm{d}t}\left(m_A g_A(T,\sigma) + (m - m_A)g_M(T,\sigma)\right) = 0. \tag{1.11}$$

The mass balance $(1.6)_2$ was evaluated to eliminate m_M . Equation (1.11) therefore depends on the three independent variables m_A , T and σ , implying three necessary conditions for global equilibrium:

$$\left(\frac{\partial g}{\partial m_A}\right)_{T,\sigma} = 0, \quad \left(\frac{\partial g}{\partial T}\right)_{m_A,\sigma} = 0, \quad \left(\frac{\partial g}{\partial \sigma}\right)_{T,m_A} = 0.$$
 (1.12)

These are the conditions for the phase equilibrium, the thermal equilibrium and the mechanical equilibrium, respectively. Especially, Eq. $(1.12)_1$ implies

$$\left(u_A - Ts_A - \frac{\sigma \varepsilon_A}{\rho_0}\right) = \left(u_M - Ts_M - \frac{\sigma \varepsilon_M}{\rho_0}\right). \tag{1.13}$$

The index "E" reminds us this eqution refers to an equilibrium state.

The phase equilibrium condition (1.13) relates the phase transformation load $\sigma(T)$ and the phase transformation temperature $T(\sigma)$. Their dependency is expressed by the Clausius–Clapeyron equation:

$$\frac{\mathrm{d}\sigma}{\mathrm{d}T} = \rho_0 \frac{s_A - s_M}{\varepsilon_M - \varepsilon_A}.\tag{1.14}$$

This relation is directly obtained from Eq. (1.13) by resolving it σ and subsequent derivation with respect to T.

Experiments reveal that under tensional loading, the transformation stress of austenite/martensite transformations $\sigma(T)$ is always increasing with temperature. So the right-hand side of Eq. (1.14) must be positive. The strain difference $(\varepsilon_M - \varepsilon_A)$ in the denominator on the right-hand side of this equation represents the transformation strain and this quantity also is positive, since the strains refer to an austenitic reference state. In order to meet the experimental observation, Eq. (1.14) therefore requires the difference of the specific entropies $(s_A - s_M)$ must be positive too. Accordingly, the specific entropy s_A of austenite must be bigger than the specific entropy of martensite s_M . An atomistic explanation of this condition is given in Sect. 3.2.3.

There are two approaches to graphically evaluate the phase equilibrium condition of Eq. (1.13). These are known as the "rule of equal areas" and the "rule of common tangents". To see this, we may re-write Eq. (1.10) assuming reversible conditions⁴ to yield the Gibbs Equation,

$$\frac{\mathrm{d}(u - Ts)}{\mathrm{d}t} = -s\frac{\mathrm{d}T}{\mathrm{d}t} + \frac{\sigma}{\rho_0}\frac{\mathrm{d}\varepsilon}{\mathrm{d}t}.$$
 (1.15)

The combination of internal energy u and entropy s and the left-hand side of this equation defines the mass-specific Helmholtz free energy $f \equiv u - Ts$. We see from

⁴ In thermodynamics, a process is called reversible if the entropy production is zero. In this case the entropy balance (1.8) turns into an equality. In nature no such processes exists, therefore the idea of reversibility must be regarded as an idealisation.

Eq. (1.15) that this free energy is depending on the variables T and ε . Therefore the total differential $df(T.\varepsilon)$ reads

$$\frac{\mathrm{d}f(T,\varepsilon)}{\mathrm{d}t} = \left(\frac{\partial f}{\partial T}\right)_{\varepsilon} \frac{\mathrm{d}T}{\mathrm{d}t} + \left(\frac{\partial f}{\partial \varepsilon}\right)_{T} \frac{\mathrm{d}\varepsilon}{\mathrm{d}t}.$$
 (1.16)

Comparing the coefficients between Eqs. (1.15) and (1.16) we see that the stress $\sigma(T,\varepsilon)$ is fundamentally related to the free energy under isothermal conditions through

$$\frac{\sigma(T,\varepsilon)}{\rho_0} = \left(\frac{\partial f}{\partial \varepsilon}\right)_T \quad \text{or, with } f \equiv u - TS:$$

$$\frac{\sigma(T,\varepsilon)}{\rho_0} = \left(\frac{\partial u}{\partial \varepsilon}\right)_T - T\left(\frac{\partial s}{\partial \varepsilon}\right)_T, \quad (1.17)$$

Equation (1.17) may be easily extended to all components of the stress tensor, see [76]. We see the stress has both an energetic and an entropic part, as indicated in Eq. $(1.17)_2$. Both parts are significant in SMA!

Figure 1.8 shows a generic (stress, strain) isotherm in subfigure (a) and the according free energy function in subfigure (b). Note that the (stress, strain) isotherm in (a) is non-monotonous, which corresponds to the non-convexity of the free energy isotherm in (b), since the two graphs are related through Eq. (1.17)₁. Instable branches of these curves are dashed: the stress exhibits a negative slope in this region and the free energy is concave. We may explain the "rule of equal areas" and the "rule of common tangents" using these illustrations.

The "rule of equal areas" represents an interpretion of the phase equilibrium condition (1.13) in the (σ, ε) space. Due to the non-monotonicity of the stress/strain curve in Fig. 1.8a, the stable branches of the stress/strain curve overlap for some stress range. The transformation stress has to be determined within this range. To see this we may re-write Eq. (1.13) employing Eq. (1.17)₁ and yield the expression

$$\int_{\varepsilon_A}^{\varepsilon_M} \sigma(T, \hat{\varepsilon}) \, d\hat{\varepsilon} = \sigma(T)(\varepsilon_M - \varepsilon_A). \tag{1.18}$$

This equation implies the graphical interpretation visualised in Fig. 1.8a: The phase transformation stress is defined by that specific constant stress line $\sigma(T)=\mathrm{const.}$ which preserves equal sizes of the two areas $\int\limits_{\varepsilon_A}^{\varepsilon_M}\sigma(T,\hat{\varepsilon})\,d\hat{\varepsilon}$ and $\sigma(T)(\varepsilon_M-\varepsilon_A)$. Or, equivalently, the grey-shaded areas indicated in that figure are of equal size. The respective transformation stress $\sigma(T)$ line is called the "Maxwell Line". Below ε_A , the specimen is homogeniously austenitic and it is homogeniously martensitic above ε_M . In these regions the material may be deformed elastically. In the strain range between ε_A and ε_M , austenite-martensite transformations occur

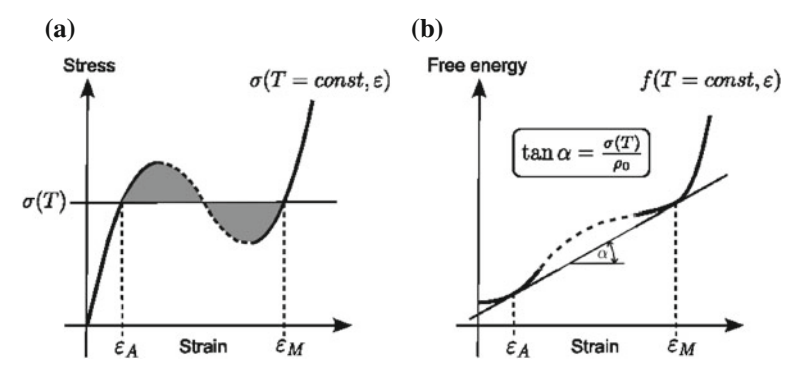


Fig. 1.8 Schematic stress/strain (a) and free energy/strain (b) isotherms. The rule of "equal areas" refers to (a) and the rule of "common tangents" to (b)

upon loading and martensite-austenite transformations occur upon unloading at the same constant stress $\sigma(T)$. Along this stress line, the specimen decomposes into a phase mixture of austenite and martenite such that the Maxwell Line is parametric in the mass-fractions of the phases.

The "rule of common tangents" represents an interpretion of the phase equilibrium condition (1.13) in the (f, ε) space. It represents an alternative interpretation of this condition. To see this, the phase equilibrium condition (1.13) and Eq. (1.17) are combined so as to give the equality

$$\frac{f_A - f_M}{\varepsilon_A - \varepsilon_M} = \frac{\sigma(T)}{\rho_0} = \left(\frac{\partial f}{\partial \varepsilon}\right)_{\varepsilon = \varepsilon_A} = \left(\frac{\partial f}{\partial \varepsilon}\right)_{\varepsilon = \varepsilon_M}.$$
 (1.19)

This equation implies a graphical interpretation in the (free energy, strain) diagram of Fig. 1.8b: At phase equilibrium, the partial derivatives of the free energy at the loci ε_A and ε_M are equal to both one another and to the transformation stress. This situation may be visualised by a common tangent attached to the respective convex branches of the free energy representing the two phases. The slope of this common tangent determines the phase transformation stress $\sigma(T)/\rho_0$. Again, below ε_A the specimen is homogeneously austenitic and homogeneously martensitic above ε_M . Elastic deformation of the two homogeneous phases is indicated by variations of the free energy within the respective convex wells of $f(\varepsilon, T)$. In between ε_A and ε_M , where the specimen decomposes into a phase mixture of austenite and martensite, the free energy evolves along the common tangent indicated in Fig. 1.8b rather than following the concave branch of the function $f(\varepsilon, T)$. Therefore, by decomposing into a mixture, the specimen "avoids" the energy barrierer of the function $f(\varepsilon, T)$ in this strain range. The path along the common tangent, parametrically in the massfractions of the phases, therefore is called a "convex hull" of the non-convex free energy in the language of mathematics.

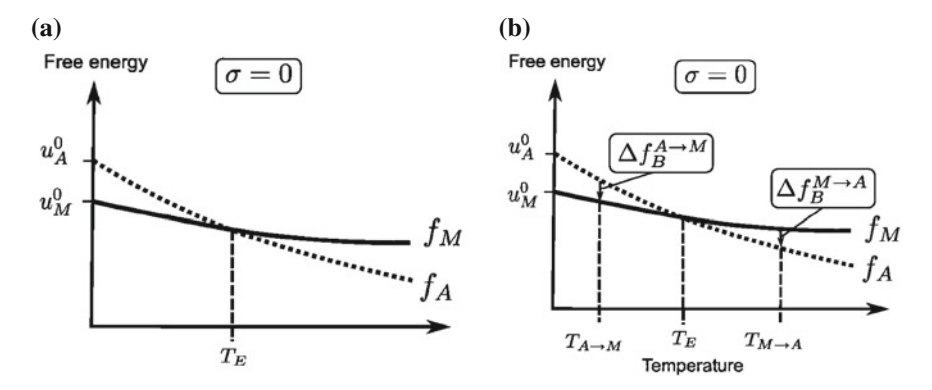


Fig. 1.9 Thermodynamic phase equilibrium criterion for the unloaded speciman. Sketches of the specific free energies of austenite (A) and martensite (M). **a** A unique transformation temperature as predicted by Eq. (1.10). No hysteresis! **b** Experimentally observed situation: Transformation hysteresis between the two observed transformation temperatures $T_{A \to M}$ and $T_{M \to A}$

We append an investigation of austenite/martenite transformations for the special situation of zero load, $\sigma(T) = 0$. In this case, the transformation is induced by change of temperature and the equilibrium theory predicts the phase fransformation occurs at the specific temperature $T_E = T(\sigma = 0)$. For this special case, the free enthalpies g_A and g_M reduce to the free energies f_A and f_M and the phase equilibrium condition of Eq. (1.13) becomes

$$(u_A(T, \sigma = 0) - T s_A(T, \sigma = 0)) \mid_E = (u_M(T, \sigma = 0) - T s_M(T, \sigma = 0)) \mid_E$$
(1.20)

All quantities in this equation refer to a mechanically unloaded state. Therefore, Eq. (1.20) may be used to calculate the phase transformation temperature T_E . An illustrative graphical interpretation of this situation can be given in the (free energy, temperature)-diagram, see Fig. 1.9a. This diagram visualises the two functions $f_A = u_A - Ts_A$ and $f_M = u_M - Ts_M$ of the unloaded specimen. Both are monotone in temperature and intercept the ordinate at $u_A^0 = u_A(T=0, \sigma=0)$ $u_M^0 = u_M(T=0, \sigma=0)$, the respective ground-state energies of the two phases. The slopes of the two free energy functions are given by the entropies $(-s_A(T\sigma=0))$ and $(-s_M(T\sigma=0))$. These are (roughly) logarithmic functions of temperature but contain phase specific constants responsable for the different slopes of $f_A(T)$ and $f_M(T)$. The intersection of the two functions f_A and f_M determines the transformations temperature T_E .

In the framework of the Clausius–Clapeyron Eq. (1.14) we have already mentioned that phenomenologically, the specific entropy of austenite must be bigger than the one of the martensite, $s_A > s_M$, therefore f_A must be steeper than f_M . In this situation, Eq. (1.20) requires the ground state energy u_M^0 of martenite must be smaller than the ground state energy u_A^0 of austenite, $u_M^0 < u_A^0$, to allow for temperature-induced transformations, see Fig. 1.9a.

Equation (1.20) suggests an interpretation of phase transformations between austenite and martensite in a broader view. Phase transformations in general occur as the result of two competing phase preferences, the ones of energy and of entropy [75]. While seeking for equilibrium, a sample tends to minimise the energy while it tends to maximise entropy at the same time. It turns out these quantities prefer different phases: Martensite produces lattice structures which minimise the internal energy, while the structure of austenite has comparably higher internal energy. This is reflected by the groundstate energies of the two phases. Therefore, martensite is the favourable phase from the energetic perspective. On the other hand, the austenite allows for a bigger specific entropy, than the martensite. Hence, austenite is the preferred phase from the perspective of entropy. Consequently, the phase stability is the result of a competition between the internal energy u and the entropy s, expressed by the free energy f = u - Ts. The temperature represents a weighting factor, which determines the influence of entropy. At low temperatures, this influence is diminished, hence allowing the specimen to follow the energetic phase preference. Accordingly, martensite is stable. With increasing temperature, the entropic influence is gradually augmented and eventuelly dominates. Therefore, austenite is stable at high T. At the phase transformation temperature T_E , energy and entropy are balanced. This mechanism is called "entropic phase stabilisation" of austenite. It represents a general concept in thermodynamics [75]. In the framework of austenite/martensite transformations discussed in this book we will explain this mechanism on the background of an atomistic model.

1.3.2 Nucleation and Hysteresis

The classical thermodynamic treatment of phase transformations in fluids is based on the Gibbs equation and implies process reversibility. Phase stability is determined by the Gibbs free energy for homogeneous bulk matter, resulting in phase diagrams which are hysteresis-free. The Maxwell line in Fig. 1.8 is identical for austenite/martensite transformations as well as for the reverse process. Similarly, a single phase transformation temperature T_E is predicted for an unloaded sample, see Fig. 1.9a. No hysteresis, neither in stress, nor in temperature arises from the thermodynamics theory presented so far. In contrast to this, hysteresis is well observed in the laboratory for both settings. In tensile tests, austenite/martensite transformations are observed at higher transformation stresses upon loading, than upon unloading for the reverse processes. Similarly, two transformation temperatures are detected for unloaded samples in DSC devices between temperatures $T_{M\to A} > T_E$ and $T_{A \to M} < T_E$. The widths and shapes of the hystereses depend on the specific alloy, the crystal structure, processing parameters or even specific tensile loading directions. Also, hystereses appear to depend on the history of the processes performed with the material: the transformation stresses and the transformation temperatures change after cyclic mechanical or thermal loading. This effect is most pronounced for virgin materials after casting/heat treatment, but also affects their service properties. Material scientists subsume such behaviour under the terminology *functional fatigue* [11–14] because of its detrimental effect on material reliability in technical applications.

Figure 1.9 (b) illustrates the situation of thermal hysteresis in the free energy/ temperature diagram. Two transformation temperatures $T_{M\to A} > T_E$ and $T_{A\to M} < T_E$ are indicated along the abscissa. The two graphs in this figure represent the same equilibrium free energies of austenite and martensite, as in the reversible case of Fig. 1.9a. At $T_{M\to A} >$ and $T_{A\to M}$, the two graphs do not coincide but differ from one another by $\Delta f_B^{A\to M}$ and $\Delta f_B^{M\to A}$, respectively. These are interpreted as nucleation barriers. This suggests that in order to model hysteresis—the effects of undercooling and overheating with respect to T_E —the thermodynamic theory must be enriched by free energy nucleation barriers Δf_B .

According to the definition of the free energy such barriers consists of an energetic part Δu_B and an entropic part $T \Delta s_B$ in general,

$$\Delta f_R = \Delta u_R - T \Delta s_R. \tag{1.21}$$

For specific materials, the contributions of the energy and entropy to the free energy barrier may vary. In the classical nucleation theory of fluids, the free energy nucleation barrier is represented by tensional interface energy raised to establish phase boundaries [77]. This ansatz yields hysteresis in condensation/evaporation processes of fluids [78–80]. The classical work has motivated similar approaches for SMA. Here, interface energies are attributed to lattice mismatch of the respective phases, hence effecting potential strain energy along the interface. Solid-solid phase transformations are affected by *local* compatibility concerns and stress fields to either side of the interface [16, 18]. Interfacial strain energies are strongly orientation-dependent and affected by defects and dislocations. According to the classical crystallographic theory [52], martensitic twinning provides a mechanism to produce a strain-free habit plane on the macroscopic scale. On the microscopic length-scale however, some degree of lattice mismatch is inevitable, causing strain fields and local disconnections at the interface [81]. On average, these microscopic effects produce a interface energy and cause hysteretic phase diagrams. In turn, hysteresis should vanish in rare situations where the parent and the product lattices match perfectly even on the microscale. For example, if the second eigenvalue of the crystallographic transformation matrix, λ_2 , is equal to 1, the habit plane can be defined without a twinned martensite [82]: Perfectly match between parent and product is expected. Experimental studies seem to prove the relationship between $\lambda_2 \approx 1$ and small hysteresis [83].

Experiments give evidence hysteresis and functional fatigue in SMA indeed related to the microstructure developed during thermo-mechanical processes [86, 87]. The formation process has to account both for lattice mismatch between parent and product as well as between product variants which gives rise to specific interface energies. These interfere the transformation process by adding energetic nucleation barriers. Nucleations typically occur at loci where some pre-existing interfaces offer favourable conditions. They are influenced by stochastic fluctuations of the field vari-

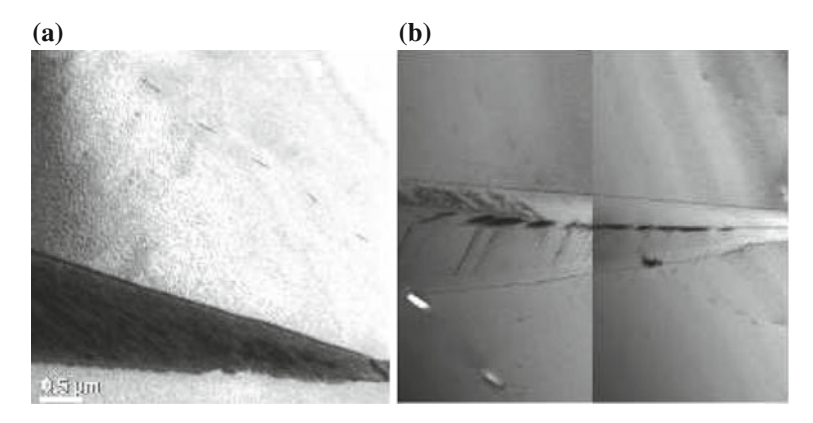


Fig. 1.10 TEM micrograph of the same region in a NiTi specimen upon temperature-induced martensitic transformation (**a**) and after the reverse transformation (**b**). The dark region in (**a**) indicates a T-induced martensite wedge. The wedge leaves faint dislocation marks in (**b**) after reverse transformation [84, 85] with courtesy of the authors

ables. Other experimental work reveals that the energetic situation at the interface between austenite and martensite is augmented by additional microstructural defects produced in both forward and reverse MT. The interaction of MT with any kind of structural defects (free surfaces, anti-phase boundaries, stacking faults, interfaces and precipitates) was intensely studied experimentally in recent years. An overview of the complexity of the physical situation is provided in [88] and applications have been made for CuZnAl [89] and AuCd [90]. The interactions of moving interfaces with such defects were investigated in [91] and [92] for Cu based alloys. The effect of aging on the temperature hysteresis in such alloys is documented in [93]. All these works refer to a strong relationship between the evolution of microstructural morphologies and the thermodynamic properties of the materials, indicating a history-dependence of the phase diagrams. Figure 1.10 illustrates a particular suggestive example of this: it shows the generation of a dislocative microstructure during forward and reverse MT in a NiTi sample. (a) and (b) show two TEM images of the same region within the sample during thermal forward MT in (a) and after completion of the reverse (b) [84, 85]. Note the wedge-shaped martensite region in (a) leaves behind a distinct dislocation footprint within the austenite matrix after reverse transformation feintly visible in (b). Thus, the forward/reverse transformation process has changed the lattice by adding new microstructural elements, dislocations in this case. Under cyclic thermal loading such microstructure develops and becomes more pronounced, see [94] for a study in Cu–Al–Mn. Sophisticated calorimetric studies unveil the influence of the temperature rates selected in an experiment [95] on thermal hysteresis.

Continuum models generally simplify solid—solid interfaces as singular surfaces (atomically sharp habit planes and twin boundaries) and assume phenomenological models for the surface energy. Typically, two approaches are taken [64]: either the interfaces are considered as singular surfaces with a localised surface energy [96],

or the interface is considered as a steep but smooth transition zone and the interface energy is modelled proportionally to the square of the strain gradient [58, 59].

Such nucleation barriers originate from mechanical effects and no entropic contributions to the nucleation barrier are regarded in these theories explicitly. However, for lattice transformations such effect must be expected. By MD simulations of nucleations events in 2D lattices we shall rationalise the nature of this entropic barrier (pages 97 ff).

1.3.3 Dynamics of Atomic Assemblies

The method of molecular dynamics is rooted in the concepts of classical mechanics. Here, the motions $\mathbf{x}_{\alpha}(t)$ of an assembly of $\alpha = 1, ..., N$ atoms are calculated as functions of time on the basis of Newton's second law,

$$m_{\alpha}\ddot{\mathbf{x}}_{\alpha} = \mathbf{f}_{\alpha} \quad (\alpha = 1, \dots, N).$$
 (1.22)

Atoms are mathematically considered as points with masses m_{α} . The Equations of Motion (1.22) represent a set of second-order differential equations. Their integration therefore involves two constants of integration per atom to be determined from initial conditions.

The forces f_{α} have two additive contributions: internal forces f_{α}^{int} and external forces f_{α}^{ext}

$$\mathbf{f}_{\alpha} = \mathbf{f}_{\alpha}^{\text{int}} + \mathbf{f}_{\alpha}^{\text{ext}}.\tag{1.23}$$

Internal forces arise from the atomic interactions, while external forces result from external force fields, such as gravitation, electrical and magnetic fields and from constraints acting on the surface of the assembly.

Internal and external forces may be represented as gradient fields of the internal and external potential functions $V^{\text{int}}(\mathbf{x}_{\gamma})$ and $V^{\text{ext}}(\mathbf{x}_{\gamma}, t)$, respectively:

$$\mathbf{f}_{\alpha}^{\text{int}} = -\nabla_{\alpha} V^{\text{int}}(\mathbf{x}_{\gamma}), \tag{1.24}$$

$$\mathbf{f}_{\alpha}^{\text{ext}} = -\nabla_{\alpha} V^{\text{ext}}(\mathbf{x}_{\gamma}, t). \tag{1.25}$$

The internal potential $V^{\rm int}$ is a material property and depends on the positions of all $\gamma=1,\ldots,N$ atoms. This quantity does not depend explicitly on time t but only implicitly through the time dependency of the atomic positions. In contrast to this, the external potential $V^{\rm ext}$ may also depend explicitly on t, as required by the external force fields.

The atomic velocities are obtained by differentiation of the motions with respect to time, $\dot{\mathbf{x}}_{\alpha}$. The centre of mass \mathbf{x} of the total assembly, the velocity of this mass centre \mathbf{v} and the excess atomic velocities \mathbf{c}_{α} are defined by

$$\mathbf{x} = \sum_{\alpha=1} \frac{m_{\alpha}}{m} \mathbf{x}_{\alpha},\tag{1.26}$$

$$\mathbf{v} = \sum_{\alpha = 1} \frac{m_{\alpha}}{m} \dot{\mathbf{x}}_{\alpha},\tag{1.27}$$

$$\mathbf{c}_{\alpha} = \dot{\mathbf{x}}_{\alpha} - \mathbf{v}.\tag{1.28}$$

Here, $m = \sum_{\alpha} m_{\alpha}$ is the total mass. Note that the N individual excess velocities \mathbf{c}_{α} are not entirely independent of each other, since the relation $\sum_{\alpha} m_{\alpha} \mathbf{c}_{\alpha} = 0$ holds true.

Regarding the Eqs. (1.23)–(1.26), summation of Newton's second law (1.22) over α yields Newton's first law, the Momentum Equation,

$$m\mathbf{v} = \sum_{\alpha=1}^{N} \mathbf{f}_{\alpha}^{\text{ext}}.$$
 (1.29)

This equation states that the momentum of the mass centre $(m\mathbf{v})$ is conserved in the absence of external forces.

The energy equation for the atomic assembly is obtained by a scalar-multiplication of Eq. (1.22) by $\dot{\mathbf{x}}_{\alpha}$ and subsequently summing over N. The result may be rewritten in the popular form by using Eqs. (1.24)–(1.28),

$$\frac{\mathrm{d}}{\mathrm{d}t} \left(\frac{m}{2} v^2 + V^{\text{ext}}(\mathbf{x}_{\gamma}, t) + V^{\text{int}}(\mathbf{x}_{\gamma}) + \sum_{\alpha=1}^{N} \frac{m_{\alpha}}{2} c_{\alpha}^2 \right) = \frac{\partial V^{\text{ext}}}{\partial t}.$$
 (1.30)

Consequently, if the external potential $V^{\rm ext}$ does not change with time, the quantity within the parenthesis—the total energy $\mathscr E$ of the system—is conserved:

$$\frac{\partial V^{\text{ext}}}{\partial t} = 0 \quad \Rightarrow \quad \frac{m}{2} v^2 + V^{\text{ext}}(\mathbf{x}_{\gamma}, t) + V^{\text{int}}(\mathbf{x}_{\gamma}) + \sum_{\alpha=1}^{N} \frac{m_{\alpha}}{2} c_{\alpha}^2 = \mathscr{E} = \text{const.}$$
(1.31)

The total energy \mathscr{E} consists of three parts: the (macroscopic) kinetic energy K, which is related to the square of the velocity of the mass centre, the potential energy of external force fields and the term underlined in Eq. (1.31). This term models the internal energy U of the assembly. It originates from the atomic interaction potential and from the kinetic excess energy.

We may also introduce the Lagrangian mechanics briefly since it is frequently used in the MD-related literature. Lagrange's approach is convenient in situations where the atomic motions need to be represented in non-Cartesian coordinates, or if special constraints need to be incorporated in the formulation. Lagrange considered the equation

$$\sum_{\alpha=1}^{n} (m_{\alpha} \ddot{\mathbf{x}}_{\alpha} - \mathbf{f}_{\alpha}) d\mathbf{x}_{\alpha} = 0, \tag{1.32}$$

which represents an alternative formulation of Newton's equations of motion (1.22), and applied a bijective variable transformation of the type

$$q_k = q_k(\mathbf{x}_{\alpha}, t) \quad (k = 1, \dots, 3N) \quad \Leftrightarrow \quad \mathbf{x}_{\alpha} = \mathbf{x}_{\alpha}(q_1, \dots, q_{3N}, t).$$
 (1.33)

In the case of an *unconstrained* system, i.e. a system not subject to any external force field, an application of the transformation (1.33) in (1.32) yields a new set of 3 N differential equations which control the motions of the atoms. These are called Lagrange's equation of motion,

$$\frac{\mathrm{d}}{\mathrm{d}t} \left(\frac{\partial \mathcal{L}}{\partial \dot{q}_k} \right) = \frac{\partial \mathcal{L}}{\partial q_k}.\tag{1.34}$$

 \dot{q}_k , as usual, denote the time-derivatives of the coordinates q_k and \mathcal{L} is called the *Langrangian*, an energy function representing the difference of the kinetic energy $T(\dot{q}_k)$ and potential energy $V^{\rm int}(q_k)$ of the unconstrained system,

$$\mathcal{L} = T(\dot{q}_k) - V^{\text{int}}(q_k). \tag{1.35}$$

Lagrange's and Newton's equations of motion (1.22), (1.34) are identical if the coordinates q_k are represented in a Cartesian frame. In this case the Lagrangian reads

$$\mathcal{L}(\mathbf{x}_{\alpha}, \dot{\mathbf{x}}_{\alpha}) = \sum_{\alpha=1}^{N} \frac{m_{\alpha}}{2} \dot{x}_{\alpha}^{2} - V^{\text{int}}(\mathbf{x}_{\alpha}). \tag{1.36}$$

Up to this point, the model's equations rest entirely on the axioms of Newton, which represent first principles of physics. To calculate the atomic motions for a specific material we need to define the potential $V^{\rm int}$ as functions of the atomic positions.

1.3.4 Statistical Thermodynamics

The macroscopic energy state of an N-atom assembly is entirely determined by the atomic micro-states $\{\mathbf{x}_{\alpha}(t), \dot{\mathbf{x}}_{\alpha}(t)\}$. This 6N-tuple indicates a *phase* of the assembly. It may be represented by a point in the 6N-dimensional phase space, in which it moves along a trajectory as a function of time. If the assembly is unconstrained, the energy state is entirely determined by the initial phase $\{\mathbf{x}_{\alpha}(t_0), \dot{\mathbf{x}}_{\alpha}(t_0)\}$ at the initial time t_0 owing to Eq. (1.31). Thus, the trajectory of the unconstrained assembly is bound to a hyperplane of the phase space determined by the initial energy $\mathscr{E}(t_0)$, which is

24 1 Preparations

constant. Since we are dealing with a classical system, this trajectory represents a continuous line, parametric in time. Along this line, ν observations of the assembly at consecutive times (t_1, \ldots, t_{ν}) yield an ensemble of phases, all indicated by the same total energy. Such an ensemble is called a "microcanonical" ensemble of phases.

A subset of S atoms of the N-atom assembly has the energy $\mathscr{E}^S(\mathbf{x}^{\hat{1}}, \dot{\mathbf{x}}^1, \ldots, \mathbf{x}^S, \dot{\mathbf{x}}^S)$. This energy is variable, since the S atoms thermally interact with the N-S residual atoms in the assembly. Thus, the residual assembly constitutes an environment of the subset. Among ν consecutive observations of the subset, we see the given phases $\{\mathbf{x}^1, \dot{\mathbf{x}}^1, \ldots, \mathbf{x}^S, \dot{\mathbf{x}}^S\}$ μ times. Therefore, if ν is big enough, the probability of observing this phase is

$$P\left(\mathbf{x}^{1}, \dot{\mathbf{x}}^{1}, \dots, \mathbf{x}^{S}, \dot{\mathbf{x}}^{S}\right) = \frac{\mu\left(\mathbf{x}^{1}, \dot{\mathbf{x}}^{1}, \dots, \mathbf{x}^{S}, \dot{\mathbf{x}}^{S}\right)}{\nu}.$$
(1.37)

By using the arguments of statistical thermodynamics, the probability of seeing the subset in the phases $\{\mathbf{x}^1, \dot{\mathbf{x}}^1, \dots, \mathbf{x}^S, \dot{\mathbf{x}}^S\}$ can be expressed in terms of the energy of the subset and T,

$$P\left(\mathbf{x}^{1}, \dot{\mathbf{x}}^{1}, \dots, \mathbf{x}^{S}, \dot{\mathbf{x}}^{S}\right) = \frac{\exp\left(-\frac{\mathscr{E}^{S}\left(\mathbf{x}^{1} \dots \dot{\mathbf{x}}^{S}\right)}{kt}\right)}{\sum_{\mathbf{x}^{1}} \sum_{\dot{\mathbf{x}}^{1}} \dots \sum_{\mathbf{x}^{S}} \sum_{\dot{\mathbf{x}}^{S}} \exp\left(-\frac{\mathscr{E}^{S}\left(\mathbf{x}^{1} \dots \dot{\mathbf{x}}^{S}\right)}{kT}\right)}.$$
(1.38)

This is the "canonical" probability distribution. It is a function of the positions and velocities of the particles belonging exclusively to the subset. The N-S residual particles contribute only to the temperature of the subset, because the subset S of N atoms shares the mean kinetic energy with the residual system of N-S atoms. Therefore, the residual body may be interpreted as a heat bath, which provides a constant temperature for the subset. The concept of microcanonical ensembles and their related subsystems originates from Maxwell and his contemporary Boltzmann. The factor 1/kT was identified by applying the concept to monatomic, ideal gases.

The concepts of Maxwell and Boltzmann were generalised by Gibbs from the special situation of "subsets within larger systems" to generic ensembles of systems. Instead of considering an ensemble of ν consecutive observations, Gibbs—in a leap of imagination—suggested an ensemble of ν replicas of one system. These replicas are supposed to "weakly interact" in order to allow them to exchange energy. The total energy of this ensemble of replicas and the ensemble size ν are supposed to be constant. Hence, all ν replicas collectively establish the energetic environment for an individual ensemble member. This metaphorically replaces the overall atomic assembly at constant energy considered by Maxwell and Boltzmann. Consequently, the studied replicas may be of arbitrary size. The assumption that the time average of a system's observable equals the ensemble average of this observable in a system of replicas is known as the ergodic hypothesis.

We may abbreviate the energy states of an individual replica in Gibbs' ensemble by \mathcal{E}_l and denote the number of replicas which are found to occupy this state by μ_l . This energy state is a single and discrete state of $1, \ldots, M$ energy states which are invariably available to the replica. Hence, the number series μ_l represents a distribution of replicas over these energy states, such that $\sum_{l=1}^{M} \mu_l = \nu$. Gibbs employed Boltzmann's formula for the ensemble's entropy, $\mathcal{S} = k \log W$ with

$$W = \frac{\nu!}{\prod_{l=1}^{M} \mu_l!},\tag{1.39}$$

in order to calculate the equilibrium distribution of $\mu_l|_E$ by maximising the entropy subject to the constraints of constant energy $\mathscr{E} = \sum \mu_l \mathscr{E}_l$ and constant ν . This procedure yields a canonical distribution of energy states:

$$P_{l} = \begin{pmatrix} \mu_{l} \mid \\ \frac{E}{\nu} \end{pmatrix} = \frac{\exp\left(-\frac{\mathcal{E}_{l}}{kT}\right)}{\sum_{l=1}^{M} \exp\left(-\frac{\mathcal{E}_{l}}{kT}\right)}.$$
 (1.40)

The suffix "E" again indicates that the result refers to thermodynamic equilibrium. Note the factor 1/kT enters Eq. (1.40) via the energy constraint during the maximisation computation.

If we interpret \mathscr{E}_l as a short form for the energy state $\mathscr{E}^S(\mathbf{x}_1 \cdots \dot{\mathbf{x}}_S)$ of Maxwell's subset ensemble, the results of Eqs. (1.40) and (1.38) are identical, although they have been derived differently. Gibbs' result, however, is more general because it applies to any ensemble at constant temperature regardless of how these isothermal conditions are maintained. Equation (1.40) may be used to calculate the expectation value of energy of an individual replica in the ensemble, $\langle \mathscr{E} \rangle$, and the expectation value of entropy, $\langle \mathscr{S} \rangle$:

$$\langle \mathscr{E} \rangle = \frac{\mathscr{E}}{v} \Big|_{E} = kT^2 \frac{\partial \log Z}{\partial T},$$
 (1.41)

$$\langle \mathscr{S} \rangle = \frac{\mathscr{S}}{v} \Big|_{E} = \frac{\langle \mathscr{E} \rangle}{T} + k \log Z.$$
 (1.42)

In these two equations, Z denotes an abbreviation for the denominator of (1.40), called the canonical partition function.

We may now consider an N-atom ensemble at constant T, irrespective of how this temperature is maintained. The partition function of such a system is given by

$$Z = \sum_{\mathbf{x}_{1,...,N}} \sum_{\dot{\mathbf{x}}_{1,...,N}} \exp\left(-\frac{\frac{m}{2}v^2 + V^{\text{int}}(\mathbf{x}_{\gamma}) + \sum_{\alpha=1}^{N} \frac{m_{\alpha}}{2}(\dot{\mathbf{x}}_{\alpha} - \mathbf{v})^2}{kT}\right). \tag{1.43}$$

26 1 Preparations

This function cannot, in general, be analytically calculated because the interaction potential is a complicated function of the atomic positions. However, an analytical result exists for crystals subject to two restrictive assumptions:

1. Einstein crystal: Atoms are considered to move independently of one another within mean potential energy functions V_{α}^{int} provided by their average environment,

$$V^{\text{int}} = \sum_{\alpha=1}^{N} V_{\alpha}^{\text{int}}(\mathbf{x}_{\alpha})$$
 (1.44)

2. Harmonic approximation: The atoms are considered as harmonic oscillators, such that the mean potential energy of an individual atom may be represented by a quadratic function:

$$V_{\alpha}^{\text{int}}(\mathbf{x}_{\alpha}) = \frac{\lambda_{\alpha}}{2} \left(\mathbf{x}_{\alpha} - \mathbf{X}_{\alpha}^{0} \right)^{2} + e_{\alpha}^{0}. \tag{1.45}$$

In Eq. (1.45), the λ_{α} denote the curvatures of the parabolic mean potential energies of atoms vibrating about the ground-state positions \mathbf{X}_{α}^{0} . Note that the second assumption excludes any anisotropy of the potential as well as thermal expansion. $e_{\alpha}^{0} = V_{\alpha}^{\text{int}}(\mathbf{X}_{\alpha}^{0})$ represents the ground-state energy at $T \to 0$. Regarding these assumptions, Eq. (1.43) can be analytically computed. For this purpose we approximate sums by integrals and obtain

$$Z \approx \exp\left(-\frac{mv^2}{2kt}\right).$$

$$\cdot \prod_{\alpha=1}^{N} \frac{1}{Y} \int_{-\infty}^{\infty} \exp\left(-\frac{m_{\alpha}(\dot{\mathbf{x}}_{\alpha} - \mathbf{v})^2 + \lambda_{\alpha} \left(\mathbf{x}_{\alpha} - \mathbf{X}_{\alpha}^0\right)^2 + 2e_{\alpha}^0}{2kT}\right) dx_1 \dots d\dot{x}_N$$

$$= \exp\left(-\frac{mv^2}{2kT}\right) \exp\left(-\sum_{\alpha=1}^{N} \frac{e_{\alpha}^0}{kT}\right) \frac{1}{Y} \prod_{\alpha=1}^{N} \frac{(2\pi kT)^3}{\sqrt{\lambda_{\alpha} m_{\alpha}^3}}.$$
(1.46)

Y is a constant factor that attends to the correct discretisation of the phase space when switching from the quantised to the continuous representation. With this result, the expectation of the energy (1.41) reads

$$\langle \mathscr{E} \rangle = \underbrace{\frac{m}{2} v^2 + 3NkT + \sum_{\alpha=1}^{n} e_{\alpha}^0}_{U}. \tag{1.47}$$

This energy consists of two parts, the kinetic energy K of the mass centre of the total ensemble and the internal energy U. It is instructive to decompose U into the two parts of Eq. (1.48), representing the expectation value of the kinetic excess energy

 $\langle \mathcal{E}_{\rm kin}^{\rm excess} \rangle = \sum m_{\alpha}/2 \, c_{\alpha}^2$, and the the expectation value of the internal potential energy $\langle V^{\rm int} \rangle$,

$$U = \underbrace{\frac{3}{2}NkT}_{\langle \mathscr{E}_{\text{kin}}^{\text{excess}} \rangle} + \underbrace{\sum_{\alpha=1}^{N} e_{\alpha}^{0} + \frac{3}{2}NkT}_{\langle V^{\text{int}} \rangle}.$$
 (1.48)

We see at mean, the internal potential energy of a vibrating atom assembly is T-dependent. Further, the temperature is proportional to the mean kinetic energy of the excess velocities $\mathbf{c}_{\alpha} = \dot{\mathbf{x}}_{\alpha} - \mathbf{v}$, while the velocity of the mass centre \mathbf{v} does not contribute to temperature.

The expectation value of the equilibrium entropy S is given by

$$S = \langle \mathcal{S} \rangle = \frac{3}{2} Nk \log(kT) + k \sum_{\alpha=1}^{N} \log \left\{ \frac{4}{3} \pi \sqrt{\frac{3kT}{\lambda_{\alpha}}}^{3} \right\} + 3Nk + k \log \left\{ \frac{1}{Y} \prod_{\alpha=1}^{N} \left(\frac{2\pi^{2}}{3m_{\alpha}^{\frac{3}{2}}} \right) \right\}$$

$$= C \qquad (1.49)$$

This entropy is composed of three terms. The last term in Eq. (1.49) represents the entropy constant denoted by C. The first term represents the usual caloric part which is identical for monatomic ideal gases. The underlined term in Eq. (1.49) results from the potential energy V^{int} . This term needs to be interpreted: According to the rules of statistics, $\sqrt{3kT/\lambda_{\alpha}}$ represents the mean amplitude (standard deviation) of the atomic oscillations about the ground state positions at a given temperature T. The magnitude of this amplitude is controlled by T and by the curvature λ_{α} of the potential, see Eq. (1.45): At a given T, broader potentials (characterised by "small" λ) allow larger amplitudes than narrower potentials (characterised by "large" λ). Hence, the logarithm's argument in the underlined term of Eq. (1.49) may be geometrically interpreted as the spherical volume available to an atom corresponding to this amplitude. It represents a measure of the atomic mobility in a quadratic potential. The larger this volume, the more microstates an individual atom may occupy in phase space and consequently, the higher the entropy. We shall return to this discussion in Chap.3 when evaluating the entropies of austenitic and martensitic lattices.

Finally, according to the harmonic potential model, the expectation of the free energy F = U - TS, results from a combination of internal energy and entropy,

$$F = 3NkT + \sum_{\alpha=1}^{N} e_{\alpha}^{0} - \frac{3}{2}NkT\log(kT) - kT\sum_{\alpha=1}^{N} \log\left\{\frac{4}{3}\pi\sqrt{\frac{3kT}{\lambda_{\alpha}}}^{3}\right\} - TC.$$
 (1.50)

28 1 Preparations

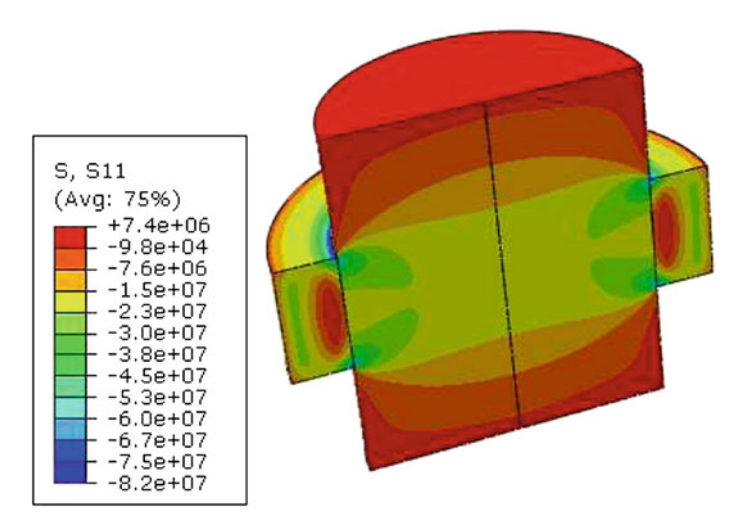


Fig. 1.11 Shrink-fit FEM simulation of a SMA bush onto a Hookean shaft during heating. The bush is radially pre-strained in the martensite phase (low T) so as to become pseudo-plastically deformed. Next, it is placed placed on the shaft and heated, thus triggering the SME. Contraction fixes the bush and visibly affects the radial stress distribution shown. The figure shows an axial cross-section of shaft and bush in the final state [97]

1.4 Engineering Models of SMA

For design studies of engineering applications it is often not necessary to model the full microscopic complexity of SMA. Rather, models must be reliably capable of the thermo-mechanical coupling: pseudo-plasticity, pseudo-elasticity, the shape memory effect and latent heat effects. Other requirements include their practical use in numerical algorithms such as FEM platforms, their numerical precision, robustness and efficiency.

Models developed for this purpose may be roughly divided into three groups: empirical models, plasticity models and energy-based models. Early empirical models use suitable ansatz functions, fitted to measurements in the state space. Such models are, however, only reliable within their circumscribed boundaries. Models are partly restricted to pseudo-elasticity [98–100]. More sophisticated models introduce internal variables to incorporate one- or two-way effects [101]. Another group of models are rooted in the classical theory of plasticity [102–105]. Physically more sophisticated models are based on free-energy descriptions of the material [106–109]. Temperature changes caused by latent transformation heats are an integral part of the behaviour of shape memory alloys and inevitably couple the thermal and the mechanical fields. This general behaviour is fully covered by the Müller–Achenbach–Seelecke (MAS) model. First published in 1979 [110], the MAS model has been explored and improved over the years. Important contributions were due to Achenbach [111] and Seelecke [112, 113]. At the Department of Materials Science

at the Ruhr-University Bochum, a research group is dealing with the implementation of this model into the FEM platform ABAQUSTM. Originally, the MAS model is restricted to uni-axial states of stress, which limits its application to cases where only these stress states prevail, such as axial loading in wires and trusses, pure beam bending, pure torsion and shrink-fit problems as well as thermally-induced processes in absence of external loading. These problems have already been studied by FEM [97, 114–117], see Fig. 1.11 for an example. To overcome this uni-axial limitation, the model has been extended to arbitrary 3D stress/strain/temperature states [118, 119].

References

- L.C. Chang, T.A. Read, Plastic deformation and diffusionless phase changes in metals the gold-cadmium beta phase. Trans. AIME 189(1), 47–52 (1951)
- W.J. Buehler, R.C. Wiley, J.W. Gilfrich, Effect of low-temperature phase changes on mechanical properties of alloys near composition TiNi. J. Appl. Phys. 34(5), 1475 (1963)
- R.J. Wasilews, S.R. Butler, J.E. Hanlon, Martensitic transformation in TiNi. J. Metals 17(9), 1965 (1059)
- M.W. Burkart, T.A. Read, Diffusionless phase change in the indium-thallium system. Trans. AIME 197(11), 1516–1524 (1953)
- 5. E. Hornbogen, G. Wassermann, Über den Einflus von Spannungen und das Auftreten von Umwandlungsplastizität bei der $\beta_1 \beta''$ -Umwandlung des Messing. Z. Metallkd. **47**(6), 427–433 (1956)
- E. Hornbogen, A. Segmüller, G. Wassermann, Martensitische Umwandlung bei der Verformung von abgeschrecktem beta-1-Messing. Z. Metallkd. 48(7), 379–384 (1957)
- H. Pops, T.B. Massalski, Thermoelastic + burst-type martensites in copper-zinc beta-phase alloys. Trans. AIME 230(7), 1662 (1964)
- C.W. Chen, Some characteristic quantities of the martensite transformation of Cu-Al-Ni alloys. Trans. AIME 209, 1202–1203 (1957)
- A. Musolff, Load-strain-temperature measurments of a NiTi wire. Department of Thermodynamics, Technical University of Berlin. Personally communicated (2003)
- M. Wagner, J. Frenzel, Cyclic experiments with a NiTi wire. Department of Materials Science, Ruhr-University Bochum. Personally communicated (2008)
- E. Hornbogen, Thermo-mechanical fatigue of shape memory alloys. J. Mater. Sci. 38, 1–15 (2003)
- G. Eggeler, E. Hornbogen, A. Yawny, A. Heckmann, M. Wagner, Structural and functional fatigue of NiTi shape memory alloys. Mater. Sci. Eng. A 378, 24–33 (2004)
- E. Hornbogen, Shape memory alloys, in *Advanced Structural and Functional Materials*, ed. by G.J. Bunk (Springer, Heidelberg, 1991), pp. 133–163
- E. Hornbogen, G. Eggeler, Surface aspects and fatigue of shape memory alloys (SMAs).
 Mat.-wiss. u. Werkstofftech. 34, 255–259 (2004)
- K. Otsuka, C.M. Wayman, (eds.) Shape Memory Materials (Cambridge University Press, Cambridge, 1998)
- J.W. Christian, The theory of transformations in metals and alloys, volume I, II (Pergamon, Amsterdam, 2002)
- K. Otsuka, C.M. Wayman, K. Nakai, Superelasticity effects and stress-induced martensitic transformations in Cu-Al-Ni alloys. Acta Metall. 24(3), 207–226 (1976)
- 18. K. Bhattacharya, Microstructure of Martensite–Why it Forms and How it Gives Rise to the Shape-Memory Effect. (Oxford University Press, Oxford, 2003)

30 1 Preparations

19. J. Philibert, Cinetique de la transformation martensitique dans und ferronickel. Comptes rendus hebdomaires des seances de l Academie des Sciences **240**(5), 529–531 (1955)

- R.C. O'Handley, Model for strain and magnetization in magnetic shape-memory alloys. Journal Appl. Phys. 83(6), 3263–3270 (1998)
- A.N. Vasil'ev, A.D. Bozhko, V.V. Khovailo, I.E. Dikshtein, V.G. Shavrov, V.D. Buchelnikov, M. Matsumoto, S. Suzuki, T. Takagi, J. Tani, Structural and magnetic phase transitions in shape-memory alloys Ni2+xMn1-xGa. Phys. Rev. B 59(2), 1113–1120 (1999)
- K. Oikawa, L. Wulff, T. Iijima, F. Gejima, T. Ohmori, A. Fujita, K. Fukamichi, R. Kainuma, K. Ishida, Promising ferromagnetic Ni-Co-Al shape memory alloy system. Appl. Phys. Lett. 79(20), 3290–3292 (2001)
- P.W. Anderson, E.I. Blount, Symmetry considerations on martensitic transformations ferroelectric metals. Phys. Rev. Lett. 14(7), 217 (1965)
- K. Otsuka, X. Ren, Physical metallurgy of Ti-Ni-based shape memory alloys. Prog. Mat. Sci. 50(5), 511–678 (2005)
- T.H. Nam, T. Saburi, K. Shimizu, Cu-content dependence of shape memory characteristics in Ti-Ni-Cu allovs. Mat. Trans. JIM 31(11), 959–967 (1990)
- J.D. Busch, A.D. Johnson, C.H. Lee, D.A. Stevenson, Shape-memory properties in Ni-Ti sputter-deposited film. J. Appl. Physics 68(12), 6224–6228 (1990)
- O. Matsumoto, S. Miyazaki, K. Otsuka, H. Tamura, Crystallography of martensitictransformation in Ti-Ni single-crystals. Acta Metall. 35(8), 2137–2144 (1987)
- S. Miyazaki, K. Otsuka, C.M. Wayman, The shape memory mechanism associated with the martensitic-transformation in Ti-Ni alloys. 1. self-accommodation. Acta Metall. 37(7), 1873– 1884 (1989)
- K. Otsuka, C.M. Wayman, K. Nakai, H. Sakamoto, K. Shimizu, Superelasticity effects and stress-induced martensitic transformations in cu-al-ni alloys. Acta Metall. 24(3), 207–226 (1976)
- K. Otsuka, H. Sakamoto, K. Shimizu, Successive stress-induced martensitic transformations and associated transformation pseudoelasticity in Cu-AL-Ni alloys. Acta Metall. 27(4), 585– 601 (1979)
- 31. K.E. Easterli, H.M. Miekkoja, Martensitic transformation of iron precipitates in a copper matrix. Acta Metall. **15**(7), 1133 (1967)
- 32. J. Perkins, R.O. Sponholz, Stress-induced martensitic-transformation cycling and 2-way shape memory training in Cu-ZNnAl alloys. Metall. Trans. A Phys. Metall. Mat. Sci. **15**(2), 313–321 (1984)
- K. Otsuka, K. Shimizu, Memory effect and thermoelastic martensite transformation in Cu-Al-Ni alloy. Scripta Metall. 4(6), 469 (1970)
- Z.-Z. Yu, P.C. Clapp, Growth dynamics study of the martensitic transformation in Fe-30 pct Ni alloys: Part II. computer simulation of martensitic growth. Metall. Trans. A 20A, 1617–1629 (1989)
- 35. K.Y. Lee, J.R. Ray, Mechanism of pressure-induced martensitic phase-transformations a molecular-dynamics study. Phys. Rev. B **39**(1), 565–574 (1989)
- P.C. Clapp, J. Rifkin, Nucleation of a martensite in a computer. in Proceedings of International Conference on Solid-Solid Phase Transformations, (TMS-AIME, Warrendale, 1982), pp. 1165–1169
- 37. R. Meyer, P. Entel, Martensite-austenite transition and phonon dispersion curves of $Fe_{1-x}Ni_x$ studied by molecular-dynamic simulations. Phys. Rev. B **57**(9), 5140–5147 (1998)
- 38. S. Rubini, P. Ballone, Quasi-harmonic and molecular-dynamics study of the martensitic-transformation in Ni-Al alloys. Phys. Rev. B **48**(1), 99–111 (1993)
- W.W. Liang, M. Zhou, Atomistic simulations reveal shape memory of fcc metal nanowires. Phys. Rev. B 73(11) (2006)
- U. Pinsook, G.J. Ackland, Atomistic simulation of shear in a martensitic twinned microstructure. Phys. Rev. B 62(9), 5427–5434 (2000)
- 41. Institute for Scientific Information. Web of science. Internet database, http://portal.isiknowledge.com

References 31

42. P.C. Clapp, How would we recognise a martensitic transformation if it bumped into us on a dark & austy night? in Proceedings of the International Conference On Martensitic Transformations, ed. by R. Gotthard, J. Van Humbeeck, vol I of Les Editions de Physique, (Lausanne, Switzerland, 1995), pp. C8–11–C8–19

- 43. G.B. Olson, W.S. Owen, *Martensite* (The Materials Information Society, ASM international, 1992)
- 44. S. Tan, H. Xu, Observations on a CuAlNi single crystall. Continuum Mech. Therm. 2, 241–244 (1990)
- A. Schäfer, O. Kastner, DSI observation of temperature-induced martensitic transforamtions in a CuNiAl single crytal plate. (Department of Material Science, Ruhr-University Bochum, Germany, 2010)
- Ch. Somsen, TEM observations in NiTi and NiTiFe. Department of Materials Science, Ruhr-University Bochum. Personally communicated (2010)
- 47. T. Waitz, The self accomodated morphology of martensite in nanocrystalline NiTi shape memory alloys. Acta Mater. **53**(8), 2273–2283 (2005)
- P. Boullay, D. Schryvers, J.M. Ball, Nano-structures at martensite macrotwin interfaces in Ni65Al35. Acta Mater. 51(5), 1421–1436 (2003)
- 49. A.-L. Cauchy, Sur l'Equilibre et le Mouvement d'un Systeme de Points Materiels. in Oevres Completes d'Augustin Cauchy, number 8 in 2, (1890), pp. 227–252
- 50. M. Born, Dynamik der Kristallgitter. (Teubner, 1915)
- 51. I. Müller, A History of Thermodynamics. (Springer, Berlin, 2007)
- 52. M.S. Wechsler, D.S. Lieberman, T.A. Read, On the theory of the formation of martensite. Trans. AIME **197**(11), 1503–1515 (1953)
- J.S. Bowles, J.K. Mackenzie, The crystallography of martensite transformations i. Acta Metall.
 129–137 (1954)
- 54. J.S. Bowles, J.K. Mackenzie, The crystallography of martensite transformations ii. Acta Metall. 2, 138–147 (1954)
- 55. C.M. Wayman, Introduction to the Crystallography of Martensitic Transformations (The MacMillan Company, New York, 1964)
- 56. H. Schumann, *Kristallgeometrie* (Einführung in die Theorie der Gittertransformationen metallischer Werkstoffe. VEB Deutscher Verlag für Grundstoffforschung, Leipzig, 1979)
- 57. J.M. Ball, R.D. James, Fine phase mixtures as minimizers of energy. Archive for Rational Mechanics And Analysis **100**(1), 13–52 (1987)
- J.D. van der Waals, The thermodynamic theory of capillarity under the hypothesis of a continuous variation of density. J. Stat. Phys. 20(2), 200–244 (1979) Translation of the original work from 1893
- J.W. Cahn, J.E. Hilliard, Free energy of a nonuniform system, I. interfacial free energy. J. Chem. Phys. 28, 258–267 (1958)
- J. Carr, M.E. Gurtin, M. Slemrod, Structured phase transition on a finite interval. Arch. Rat. Mech. Anal. 86, 317–351 (1984)
- L. Modica, Gradient theory of phase transitions and minimal interface criteria. Arch. Rat. Mech. Anal. 98(2), 132–142 (1987)
- 62. I. Fonseca, The gradient theory of phase transitions for systems with two potential wells. Proc. R. Soc. Edinb. **111A**, 89–102 (1989)
- L. Truskinovsky, G. Zanzotto, Finite-scale microstructures and metastability in onedimensional elasticity. Meccanica 30, 577–589 (1995)
- 64. Y. Huo, I. Müller, Interfacial and inhomogeneity penalties in phase transitions. Continuum Mech. Therm. **15**, 395–407 (2003)
- 65. A.G. Khachaturyan, *Theory of Structural Transformations in Solids*. (John Wiley & Sons, New York, 1983)
- Y. Wang, A.G. Khachaturyan, Three-dimensional field model and computer modeling of martensitic transformations. Acta Mater. 45(2), 759–773 (1997)
- 67. R. Abeyaratne, J.K. Knowles, Kinetic relations and the propagation of phase boundaries in solids. Arch. Rat. Mech. Anal. **114**, 119–154 (1991)

32 1 Preparations

68. R. Abeyaratne, J.K. Knowles, Dynamics of propagating phase boundaries: Thermoelastic solids with heat conduction. Arch. Rat. Mech. Anal. 126, 203–230 (1994)

- L.M. Truskinovsky, Dynamics of non-equlibrium phase boundaries in a heat conducting nonlinearly elastic medium. J. Appl. Math. Mech. (PMM) 53, 777–784 (1987)
- 70. I. Müller, Thermodynamics. (Pitman Advanced Publishing Program, Pitman, Bosten, 1985)
- 71. I. Müller, W.H. Müller, Fundamentals of Thermodynamics and Applications: With Historical Annotations and Many Citations from Avogadro to Zermelo. (Springer, Berlin, 2009)
- I. Müller, Lectures on Statistical Mechanics, Parts I and II. (Johns Hopkins University, Baltimore, 1974) Lecture Script
- 73. C. Truesdell, Lectures on Rational Mechanics. Statistical Mechanics. (Johns Hopkins University, Baltimore) Lecture Script
- 74. E. Schroedinger, Statistische Thermodynamik (Johann Ambrosius Barth, Leipzig, 1952)
- 75. I. Müller, W. Weiss, *Entropy and Energy*. (Springer, Berlin, 2005)
- L.D. Landau, E.M. Lifshitz, *Theory of Elasticity*, vol 7, Course of Theoretical Physics. 3 edn (Elsevier, Amsterdam, 1986)
- 77. W. Thomson, On the equilibrium of vapour at a curved surface of liquid. Proc. Roy. Soc. Edinburgh 7, (1872)
- 78. I. Müller, Boiling and condensation with interfacial energy. Meccanica **31**, (1996)
- 79. Y. Huo, I. Müller, Nucleation of droplets in a binary mixture. Meccanica 38, 493–504 (2003)
- J. Ansorg, I. Müller, Phase diagrams—heat of mixing and interfacial energy. In Solid Mechanics and its Applications, ed. by P. Argoul, M. Fremond, Q.S. Nguyen, IUMTAM Symposium on Variations of Domains and Free-Boundary Problems in Solid Mechanics. (Kluwer Academic Press, Dordrecht, 1999)
- R.C. Pond, S. Celotto, J.P. Hirth, A comparison of the phenomenological theory of martensitic transformations with a model based on interfacial defects. Acta Mater. 51, 5385–5398 (2003)
- 82. Z. Zhang, R.D. James, S. Müller, Energy barriers and hysteresis in martensitic phase transformations. Acta Mater. **57**, 4332–4352 (2009)
- J. Cui, Y. Chu, O.O. Famodu, Y. Furuya, J. Hattrick-Simpers, R.D. James, A. Ludwig, S. Thienhaus, M. Wuttig, Z. Zhang, I. Takeuchi, Combinatorial search of thermoelastic shape memory alloys with extremely small hysteresis width. Nature Mat. 5, 286–290 (2006)
- T. Simon, A. Kröger, A.Dlouhy, G. Eggeler. In-situ tem cooling/heating experiments on deformed NiTi shape memory single crystals. in ESOMAT 2009. EDP Sciences (2009)
- T. Simon, A. Kröger, A. Dlouhy, G. Eggeler, On the multiplication of dislocations during martensitic transformations in NiTi shape memory alloys. Acta Mater. 58(5), 1850–1860 (2010)
- H. Sitepu, W.W. Schmahl, J. Khalil-Allafi, G. Eggeler, A. Dlouhy, D.M. Többens, M. Tovar, Neutron diffraction phase analysis during thermal cycling of a Ni-rich NiTi shape memory alloy using the rietveld method. Scripta Materialia 46, 543–548 (2002)
- A. Dlouhy, J. Khalil-Allafi, G. Eggeler, Multiple-step martensitic transformations in Ni-rich NiTi alloys — an in-situ transmission electron microscopy investigation. Phil. Mag. 83, 339– 363 (2003)
- E. Hornbogen, Lattice defects and martensitic transformation, in *Micromechanics of advanced materials*, ed. by S.N.G. Chu, P.K. Liaw, R.J. Arsenault, K. Sadananda, K.S. Chan, W.W. Gerberich, C.C. Chau, T.M. Kung (The Minerals, Metals & Materials Socienty, 1995), pp. 307–315
- F.C. Lovey, V. Torra, Shape memory in Cu-based alloys: phenomenological behavior at the mesoscale level and interaction of martensitic transformation with structural defects in Cu-Zn-Al. Progress in Materials Science 44, 189–289 (1999)
- 90. M. Inami, T. Ishii, X. Ren, K. Otsuka, A study of martensitic transformation in Au-51.5at%Cd alloy. in Materials Science Forum, (Kanazawa, Japan, 2000), pp. 397–400
- 91. S. Kustov, J. Pons, E. Cesari, J. Van Humbeeck, Pinning-induced stabilization of martensite PartII. Kinetic stabilization in cu-zn-al alloy due to pinning of moving interfaces. Acta Mater. **52**, 3083–3096 (2004)

J.I. Pérez-Landazábal, V. Recarte, V. Sánchez-Alarcos, R.G. Leisure, Defect pinning of interface motion in thermoelastic structural transitions of Cu-Al-Ni shape-memory alloy. Phys. Rev. B 73(224101), 1–9 (2006)

- J.I. Pérez-Landazábal, V. Recarte, V. Sánchez-Alarcos, R.G. Leisure, Defect pinning of interface motion in thermoelastic structural transitions of Cu-Al-Ni shape-memory alloy. Phys. Rev. B 73(224101), 1–9 (2006)
- F.J. Pérez-Reche, E. Vives, M. Stipcich, L. Mañosa, A. Planes, Kinetics of martensitic transitions in Cu-Al-Mn under thermal cycling: Analysis at multiple length scales. Phys. Rev. B 69(64101), 1–7 (2004)
- M.C. Gallardo, J. Manchado, F.J. Romero, J. del Cerro, E.K.H. Salje, A. Planes, E. Vives, Avalache criticality in martensitic transition of Cu_{67.64}Zn_{16.71}Al_{15.65} shape memory alloy: A calorimetric and acoustic emission study. Phys. Rev. B 81(174102), 1–8 (2010)
- 96. J.C. Maxwell, Capillary Action. Encyclopaedia Britannica. 9th edn (1876)
- F. Richter, O. Kastner, G. Eggeler, Finite-element model for simulations of fully coupled thermomechanical processes in shape memory alloys. in ESOMAT 2009. EDP Sciences (2009)
- 98. K. Tanaka, S. Kobayashi, Y. Sato, Thermomechanics of transformation pseudoplasticity and shape memory effect in alloys. Int. J. Plasticity 2(1), 59–72 (1986)
- C. Liang, C. Rogers, One-dimensional thermomechanical constitutive relations for shape memory materials. J. Intel. Mat. Syst. Str. 1, 207–234 (1990)
- F. Auricchio, A robust integration algorithm for a finite-strain shape-memory-alloy superelastic model. Int. J. Plasticity 17, 971–990 (2001)
- L.C. Brinson, One-dimensional constitutive behavior of shape memory alloys: Thermomechanical drivation with non-constant material functions and redefined martensite internal variable. J. Intel. Mat. Syst. Str. 4, 229–242 (1993)
- D. Helm, Formgedächtnislegierungen—Experimentelle Untersuchung, phänomenologische Modellierung und numerische Simulation der thermomechanischen Materialeigenschaften. PhD thesis, (University Kassel, Germany, 2001)
- 103. C. Müller, O.T. Bruhns, Modelling of ploycrystalline shape memory alloys at finite strains based upon the logarithmic stress state. J. Phys. **IV**(112), 187–190 (2003)
- F. Auricchio, L. Petrini, A three-dimensional model describing stress-temperature induced solid phase transformations: solution algorithm and boundary value problems. Int. J. Numer. Meth. Eng. 61, 807–836 (2004)
- S. Reese, D. Christ, Finite deformation pseudo-elasticity of shape memory alloys— Constitutive modelling and finite element implementation. Int. J. Plasticity 24(3), 455–482 (2008)
- F. Falk, Model free energy, mecahnics and thermodynamics of shape memory alloys. Acta Metall. 28, 1773–1780 (1980)
- B. Raniecki, C. Lexcellent, Thermodynamics of isotropic pseudoelasticity in shape memory alloys. Eur. J. Mech. A-Solid 17(2), 185–205 (1998)
- 108. D.C. Lagoudas, Z. Bo, A. Bhattacharyya, A thermodynamic constitutive model for gradual phase transformation of sma materials. in Mathematics And Control In Smart Structures -Smart Structures And Materials, ed. by V.V. Varadan, J. Chandra, vol 2715 of Proceedings of Society of Photo-Optical Instrumentation Engineering (SPIE), (SPIE, San Diego, CA, 1996), pp. 482–493
- R. Heinen, K. Hackl, On the calculation of energy-minimizing phase fractions in shape memory alloys. Comput. Method. Appl. M. 196(21–24), 2401–2412 (2007)
- 110. I. Müller, A model for a body with shape-memory. Arch. Ration. Mech. An. 70, 61–77 (1979)
- 111. M. Achenbach, A model for an alloy with shape memory. Int. J. Plasticity 5, 371–395 (1989)
- I. Müller, S. Seelecke, Thermodynamic aspects of shape memory alloys. Math. Comput. Model. 34, 1307–1355 (2001)
- 113. S. Seelecke, Modeling the dynamic behavior of shape memory alloys. Int. J. Nonlin. Mech. 37, 1363–1374 (2002)
- F. Richter, O. Kastner, G. Eggeler, Finite-element simulation of the anti-buckling-effect of a shape memory alloy bar. J. Mater. Eng. Perform. 20, 719–730 (2011)10.1007/s11665-010-9797-8

34 1 Preparations

115. F. Richter, O. Kastner, G. Eggeler, Implementation of the Müller-Achenbach-Seelecke model for shape memory alloys in ABAQUS. J. Mat. Eng. Perf. 18(5–6), 626–630 (2009) Special issue containing contributions from the Shape Memory and Superelastic Technology Conference, Stresa, Italy, September 21–25 2008

- F. Richter, Finite-element-simulations of polycrystalline shape memory alloys. In Smart Structures and Materials and Nondestructive Evaluation and Health Monitoring 2008, (San Diego, CA, USA, 2008)
- 117. S. Jaeger, Experimentelle und theoretische Untersuchungen zu Phasenumwandlungen in NiTi-Blechen Master's thesis (Ruhr-University, Bochum, 2010)
- 118. Y. Xie, Modell zur Simulation einer mehrphasigen Gedächtnislegierung unter mehrachsiger Belastung. PhD thesis, (Technical University of Berlin, 1994)
- O. Kastner, F. Richter, G. Eggeler, Multivariant formulation of the thermomechanically coupled müller-achenbach-seelecke-model for shape memory alloys. in Proceedings of the ASME 2009 Conference on Smart Materials, Adaptive Structures and Intelligent Systems, (ASME, Oxnard, 2009)

Chapter 2 The Method of Molecular Dynamics Simulations

Molecular dynamics simulations are in principle the most versatile way of describing solid—solid phase transitions: the crystal and interfacial structures emerge automatically from the interatomic potential. So there is no need for implicit assumptions about microscopic details and symmetry entailed in continuum methods. In particular, the thermodynamics emerges from the molecular dynamics rather than being an input, so that all the fluctuations are incorporated properly [1]. In this chapter we present, in a nutshell, the concept of the MD method and the numerical techniques employed. We restrict ourselves to aspects essential for this work and refer to textbooks on the literature for more extensive treatises, e.g. [2–4].

2.1 Interaction Models

The method of molecular dynamics (MD) simulations represents a numerical method for solving classical many-body problems. Here, the term "classical" refers to the underlying Newtonian mechanics presented in the previous chapter. Accordingly, atoms are treated as mathematical points, endowed with mass but without spatial extension. Especially, energy is considered to be a continuous quantity, deliberately neglecting its quantifisation. This ansatz of course restricts physics to the time and length scales to microscale orders of magnitude, where the quantisation is assumed to be less significant. Energy quantisation becomes important on the sub-micro scale, where it determines the structure of charge distributions in the electron shell of an atom. Certainly, these distributions effect the interaction forces between the atoms. However, the dynamical calculation of the subatomic charge distributions in parallel with the atomic trajectories exceed contemporary computation resources. Such sub-micro/micro scale approaches (known as ab-initio MD methods) represent the scientific cutting edgde of theoretical physics.

The classical MD method avoids these restrictions by compromise: atomic interactions are reduced to functions of mass-point trajectories, thus neglecting subatomic

entities as variables. The functions employed may be derived from sub-micro knowledge, or they may be chosen entirely on a phenomenological basis. These model functions may be fitted to the physical properties of specific materials. Hence, depending on the degree of model sophistication, MD simulation results may gradually approximate physical processes from the micro- up to the mesoscale.

In the literature, MD simulations of martensitic transformations have been reported since the 1980s, see Fig. 1.2 on p. 4. Early works by Clapp et al. [5, 6] hinge on semi-empirical potentials, which were constructed on the basis of Morse potentials. Using the pure Morse or Lennard–Jones potentials led these authors to doubt the existence of metastable structures and they therefore modified a Morse potential by adding oscillatory functions. The resulting potential exhibited several minima, which instantaneously incorporated several possible stable lattice configurations. Thermally induced transitions between cubic and triangular configurations were simulated and interpreted as martensitic transformations.

The physics of metals and alloys can be modelled by the use of central pair potentials qualitatively only. These potentials reduce the atomic interactions to pairwise interactions, being described by only very few parameters. To simulate more complex crystal structures, and also to quantitatively appropriate more satisfactory results, further sophisticated models were introduced. In 1989, Yu and Clapp [7] made use of a semi-empirical potential, which was fitted to the physical properties of Fe-Ni, to simulate martensitic growth processes in a 432-atom body.

In the 1990s, a new class of potentials based on the density functional theory became prominent. A new type was derived by using the embedded-atom method (EAM), which was originally developed by Daw and Baskes [8] at the beginning of the 1980s. EAM potentials consist of two parts for repulsive interactions between ionic atom cores and cohesive interactions due to the electrons. The proportions of these two contributions can be assessed by ab initio calculations. EAM-type potentials have been fitted to the properties of several materials and alloys and have been widely used in MD simulations of martensitic transformations. We provide here an incomplete list: Cheung et al. (1992, α -iron, [9]), Grujicic et al. (1995, FeNi, [10]; 1996, TiV, [11] and [12]; 1997, FeNi, [13]), Shao et al. (1996, NiAl, [14]), Meyer (1998, FeNi, NiAl, [15]), Zhang et al. (2000, NiAl, [16]), Kuznetsov et al. (2001, Zr, [17]) Kadau (2001, FeNi and FeCu, [18]) and Mendelev/Ackland (2007, Zr, [19]). Other works employ similar many-body potentials, like Finnis-Sinclair-type potentials and its extensions. Like EAM potentials, these must be fitted to the properties of specific materials. We mention the work of Ackland and Pinsook on zirconium (1998, [20–22]). This brief overview shows that, if suitably constructed potential functions are used, austenite-martensite phase transitions can be successfully simulated by using the MD method. The phenomena being investigated cover a wide range of aspects: the time evolution of the microstructure under martensitic transformation, temperature- and tension-induced martensitic growth, the effects of dislocations and crystal defects as well as the influence of surface effects on the nucleation process.

In this work, we shall choose the simplest possible MD model: the model employs central pair potentials of the Lennard–Jones-type, thereby contradicting the popular opinion that these types of potentials are too primitive to use for simulating 2.1 Interaction Models 37

transitions in crystal lattices. Indeed, it was shown that this approach, although of great conceptual simplicity, is capable of qualitatively covering all the important characteristics of martensitic transformations [23–25]. Thus, such a model may help in fundamentally understanding these processes. The model will be explained in detail in Chap. 3. Similar models were successfully considered in the literature [26–28].

2.2 Numerics

2.2.1 Accuracy Issues

The fundamental model equations in MD simulations are Newton's equations of motion (1.22). Once an interaction model is chosen, the atomic trajectories are calculated by solving a system of *N*-dimensional coupled, second order differential equations. Two sets of initial conditions need to be provided, initial atomic positions and velocities, which determine the initial potential and kinetic energies, respectively. Analytical solutions to such many-body systems do not exist, we therefore have to rely on numerical techniques. However, from mechanical and thermodynamical considerations, we know some properties of the theoretically existing "true" solution:

- 1. Energy conservation: according to Eq. (1.31), unless external force fields are applied to the system, the total energy is constant.
- 2. Time reversibility: if at some time $t > t_0$ the atomic velocities were reversed by multiplying by (-1), then the trajectories are exactly retraced back to the initial conditions.
- Equilibrium: an unconstrained system will tend to establish an equilibrium state corresponding to the set energy. At equilibrium, the velocity distributions of the atoms are Maxwellian.

The numerical solution inevitably deviates from the true solution for two reasons: first, because computers restrict the accuracy of the calculated numbers (hardware accuracy) and second, because the numerical integration schemes used only approximate the true solution at discrete time steps and within certain convergence limits (software accuracy).

The hardware accuracy is related to the representation of numbers on a computer. Real numbers *x* are represented by

$$x = \pm m b^{\pm e}, \tag{2.1}$$

where m is the mantissa, b the base and e the exponent of the base. The sizes of these quantities depend on the compiler that produces the executable binary code. For example, many C-compilers will allocate 64 bits of memory to represent the realtype "double". Of these 64 bits, 53 bits are used to represent the mantissa, and the

remaining bits for the sign and the exponent. The type "float" is only represented by 32 bits. The accuracy is defined as the smallest deviation from 1.0 that can be represented by the real number type which is chosen. This is determined by the mantissa. In C, 64-bit "doubles" consequently have an accuracy of $2.2204460492503131 \times 10^{-16}$. This figure is defined by the *IEEE standard for binary floating point arithmetic*. Real numbers consequently have to be rounded to this accuracy on a computer. In general, the resulting inaccuracy a priori destroys absolute energy conservation (1) and veridical time reversibility (2) of numerically calculated solutions.

Luckily, these issues do not disqualify the method, at least if we are willing to compromise and accept approximate, numerical solutions as solutions of the mathematical problem in general. Physical reasons sustain us: MD simulations do not precisely predict evolutions of systems as function of the initial data rather, at some average on the atomic level. Exact solutions, however, are not required: in solids, for example, atoms move in convex potential wells provided by their neighbours. These wells force the atomic motions to fluctuate about mean lattice positions. While the numerical method cannot exactly resolve the atomic trajectories within the energy wells, we trust that the mean positions, numerically obtained, may represent the physical positions. Time-reversal will not exactly retrace the trajectories, but the initial mean positions and initial temperature conditions will be met. Thus in these cases, we may accept the fact of numerical time-irreversibility. Some authors add the remark that indeed nature also produces time-irreversibility on the atomic scale due to Heisenberg's Uncertainty Principle of quantum mechanics [2]. Such an argument is, of course, beyond the scope of a classical theory. Here, we rely on the statistical convergence of the atomic trajectories, although there is no mathematical proof for any class of systems that is of interest to MD simulations. In their textbook, Frenkel and Smit mischievously comment on this situation: "To close this discussion, let us say that there is clearly still a corpse in the closet. We believe this corpse will not return to haunt us, and we quickly close the closet door" [3] (p. 73).

Care, however, has to be taken with regard to the requirement of energy conservation (1), which represents an important criterion for choosing the integration scheme. Sophisticated, higher order schemes tend to provide very good energy conservation over short times, but often have the undesirable feature of an overall drift over long periods. Schemes used for MD simulations, such as the Verlet algorithm explained below, typically provide only moderate short-term energy conservation, but minimal long-term drift [3]. In general, the quality of algorithms scales with the width of the discrete time step. This width must be selected with regard to stability, energy conservation and global simulation settings. For example, if a thermostat is applied, the mean kinetic energy of the system is controlled by some additional algorithm such that a slight "numerical energy dissipation" can be compensated.

2.2.2 Integration Schemes

In MD simulations, codes typically employ the Verlet algorithm (coordinate or velocity formulation), or predictor–corrector schemes. We proceed by briefly introducing these three techniques.

The atomic motions \mathbf{x}_{α} may be expanded forwards and backwards in time as a Taylor series about the current time t:

$$\mathbf{x}_{\alpha}(t + \Delta t) = \mathbf{x}_{\alpha}(t) + \dot{\mathbf{x}}_{\alpha}(t)\Delta t + \frac{1}{2}\ddot{\mathbf{x}}_{\alpha}(t)\Delta t^{2} + \mathcal{O}(\Delta t^{3}),$$

$$\mathbf{x}_{\alpha}(t - \Delta t) = \mathbf{x}_{\alpha}(t) - \dot{\mathbf{x}}_{\alpha}(t)\Delta t + \frac{1}{2}\ddot{\mathbf{x}}_{\alpha}(t)\Delta t^{2} - \mathcal{O}(\Delta t^{3}).$$
(2.2)

Adding these two equations, and eliminating the acceleration terms by using Newton's equations (1.22), the scheme yields

$$\mathbf{x}_{\alpha}(t + \Delta t) = 2\mathbf{x}_{\alpha}(t) - \mathbf{x}_{\alpha}(t - \Delta t) + \frac{\Delta t^{2}}{m_{\alpha}}\mathbf{f}_{\alpha} + \mathcal{O}(\Delta t^{4}). \tag{2.3}$$

This is Verlet's algorithm [29], which is an explicit recursive scheme for computing the new atomic positions $\mathbf{x}_{\alpha}(t+\Delta t)$ as a function of the current positions $\mathbf{x}_{\alpha}(t)$ and the most recent positions $\mathbf{x}_{\alpha}(t-\Delta t)$. Δt is the time step. The accuracy of Verlet's algorithm is of the order (Δt^4) , providing fair short-term energy conservation and minimal long-term drift. It is fast because the interaction forces need only be computed once per time increment. Another advantage is the algorithm requires little extra memory which becomes important for larger ensembles. For all these reasons, Verlet's algorithm is our first-choice integration scheme.

Note that Verlet's algorithm only deals with positions and does not explicitly provide the atomic velocities. The velocities must be calculated independently, which implies they are not computed exactly at the same time as the positions. The velocities are calculated as ratios of the spatial and temporal increments,

$$\dot{\mathbf{x}}_{\alpha}(t) = \frac{\mathbf{x}_{\alpha}(t + \Delta t) - \mathbf{x}_{\alpha}(t - \Delta t)}{2\Delta t}.$$
(2.4)

The Equations of Motion (1.22) represent a set of second-order differential equations. Their integration involves two constants of integration per atom. Commonly, these are determined by the initial atomic positions $\mathbf{x}_{\alpha}(t=0)$ and the initial atomic velocities $\dot{\mathbf{x}}_{\alpha}(t=0)$. The former has to be selected with respect to the interaction potentials and can be determined from static lattice relaxation, for example. The initial set of atomic velocities may then be set with respect to Maxwellian velocity distributions of the components. These two sets of initial conditions are employed to compute the $\mathbf{x}_{\alpha}(t-\Delta t)$ and $\mathbf{x}_{\alpha}(t)$ required to initiate Verlet's recursive scheme.

Occasionally, the delay of the velocity computation is undesirable. To improve this situation, the Verlet algorithm was modified [30]: we use Eq. $(2.2)_1$, eliminate

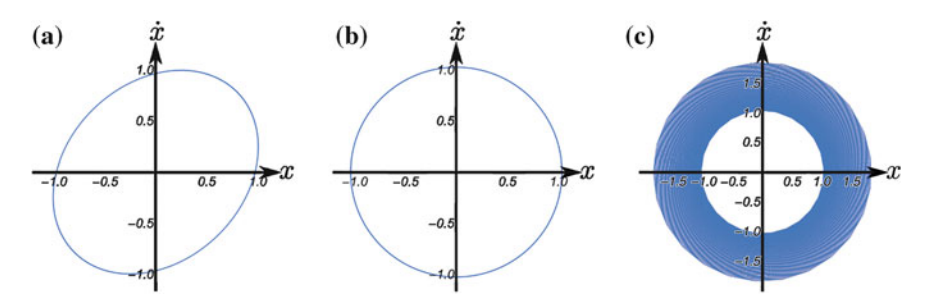


Fig. 2.1 Trajectory of the linear ODE $\ddot{x}=-x$ with x(t=0)=0 and $\dot{x}(t=0)=1$ in the phase space (x,\dot{x}) . The analytic solution represents a concentric circular trajectory with constant radius 1. a Coordinate Verlet, **b** velocity Verlet, **c** predictor–corrector. An unrealistically large time step of $\Delta t=0.25$ was used to augment the differences between the three schemes. In total 5,000 time steps in total were calculated

the acceleration term by (1.22) and linearly expand the velocities. This produces a scheme consisting of two parts which are computed recursively:

$$\mathbf{x}_{\alpha}(t+\Delta t) = \mathbf{x}_{\alpha}(t) + \dot{\mathbf{x}}_{\alpha}(t)\Delta t + \frac{\mathbf{f}_{\alpha}(\mathbf{x}_{\gamma}(t))}{2m}\Delta t^{2}$$

$$\dot{\mathbf{x}}_{\alpha}(t+\Delta t) = \dot{\mathbf{x}}_{\alpha}(t) + \frac{\mathbf{f}_{\alpha}(\mathbf{x}_{\gamma}(t+\Delta t)) + \mathbf{f}_{\alpha}(\mathbf{x}_{\gamma}(t))}{2m_{\alpha}}$$
(2.5)

This scheme is equivalent to Verlet's algorithm, with which it shares its consummate stability, but it yields positions and velocities at identical instants in time. Its drawback, however, is the fact that the interaction forces must be computed twice for each single time increment of the trajectories, thus doubling the computational effort.

Another integration scheme, which also explicitly yields positions and velocities, is based on the predictor–corrector method. This method splits the computation of the phases $\{\mathbf{x}_{\alpha}, \dot{\mathbf{x}}_{\alpha}\}$ into two steps: in the predictor step, a preliminary solution is calculated on the basis of current and recent phases. This predicted solution is then used to adjust the interaction force in the subsequent corrector step. The method is based on Taylor expansions of atomic motions and velocities, modified by weight factors that reduce the error. This method comes in different flavours. The available algorithms differ in their Taylor expansion orders, their weight functions and weight coefficients. The example, the expression below represents a higher order algorithm taken from [31]:

Predictor step:

$$\mathbf{x}_{\alpha}^{\text{pre}}(t+\Delta t) = \mathbf{x}_{\alpha}(t) + \dot{\mathbf{x}}_{\alpha}(t)\Delta t + \frac{\Delta t^{2}}{m_{\alpha}} \left(\frac{19}{24}\mathbf{f}(\mathbf{x}_{\gamma}(t) - \frac{10}{24}\mathbf{f}(\mathbf{x}_{\gamma}(t-\Delta t)) + \frac{3}{24}\mathbf{f}(\mathbf{x}_{\gamma}(t-2\Delta t)) - \Delta t^{5}\frac{19}{180}\mathbf{x}_{\alpha}(t)^{5},\right)$$

The corrected equation reads:

$$\mathbf{x}_{\alpha}(t+\Delta t) = \mathbf{x}_{\alpha}(t) + \dot{\mathbf{x}}_{\alpha}(t)\Delta t + \frac{\Delta t^{2}}{m_{\alpha}} \left(\frac{3}{24} \mathbf{f}(\mathbf{x}_{\gamma}^{\text{pre}}(t+\Delta t)) + \frac{10}{24} \mathbf{f}(\mathbf{x}_{\gamma}(t)) - \frac{1}{24} \mathbf{f}(\mathbf{x}_{\gamma}(t-\Delta t)) \right) - \Delta t^{5} \frac{7}{36} \mathbf{x}_{\alpha}(t)^{5},$$

$$\dot{\mathbf{x}}_{\alpha}(t+\Delta t) = \frac{\mathbf{x}_{\alpha}(t+\Delta t) - \mathbf{x}_{\alpha}(t)}{\Delta t} + \frac{\Delta t}{m_{\alpha}} \left(\frac{7}{24} \mathbf{f}(\mathbf{x}_{\gamma}^{\text{pre}}(t+\Delta t)) + \frac{6}{24} \mathbf{f}(\mathbf{x}_{\gamma}(t)) - \frac{1}{24} \mathbf{f}(\mathbf{x}_{\gamma}(t-\Delta t)) \right) - \Delta t^{4} \frac{1}{45} \mathbf{x}_{\alpha}(t)^{5}. \tag{2.6}$$

In the long term, predictor-corrector methods are not as accurate as the Verlet scheme, see Fig. 2.1 for a simple benchmark test with the three methods discussed. Here, we recursively calculated the linear ODE $\ddot{x} = -x$ for 5,000 time steps, using an artificially large time step of $\Delta t = 0.25$ to augment the differences. The analytic solution is given by a unit circle about the origin in these phase diagrams. The Verlet algorithm for the velocity formulation (2.5) nicely reproduces the analytical solution, Fig. 2.1b. The phase curve is circular and clearly coincides with the solution. The tiny radial deviation from the unit circle is due to the large time step chosen. In the coordinate formulation, Fig. 2.1a, the Verlet algorithm has the same stability characteristic, however, the phase curve is slightly deformed into an ellipse, since positions and velocities are calculated at slightly different times. The predictor-corrector code, Fig. 2.1c, exhibits a significant drift in the phase diagram. The trajectory spirals outwards about the origin, beginning with a radius of 1. Note that in a real MD application, the time steps used are two to three orders of magnitude smaller than the one used with this benchmarking example. In this case, even the stability of the predictor-corrector method is sufficient, although using this scheme without a thermostat is not recommended.

2.2.3 Non-Dimensionalisation

The physical time and length scales of atoms incorporate small numbers into the computation of the atomic trajectories. For numerical reasons (and for convenience), equations are non-dimensionalised by characteristic physical quantities, such that all model quantities range in the order of one. For this purpose, the characteristic length σ_0 , mass μ_0 and time τ_0 are used. In solids, an obvious choice for σ_0 is the nearestneighbour distance between the atoms (ranging in the order of $1\text{ Å }(10^{-10}\text{ m}))$ and for μ_0 , the atomic mass of an atom (ranging in the order of 10^{-26} kg for most metals). However, an argument is required for the choice of the characteristic time τ_0 .

The MD method must be capable of resolving the fluctuating atomic motions about their mean lattice sites restricted by the potential function $V^{\rm int}$. The amplitudes of these fluctuation are small and, corresponding to the atomic motions, may be idealised as harmonic oscillations within individual atomic potentials $V_{\alpha}^{\rm int}$. We may

then identify τ_0 with the period of such harmonic oscillations which is given by

$$\tau_0 = 2\pi \sqrt{\frac{\mu_0}{\lambda}}. (2.7)$$

 λ denotes the curvature of the potential function $V_{\alpha}^{\rm int}$ in the harmonic limit, thus relating τ_0 to the potential.

 σ_0 , μ_0 and τ_0 may be combined to give a characteristic energy ε_0 , used to non-dimensionalise the potential energy,

$$\varepsilon_0 = \mu_0 \left(\frac{\sigma_0}{\tau_0}\right)^2. \tag{2.8}$$

Alternative choices are possible. For example, one may choose ε_0 independently of τ_0 and calculate the latter directly from Eq. (2.8). In this case, however, τ_0 cannot be interpreted as a characteristic period of the oscillation. It is also possible to choose ε_0 and τ_0 entirely independently of each other. In this case, the ratio of the characteristic potential energy and the characteristic kinetic energy, denoted by Λ ,

$$\Lambda = \frac{\varepsilon_0}{\mu_0 \left(\frac{\sigma_0}{\tau_0}\right)^2},\tag{2.9}$$

deviates from the numerical value of one.

Using the characteristic quantities, the non-dimensionalised equations of motion eventually read as

$$\hat{m}_{\alpha} \frac{\mathrm{d}^2 \hat{\mathbf{x}}_{\alpha}}{\mathrm{d}\hat{t}^2} = -\Lambda \hat{\nabla}_{\alpha} \hat{V}. \tag{2.10}$$

with $\hat{m}_{\alpha} = m_{\alpha}/\mu_0$, $\hat{\mathbf{x}}_{\alpha} = \mathbf{x}_{\alpha}/\sigma_0$, $\hat{t} = t/\tau_0$ and $\hat{V} = V/\varepsilon_0$. $\hat{\nabla}_{\alpha}$ denotes the gradient with respect to the non-dimensionalised coordinates. In our simulations we shall always deal with non-dimensionalised quantities but for simplicity, the hats (^) will be dropped.

2.2.4 Thermostats

It is often required to control the temperature of the simulated atomic assembly, because the lattice transformations considered in this work incorporate latent heat effects. This effect may interfere with the progressing transformation process and it is therefore desirable to compensate for these effects in order to maintain a constant temperature. This can be achieved by using numerical algorithms called *thermostats*. Here, we briefly discuss three methods: the Nosé-Hoover thermostat, the Andersen thermostat and the velocity scaling method.

2.2.4.1 Nosé-Hoover Thermostat

Nosé [32, 33] considered a scaled time τ which is related to the physical time t by the transformation

$$s = \frac{\mathrm{d}\tau}{\mathrm{d}t}.\tag{2.11}$$

This transformation implies

$$\dot{\mathbf{x}}_{\alpha} = \frac{\mathbf{d}\mathbf{x}_{\alpha}}{\mathbf{d}t} = s \frac{\mathbf{d}\mathbf{x}_{\alpha}}{\mathbf{d}\tau} = s \dot{\mathbf{x}}_{\alpha}^{\tau}.$$
 (2.12)

(Derivatives with respect to the scaled time τ are denoted by $\cdot \tau$). Employing this transformation, Nosé introduces an extended Lagrangian, which—in Cartesian coordinates—reads as

$$\mathcal{L}^{\text{Nos\'e}} = \sum_{\alpha=1}^{N} \frac{m_{\alpha}}{2} s^{2} \left(\mathbf{x}_{\alpha}^{\tau}\right)^{2} - V^{\text{int}}(\mathbf{x}_{\alpha}) + \frac{Q}{2} \left(\mathbf{s}^{\tau}\right)^{2} - 3NkT \log s. \tag{2.13}$$

The first two terms on the right-hand side of this equation result from eliminating the velocities in the Lagrangian of Equation (1.36) by (2.12). Q is a positive constant interpreted as the mass of a virtual heat source which controls the temperature of the atomic assembly. The term $Q/2(\tilde{s}^{\tau})^2$ is accordingly interpreted as the "kinetic energy" of this virtual mass, while $(3NkT \log s)$ represents its "potential energy". Nosé and Hoover were able to show that the Lagrangian (2.13) produces a canonical equilibrium distribution at a temperature T in the phase space.

The extended Lagrangian of Equation (2.13) implies a new set of equations of motion which reads as

$$m_{\alpha} \overset{\cdot \tau}{\mathbf{x}}_{\alpha} = -\frac{1}{s^{2}} \nabla_{\alpha} V^{\text{int}} - \frac{2}{s} \overset{\cdot \tau}{\mathbf{x}}_{\alpha} \overset{\cdot \tau}{s^{2}}$$

$$Q \overset{\cdot \tau}{s} = \frac{1}{s} \left(\sum_{\alpha=1}^{N} \frac{m_{\alpha}}{2} s^{2} \left(\overset{\cdot \tau}{\mathbf{x}}_{\alpha} \right)^{2} - 3NkT \right)$$
(2.14)

This is the Nosé-Hover algorithm. It represents a second-order system of ODE for \mathbf{x}_{α} and s as functions of the scaled time τ . Note that the velocities $\dot{\mathbf{x}}_{\alpha}^{\tau}$ and the pseudo-velocity \dot{s} appear explicitly on the right-hand side, thus requiring velocity-explicit integration schemes. A Nosé-Hoover thermostat is designed to control the temperature and to also maintain the Maxwellian equilibrium distributions.

This latter aspect of "forced" equilibrium properties of the trajectories raises a doubt about the applicability of this algorithm within the framework of nonequilibrium processes. Our MD simulations are aimed to address such processes since we intend to investigate the formation processes of microstructures in phase transformations as transients. Therefore, we shall not apply this method in our MD simulations.

2.2.4.2 Andersen Thermostat

Another, more heuristic thermostat algorithm was provided by Andersen [34]. By means of his approach, the atoms change velocities due to stochastic collisions with photons emitted by a radiator at the set temperature. Technically, this is performed by setting the velocities of randomly selected atoms, with respect to the Maxwellian velocity distribution, at this temperature. A drawback of this method is that the velocities change suddenly and the trajectory in phase space is accordingly discontinuous. Also, the Maxwellian velocity distribution allows for very large speeds. Such events of course are rare, but once they occur, instabilities may result.

2.2.4.3 Velocity Scaling Thermostat

An even simpler, but efficient method is that of "velocity scaling and relaxation". It can be used with the coordinate-Verlet algorithm: during the computation of the trajectories, the atomic displacements \mathbf{u}_{α} ,

$$\mathbf{u}_{\alpha} = \mathbf{x}_{\alpha}(t + \Delta t) - \mathbf{x}_{\alpha}(t), \tag{2.15}$$

are frequently scaled by a factor q. The positions $\mathbf{x}_{\alpha}(t + \Delta t)$ are then adjusted according to the scaled displacements,

$$\mathbf{x}_{\alpha}^{\text{scaled}}(t + \Delta t) = \mathbf{x}_{\alpha}(t) + q\mathbf{u}_{\alpha}, \tag{2.16}$$

which effectively scales the velocities according to Eq. (2.4). The magnitude of the factor q may be controlled proportional to the deviation of the system temperature from the desired set temperature,

$$q = 1 + k_p(T_{\text{set}} - T).$$
 (2.17)

 k_p is a (positive) control parameter. The system temperature is, as usual, calculated from the kinetic excess energy in Eq. (1.48). k_p has to be carefully adjusted such that q varies only moderately about the value of 1 in the per-mill range.

Scaling events are frequently performed during the computation at intervals of a few hundred time steps such that, during the intervening periods, the system is allowed to relax into its natural state. Therefore, the method gently influences the kinetic energy and thus no artificial situations are anticipated. An additional advantage is that this method can be used with the Verlet algorithm in coordinate formulation, thus emphasising its efficiency. For slow processes close to equilibrium,

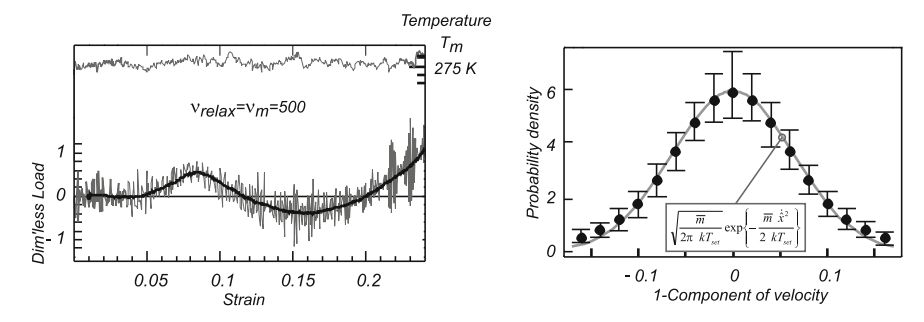


Fig. 2.2 Test of the "velocity scaling and relaxation" thermostat under tensile loading. Loading affects the temperature of the assembly by means of mechanical energy dissipations such that thermostats are required to maintain isothermal conditions. The diagram on the *left* shows an arbitrary load/strain response of a small assembly subject to tensile loading. The *bold line* indicates the trend. The system temperature is plotted onto the same diagram with respect to the *right-hand* axis. The thermostat maintains the set temperature at an average of $T_{\rm set} = 275 \, \text{K}$. The diagram on the *right* depicts the velocity distribution. Time/ensemble averages (*black bullets*) coincide well with the analytical Maxwellian at $T_{\rm set}$ (*grey curve*)

the method reproduces Maxwellian velocity distributions. This is demonstrated in Fig. 2.2 showing an isothermal tensile test with a small crystallite [25].

2.2.5 Periodic Boundary Conditions

In the bulk of crystalline atomic assembly, an individual atom's mean lattice position conforms to the interactions with the atom's neighbours located within its spherical interaction range. In contrast to this, an individual surface atom only experiences interactions from within the crystal since the interaction partners beyond the surface are absent. In this situation, surface atoms are forced slightly towards the bulk solid. Accordingly, the lattice parameters are slightly smaller compared to those in the bulk positions and the affected atoms have slightly increased potential energies. This effect is short ranged and decays over the distance of few unit cells. The difference between the specific potential energies of bulk and surface atoms defines the *surface energy*. It is clear that this quantity is more dominant in smaller assemblies than in larger. Also, 3D assemblies are more affected than 2D assemblies, where the surface is represented by a line rather than by a 2D entity. However, even in large assemblies, where the fraction of the surface energy is reduced, they cannot be ignored since they incorporate localised effects which are important for the nucleation of phase transformations. This is experimentally well known and has already been illustrated in Fig. 1.4 on p. 5. Thus, since surfaces represent such important objects in nature, any attempt to artificially exclude them from simulations appears, at the first glance, to be an absurd idea.

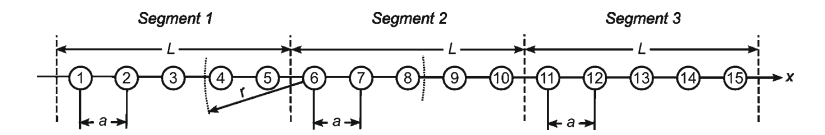


Fig. 2.3 A 1D chain of 15 atoms at identical nearest-neighbour distances a. The atoms are uniformly assigned to 3 segments of equal length L=5a

Nevertheless despite this, there is reasonable justification to exclude surfaces: for technical reasons (because the computational resources are limited) or to intentionally suppress any surface reaction in order to focus on the bulk situation. The common technique for excluding the surface is to apply *periodic boundary conditions* (PBC) [35]. We explain the principle by considering a 1D chain of pairwise interacting atoms, see Fig. 2.3.

The chain consists of 15 atoms which are uniformly assigned to three segments of equal length L. The lattice parameter a of the chain is assumed to be constant along the chain, such that L=5a holds, and the atoms possess unit mass. We further assume the atomic interactions are short ranged, with an interaction radius of r=2a say, such that only the nearest and next-nearest neighbours effectively interact. Hence, the equations of motion for the atoms 6–10 in the middle segment 2 are expressed as

$$\begin{pmatrix}
\ddot{x}_{6} = \frac{f(r_{6,4}) + f(r_{6,5}) + f(r_{6,7}) + f(r_{6,8})}{\ddot{x}_{7} = \frac{f(r_{7,5}) + f(r_{7,6}) + f(r_{7,8}) + f(r_{7,9})}{\ddot{x}_{8} = \frac{f(r_{8,6}) + f(r_{8,7}) + f(r_{8,9}) + f(r_{8,10})}{\ddot{x}_{9} = f(r_{9,7}) + f(r_{9,8}) + f(r_{9,10}) + \frac{f(r_{9,11})}{\ddot{x}_{10} = f(r_{10,8}) + f(r_{10,9}) + \frac{f(r_{10,11})}{f(r_{10,11})} + \frac{f(r_{10,12})}{\ddot{x}_{10,12}}
\end{pmatrix} (2.18)$$

 $r_{\alpha,\beta}$ denotes the separation between two atoms α and β . The underlined terms on the right-hand side indicate cross-segment interactions. Since the interactions are of finite range, atoms 1–3 and 13–15 do not directly interact with the middle segment atoms. Also, there are no direct interactions between the atoms at the front and the rear of the second segment. Therefore, one might think of replacing the segments 1 and 3 by copies of segment 2, which are translated by $\pm L$ for this purpose. With this idea, the underlined terms in Eq. (2.18) may be exclusively expressed in terms of the positions of segment 2 atoms and L. Accordingly, the underlined terms are now rewritten and Eq. (2.18) becomes

$$\begin{pmatrix}
\ddot{x}_{6} = f(L - r_{9,6}) + f(L - r_{10,6}) + f(r_{6,7}) + f(r_{6,8}) \\
\ddot{x}_{7} = f(L - r_{10,7}) + f(r_{7,6}) + f(r_{7,8}) + f(r_{7,9}) \\
\ddot{x}_{8} = f(r_{8,6}) + f(r_{8,7}) + f(r_{8,9}) + f(r_{8,10}) \\
\ddot{x}_{9} = f(r_{9,7}) + f(r_{9,8}) + f(r_{9,10}) + f(L - r_{9,6}) \\
\ddot{x}_{10} = f(r_{10,8}) + f(r_{10,9}) + f(L - r_{10,6}) + f(L - r_{10,7})
\end{pmatrix} (2.19)$$

This equation represents a closed system of ODE for calculating the motions of atoms located in the second segment (provided that f is known and the initial conditions are set). Similar to the original chain, the atoms of segment 2 are not affected by the free "surface", i.e. the ends of the chain. Note, the size of L needs to be chosen with respect to the interaction range, L > r must hold. This method is easily extended into all three spatial directions, where the segment is expanded into a 3D super-cell placed in a simulation box of edge length L.

Care must be taken since, according to Eq. (2.19), the computed trajectories depend on L. One consequence is restricted eigenmodes, thus restricting the physics of the investigated assembly. Another complication arises from the fact that in realistic materials, the lattice parameter depends on temperature, a = a(T), and thus L = L(T). Therefore during non-isothermal simulations, the size of the simulation box must be adjusted according to a(T). The situation can become even worse: if the super-cell undergoes a lattice transformation, the size and shape of the simulation box must be adjusted accordingly, otherwise anisotropic transformation stresses are induced. Techniques providing these tasks have already been developed.

2.2.6 Parrinello-Rahman

The technique of simultaneously controlling the size and shape of the simulation box is named after the work of Parrinello and Rahman [36, 37], who generalised the earlier work of Andersen [34]. Andersen employed an extended Lagrangian formulation for the derivation of a barystat.¹

Up to this point, atomic positions and velocities were implicitly represented with respect to the rectangular Cartesian coordinate (r.C.c.) system E_i . According to the rules of tensor algebra, their vectors may alternatively be represented with respect to the skew bases \mathbf{e}_i . This base system may be obtained from E_i by a linear transformation A,

$$\mathbf{e}_j = A_i^i \mathbf{E}_i. \tag{2.20}$$

Accordingly, the r.C.c. components x^i transform into the coordinates z^i in the skew system by 2

$$x^i = A^i_j z^j. (2.21)$$

¹ We have already cited this article in the discussion of thermostats, but it was more influential in regard to the extended Langrangian method used.

² Notation: lower case Latin letters indicate 3D tensor components. Einstein's summation convention is adopted. In a skew system, two sets of coordinates exist, obtained by a perpendicular projection to (covariant components) and by parallel projection along (contravariant components) the base vectors. Contravariant components are indicated by raised (row, column) indices and covariant components by lower (row, column) indices. The co- and contravariant skew bases \mathbf{e}_j and \mathbf{e}^i are reciprocal, such that $\mathbf{e}^i\mathbf{e}_j = \delta^i_j$ holds true (with δ^i_j —Kronecker Delta). In normalised, orthogonal bases systems, $\mathbf{E}^i = \mathbf{E}_j$ holds true and accordingly co- and contravariant tensor components are identical.

Parrinello and Rahman consider a time-dependent transformation, $A^i_j = A^i_j(t)$, such that the base system may be adjusted according to the current crystal structure. The aim is to simultaneously determine the nine components of $A^i_j(t)$ with the computation of the trajectories. For this purpose, Parrinello and Rahman proposed an extended Lagrangian of the form

$$\mathscr{L}^{PR} = \sum_{\alpha=1}^{N} \frac{m_{\alpha}}{2} g_{ij} \dot{z}_{\alpha}^{i} \dot{z}_{\alpha}^{j} - V^{\text{int}}(A_{j}^{i} z_{\gamma}^{j}) + \frac{W}{2} \dot{A}_{j}^{i} \dot{A}_{j}^{i} - p \det(A) - \frac{1}{2} g_{ij} S^{ij}. \tag{2.22}$$

 $g_{ij} = A_i^k A_j^k$ denotes the metric of the skew base system. W denotes a constant with mass dimension. The term $W/2\dot{A}_j^i\dot{A}_j^i$ therefore may be vaguely interpreted as a "kinetic energy" associated with the time changes of $A_j^i(t)$. p represents a superimposed isotropic pressure and S^{ij} is related to the stresses σ^{ij} through

$$S^{ij} = (\tilde{A}^{-1})_{l}^{i} (\sigma^{kl} - p\delta^{kl}) (\tilde{A}^{-1})_{l}^{j} \det(\tilde{A}). \tag{2.23}$$

The tildes () denote a reference configuration.

Equation (2.22) implies a new set of equations of motion, which read as

$$m_{\alpha}g_{ik}\ddot{z}_{\alpha}^{k} = \sum_{\beta=1,\beta\neq\alpha}^{N} \frac{\partial V^{\text{int}}}{\partial r_{\beta\alpha}} \frac{r_{\beta\alpha}^{i}}{r_{\beta\alpha}} - m_{\alpha}\dot{g}_{ik}\dot{z}_{\alpha}^{k},$$

$$WA_{j}^{i}\ddot{A}_{j}^{k} = \sum_{\alpha=1}^{N} A_{m}^{i} A_{n}^{k} \dot{z}_{\alpha}^{m} \dot{z}_{\alpha}^{n} - \sum_{\alpha,\beta=1,\beta\neq\alpha}^{N} \frac{\partial V^{\text{int}}}{\partial r_{\beta\alpha}} \frac{r_{\beta\alpha}^{i} r_{\beta\alpha}^{k}}{r_{\beta\alpha}} - p \det(A) \delta^{ik} - A_{m}^{i} A_{n}^{k} S^{mn}$$

$$(2.24)$$

 $r_{\beta\alpha}=(g_{ij}(z^i_{\beta}-z^i_{\alpha})(z^j_{\beta}-z^j_{\alpha}))^{1/2}$ are the atomic separations and $r^i_{\beta\alpha}=A^i_k(z^k_{\beta}-z^k_{\alpha})$ denotes the distance vector pointing from atom α to atom β . Equations (2.24) may be used to compute the trajectories of an N-atom ensemble subject to constant stress conditions. Note that the atomic velocities explicitly appear on the right-hand side of Eq. (2.24)₁, thus demanding an integration scheme capable of simultaneously computing the atomic positions and velocities. Equation (2.24)₂ represents nine equations for computing the components of the transformation matrix $A^i_j(t)$.

Two critical remarks on this method are warranted. The first concerns the derivation of the extended Lagrangian (2.22) and the second, the idea of a "volumetric" stress control implied by the method.

Regarding $A_j^i = A_j^i(t)$, the atomic velocities in the skew system are obtained by differentiating Eq. (2.21) with respect to t,

$$\dot{x}^i_{\alpha} = A^i_j \dot{z}^j_{\alpha} + \dot{A}^i_j z^j_{\alpha}. \tag{2.25}$$

The squares of the velocities therefore read

$$\dot{x}_{\alpha}^2 = g_{ij}\dot{z}_{\alpha}^i\dot{z}_{\alpha}^j + \dot{A}_i^k\dot{A}_j^kz_{\alpha}^iz_{\alpha}^j + 2\dot{A}_i^kA_j^kz_{\alpha}^i\dot{z}_{\alpha}^j. \tag{2.26}$$

Of the three terms on the right-hand side of this equation, only the first appears in the extended Lagrangian of Equation (2.22), while the other two, which are underlined, are dropped, raising concerns about the consistency of the Lagrangian thus derived. While Andersen comments on a similar inconsistency in his work [34], Parrinello and Rahman flatly note "whether such a Lagrangian is derivable from first principles is a question of further study; its validity can be judged, as of now, by the [...] statistical ensembles that it generates" [36].

The second remark concerns the "volumetric" nature of the stress control: by the Parrinello and Rahman method, stress is controlled simultaneously at any location in the crystal by a virtual body force with respect to statistical equilibrium conditions. In contrast to this, in the laboratory, stress is only controlled on surfaces since internal stress states are not directly accessible. Thus, in an actual sample, mechanical equilibrium is dynamically established by the propagation of stress waves which may interact with the microstructure. It is not a priori clear, how such processes are constrained in simulations employing the Parrinello and Rahman method.

Despite these critical remarks, the method appeared to produce encouraging results for small super-cells under PBC and therefore quickly became popular at a time of limited computational resources. Scientists justify its application a posterior from the reasonableness of the results and ignore the absence of the justification.

2.2.7 Parallelisation

For technical reasons, the computer hardware limits both the size N of the ensemble investigated and the simulated physical time period $t_{\rm sim}$. Limitations are due to both hardware speed and data storage limits. The speed is primarily a function of the hardware clock rate the central processing unit (CPU) of a computer is running at. This rate is typically measured in floating-point operations per second (FLOP/s). Other hardware parameters like memory management contribute to a minor extent to the speed. Ensemble sizes are primarily limited by the amount of random access memory (RAM) available on a system. Further, the capacity of the permanent data storage system (hard drives) limits the total amount of data that can be recorded through the entire simulation run. We may denote the significant hardware characteristic by the hardware parameter array $\bf p$.

A measure for the performance of a specific MD simulation program run on a given hardware is the computer runtime needed to compute a single time step Δt , denoted by $\tau_{\text{CPU}}(\Delta t, \mathbf{p}, N)$. Suppose that the program is executed on a single computer such that \mathbf{p} is fixed. Hence the total runtime needed to simulate an N-atom ensemble is proportional to the total number of time steps $t_{\text{sim}}/\Delta t$,

$$\tau_{\text{CPU,serial}}^{\text{tot}} = \frac{t_{\text{sim}}}{\Delta t} \tau_{\text{CPU}}(\Delta t, \mathbf{p}, N). \tag{2.27}$$

Note that in this equation, two different time measures appear: the simulated time period t_{sim} has a microscale order of magnitude and it is discretised into time steps of Δt . This time has to be distinguished from the runtime τ_{CPU} the computer requires to calculate the trajectories, which may even scale in weeks or months.

According to Eq. (2.27), the total runtime is related to the hardware parameters \mathbf{p} , the ensemble size N and the desired simulation time t_{sim} on a single serial computer. For technical and practical reasons, this runtime is obviously limited. Hence, for the given available runtime $\tau_{\text{CPU}}^{\text{tot}}$ on a selected machine, Eq. (2.27) relates the accessible simulated time t_{sim} to the ensemble size N.

The computational costs of the MD method basically result from the calculation of the interaction forces \mathbf{f}_{α} which are functions of the atomic separation matrix $r_{\beta\alpha}$ $|\mathbf{x}_{\beta} - \mathbf{x}_{\alpha}|$ ($\alpha, \beta = 1...N$). The computational effort to calculate the total separation matrix scales with N^2 . Physics helps to reduce this effort: because the interaction forces are short ranged in comparison to typical system sizes, the interaction force \mathbf{f}_{α} of an individual atom is no longer a function of the full separation matrix, rather of only those separations which fall below a specific interaction horizon and any other interactions are neglected. In MD, this horizon is modelled by a cut-off radius denoted by r_c . Neighbourhood lists (sometimes called Verlet lists) are used to bookkeep the interaction partners of all atoms and these lists—frequently updated during the simulation run to keep track of changing interactions—are used to compute the forces. In solids, where atoms are merely immobile on the short and medium term, typical update periods are 1,000-5,000 time steps. Only at update events is the total separation matrix computed, meanwhile only separations between neighbourhood atoms are computed. This method reduces the computational effort to scale with Nrather than N^2 .

The concept of limited interaction horizons also suggests that the computational effort be distributed over a grid of machines which perform the integrations in parallel. For this purpose, the ensemble is spatially decomposed into domains as illustrated in Fig. 2.4. These domains are computed in parallel on a computer grid that logically represents the domain structure. Domain sizes are typically set larger than the cut-off radius, thereby restricting inter-domain interactions to adjacent domains. These interactions require data communication between the computation nodes of the grid. Hence, new hardware and software components are introduced, which are needed to maintain this data communication.

Since in a grid the individual computation nodes only have to integrate a subset N_S out of the N trajectories, the runtime needed for computing a single time step is significantly reduced to $\tau_{\text{CPU}}(\Delta t, N_S) < \tau_{\text{CPU}}(\Delta t, N)$. The drawback of this method is the inter-domain data communication, which causes some delay $\tau_{\text{comm}}(\Delta t, N_S)$ in every single time step. Hence the total runtime needed to simulate the atomic trajectories on a parallel computer is given by

$$\tau_{\text{CPU,parallel}}^{\text{tot}} = \frac{t_{\text{sim}}}{\Delta t} \left(\tau_{\text{CPU}}(\Delta t, N_S) + \tau_{\text{comm}}(\Delta t, N_S) \right),$$
 (2.28)

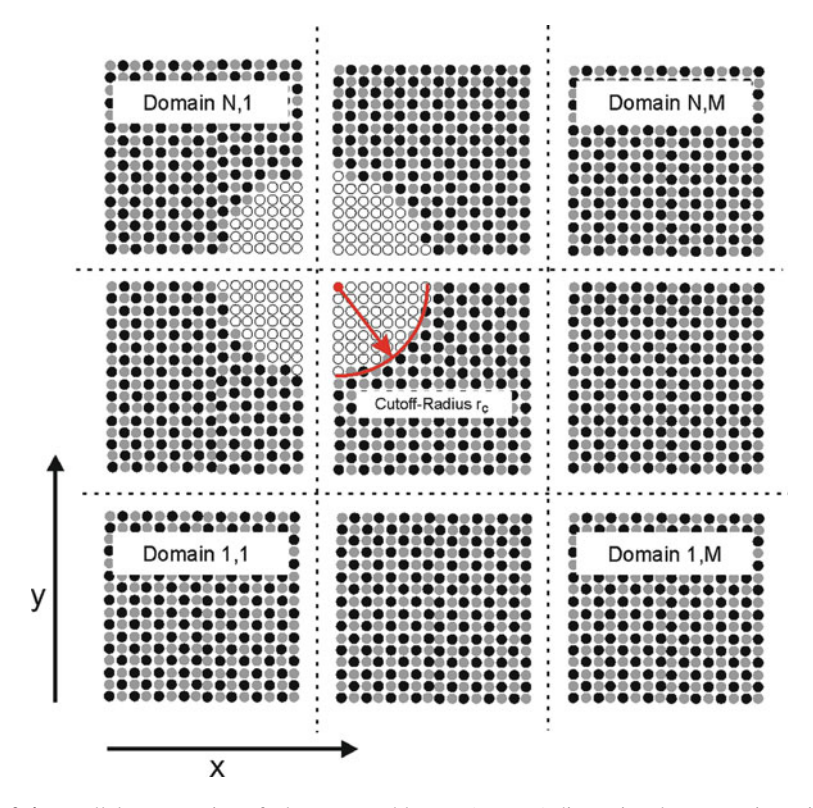


Fig. 2.4 Parallel computation of a large ensemble on a $(N \times M)$ dimensional computation grid by logical domain decomposition (2D sketch). The interaction radius r_c determines how far interactions may penetrate into adjacent domains ("halo-regions")

(assuming that the computation grid consists of identical nodes). This Eq. (2.28) states an optimisation problem for determining the domain size N_S . To explain this relation, we define the runtime speed-up σ achievable by means of parallelisation by the ratio of Eqs. (2.27) and (2.28),

$$\sigma = \frac{\tau_{\text{CPU}}(N)}{\tau_{\text{CPU}}(N_S) + \tau_{\text{comm}}(N_S)}.$$
 (2.29)

As an illustration, we may evaluate this equation by using general assumptions: $\tau_{\text{CPU}}(N)$ and $\tau_{\text{CPU}}(N_S)$ may be assumed to be proportional to N and $N_S = N/s$, respectively, where s is the number of computation nodes. The communication overhead $\tau_{\text{comm}}(N_S)$ may be set proportional to s multiplied by the amount of data to be communicated for a single domain. This amount depends of the number of atoms affected by the cross-domain interactions, called the interaction "halo" of adjecent domains in the jargon of parallel coding. The latter may be assumed to scale with $\sqrt[3]{N/s}^2$. Hence we get $\sigma = s/(1 + ps\sqrt[3]{s/N}^2)$, which has a maximum at $s = 3^{3/4}N^{1/4}p^{-3/4}$ (p represents the combined proportionality factors). If we



Fig. 2.5 Flow chart of a generic MD simulations program

arbitrarily set p=1 and $N=10^6$, say, the maximum speedup is achieved at $s\approx73$ computation nodes. This is not a realistic figure, but it nicely illustrates the general limits of code parallelisation. In reality, parallelisation has to additionally take into account the computational resources available at a specific high-performance computation (HPC) facility and the CPU quota allowances set by the facility's administration.

2.2.8 MD Simulation Computer Program

Figure 2.5 shows a flowchart of a generic MD simulation program used for the investigation of martensitic transformations in this work. We use the Verlet algorithm in its coordinate formulation, Eq. (2.3), to recursively compute, in parallel on a

computation grid, the trajectories of crystalline atomic ensembles. The initial atomic velocities are selected randomly with respect to the initial temperatures. For the reasons pointed out above, we shall not employ methods based on extended Lagrangians. Our thermostat uses the method of velocity scaling and relaxation. Since we shall not employ PBC, we are able to avoid the otherwise mandatory use of the Parrinello and Rahman method for controlling the size and shape of the simulation box. In simulations where external loads need to be applied in order to simulate tensile tests, these loads are always directly added to the force vectors of individual atoms as a function of time. This simulates a tensile test under load control mode. In contrast, a tensile test under displacement control mode is effectively modelled by collectively controlling the positions of selected atoms located at surface layers as a function of time.

We use neighbourhood lists to reduce the computational effort per computation node. These are updated within periods of 1,000–2,000 time steps. Fixed halo-regions are considered for the inter-domain communication of the parallel computer grid. The size of the halo-regions at every node is determined in the cubic crystal structure. Since atoms may slightly change their interaction neighbourhoods due to the dislocation mechanism, the sizes of the halo-regions are conservatively chosen to be larger than the cut-off radius.

In the course of the project, different computing facilities were employed. For the purpose of code development and also for the investigation of small-size ensembles, a parallel Linux Cluster was established at the Department of Materials Science in Bochum. Here, a low-latency Infiniband network guaranteed fast communication between the processors. The code was ported to professional HPC facilities to study larger problems. The facilities used are located at the University of Edinburgh (HPCx, bluegene [38]) and at Germany's National Research Centre in Jülich (JUMP and JUROPA at NIC [39]). The parallel code was developed with consultative support from the Edinburgh Parallel Computing Centre (EPCC). Here, the Message-Passing-Interface (MPI) library is employed [40] to implement the inter-domain communication. MPI is highly flexible and is independent of specific platforms and thus nicely supports code porting between the platforms used. The code was optimised by using the VAMPIR-profiling software (Visualisation and Analysis of MPI Programs [41]).

The simulation results are frequently recorded during their computations. Since the storage devices have limited space, it is necessary to reduce the amount of stored data. For a preliminary investigation, it is sufficient to record a chosen set of primary data (atomic phases and potential energy) at only selected time steps. The recording frequency must be selected with respect to a timescale of the specific processes under consideration.

2.3 Post-Processing

MD simulations produce immense amounts numerical data. Thus, the analysis of the results is a distinct issue in its own right and requires another set of computational post-processing tools. The analysis of the results is mainly based on visualisation.

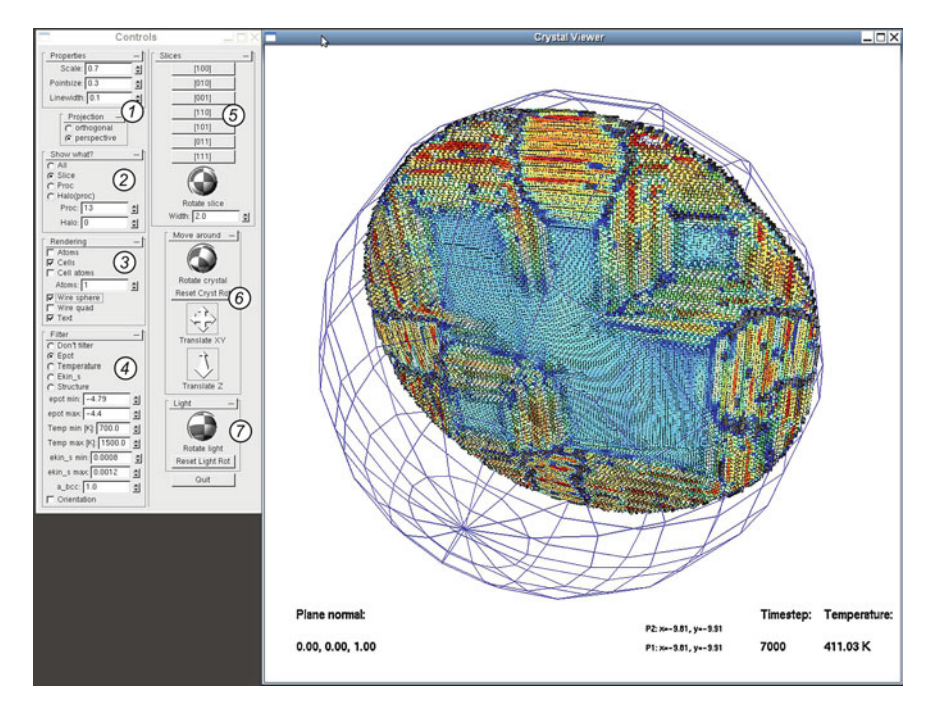


Fig. 2.6 Screenshot of the Crystal Viewer program written for the visualisation of lattice transformations and microstructures in crystals. The program analyses and visualises the simulated atomic positions in different render modes (1, 2, 3) which can be interactively controlled. Here, the main window shows a narrow [001] section through the centre of a 5.5 million atom crystal sphere during an MT. The present crystal structure is visualised by unit cells coloured according to their potential energies defined in the BCC phase. Martensite (*white/red/orange*) has lower potential energy than austenite (*blue*), thus providing a visible colour contrast. Domain boundaries and the free surface are accompanied by excess energies shifting the potential energy to a higher level (*grey*). The colour contrast can be adjusted by means of the filter settings and different filter options may be selected (4). The orientation of the section can be varied (5) or be viewed from different perspectives (1, 6). Light settings may be adjusted to accentuate surface reliefs (7). Interesting local regions may be marked interactively and the corresponding simulation data can then be exported for further external analysis

The visualisation software must merge the data produced on the parallel computation facility and produce a comprehensive display output. Appropriate software should be capable of distinguishing lattice- and microstructures, permit sectional representations and enable the observer to isolate and magnify local effects. Owing to these specific demands, it is advantageous to use a customised code. Furthermore, algorithms are needed to relate the simulation data to the relevant field variables of mechanics and thermodynamics.

Figure 2.6 shows a screenshot of the Crystal Viewer program developed to meet the needs of data visualisation within the framework of this project. Written in C, the program benefits from its streaming capabilities. The Open Graphics Library [42] and the GLUI toolbox [43] were employed to implement the graphics core and to

2.3 Post-Processing 55

deal with interactive control elements, respectively. The lattice may be visualised in either atom render mode (by points) or in unit cell render mode (by polygons). Unit cells may be defined in the perfect BCC structure by means of the nearest and next nearest neighbouring atoms located about individual central atoms of cubic unit cells. Any render mode may use colour codes according to selected analysis settings:

- Potential energy analysis: atoms or cells located in identical crystal phases have the same potential energy, while the potential energy differs between phases. This may be used to distinguish the phases by colour codes. Potential energy analysis also reveals lattice artefacts, dislocations, surface and interface energies.
- Temperature analysis: the evolution of lattice transformations is accompanied by the release/absorption of latent heat, thus providing a temperature signal at the locations of the travelling transformation fronts. This may be visualised by utilising the temperature filter settings.
- Mesoscopic kinetic energy analysis: martensitic transformations are locally indicated by regimented atomic motions (military transformation). These motions may build up a kinetic energy on the mesoscopic length scale, which can be detected in order to isolate transformation zones.
- Crystal structure: transformation modes of BCC unit cells may be used to identify martensite variants in 2D (Chap. 4). In 3D (Chap. 5), we employ the "Ball Viewer"- algorithm by Ackland and Jones [44] to define and analyse local BCC, FCC and HCP crystal structures. This algorithm is based on a combined evaluation of the radial distribution functions and the angular distribution functions of the direction cosines between nearest and next nearest neighbours of individual atoms. It was slightly modified to utilise additional information on the interaction neighbourhoods available from the MD code, improving the speed in large-scale applications.

References

- G.J. Ackland, Atomistic modelling of the shape memory effect. in *Solid–Solid Phase Trans-formations in Inorganic Material 2005*, ed. by J.M. Howe, D.E. Laughlin, J.K. Lee, U. Dahmen, W.A. Soffa. International Conference on Solid–Solid Phase Transformations in Inorganic Materials (PTM 2005), vol. 2 (Phoenix, AZ, 2005), pp. 153–164, MAY 29–JUN 03, 2005
- 2. W.G. Hoover, Molecular Dynamics. Lecture Notes in Physics. (Springer, 1986)
- 3. D. Frenkel, B. Smit, *Understanding Molecular Simulation. From Algorithms to Applications* (Academic Press, San Diego, 1996)
- 4. D. Rapaport, *The Art of Molecular Dynamics Simulation*, 2nd edn. (Cambridge University Press, Cambridge, 2004)
- P.C. Clapp, J. Rifkin, Nucleation of a martensite in a computer. in *Proceedings of International Conference on Solid–Solid Phase Transformations*, (Warrendale, PA, 1982), pp. 1165–1169, TMS-AIME
- P.C. Clapp, J. Rifkin, Simulated martensitic transformations. Proc. Mater. Res. Soc. Symp. 21, 643–656 (1983)
- Z.-Z. Yu, P.C. Clapp, Growth dynamics study of the martensitic transformation in Fe-30 pct Ni alloys: Part II. computer simulation of martensitic growth. Metall. Trans. A 20A, 1617–1629 (1989)

- 8. M.S. Daw, M.I. Baskes, Embedded-atom method: Derivation and application to impurities, surfaces and other defects in metals. Phys. Rev. B **29**, 6443–6453 (1984)
- K.S. Cheung, R.J. Harrison, S. Yip, Stress induced martensitic transformation in a molecular dynamics model of α-iron. J. Appl. Phys. 71(8), 4009–4014 (1992)
- M. Grujicic, P. Dang, Computer simulation of martensitic transformation in Fe-Ni face-centered cubic alloys. Mater. Sci. Eng. A 201, 194–204 (1995)
- M. Grujicic, P. Dang, Atomic-scale analysis of martensitic transformation in titanium alloyed with vanadium. Part II: Molecular dynamics simulations. Mater. Sci. Eng. A 205, 153–165 (1996)
- 12. P. Dang, M. Grujicic, An atomistic simulation of the effect of crystal defects on the martensitic transformation in ti-v bcc alloys. Model. Simul. Mater. Sci. Eng. 4, 123–136 (1996)
- 13. M. Grujicic, S.G. Lai, P. Gumbsch, Atomistic simulation study of the effect of martensitic transformation volume change on crack-tip material evolution and fracture toughness. Mater. Sci. Eng. A 231, 151–162 (1997)
- Y. Shao, P.C. Clapp, J.A. Rifkin, Molecular dynamics simulation of martensitic transformations in NiAl. Metall. Mater. Trans. A 27A, 1477–1489 (1996)
- R.J. Meyer, Computersimulation martensitischer Phasenübergänge in Eisen-Nickel- und Eisen-Aluminium-Legierungen, Ph.D. thesis, Gerhard-Mercator-Universität-Gesamthochschule Duisburg, 15 April 1998, Group of Prof. Entel
- A.R. Kuznetsov, Y.N. Gornostyrev, M.I. Katsnelson, A.V. Trefilov, Effect of the dislocations on the kinetics of a martensitic transition md simulation of bcc-hcp transformation in Zr. Mater. Sci. Eng. A 309–310, 168–172 (2001)
- 18. K. Kadau, Molekulardynamik-Simulation von strukturellen Phasenumwandlungen in Festkörpern, Nanopartikeln und ultradünnen Filmen, Ph.D. thesis, Gerhard-Mercator-Universität-Gesamthochschule Duisburg, 9. März 2001, Group of Prof. Entel
- M.I. Mendelev, G.J. Ackland, Development of an interatomic potential appropriate for simulation of phase transformations in zirconium. Phil. Mag. Lett. 87, 349–359 (2007)
- G.J. Ackland, S.J. Wooding, D.J. Bacon, Defect, surface and displacement-threshold properties of -zirconium simulated with a many-body potential. Phil. Mag. A 71, 553–565 (1995)
- U. Pinsook, G.J. Ackland, Simulation of martensitic microstructural evolution in zirconium. Phys. Rev. B 58(17), 11252 (1998)
- U. Pinsook, G.J. Ackland, Atomistic simulation of shear in a martensitic twinned microstructure. Phys. Rev. B 62(9), 5427–5434 (2000)
- 23. O. Kastner, Molecular dynamics of a 2D model of the shape memory effect. Part I: Model and simulations. Continuum Mech. Therm. **15**(5), 487–502 (2003)
- 24. O. Kastner, Zweidimensionale molekular-dynamische Untersuchung des Austenit ↔ Martensit Phasenübergangs in Formgedächtnislegierungen, Ph.D. thesis, Technical University of Berlin, 2003
- 25. O. Kastner, Molecular dynamics of a 2D model of the shape memory effect. Part II: Thermodynamics of a small system. Continuum Mech. Therm. **18**(1–2), 63–81 (2006)
- R.S. Elliott, J.A. Shaw, N. Triantafyllidis, Stability of thermally-induced martensitic transformations in bi-atomic crystals. J. Mech. Phys. Solids 50, 2463–2493 (2002)
- X.D. Ding, T. Suzuki, X.B. Ren, J. Sun, K. Otsuka, Precursors to stress-induced martensitic transformations and associated superelasticity: Molecular dynamics simulations and an analytical theory. Phys. Rev. B 74, 104111-1-104111-10 (2006)
- F.E. Hildebrand, R. Abeyaratne, An atomistic investigation of the kinetics of detwinning. J. Mech. Phys. Solids 56(4), 1296–1319 (2008)
- L. Verlet, Computer "experiments" on classical fluids. i. thermodynamical properties of lennard–jones molecules. Phys. Rev. 159(1), 98 (1967)
- W.C. Swope, H.C. Andersen, P.H. Berens, K.R. Wilson, A computer simulation method for the calculation of equilibrium constants for the formation of physical clusters of molecules: Application to small water clusters. J. Chem. Phys. 67, 637–649 (1982), The scheme is derived in the appendix

References 57

31. D. Beeman, Some multistep methods for use in molecular dynamics calculations. J. Comput. Phys. **20**(2), 130–139 (1976)

- 32. S. Nose, A molecular dynamics method for simulations in the canonical ensemble. Mol. Phys. **52**(2), 255–268 (1984)
- W.G. Hoover, Canonical dynamics: Eqilibrium phase-space distributions. Phys. Rev. A 31(3), 1695–1697 (1985)
- H.C. Andersen, Molecular dynamics simulations at constant pressure and/or temperature. J. Chem. Phys. 72(4), 2384–2393 (1980)
- N. Metropolis, A.W. Metropolis, M.N. Rosenbluth, A.H. Teller, E. Teller, J. Chem. Phys. 21, 1097 (1953)
- M. Parrinello, A. Rahman, Polymorphic transitions in single crystals: A new molecular dynamics method. J. Appl. Phys. 52(12), 7182–7190 (1981)
- M. Parrinello, A. Rahman, Crystal structure and pair potentials: A molecular-dynamics study. Phys. Rev. Lett. 45(14), 1196–1199 (1980)
- 38. Edinburgh Parallel Computing Centre (EPCC), Internet resource, http://www.epcc.ed.ac.uk
- John von Neumann Institute for Computing (NIC), Internet resource, http://www.fz-juelich. de/nic
- 40. W. Gropp, W. Lusk, A. Skjellum, in *Using MPI. Portable parallel programming with the Message-passing interface*, Scientific and Engineering Computation Series, 1999
- 41. H. Brunst, D. Kranzlmüller, M.S. Muller, W.E. Nagel, Tools for scalable parallel program analysis: VAMPIR NG, MARMOT, and DeWiz. Int. J. Comput. Sci. Eng. 4(3), 149–161 (2009)
- 42. M. Woo, J. Neider, T. Davis, D. Shreiner, *OpenGL Programming Guide* (Addison-Wesley, Reading, 1999)
- 43. P. Rademacher, GLUI user interface library. Internet resource (2006), http://glui.sourceforge.
- 44. G.J. Ackland, A.P. Jones, Applications of local crystal structure measures in experiment and simulation. Phys. Rev. B **73**(5), 054104-1–054104-7 (2006)

Chapter 3 2D Model Material

In this chapter we present MD simulations of martensitic phase transformations in 2D Lennard–Jones (L–J) crystals. A binary L–J potential is used to describe a square-to-hexagonal transformation by shear-and-shuffle processes. The model material is capable of the complex thermo-mechanical coupling present in SMA—pseudo-plasticity, pseudo-elasticity and the shape memory effect [1, 2].

3.1 The Model Material

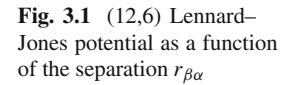
In a Lennard–Jones (L–J) crystal, atomic interactions only depend on the separations $r_{\beta\alpha} \equiv |\mathbf{x}_{\beta} - \mathbf{x}_{\alpha}|$ between atom pairs α and β according to the interaction potential

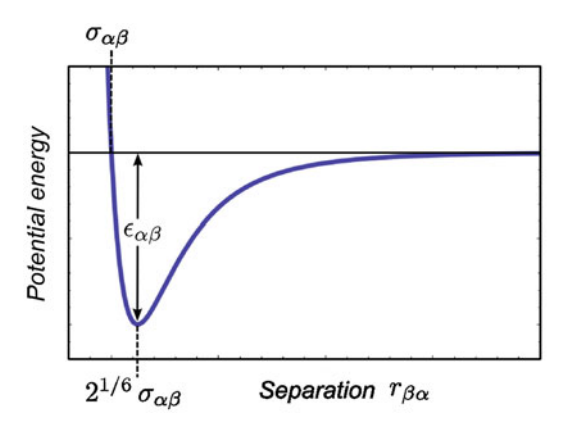
$$\Phi_{\alpha\beta} = 4 \,\varepsilon_{\alpha\beta} \left(\left(\frac{\sigma_{\alpha\beta}}{r_{\beta\alpha}} \right)^{12} - \left(\frac{\sigma_{\alpha\beta}}{r_{\beta\alpha}} \right)^{6} \right). \tag{3.1}$$

L–J potentials therefore are called "pair potentials". $\varepsilon_{\alpha\beta}$ and $\sigma_{\alpha\beta}$ are the pair interaction parameters. Their significance is indicated in Fig. 3.1: σ determines the root while ε determines the depth of the potential well, thus setting its strength. The minimum is located at $r_{\beta\alpha}=2^{1/6}\sigma_{\alpha\beta}$. At smaller distances the potential behaves repulsive and attractive beyond. For large separations, the interactions decay asymptotically to zero. Therefore, at $r_{\beta\alpha}=2^{1/6}\sigma_{\alpha\beta}$, the interactions of a single (α,β) atom pair vanish, providing a stable ground state separation of an isolated atom pair.

An individual atom α located in a lattice experiences a potential V^{α} due to pair interactions with all surrounding atoms

$$V^{\alpha} = \sum_{\beta=1,\beta\neq\alpha}^{N} \Phi_{\alpha\beta}(r_{\beta\alpha}). \tag{3.2}$$





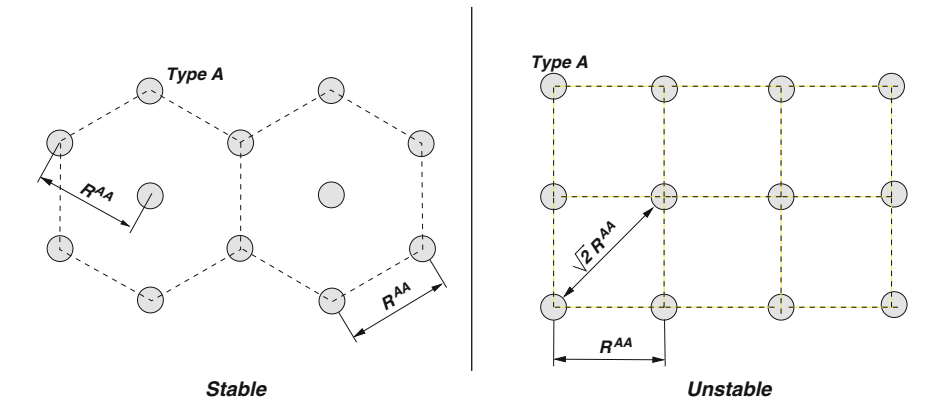


Fig. 3.2 In 2D, stable monatomic L–J crystals have hexagonal lattices; other structures are unstable

In a cohesive crystal, an individual atom α is symmetrically encompassed by interaction partners β . Accordingly, the superposition of pair-potentials potential $\Phi_{\alpha\beta}$ in Eq. (3.2) effects V^{α} is convex in regard to the co-ordinates \mathbf{x}_{α} of atom α and the nearest neighbour distance slightly deviates from $2^{1/6}\sigma_{\alpha\beta}$ in general. The total internal potential energy of an N-atomic assembly reads

$$V^{\text{int}} = \frac{1}{2} \sum_{\alpha=1}^{N} V^{\alpha},\tag{3.3}$$

since the pair potentials are symmetric in α and β .

Monatomic L–J crystals do not exhibit lattice transformations, Fig. 3.2. In this situation, the lattice structure is determined by a single set of interactions parameters (ε, σ) . In 2D, the solely stable structure is closed-packed hexagonal and any other

3.1 The Model Material 61

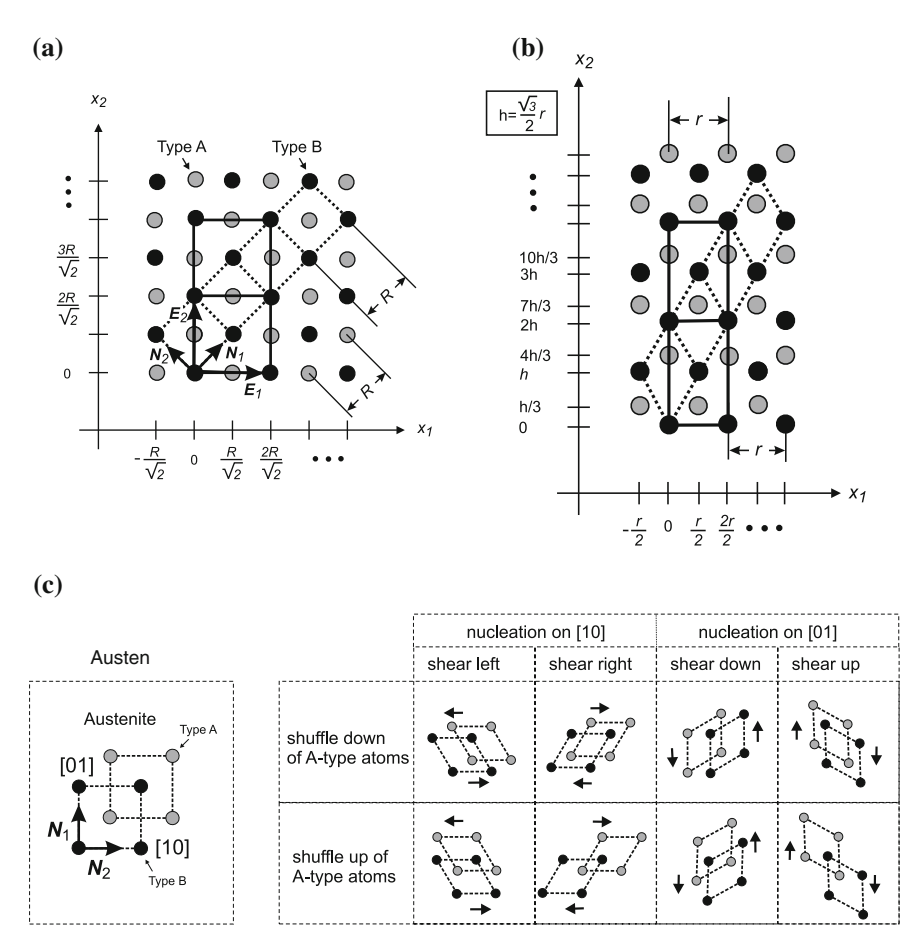
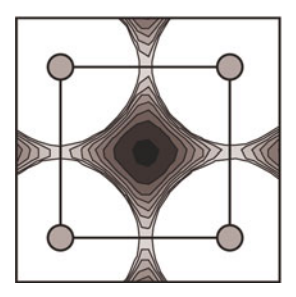
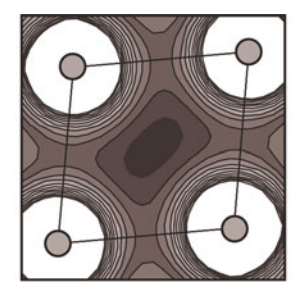


Fig. 3.3 Binary L–J lattices in 2D in the austenite (a) and the martensite (b). c Variants of martensite arising due to opposite shear directions of an austenitic unit cell with respect to both principle directions [01] and [10] and due to opposite shuffle directions of sub-lattices, respectively

structures are dynamically instable. Such model is too poor to represent lattice transformations.

The situation changes if two atom species are taken into account. In a binary model three potential functions are needed to model interactions A–A, B–B and A–B interactions of the generic atom species A and B. A–A and B–B potentials model bonds between the pure species while the A–B potential defines the cross-species interaction. Hence there are six interaction parameters (ε_{AA} , σ_{AA}), (ε_{BB} , σ_{BB}) and (ε_{AB} , σ_{AB}) to be selected. Here, the balance between pure- and cross-species potentials determines the crystal structure of the binary lattice. Thus, our 2D model material consists of two atomic species, A and B. Such model allows for





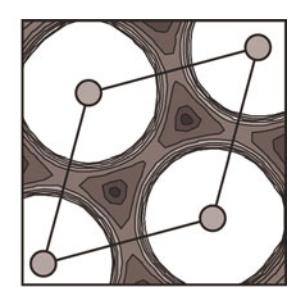


Fig. 3.4 Potential energy landscape of the interstitial type-B atom within a type-A unit cell for three different shearing events. The contour plot portrays the potential energy using various shades of *grey*; from high values (*white*) to low values (*black*)

the crystal structures shown in Fig. 3.3. The model austenite, Fig. 3.3a, is represented by nested square sub-lattices of A and B type. In the binary L–J system, the square lattice can be stabilised by temperature if the cross-species (A,B) interactions are properly adjusted. The model martensite, Fig. 3.3b, is produced by a shear/shuffle transformation of the square lattice: square unit cells are sheared into diamonds, accompanied by shuffle of the sub-lattices.

The energetic situation which determines this shuffle on the scale of a unit cell is illustrated in Fig. 3.4, showing contour plots of the potential energy V^{α} of an individual B-atom within an A-type unit cell. In the square lattice the potential energy exhibits a single minimum at the cell's centre. Shearing provokes a bifurcation of the energy landscape into two equivalent, lateral minima, which are separated by an energy barrier. In the final state, the unit cell exhibits a rhombic shape consisting of two equilateral triangles with local minima at their centres. The interstitial atom selects one of these two minima, by shuffling from its former central position, where it is then trapped by the energy barrier. Many type-B rhombi may be combined to form a hexagonal type-B sub-lattice as shown in Fig. 3.3b. The shuffle direction is not arbitrary, rather it is selected with respect to the shuffle of the nearest and nextnearest A-atoms. Thus, this mechanism of shear and shuffle locally forms—within the interaction range of atoms—a homogeneous product lattice which is characterised by the same shear direction of unit cells and the same shuffle direction of the sub-lattices.

Since there are two shear and two shuffle directions possible in 2D, four variants of martensite can be identified, see Fig. 3.3c. All of these four variants may nucleate on the two principle axes of the austenitic lattice, thus making for a total of eight possible variants with this 2D L–J model. Of these eight variants, congruent pairs exist, which may nevertheless nucleate independently of each other at different places. Note there is no group–subgroup relationship between our model martensite and the austenite because the martensite develops a threefold symmetry. This leads to an unusual situation where the crystal structure is preserved across a compatible-variant boundary. Such twin boundaries have zero excess energy and can be located only by reference to the parent austenite.

3.1 The Model Material 63

It turns out that the lattice stability is dominated by the heterogeneous interaction parameters ε_{AB} and σ_{AB} . Thus we may fix the interaction parameters of the pure species (ε_{AA} , σ_{AA}) and (ε_{BB} , σ_{BB}) at

$$\varepsilon_{AA} = 1.2 \,\varepsilon_0
\varepsilon_{BB} = 0.61 \,\varepsilon_0
\sigma_{AA} = \sigma_{BB} = 2^{-1/6} \,\sigma_0,$$
(3.4)

say. $\varepsilon_{AA} > \varepsilon_{BB}$ means that A–A bounds are stronger than B–B bounds. For convenience we use non-dimensionalised quantities and choose the values

$$\sigma_0 = 10^{-10} \text{ m}$$

$$\mu_0 = 58.0 \times 10^{-27} \text{ kg}$$

$$\varepsilon_0 = 2.5 \times 10^{-19} \text{ J}$$

$$\tau_0 = 4.0 \times 10^{-14} \text{ s}$$
(3.5)

to eliminate length, energy, mass and time units from the model equations. The natural unit of time $\tau_0=4\times 10^{-14} {\rm s}$ represents the period of a harmonic oscillation of an atom of mass μ_0 about the minimum of the pair potential with parameters σ_0 and ε_0 . With these characteristic quantities, Eq. (2.9) yields the proportionality factor between the characteristic potential energy and the characteristic kinetic energy, which is deviating from one,

$$\Lambda = \frac{\varepsilon_0}{\mu_0 \sigma_0^2 / \tau_0^2} \approx 0.69. \tag{3.6}$$

The heterogeneous interaction parameters ε_{AB} and σ_{AB} are selected so as to allow for lattice transformations in dynamical simulations. We shall rationalise the selection of these parameters in the subsequent section, distinguishing between mechanical and thermodynamical aspects of the lattice stability. The former refers to the ground state of the atoms at $T \to 0$ and thereby relates the lattice stability to the potential energy only. The thermodynamic stability relies on the free energy, which reflects the impact of potential energy and entropy.

We may note the choices taken in Eq. (3.4) are arbitrary and no attempt is made to fit the pure species potentials to any real metal. Similar models was presented in [3] and basic thermodynamic properties were investigated in [1]. Other similar models have previously been applied, even in 3D [4–9], but there are serious difficulties with finite size effects and, therefore, boundary conditions. In order to effectively reduce finite size effects, we will concentrate on 2D. This makes it impossible to directly relate our results to any specific material. For example, the lattice defects obtained from the 2D simulations cannot be directly related to any 3D topological defect. However, qualitative explanations of hysteresis and shape memory, as well as continuum and crystallographic theory, can be equally well applied in 2D. It is these more fundamental concepts that we intend to test.

3.2 Infinite and Perfect Single Crystals

3.2.1 Harmonic Limit: Linearised Equations of Motion

The classical mechanical treatment of lattices refers to the relaxed ground state at $T \to 0$ and considers a harmonic analysis of the equations of motion [10–12]. We may use this method in order to study the lattice stability as function of the heterogeneous interaction parameters ε_{AB} and σ_{AB} , while the homogeneous interaction parameters are considered as given.

The ground state positions of atoms in the model austenite and martensite are determined by relaxation of the potential energy as function of the single lattice parameters R or r indicated in Fig. 3.3a and b, respectively. We denote the ground state lattice sites by $\mathbf{X}^{0,\alpha}$ and define the displacements off these positions by $\mathbf{u}^{\alpha}(t) = \mathbf{x}^{\alpha}(t) - \mathbf{X}^{0,\alpha}$. The linearised equations of motion (1.22) hence read

$$m_{\alpha}\ddot{u}_{i}^{\alpha} = \sum_{\beta} A_{ij}^{\alpha\beta} u_{j}^{\beta}, \tag{3.7}$$

where

$$A_{ij}^{\alpha\beta} = \left(\frac{\partial^2 V^{\text{int}}}{\partial x_i^{\alpha} \partial x_j^{\beta}}\right)_{\mathbf{X}^{0,\gamma}}$$
(3.8)

is a matrix set by the interaction parameters and the ground state positions.

The harmonic analysis employs Fourier transformations of the displacements in time and space according to

$$u_i^{\alpha}(t) = \overline{u}_i^{\alpha}(k_i) \exp(ik_l X_l^{0,\alpha} - i\omega t). \tag{3.9}$$

 ω denotes the frequency and k_l the wave vector of a plane, harmonic wave mode with the complex amplitude \overline{u}_i^{α} . Using this ansatz, the linearised equations of motion (3.7) furnish the following eigenvalue problem for the determination of the normal wave modes.

$$\sum_{\beta=1}^{N} \left(D_{ij}^{\alpha\beta}(k_l) - \omega^2 \delta_{ij}^{\alpha\beta} \right) \overline{u}_j^{\beta} = 0, \tag{3.10}$$

where $D_{ij}^{\alpha\beta}(k_l)=\frac{1}{\sqrt{m_\alpha m_\beta}}A_{ij}^{\alpha\beta}\exp\left(\mathrm{i}\,k_l(X_l^{0,\beta}-X_l^{0,\alpha})\right)$ denotes the dynamic matrix and $\delta_{ij}^{\alpha\beta}=\delta_{ij}\delta^{\alpha\beta}$ is an extended Kronecker symbol with respect to space components (i,j) and atom numbers (α,β) . The lattice periodicity allows to reduce the eigenvalue problem to the situation of two oscillating atoms which represent the Bloch basis of austenite and martensite (Fig. 3.5), see [10]. In 2D, the eigenvalue problem hence yields four independent eigenvalues ω^2 as function of the wave vector k_l . Since the dynamic matrix is Hermitian, these eigenvalues are all real numbers. Their roots,

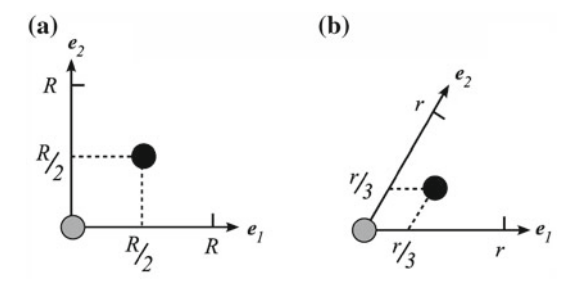


Fig. 3.5 Bloch basis of austenite (**a**) and martensite (**b**). The (covariant) base vectors are $\mathbf{e}_1 = R(1,0)$ and $\mathbf{e}_2 = R(0,1)$ for austenite and $\mathbf{e}_1 = r(1,0)$ and $\mathbf{e}_2 = r/2(1,\sqrt{3})$ for martensite. The according reciprocal (contravariant) base vectors are $\mathbf{e}^1 = 1/R(1,0)$ and $\mathbf{e}^2 = 1/R(0,1)$ for austenite and $\mathbf{e}^1 = 1/r(1,-1/\sqrt{3})$ and $\mathbf{e}^2 = 1/r(0,2/\sqrt{3})$ for martensite, respectively. Components of positions vectors refer to \mathbf{e}_i , components of wave vectors to \mathbf{e}^i

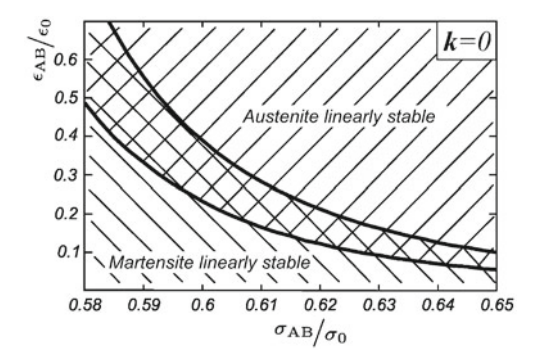


Fig. 3.6 "Phonon stability limits" of square and hexagonal L–J lattices in 2D as function of the cross-species interaction parameters (ε_{AB} , σ_{AB}). Other interaction parameters according to Eq. (3.4)

 $\omega(k_l)$, represent the dispersion relations. These are evaluated along selected directions of the wave vector k_l . In the present case there are four dispersion relations, representing two sets of branches called acoustic and optical. They are plotted for austenite and martensite in Figs. 3.7 and 3.8 for a fixed value of the interaction parameter $\sigma_{AB}=0.6\,\sigma_0$ and different values of ε_{AB} , respectively. Modes with negative ω^2 are mechanically unstable: here, the crystal can lower its energy by spontaneously deforming according to these modes. We see in Figs. 3.7 and 3.8 that as a function of increasing ε_{AB} we move from a regime of unstable austenite to one of unstable martensite.

Studying the whole (ε_{AB} , σ_{AB}) parameter space reveals a region in which both phases are mechanically stable. The result of such analysis is represented in the stability map shown in Fig. 3.6. Inspection shows the stability limits of austenite and martensite overlap, hence providing a distinct region in the parameter space where either phase may exist, perhaps metastably, at zero temperature.

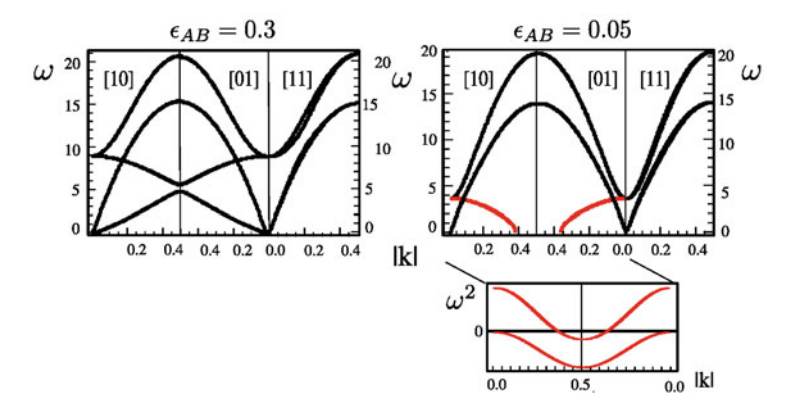


Fig. 3.7 Dispersion relation $\omega(|k|)$ of stable austenite for $\varepsilon_{AB}=0.3\,\varepsilon_0$ (left) and of unstable austenite for $\varepsilon_{AB}=0.05\,\varepsilon_0$ (right). The latter exhibits two unstable modes, one acoustic and one optical one, indicated in red. The classical energy $\propto \omega^2(|k|)$ of these two modes (below diagram) shows that the acoustic mode is unstable for all k, while the optical mode is only unstable near the zone boundary. [10], [01] and [11] indicate the selected wave vectors in the Brillouin zone. $((\sigma_{AB}=0.6\,\sigma_0, \text{ all remaining interaction parameters according to Eq. (3.4))$

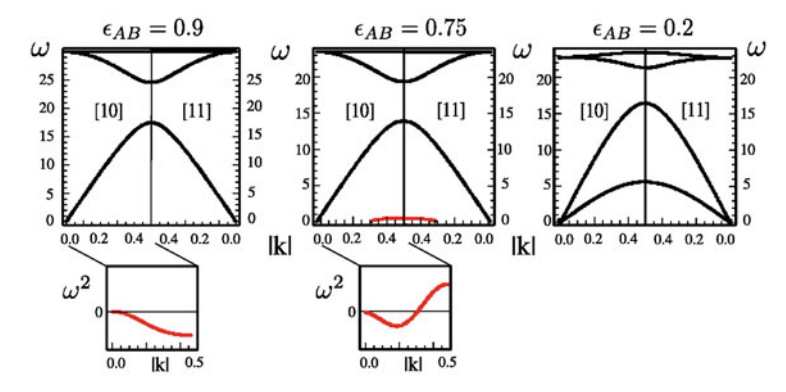


Fig. 3.8 Dispersion relation $\omega(|k|)$ of stable martensite for $\varepsilon_{AB}=0.2$ (right) and unstable martensite for $\varepsilon_{AB}=0.9$ (left) and $\varepsilon_{AB}=0.75$ (centre). [10] and [11] indicate two selected directions in the Brillouin zone ([10] and [01] being identical). Soft modes (red) are found for high values of ε_{AB} . The respective eigenvalues $\omega^2(|k|)$ in [10] direction are shown in the diagrams included below. (($\sigma_{AB}=0.6\,\sigma_0$, all remaining interaction parameters according to Eq. (3.4))

We have to recall the criterion of stable phonons is not fully equivalent to the thermodynamic stability criterion: rather, it represents the mechanical lattice stability against spontaneous small deformations from a perfect lattice. To study the thermodynamic phase stability at finite temperature, and thus produce a set of model parameters which exhibits a martensitic transition, it is necessary to determine energy and entropy independently. This is shown in the next subsection.

3.2.2 Phase Stability of 2D Lattices

The free energy may be analytically calculated as function of the temperature from the partition function regarding the two fundamental assumptions of Eqs. (1.44) and (1.45), see Eq. (1.50) in Chap. 2. Here we adopt the result given by Eq. (1.50) to the 2D case and obtain the free energy of the model austenite and martensite per atom. It reads

$$f_{\text{(aust/mart)}} = \underbrace{e_{\text{(aust/mart)}}^{0, \text{id}} + kT}_{u_{\text{(aust/mart)}}} - T \underbrace{k \left\{ \log T + \log \frac{2\pi kT}{\lambda_{\text{aust/mart}}} \right\}}_{S_{\text{aust/mart}}} + C(T). \quad (3.11)$$

The terms are arranged such that the contributions from the atom-specific internal energy u and entropy s are emphasised. Here, $e_{\text{aust/mart}}^{0,\text{id}} = 1/2(e_A^{0,\text{id}} + e_B^{0,\text{id}}) \mid_{\text{aust/mart}}$ denote the mean ground state energies of atoms in ideal, infinite and perfect lattices, where any interfaces, defects and surfaces are absent. $\lambda_{\text{aust/mart}} = \sqrt{\lambda_A \lambda_B} \mid_{\text{aust/mart}}$ denote the mean curvatures of the respective parabolic potentials assumed for A and B species. C(T) denotes a constant which contains terms common to both phases.

The curvatures $\lambda_{A,B}$ are determined from the according L–J potential energy landscapes of single A- and B-type atoms in statically relaxed lattices. For illustration, Fig. 3.9 visualises the equi-potential curves of a single B-type atom inside austenitic and martensitic unit cells; the functions look similar for A-type atoms. The anisotropic character of the potential energy in a L–J crystal is obvious. However, for small amplitudes the approximation of this potential energy by parabolic functions is justified. The respective curvatures $\lambda_{A,B}$ are determined into the direction of the steepest ascend of the A–B paths indicated in Fig. 3.9.

Both the ground state energies $e_{\text{aust/mart}}^{0,\text{id}}$ and the curvatures $\lambda_{\text{aust/mart}}$ depend on the L–J interaction parameters. Again we study the significance of the cross-species interaction parameter ε_{AB} on the lattice stability and set σ_{AB} to

$$\sigma_{AB} = 0.60\,\sigma_0\tag{3.12}$$

for this purpose. And again, all the remaining interaction parameters are set according to Eq. (3.4). The diagrams in Fig. 3.10 show the dependence of the ground state energies $e_{\text{aust/mart}}^{0,\text{id}}$ (a) and the mean curvatures $\lambda_{\text{aust/mart}}$ (b) on the single free parameter ε_{AB} . We see that the ground state energies $e_{\text{aust/mart}}^{0,\text{id}}$ in (a) exhibit a significant dependency of ε_{AB} . For high ε_{AB} the austenite also has lower potential energy, and so is always stable. For $\varepsilon_{AB} < 0.237$ martensite has lower potential energy, and there will be a phase transition. The mean curvatures λ_{aust} and λ_{mart} , Fig. 3.10b, in contrast exhibit negligible dependencies on ε_{AB} . We see that $\lambda_{\text{mart}} > \lambda_{\text{aust}}$ holds for any value ε_{AB} in the plotted interval and conclude the atoms move in softer potentials in the austenite as compared to the martensite. Their ratio is approximately a constant,

$$\lambda_{\text{mart}}/\lambda_{\text{aust}} \approx 2.45.$$
 (3.13)

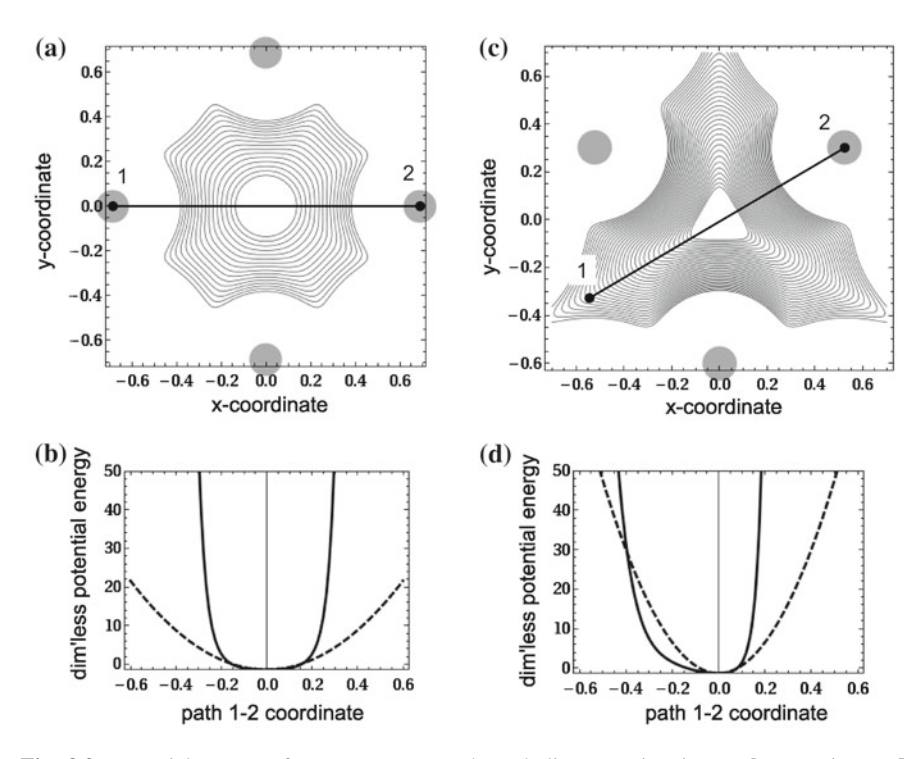


Fig. 3.9 Potential energy of a B-type atom and parabolic approximation. **a, b** austenite, **c, d** martensite. One-dimensional representations along the path 1-2 are provided in (**b**) and (**d**), where solid lines refer to the anisotropic L–J potential energies and dashed lines to the fitted, parabolic potentials used for the evaluation of the partition function. The situation is similar for A-type atoms

The thermodynamic phase transformation temperature is calculated from equilibrating the free energies of austenite and martensite,

$$e_{\text{aust}}^{0,\text{id}} - kT \log \frac{2\pi kT}{\lambda_{\text{aust}}} = e_{\text{mart}}^{0,\text{id}} - kT \log \frac{2\pi kT}{\lambda_{\text{mart}}}.$$
 (3.14)

The resulting phase transformation temperature for transformations between the ideal lattices is denoted by $T_E^{\rm id}$. It is given by the expression

$$T_E^{\text{id}} = \frac{e_{\text{aust}}^{0, \text{id}} - e_{\text{mart}}^{0, \text{id}}}{k \log (\lambda_{\text{mart}} / \lambda_{\text{aust}})}.$$
 (3.15)

The right-hand side of this equation depends on the one remaining independent variable interaction parameter, ε_{AB} . Figure 3.11 depicts the dependence of $T_E^{\rm id}$ on this parameter. Inspections shows this quantity monotonically decreases with ε_{AB} and has a root at $\varepsilon_{AB}=0.237\,\varepsilon_0$, where the ground state energies of the two phases are identical. Above $\varepsilon_{AB}=0.237\,\varepsilon_0$, the material remains austenitic. Below

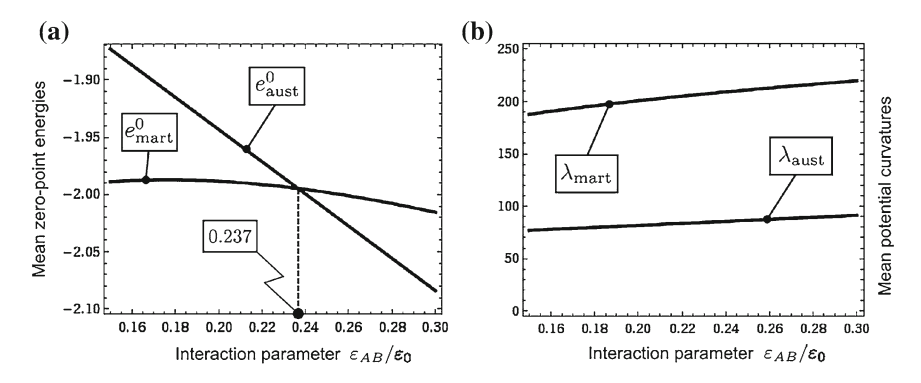


Fig. 3.10 a Ground state energies $e_{(\text{aust,mart})}^{0,\text{id}} = 1/2(e_A^{0,\text{id}} + e_B^{0,\text{id}})|_{\text{aust/mart}}$, **b** mean curvatures $\lambda_{\text{aust/mart}} = \sqrt{\lambda_A \lambda_B}|_{(\text{aust,mart})}$ of statically relaxed (austenite, martensite) lattices versus the interaction parameter ε_{AB} . Other interaction parameters: $\varepsilon_{AA} = 1.2\varepsilon_0$, $\varepsilon_{BB} = 0.61 \varepsilon_0$, $\sigma_{AA} = \sigma_{BB} = 0.89 \sigma_0$, $\sigma_{AB} = 0.60 \sigma_0$

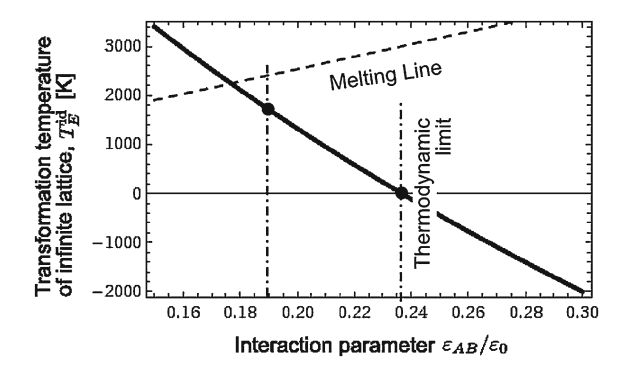


Fig. 3.11 Transformation temperature $T_{\rm E}^{\rm id}$ at the phase equilibrium of infinite and perfect austenite and martensite lattices as a function of the interaction parameter ε_{AB} . Other interaction parameters: $\varepsilon_{AA} = 1.2\varepsilon_0$, $\varepsilon_{BB} = 0.61 \varepsilon_0$, $\sigma_{AA} = \sigma_{BB} = 0.89 \sigma_0$, $\sigma_{AB} = 0.60 \sigma_0$

 $\varepsilon_{AB}=0.237\,\varepsilon_0$, martensite has a lower potential energy than the austenite and here T-induced transformations can take place. Also indicated in Fig. 3.11 is the melting line of the infinite lattice, which is estimated on the basis of reference [13]. Its intersection with the transformation temperature line at $\varepsilon_{AB}\approx 0.18\,\varepsilon_0$ gives a lower bound for the interaction parameter. Between these two limits, the transformation temperature depends almost linearly on ε_{AB} , while the crystallographies of the model austenite and martensite remain unaffected. MT processes may therefore be induced by a change in the temperature at values of ε_{AB} within this range (temperature-induced process) or alternatively, they can be induced by a variation of ε_{AB} at a fixed temperature (energy-induced process).

3.2.3 Entropic Stabilisation of Austenite

We have pointed out that the phase equilibrium is determined by balancing the competing phase preferences of the potential energy and the entropy. Having approximately determined the free energies of the phases by statistical thermodynamics, we are now able to interpret this mechanism from the statistical point of view.

According to Eq. (3.14), the energetic and the entropic phase preference is expressed in terms of the potential ground state energies $e_{\text{aust/mart}}^{0,\text{id}}$ and the curvatures of the atomic potential $\lambda_{\text{aust/mart}}$, respectively. T-induced phase transformations are possible if the ground state energy of martensite is more favourable than that of austenite, $e_{\text{mart}}^{0,\text{id}} < e_{\text{aust}}^{0,\text{id}}$. We recall the effect of the potential curvature on entropy which was discussed in the framework of statistical thermodynamics in Chap. 2. In the 2D case, the interpretation of entropy is similar: here, the argument of the logarithm $(2\pi kT/\lambda)$ in Eqs. (3.11) and (3.14) may be interpreted as the mean area that an individual atom may occupy at a thermal activation level determined by T. We have seen that the model austenite provides a softer potential than the model martensite, $\lambda_{\text{mart}} > \lambda_{\text{aust}}$. With reference to Eq. (3.13), the entropy difference thus reads

$$s_{\text{aust}} - s_{\text{mart}} = k \log \frac{\lambda_{\text{aust}}}{\lambda_{\text{mart}}} = k \log 2.45$$
 (3.16)

Since $\lambda_{mart} > \lambda_{aust}$, the austenite has a higher entropy at identical temperatures. Therefore, austenite is the entropically preferred phase. This result is in perfect agreement with the requirement of the Clausius–Clapeyron Eq. (1.14) in Chap. 1.

It is possible to illustrate the atomic mobilities by MD simulations using the original L–J potential. For this purpose, the spatial distributions of individual atoms in austenite and martensite are measured, see Fig. 3.12. This Figure shows the atomic positions for an individual unit cell in austenite (a) and martensite (b) detected by a series of snapshots. The observed positions are visualised by clouds of dots about the mean atomic lattice sites and may be statistically evaluated. Figure 3.12c shows the respective distributions measured in this manner (indicated by dots in that subfigure). These may be nicely fitted by the canonical distributions regarding parabolic potentials, i.e. distribution functions of the type $\exp(-\lambda(x-X^0)^2/2kT)$, indicated by solid lines in Fig. 3.12c. Here, the curvature λ of the potential determines the shape of the distribution. Accordingly, the broader distribution of the austenite (grey) is affected by a softer curvature in comparison to the martensite (b). This observation proves ex post facto the approximation of the atomic mean potential energies by parabolae. In 2D, the standard deviation of this canonical distribution is $\sqrt{2kT/\lambda}$. Hence, the terms $2\pi kT/\lambda$ in Eqs. (3.11) and (3.14) can be interpreted as circular areas which the atoms may on average occupy while moving at a temperature T within the parabolic potentials which have the curvatures λ . The larger these areas are, the higher the entropy. We conclude that the larger specific entropy of austenite results from a higher atomic mobilty in the lattice.

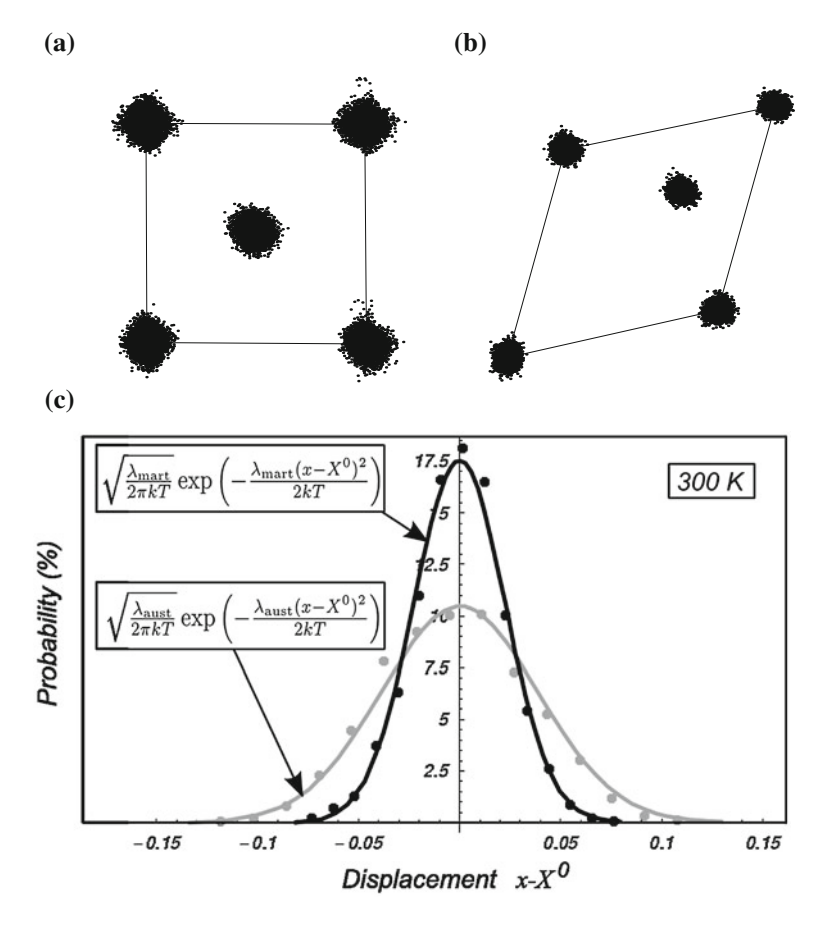


Fig. 3.12 Spatial distribution of atomic positions. **a**, **b** 10,000 observations of an austenitic and a martensitic unit cell. The mean shape of the cell is indicated by the *drawn lines* and the observed atom positions are indicated by the *clouds of dots*. $T \approx .300 \, \text{K}$. In austenite, the atoms move over broader ranges than those in martensite. **c** Spatial probability distribution (1-component of position) of the interstitial atom. Data points represent MD simulation measurements and the graphs represent the canonical distribution functions. *Black* martensite. *Grey* austenite

3.3 Crystallographic Theory

We proceed to apply the crystallographic theory to the infinite (austenite, martensite) single crystals in 2D. The compatibility condition of Eq. (1.1) leads to an invariant line instead of an invariant plane. Therefore, the crystallographic equation reduces to

$$\mathbf{I} + \mathbf{d} \otimes \mathbf{p} = \mathbf{R}(\varphi) \mathbf{B}(\eta_1, \eta_2). \tag{3.17}$$

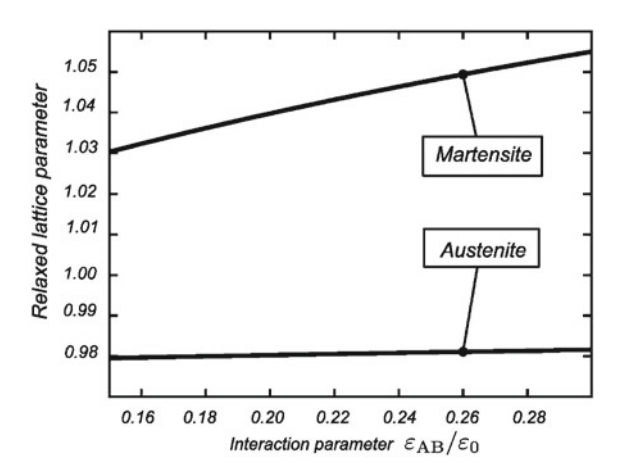


Fig. 3.13 Relaxed lattice parameters of austenite and martensite versus the interaction parameter ε_{AB} . Other interaction parameters: $\varepsilon_{AA}=1.2\varepsilon_0,\ \varepsilon_{BB}=0.61\varepsilon_0,\ \sigma_{AA}=\sigma_{BB}=0.89\sigma_0,\ \sigma_{AB}=\sigma_{BB}=0.60$

The 2D Bain transformation $\mathbf{B}(\eta_1, \eta_2)$ is defined with respect to the coordinates $(\mathbf{E}_1, \mathbf{E}_2)$ which span the edges of a line-centred-square (Fig. 3.3a). Two sets of Bain parameters can be identified, representing the two possible, fundamental shear directions, viz.

Set 1:
$$\eta_1 = \frac{1}{\sqrt{2}} \frac{r}{R}$$
, $\eta_2 = \sqrt{\frac{3}{2}} \frac{r}{R}$. (3.18)

Set 2:
$$\eta_1 = \sqrt{\frac{3}{2}} \frac{r}{R}$$
, $\eta_2 = \frac{1}{\sqrt{2}} \frac{r}{R}$. (3.19)

For each of these sets, Eq. (3.17) produces four analytical solutions for **d**, the unit normal **p** and the rotation angle φ as functions of the Bain parameters η_1 and η_2 , see Table 3.1.

R and r denote the lattice parameters of austenite and martensite in the ground state, as indicated in Fig. 3.3. Figure 3.13 shows their dependency on the interaction parameter ε_{AB} . Here, we use the values R=0.98 and r=1.04, which correspond to $\varepsilon_{AB}=0.2$, and depict the eight solutions, according to the two sets of Bain parameters from Eqs. (3.18) and (3.19), in Table 3.2. Exploiting the crystallographic condition (1.3) now yields twin pairs. For example, solutions no. 1 and 4 of Table 3.2 may form twins, however, these pairs are trivial since they indicate simply rotations by 180° . More interesting are pairs between solutions 1 and 2 since these form twins determined by opposite shear directions of their unit cells. From a strictly crystallographic viewpoint, such pairs are incompatible since the respective habit lines deviate by approx. 13° , for example the solutions no. 3 and 5 of Table 3.2.

Table 3.1 Four solutions for **d**, **p** and φ according to Eq. (3.17). $\chi = \left(1 - \sqrt{\frac{1+\eta_1\eta_2}{\eta_1+\eta_2}}\right) / \left(\sqrt{\eta_1-\eta_2}(\eta_2^2-1)\right), \psi = \sqrt{\frac{1-\eta_2^2}{\eta_1+\eta_2}}, \omega = \frac{1+\eta_1\eta_2}{\eta_1+\eta_2}$

No.	d_1	d_2	p_1	p_2	φ
1	$\eta_2(\eta_2^2-\eta_1^2)\chi\psi$	$\eta_1\sqrt{\eta_1-\eta_2}\psi$	$-(\eta_1+\eta_2)\chi$	$-\psi/\sqrt{\eta_1-\eta_2}$	$\arccos \omega$
2	$\eta_2(\eta_2^2-\eta_1^2)\chi\psi$	$-\eta_1\sqrt{\eta_1-\eta_2}\psi$	$-(\eta_1+\eta_2)\chi$	$\psi/\sqrt{\eta_1-\eta_2}$	$-\arccos\omega$
3	$-\eta_2(\eta_2^2-\eta_1^2)\chi\psi$	$\eta_1\sqrt{\eta_1-\eta_2}\psi$	$(\eta_1 + \eta_2)\chi$	$-\psi/\sqrt{\eta_1-\eta_2}$	$-\arccos\omega$
4	$-\eta_2(\eta_2^2-\eta_1^2)\chi\psi$	$-\eta_1\sqrt{\eta_1-\eta_2}\psi$	$(\eta_1 + \eta_2)\chi$	$\psi/\sqrt{\eta_1-\eta_2}$	$\arccos \omega$

Table 3.2 Solutions of the 2D crystallographic Eq. (3.17) with respect to the two sets of Bain parameters of Eqs. (3.18) and (3.19). $R(T \to 0) = 0.98$ and $r(T \to 0) = 1.04$. φ —relative lattice rotation between martensite and austenite, γ —orientation of the habit line. Last column: Sketch of the transformation. *Grey* austenitic squares are transformed into *black* martensitic rectangles. The lattice rotations are $\pm 15.5^{\circ}$. The inclinations of the habit lines are approximately multiples of 45° with deviations of 13° between the sets

Set 1: $\eta_1 = 0.75$, $\eta_2 = 1.30$			Set 2: $\eta_1 = 1.293$, $\eta_2 = 0.747$				
Solution No.	$\varphi[^{\circ}]$	γ[°]	Sketch	Solution No.	$\varphi[^{\circ}]$	γ[°]	Sketch
1	15.5	141.5	Y	5	15.5	231.5	
2	-15.5	38 5		6	-15.5	308.5	
3	-15.5	218.5		7	-15.5	128.5	
4	15.5	321.5		8	15.5	51.5	

However, this deviation is small and we shall later, how these pairs may dynamically form twins in large crystals. Before these larger samples are investigated, we shall focus attention on the thermodynamics of small, unconstraint crystallites.

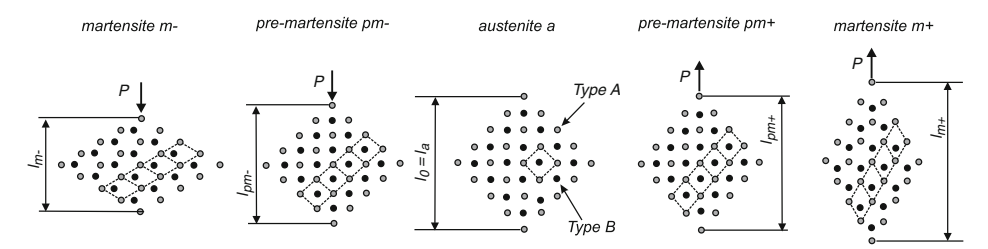


Fig. 3.14 The 41-atom crystal model considered in [1]. The finite size effect induces homogeneous shear/shuffle transformations between five possible lattice structures: Austenite a, stable martensite variants "m+" and "m-" and the metastable pre-martensites " $pm\pm$ ". The shearing is measured by the diagonal strain $\varepsilon = (l-l_0)/l_0$, where l_0 is the diagonal length of the undeformed austenite at a reference temperature (Video available online)

3.4 Thermo-Mechanical Properties

3.4.1 Individual Crystallites

So far, the properties of the model material were investigated by means of idealisations. Surfaces were neglected and atomic potentials were approximated by harmonic potentials in order to derive analytical results, hence avoiding non-linearities. The phase equilibrium was investigated by comparing thus calculated free energies of austenite and martensite separately. In order to investigate the genuine anharmonic model it is required to directly integrate Newton's Equtions (1.22) by means of MD simulations. In this section, we shall approach this method referring to a small assembly of 41 atoms under free surface conditions. We shall firstly investigate the free energy of an isolated crystallite before we proceed to investigate the properties of an array of such crystallites ("chain") exposed to thermo-mechanical testing. Employing such setting we show the model is capable of complex thermo-mechanical properties of SMA: pseudo-plasticity, pseudo-elasticity and the shape memory effect.

An individual test crystallite of 41 atoms is shown in Fig. 3.14. Owing to its small size, the surface energy contributes to some extend to the potential energy of the crystallite, which must be regarded when selecting the interaction parameters. Therefore in this case, we have heuristically selected the parameters, see Table 3.3. Note that these choices are not unique; other combinations of parameters may also exist which lead to similar material behaviour. The non-dimensionalised time step is set to $\Delta t = 1/100 \, \tau_0$.

Owing to the small ensemble size, all atoms effectively interact with each other in the crystallite, inducing homogeneous transformations between austenite and selected martensite variants. Despite the surface, we may therefore interpret the crystallite as a mesoscopic representative of a crystallographic layer that forms into a single martensitic lamella. Therefore, out of the eight variants of martensite possible with the model material, only two homogeneous variants are exhibited during the simulations, distinguished by the shearing.

A–A	В–В	A–B
$1.14 \varepsilon_0$	$1.0\varepsilon_0$	$0.223 \varepsilon_0$
$0.9\sigma_0$	$0.865\sigma_0$	$0.6\sigma_0$
$m_A = 3.5 \mu_0$	$m_B = 1.0\mu_0$	
	$1.14\varepsilon_0$ $0.9\sigma_0$	$1.14 \varepsilon_0$ $1.0 \varepsilon_0$ $0.865 \sigma_0$

Table 3.3 Choice of the interaction parameters for the 41-atom crystallite [1]

The crystallite was investigated by considering two types of tensile loading tests referred to as *displacement control* and *load control*. In the former case, the length l indicated in Fig. 3.14 is controlled by means of the positions of the diagonal's corner atoms, and their interactions with the free atoms determine the measured load signal P. Under load control, the base atom is fixed and the top atom is vertically loaded by the application of an external load P. The resulting diagonal length l of the crystal is recorded. We use the strain $\varepsilon = (l-l_0)/l_0$ to characterise the deformation, where l_0 denotes the size of unloaded austenite at a reference temperature of 300 K and plot load/strain-curves. The dynamics of the small system causes high frequency fluctuations in the recorded load/strain data. To facilitate a clearer representation of the data, these fluctuations are filtered out by using low-pass filter techniques.

Typical load/strain-curves for low (100 K) and high temperatures (800 K) obtained from such tensile tests are shown in Fig. 3.15. The strains $\varepsilon_a = 0$ and $\varepsilon_{m\pm} \approx \pm 0.22$ indicate austenite and two martensitic twin variants, respectively.

Under displacement control (broken-line curves), the measured isotherms are distinct, non-monotonic functions. Both exhibit unstable branches indicated by negative slopes. Under load control (solid lines), the unstable regions are avoided and phase transformations occur, which are indicated by sudden strain bursts which occur at specific critical loads. Hence monotonic load/strain-curves result during loading and unloading, respectively.

At low temperature (100 K), austenite is unstable and the two martensitic variants $m\pm$ represent stable configurations of the small system. Figure 3.15a shows how much load (tensile and compressive) is needed to mechanically induce a transition from m- to m+ and back again. Note that this process is associated with a large hysteresis.

In contrast to this, austenite is stable at high temperature (800 K). The slope of the $P(\varepsilon)$ -curve in Fig. 3.15b is positive for small strains of about $\varepsilon_a=0$ and represents the shear modulus of the 2D austenite lattice. At the critical loads $P_c^{a\leftrightarrow m\pm}(T)$ indicated in Fig. 3.15b, austenite transforms to m+ and m- when loaded in tension and compression, respectively. Note that under such loading conditions, the isolated crystallite transforms reversibly back and forth in the load/strain-diagram without hysteresis effects.

According to the thermodynamic stability condition of Eq. (1.10), the phase stability for an unloaded sample is determined by the minimum of the free energy. We may calculate the free energy of the crystallite along the transition path by integrating the load/strain curve obtained in displacement control (broken lines in Fig. 3.15).

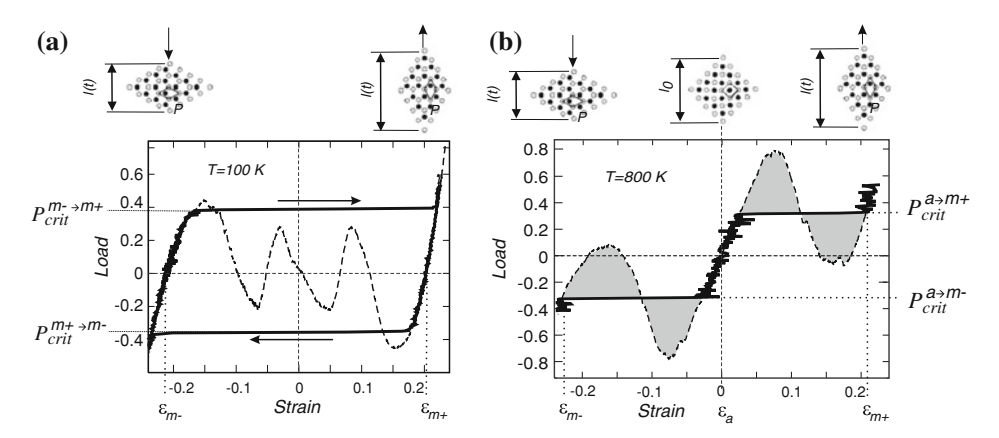


Fig. 3.15 (Load, strain)-curves numerically measured in tensile tests with the 41-atom ensemble. Displacement control: *broken lines*, load control: *solid lines*. **a** Low temperature (100 K). **b** High temperature (800 K)

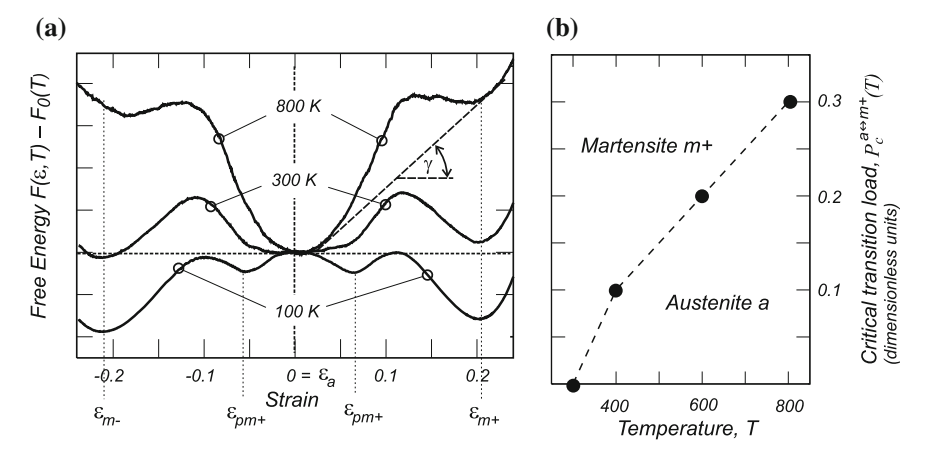


Fig. 3.16 a Free energy of the 41-atom ensemble along the $a \leftrightarrow m \pm$ transition path for three distinct temperatures, obtained from the measured load/strain data by integration. The constant of integration $F_0(T)$ is always subtracted. The slope $\tan \gamma$ of the common tangent determines the transformation load $P_c^{a \leftrightarrow m \pm}$. b Transformation load $P_c^{a \leftrightarrow m \pm}$ as a function of temperature

Three isotherms obtained in this manner are shown in Fig. 3.16a for the temperatures 100, 300 and 800 K. We see that the free energy curves are non-convex along the transformation path, thus showing local minima at ε_a , $\varepsilon_{m\pm}$ and additionally—only for the 100 K isotherm—at $\varepsilon_{pm\pm}$. The latter indicates a pre-martensitic state which is characterised by slight shearing of the square configuration illustrated in Fig. 3.14.

The absolute minima of these functions determine the stable configurations of the unloaded ensemble. At low temperature (100 K), the martensitic variants provide minimal free energy at $\varepsilon_{m\pm}$. Therefore the two martensite variants are equally stable at this temperature. From the 100 K isotherm, it is also obvious that the

pre-martensitic configurations $pm\pm$ are not stable because their respective potential wells in Fig. 3.16a represent only local and not absolute minima.

For a temperature of $\approx 300\,\mathrm{K}$, the free energy in Fig. 3.16a exhibits three minima at approximately the same energy level. Thus we confirm that $T=T_E\approx 300\,\mathrm{K}$ represents the phase transition temperature of the unloaded ensemble. We denote this transformation temperature of the unloaded sample by T_E . For $T>T_E$, the absolute free energy minimum is located at ε_a , thus austenite is stable and any other configuration is unstable. At this temperature, however, martensite may form if the austenite is mechanically loaded (load-induced transformation). Two alternative formulations for the phase stability criterion yield the transformation load as functions of the temperature. These are known as the rule of "common-tangents" and the rule of "equal-areas"; both are related to the Gibbs Equation (see Chap. 1). The small crystllite obeys these rules.

We see that according to the "common-tangent rule", the slope of the common tangent at the free energy wells of austenite and one selected martensite variant determines the transformation load $P_c(T)$. One such tangent is indicated in Fig. 3.16a for the transformation between a and m+ at 800 K. For this particular case, their slopes are $\tan \gamma \approx .0.3$ which coincides well with the critical load detected under load control in the load/strain diagram of Fig. 3.15b. In the latter diagram, the rule of "equal-areas" may be evaluated. It refers to the two grey-shaded areas indicated above and below the detected critical yield load. The "equal-area rule" states that at equilibrium, these two areas must be equal in size. This is approximately true for the case discussed here. Hence, the two alternative equilibrium conditions for the observed transformation load are consistently met. We may conclude that the observed transformation load indeed represents the equilibrium phase transformation load between austenite and martensite at this particular temperature. Figure 3.16b shows the temperature dependency of the transformation load measured in this manner. We conclude that the small, 41-atom crystallite represents a fully thermo-mechanically coupled system and it obeys the equilibrium thermodynamics of macroscopic matter. Phenomenologically the model material is capable of representing typical shape memory alloys properties in a qualitative way.

3.4.2 Chains of Crystallites

3.4.2.1 Tensile Testing

From the thermodynamical investigation of an individual 41-atom crystallite we know that the load/strain curves are temperature dependent, Fig. 3.15. We now consider the macroscopic (collective) behaviour of many such crystallites in a 1281-atomic "chain" ensemble formed by 32 crystals, see Fig. 3.17. The thermo-mechanical behaviour of the chain is determined by the superposition of the individual crystals' load/strain functions. This procedure enables us to study the features of pseudoplasticity, pseudo-elasticity and the shape memory effect. Clearly, this approach

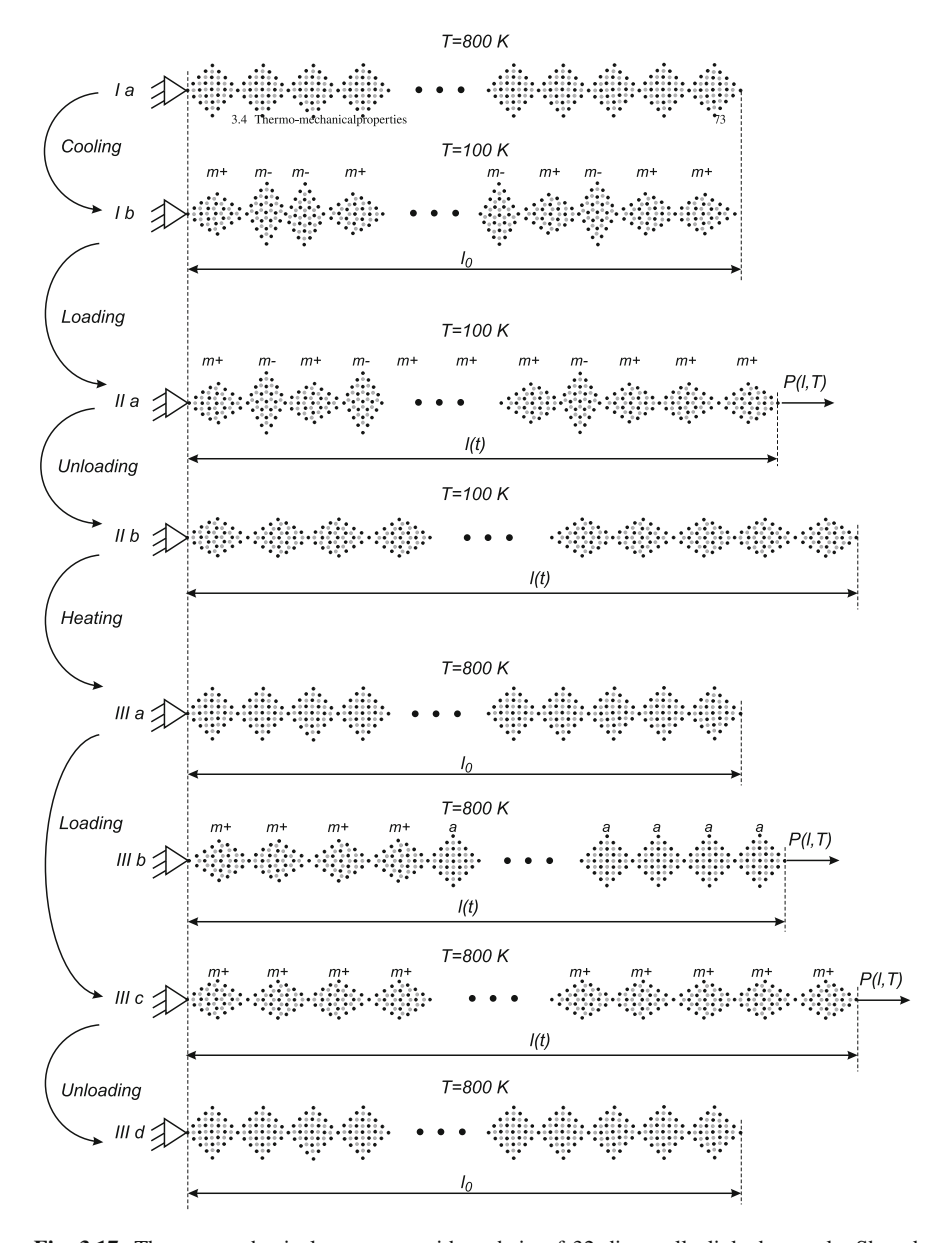


Fig. 3.17 Thermo-mechanical processes with a chain of 32 diagonally linked crystals. Shared corner atoms are restricted to horizontal motion. Ia, b: Martensitic twinning upon cooling at constant length. IIa, b: Pseudo-plastic deformation during loading and unloading at low temperature (de-twinning). IIb–IIIa: One-way shape memory effect: $m+\to a$ transition induces deformation recovery upon heating. IIIa–d: Pseudo-elastic yield and recovery of strain upon loading and unloading at high temperature (Video available online)

represents an idealisation and may be considered as a first step to bridge both the atomic and the mesoscopic as well as the macroscopic properties of the MT. The chain ensemble studied here is inspired by the works of Müller, Truskinovsky at al. [14, 15]. These authors modelled elastic-plastic behaviour by considering bistable snap springs as unit elements. In the chain model considered here, the snap springs are metaphorically replaced by the tri-stable 41-atom crystallites.

The crystallites are linked diagonally and only interact across their corner atoms. Consequently, long-distance interactions between atoms in adjacent crystals are not considered and the inter-crystal interactions are reduced to points ("weak inter-crystal interaction"). In addition to this, these corner atoms are restricted to axial movements in order to prevent buckling.

A series of numerical tests have been carried out with the chain ensemble shown in Fig. 3.17. Under displacement control, the corner atom at the very left of the chain is anchored in place and the atom at the opposite end of the chain (reference atom) is horizontally displaced. The force P is then measured as the interaction force which is exerted by the chain on the reference atom. Under load control, an external axial force P acts horizontally on the reference atom and the resulting chain length is observed. To operate subject to equilibrium conditions, displacements or loads must increase/decrease slowly. Appropriate length or load increments were heuristically identified as $\Delta l = 0.003$ and $\Delta P = 5 \times 10^{-5}$, respectively. Between two load/strain increments, 500 time steps are considered to allow for the model's relaxation. The temperature is controlled by the method of velocity scaling and relaxation, explained in Chap. 2.

Due to the small size of our system, all recorded quantities exhibit significant, high-frequency fluctuations superimposed on their macroscopic evolutions. In order to monitor the tendencies of the macroscopic process variables, we average the recorded data over small time intervals and then use a low-pass filter.

Figures 3.18, 3.19, 3.20 and 3.21 show process diagrams exhibiting thermomechanical processes which are simulated using the chain. In particular, Figs. 3.18 and 3.19 show load/strain curves associated with low (Fig. 3.18) and high (Fig. 3.19) temperature, respectively, and Figs. 3.20 and 3.21 depict strain/temperature curves for different loading constraints. In Fig. 3.20, the strain/temperature subject to two different constant loads are compared. Figure 3.21 shows a simulation of the shape memory effect. Loads/displacements and temperature determine the thermodynamic state of the chain in which individual crystals are either austenite (a) or martensite (m+ or m-), Fig. 3.14. Thus, the internal state of the chain is characterised by the phase fractions of austenite ($X_a = N_a/32$) and martensite ($X_{m\pm} = N_{m\pm}/32$). In the following, we discuss the details of the results.

3.4.2.2 Pseudo-Plasticity

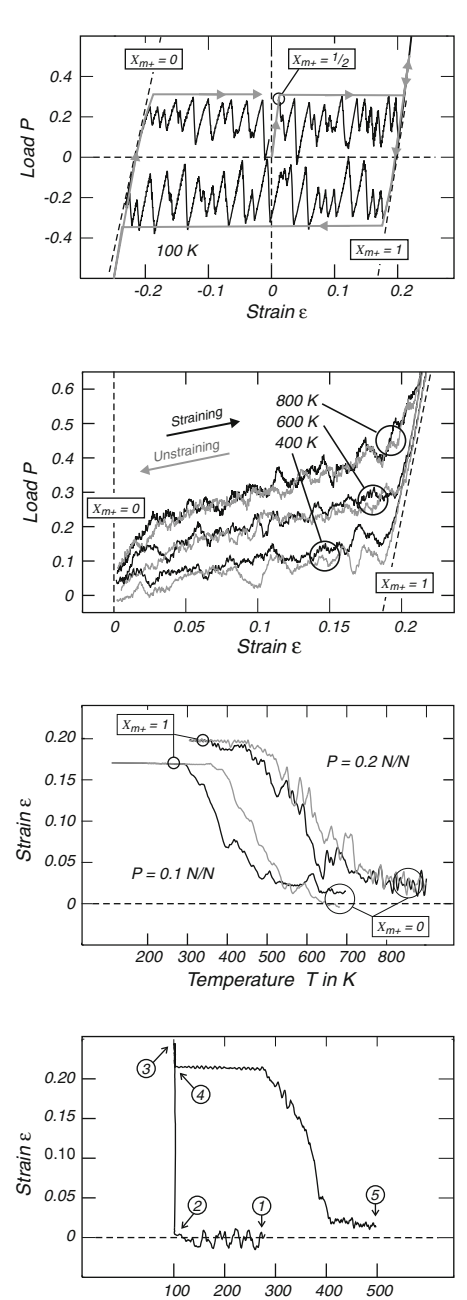
Thermal martensite is formed below the phase transformation temperature T_E , as sketched by Fig. 3.17(la–lb), during the cooling of an initially austenitic, unloaded chain. In the weakly interacting chain, austenite–martensite transitions occur with

Fig. 3.18 Tensile testing of the chain with 32 crystals under displacement control at low temperature. $T = 100 \, \text{K}$

Fig. 3.19 Tensile testing of the chain with 32 crystals under displacement control at high temperatures. T=400, 600 and 800 K

Fig. 3.20 Cooling (black) and heating (grey) cycles at the two constant loads P = [0.1]N/N and P = [0.2]N/N

Fig. 3.21 Simulation of the shape memory effect. Discussion of points ① to ⑤ see text



Temperature T in K

the same probability for both martensite variants, therefore the product represents a twinned chain at $X_{m\pm} = 1/2$. If the twinned chain is mechanically strained below T_E , Fig. 3.17(lb), the number fraction of X_{m+} for the favourably oriented martensite variant m+ increases. Figure 3.18 shows a load/strain diagram documenting the response of a martensite chain to tensile straining at 100 K. The numerical experiment starts at P=0 and $\varepsilon=0$. During straining, the m+ variant fraction increases from 1/2 to 1 as the strain increases from 0 to 0.22. Sudden load drops can be clearly recognised which represent martensite-martensite transitions from m- to m+ of individual crystals. These can be logically explained as follows: Tensile straining of the chain results in an increase in the measured reaction load exerted on the reference atom. This load is macroscopically homogeneous along the chain, superposed by small local modulations in the vibrating system. While the overall chain deforms under displacement control, individual crystals select their martensite variant under the influence of this modulated load. Transformations from m- to m+ are triggered as the macroscopic load approaches the $m-\to m+$ transition load. This transition load can be taken from Fig. 3.15a as $P_c^{m-\to m+} \approx 0.3$. Under displacement control of the chain, single transition events of individual crystallites induce sudden relaxations in the measured load signal. Further straining of the chain results in a new increase in load until one of the remaining m- crystallites reaches the critical load and consequently transforms. Eventually, as m- crystallites successively transform into m+, a serrated shaped load-displacement curve is obtained in which the local load peaks represent the critical transition load $P_c^{m-\to m+}$ of individual martensite-martensite transitions at 100 K. This branch of the curve characterises the de-twinning process of the chain. Since the twinned chain initially consists of 16 m+ and m- crystals each, a total of 16 $m-\to m+$ transition events occur during the tensile straining. It is easily envisaged that the serrations will decrease in intensity with an increasing number of crystals in the chain such that the load-displacement curve asymptotically approaches the grey envelope curve at infinity, indicated in Fig. 3.18. Finally, all m- crystals have transformed and a sharp increase in the load at $\varepsilon = 0.2$ indicates an elastic deformation of the chain consisting of m+ crystals.

On load reversal the m+ crystal chain elastically unloads. No variant transitions occur when the chain is fully unloaded, Fig. 3.17(IIb), because m+ and m- variants are energetically equivalent with respect to their free energies, compare to Fig. 3.16. Thus, unloading is associated with a large remaining strain which is referred to as pseudo-plastic strain. The term pseudo-plasticity is often used to emphasise the similarity between dislocation plasticity and the growth of favourably oriented martensite variants. Both processes depend on critical stresses and accumulate large strains.

Strain controlled compression loading consequently triggers reverse transition events which correspond to what we have elaborated for tensile loading. At a strain $\varepsilon \approx 0.18$ in Fig. 3.18, the critical load $P_c \approx -0.3$ is exceeded, and thus the crystals in the chain successively transform from m+1 into m-1. As described for the tensile loading, this process is characterised by the serrated shape of the load/strain branch, due to relaxation of the load accompanying single transitions events. Finally, a full tension/compression straining cycle is obtained which is clearly represented

by the grey envelope curve in Fig. 3.18. This is hysteretic owing to the mechanical character of martensite–martensite transformations at low temperature as shown in Fig. 3.15a.

3.4.2.3 Pseudo-Elasticity

We now consider the chain ensemble at temperatures of 400, 600 and 800 K where, in the absence of an external load, austenite is stable. Displacement controlled straining now produces load/strain curves in which martensite forms on loading and fully re-transforms on unloading, Fig. 3.17(IIIa-d). This represents a pseudo-elastic material behaviour. In agreement with experimental data, the martensitic transformation starts upon loading to critical loads at which the slope of the load/strain curve drastically decreases. However, even in the absence of strain rate effects, our simulation experiments do not yield a flat load plateau which may be related to the non-linear character of the inter-crystalline forces. The temperature dependence of the chain's transformation load is determined by the critical load $P_c^{a\leftrightarrow m\pm}(T)$ which is identified with the individual 41-atom crystal, see Fig. 3.16b. However, while isolated crystals undergo sudden jump-like forward/reverse transitions between austenite and martensite, a chain of crystals allows phase mixtures to be established and thus transformation strains can be accumulated. As the load/strain curves run through the plateau region, the phase fraction X_{m+} changes progressively from 0 to 1. On the other hand, steep branches of the load/strain curves, indicated by $X_{m+} = 0$ and $X_{m+} = 1$ in Fig. 3.19, represent elastic loading of pure austenite and martensite, respectively. Similar to the case of pseudo-plastic deformation at low temperature, austenitemartensite transformations of individual crystals are accompanied by relaxations of the load signal, resulting in serrations of the load/strain curves in the plateau region. However, relaxation events are less pronounced in the pseudo-elastic case because individual $a \rightarrow m +$ transitions yield smaller transformation strains than those of the $m-\rightarrow m+$ transitions.

Despite these serrations and other small-scale fluctuations, it is obvious from the resulting load/strain curves in Fig. 3.19 that the loading/unloading curves show no other deviations; most importantly, there is no hysteresis. The absence of hysteretic effects in our MD simulations reflects the absence of internal interfaces since individual chain crystals are limited to only weak interactions through individual points rather than through interfaces.

3.4.2.4 Shape Memory Effect

In Fig. 3.20, we activate our chain at constant external loads of P = 0.1 and P = 0.2 and obtain characteristic strain/temperature curves. These loads affect the phase transformations in single crystals according to Fig. 3.16b. Figure 3.20 shows this behaviour for our chain of crystals where, upon heating and upon cooling, the contraction of the chain corresponds to a change of martensite phase fraction from 1 to

0 and 0 to 1, respectively. Roughly, the cooling and heating branches again exhibit no hysteresis. Note that, according to the load/temperature diagram of Fig. 3.16b, at the higher load, the transition occurs at higher temperature.

The shape memory effect is modelled by the chain using a sequence of simulations under temperature and under load control mode, Fig. 3.21. In the unloaded reference state, the chain is fully austenitic as shown in Fig. 3.17(la). Upon cooling below T_E , individual crystals become unstable and transform randomly into $m\pm$ to form a twinned chain $(\bigcirc \rightarrow \bigcirc$ in Fig. 3.21). Since the transformation strains caused by $a \rightarrow$ m+ transitions are balanced by the transformation strains of the $a \rightarrow m-$ transitions, the total strain of the entire chain fluctuates about zero during this twinning process. At a temperature of 100 K, the chain is fully twinned (2 in Fig. 3.21) and exhibits a configuration similar to that displayed in Fig. 3.17(lb). We now switch to load control and apply an increasing axial load at 100 K. Thus, pseudo-plastic deformation is activated once the $m-\to m+$ transition load is exceeded (2 \to 3 in Fig. 3.21). At position 3 in Fig. 3.21, the chain is fully de-twinned and elastically loaded. Upon unloading at 100 K, a remaining transformation strain of \approx 22% results (3) \rightarrow 4 in Fig. 3.21). This is illustrated in Fig. 3.17(IIb). Finally, this deformation can be fully recovered by heating the unloaded chain above T_E , (\circledast \to \circledast in Fig. 3.21). At T_E , the individual 41-atom crystal ensembles start to progressively re-transform into austenite and the chain thus returns to its reference configuration. Thus MD simulations of a chain of crystals can fully account for the characteristic features of the shape memory effect.

3.4.2.5 Conclusions

The MD simulations show that binary L–J crystallites which are axially linked together into a chain can be used to qualitatively model complex thermo-mechanical material behaviour, even in a two-dimensional setting. The material model is capable of logically systematising the phenomena of pseudo-plasticity, pseudo-elasticity and the shape memory effect.

A small L–J crystal with only 41 atoms induces homogeneous transformation strains in austenite/martensite transitions and consequently cannot be used to model the shape memory effect associated with real microstructures. A first step towards addressing shape memory effects in polycrystalline microstructures can be achieved using the chain model where adjacent crystals interact through individual atomic links. In this situation, interfacial energies are absent and the free energy landscapes of the isolated crystals (Fig. 3.16) are preserved. The chain, consisting of appropriate combinations of martensite and austenite crystals, represents a mixture of phases. Complex material properties, such as pseudo-plasticity, pseudo-elasticity and the shape memory effect, appear as collective responses to the phase mixture where individual crystals adjust to the local thermodynamic conditions.

In this regard, the simulations using the chain imply two levels of statistical averaging; microscopic and mesoscopic. Averaging on the atomistic level yields the free energy which determines the fundamental phase stability of the individual crystals.

Averaging on the mesoscopic level yields the load/strain/temperature function of the entire chain. This function represents the collective response of the linked crystals to the macroscopic loading conditions.

These two levels of averaging are usually separated. On the atomistic level, the free energy functions are typically calculated by the methods of statistical mechanics. On the other hand, mesoscopic models rely on phenomenological, multi-well energy functions [14–19]. Our MD simulations give a simple example of how these two levels of length-scale can be linked. The chain model shows that in the absence of interfacial energy, austenite/martensite transformations are not hysteretic.

To incorporate hysteretic effects into the MD model, larger ensembles need to be considered where microstructures can freely evolve. This situation is studied in the sequel. However, before we proceed to explain the MD simulations in larger finite samples, in the next section we briefly attend to the special case of infinite single-crystalline lattices.

References

- O. Kastner, Molecular dynamics of a 2D model of the shape memory effect. Part II: thermodynamics of a small system. Continuum Mech. Therm. 18(1–2), 63–81 (2006)
- O. Kastner, G. Eggeler, Molecular dynamics simulations of the shape memory effect in a chain of Lennard-Jones crystals. MMMS 6(1), 78–91 (2010)
- O. Kastner, Molecular dynamics of a 2D model of the shape memory effect. Part I: model and simulations. Continuum Mech. Therm. 15(5), 487–502 (2003)
- U. Pinsook, G.J. Ackland, Simulation of martensitic microstructural evolution in zirconium. Phys. Rev. B 58(17), 11252 (1998)
- U. Pinsook, G.J. Ackland, Atomistic simulation of shear in a martensitic twinned microstructure. Phys. Rev. B 62(9), 5427–5434 (2000)
- T. Suzuki, M. Shimono, A simple model for martensitic transformations. J. Phy. IV France 112, 129–132 (2003)
- X.D. Ding, T. Suzuki, X.B. Ren, J. Sun, K. Otsuka, Precursors to stress-induced martensitic transformations and associated superelasticity: molecular dynamics simulations and an analytical theory. Phys. Rev. B 74, 104–111 (2006)
- F.E. Hildebrand, R. Abeyaratne, An atomistic investigation of the kinetics of detwinning. J. Mech. Phys. Solids 56(4), 1296–1319 (2008)
- R.S. Elliott, J.A. Shaw, N. Triantafyllidis, Stability of thermally-induced martensitic transformations in bi-atomic crystals. J. Mech. Phys. Solids 50, 2463–2493 (2002)
- 10. M. Born, K. Huang, Dynamical Theory of Crystal Lattices. International Series of Monographs on Physics (Oxford University Press, New York, 1954)
- 11. D.C. Swift, G.J. Ackland, A. Hauer, G.A. Kyrala, First principles equations of state for simulations of shock waves. Phys. Rev. B **64**, 214107 (2001)
- 12. J. Solyom, Fundamentals of the Physics of Solids, Volume 1: Structure and Dynamics (Springer, Berlin, 2007)
- E.A. Mastny, J.J. de Pablo, Melting line of the Lennard-Jones system. J. Chem. Phys. 127, 104504 (2007)
- I. Müller, P. Villaggio, A model for an elastic-plastic body. Arch. Rational. Mech. Anal. 65(1), 25–46 (1977)
- G. Puglisi, L. Truskinovsky, Mechanics of a discrete chain with bi-stable elements. J. Mech. Phys. Solids 48(1), 1–27 (January 2000)

References 85

- 16. I. Müller, A model for a body with shape-memory. Arch. Ration. Mech. An. 70, 61–77 (1979)
- 17. R. Abeyaratne, J. Knowles, A continuum model of a thermoelastic solid capable of undergoing phase transitions. J. Mech. Phys. Solids **41**, 541–571 (1993)
- 18. A. Vainchtein, T. Healey, P. Rosakis, L. Truskinovsky, The role of the spinodal region in onedimensional martensitic phase transitions. Phys. D **115**(1–2), 29–48 (1998)
- I. Müller, S. Seelecke, Thermodynamic aspects of shape memory alloys. Math. Comput. Model. 34, 1307–1355 (2001)

Chapter 4 Lattice Transformations in 2D Crystals

In the following chapter we shall gradually extend the geometrical size of the model assemblies in order to allow for microstructure evolutions during both thermal and mechanical induced phase transformation processes. We shall explain how larger test assemblies consisting of up to a quarter million atoms shall produce martensitic domain structures and how these structures evolve during transformation/reverse transformation cycles simulated with these assemblies. The conceptual restriction of two spatial dimensions reallocates the computational resources in favour of the time periods available for the simulations. This geometrical restriction also reduces the model's sensitivity in regard to surface effects such that free surface conditions may be applied. Accordingly, the simulation algorithm may be kept comparatively lean and transparent since the additional and cumbersome algorithms needed to artificially exclude the surface—and to maintain the mandatory stress control involved—are redundant [1–7].

4.1 Temperature-Induced Transformations

We exploit a collection of MD simulations which use finite-sized rectangular crystals of variable size (10,000–250,000 atoms) and shape (strips, quads).

During these simulations, the initial configuration was always defined in the austenitic phase (perfect square single crystals) and equilibrated to the free boundary condition at high temperature. Thus prepared models were subsequently subjected to cooling processes controlled by a thermostat. In this situation, the crystals experience temperature-induced transformations once a critical temperature is undergone, initiating nucleation and growth processes. These processes are explained in detail in this section.

The model parameters used in this study are documented in Table 4.1. The computer model uses the algorithm outlined in the section presention the method (p. 52), adjusted to the 2D setting. During the computations, we used the velocity

Interaction parameters	
A–A interactions	$\varepsilon_{A-A} = 1.2 \varepsilon_0$ $\sigma_{A-A} = 0.89 \sigma_0$
B–B interactions	$\varepsilon_{B-B} = 0.61 \varepsilon_0$ $\sigma_{B-B} = 0.89 \sigma_0$
A–B interactions	$\varepsilon_{A-B} = \begin{cases} 0.20 \varepsilon_0 & \text{(strip-shaped assembly)} \\ 0.19 \varepsilon_0 & \text{(quad-shaped assembly)} \end{cases}$
	$\sigma_{\rm A-B} = 0.6 \sigma_0$
Other parameters	
A mass	$m_{\rm A} = 1.0 \mu_0$
B mass	$m_{\rm B}=1.0\mu_0$
Time step	$\Delta t = 0.01 \tau_0$
Cutoff radius	$r_c = 4.0 \sigma_0$

Table 4.1 Model parameters used with simulations of temperature-induced martensitic transformations in larger rectangular model crystals

scaling algorithm to control the temperature. Domain decomposition was implemented at cut-off radii of $r_c = 4.0 \,\sigma_0$ to distribute the computational effort over a parallel computing grid.

4.1.1 Strip-Shaped Rectangles

The first MD simulation example represents a rectangular-shaped assembly of $32 \times 288 = 9$, 216 atoms $(2.3 \times 19 \text{ nm})$ with a free surface. Figure 4.1a shows the initial shape of this strip at 400 K in the austenitic configuration, which was stabilised prior to the simulation by means of a relaxation at this temperature. The slight curving of the surface visible at the strip's ends reflects the influence of the surface tension. On stepwise quenching the strip at a steady rate (5 K/ps), martensite nucleates at $M_S \approx 150 \text{ K}$ at the left end of the strip, from where the transformation evolves from left to right by a travelling transformation wave. During the transformation, the temperature temporarily increases owing to the release of latent heat; see the graph in Fig. 4.1b, prior to the thermostat compensating this effect. The strip's final configuration is depicted in Fig. 4.1c using a colour code to indicate the microstructure.

The simulation resolves the evolution of MT in remarkable detail. Figure 4.1d–f show snapshots of the strip's central segment at the simulation times of 87.6, 88.4 and 89.6 ps, respectively. The mean axial phase speed of the transition front is ca. 2,000 m/s, which is approximately half of the speed of sound. Thus, sound waves can propagate ahead of the transition front. An elastic precursor is observed in the simulations, indicated by the green broken lines in Fig. 4.1d–f.

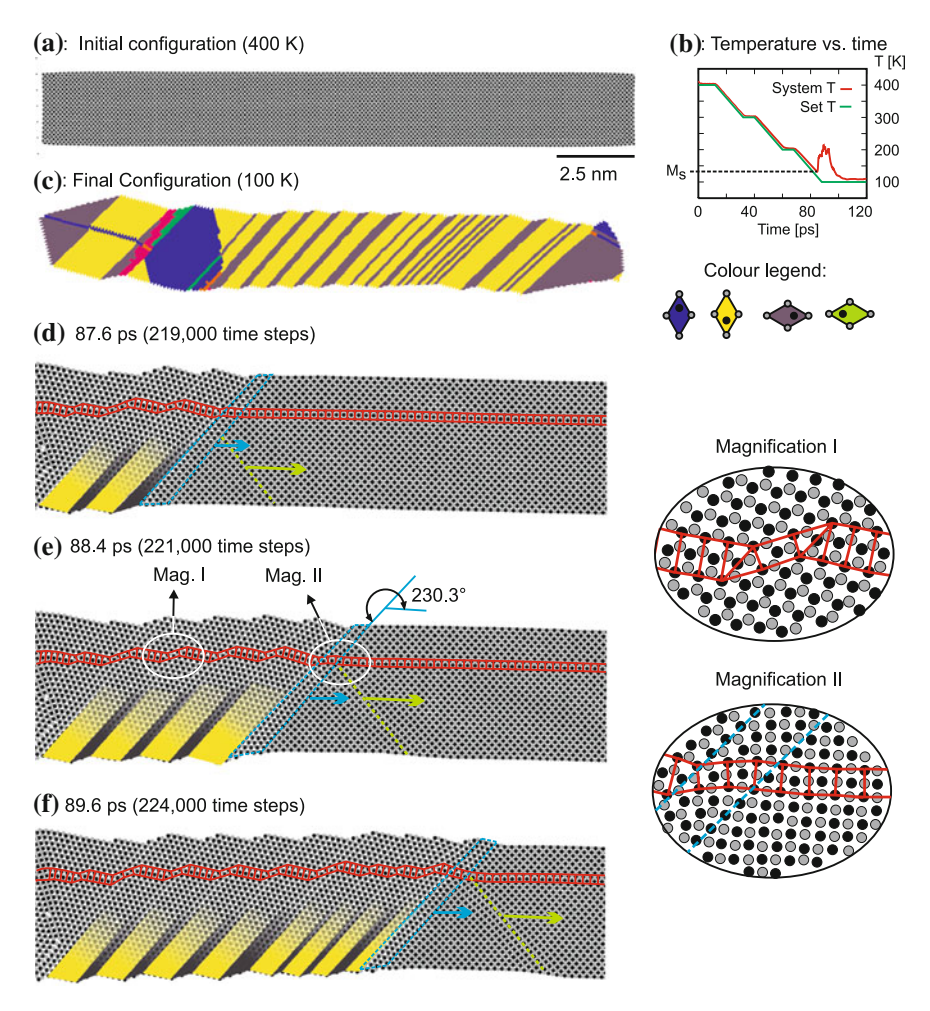


Fig. 4.1 MT in a strip-shaped assembly of 9,216 atoms. The simulation period involves 3×10^5 time steps or 120 ps on a physical time scale. a Initial configuration, showing atomic positions. c Final configuration with four differently coloured variants. Note the imperfections in the transition dynamics: a dislocation (imaged as a blue line, on the left) and the finite-energy, incoherent blue–purple interface (red band). b Temperature versus time graphs (system temperature red line, set-temperature green line). The transformation lasts for only approx. 10 ps; it is indicated by increasing temperature due to the release of latent heat, which is later cooled by the thermostat. d–f Snapshots of the central strip segment during the transformation. Red lines, blue broken lines and green broken lines indicate a train of unit cells, the transformation zone and an elastic precursor, respectively. Magnifications I and II show martensite/martensite (I) and austenite/martensite (II) interfaces (Video available online)

The transformation front is not atomically sharp: it covers 2–3 unit cell widths and, for this reason, a discrete habit line is not observed. Across this *transformation zone* the austenitic unit cells are smoothly curved into martensite such that the

deformation gradient is continuous, see the magnification II in Fig. 4.1. Consequently, the transformation zone may tolerate a slight lattice misfit and thereby allows for the formation of twin variants which are not strictly compatible according to the crystallographic compatibility condition of Eq. (1.3). In fact, variants from Table 3.2 that are "almost" compatible, for example the variants 3 and 5, may be joined along their diagonals which have identical lengths, as is shown in the magnification I in Fig. 4.1. Hence these two variants can be combined such that the hexagonal symmetry of the product phase *across* the interface is preserved. As a consequence of this, the interfacial energy is zero. However to achieve this energetically favoured state, the orientation of the transformation zone must rotate by approx. $\pm 6.5^{\circ}$.

Our simulations show that the transition zone may accomplish such slight rotations. In the snapshot of Fig. 4.1e, its orientation is approx. 230° , which corresponds to the evolving formation of variant 5. The transformation process forms uniform, mesoscopic regions of martensite which we refer to as crystallographic layers. The layers formed by the two variants no. 3 and 5 are colour coded yellow and purple, respectively, in Fig. 4.1c–f. The unit cells of the affected variants have different shear directions but identical shuffle directions of their sublattices. Inspection of magnification I in Fig. 4.1 shows that these two variants in fact form a hexagonal lattice such that twin–twin interfaces possess zero interfacial energies; evidence of this is provided by a typical potential energy landscape plotted in Fig. 4.11a and also in Fig. 4.4. Thus, in the 2D model, twin variants can be identified only from the deformation history: they are indistinguishable from the perfect lattice in the bulk material.

4.1.2 Quad-Shaped Rectangles

The simulations using the strip raise concern about how the transformation process is influenced by size and surface effects. In particular, stress in the bulk is relieved by relaxation of the surface forming facets corresponding to each variant. To reduce the surface effects, it is necessary to have a simulation geometry which is larger than the typical size of martensite plates. Therefore, we conducted 2D simulations using a 262,144-atomic quad ensemble with free surfaces shown in Fig. 4.2.

Similar to the case of the strip-shaped assembly, MT was induced by lowering the temperature. Upon cooling towards the transition temperature, the austenitic lattice shears slightly prior to MT, in order to form metastable pre-martensitic phases, which are colour coded orange and pink in Fig. 4.2a–c. Upon quenching the austenite below the critical transformation temperature, martensite typically nucleates at the free surface line of the specimen where the nucleation barrier is locally lower than that in the bulk, Fig. 4.3a. Two martensitic twin variants nucleate simultaneously along a principal axis ([01] or [10] in 2D) by a folding of the parent phase. Two independent nuclei are observed. Both grow axially on [01], and spread laterally. This process brings about wedge-shaped martensite plates which are finely twinned; see magnification area I in Fig. 4.2d. Each plate consists of compatible twin variants which are characterised by alternating shear directions of their unit cells but exhibit

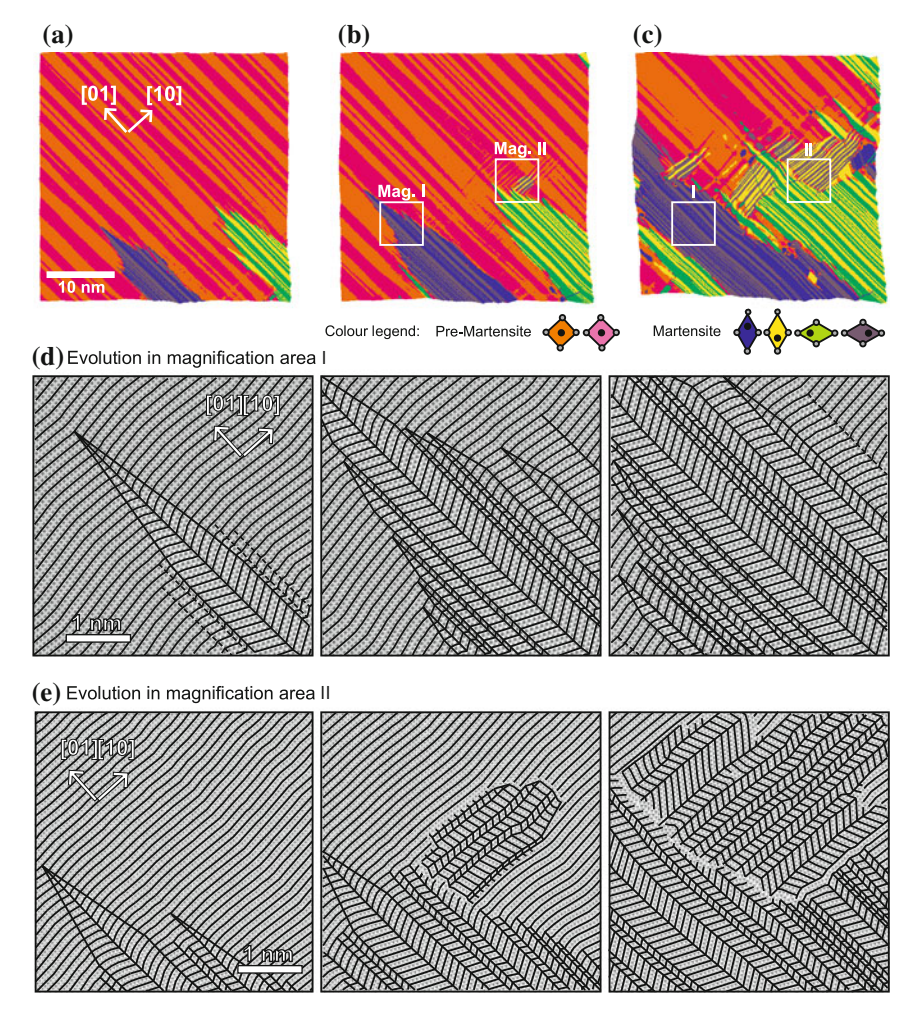


Fig. 4.2 MT in a 2D quad of 262,144 atoms. The quad has a free surface and temperature control was used to induce MT. **a–c** Time resolved snapshots of the entire quad's transformation process. Preceding the transformation wave is the strained austenite which does not exhibit hexagonal symmetry. This "pre-martensite" tweed structure, which predisposes the transition to a particular variant, is a strained austenite which does not exhibit hexagonal symmetry: atomic shuffles accompany the strain. **d** Magnification area I shows the tip of the growing martensite plate. **e** Magnification area II shows the nucleation of secondary plates (Video available online)

identical shuffle directions of the sublattices, forming the typical "herringbone pattern". When the martensitic wedges grow into the parent phase, strain fields are induced in their vicinity which eventually induce secondary nucleations of martensite. An example is detailed in the enlargement of area II in Fig. 4.2e. Comparable to the primary martensite plates, the secondary plates consist of compatible twin

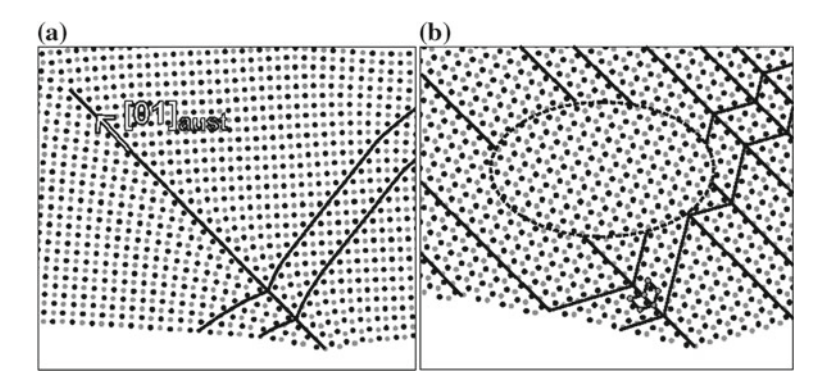


Fig. 4.3 Nucleation of martensite. **a** Nucleation sites are located at the free surface. The nucleation begins by the parent phase folding along one crystallographic principal direction (here, [01]) such that a twin nucleus forms. The nucleus grows along the axis and spreads laterally by spontaneous formation of finite-sized martensite laminates; compare with Fig. 4.2. **b** The laminates consist of variants with opposite shear directions but identical shuffle directions of the sublattices. Owing to the hexagonal variant symmetry, these can only be distinguished by their deformation history and at the surface: they are indistinguishable in the bulk material, see oval area

variants. However, since the secondary plates nucleate on [10], no compatibility exists with the primary plates that nucleated on [01]. Consequently, incoherent contact zones are formed where the respective martensite plates come into contact. These zones indicate martensitic domain boundaries; they are obvious in Fig. 4.2e.

Similar to the case of the strip, the plate's growth process is represented by travelling transformation zones where a regular microtwin pattern is instantaneously formed. Once more, we observe that in 2D the twinned variants are perfectly compatible, which indicates that their interfacial energy is zero. Evidence is provided by both Figs. 4.3b and 4.4, the latter depicting the potential energy field of fine-twinned martensite domains. The enlargements of areas I and III show twinned domains consisting of perfectly compatible variants with opposite shear directions and identical shuffle directions of the sublattices. Owing to the hexagonal symmetry of the model martensite, the respective variants can only be distinguished by knowing the transformation history of their unit cells, indicated by the narrow, solid lines in the magnifications. Apart from this, the variants observed at I and III are indistinguishable and both have zero interfacial energy. This is confirmed by the potential energy plot in (b). In the enlargement of area II, a line is visible along which a dislocation moved producing plastic deformation. This locally changes the energy only at the current position of the dislocation (green). Domain boundaries and lattice defects are also clearly recognisable in the potential energy field. The enlargement of area IV shows a triple junction.

The influence of the temperature level on the morphology of the martensite phase is illustrated in Fig. 4.5. We show two configurations of the 262,144-atom rectangle which were produced from identical nucleation situations but whose thermostats were set at different temperatures (150 and 600 K). At the lower temperature, the

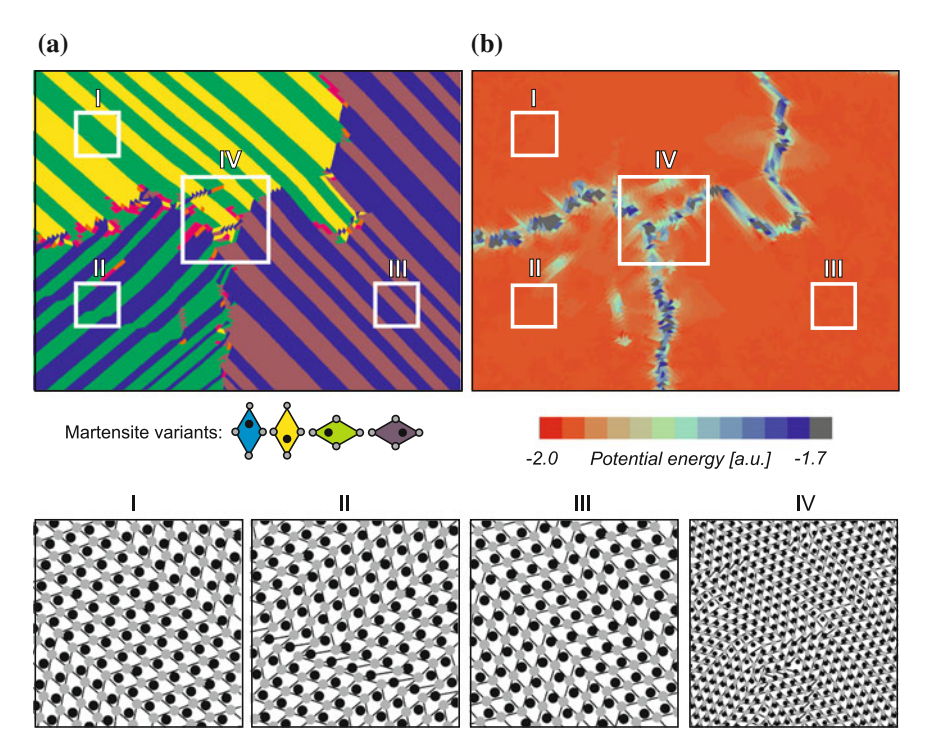


Fig. 4.4 Martensite twin-domains and the corresponding potential energy field. **a** Morphology of the product phase obtained by temperature-induced MT. Enlargements of I–IV show detailed close-ups (Video available online)

thermodynamic driving force is higher which enhances the nucleation of martensite. For this reason, the product exhibits a slightly finer domain structure. A higher temperature level reduces the thermodynamic driving force for nucleations and produces a coarser domain structure. It also slows down the plate growth which, on average, produces slightly finer martensite laminates. A layer statistics supporting this view is presented in Fig. 4.5c.

Another example of MT in a slightly smaller quad-shaped ensemble is shown in Fig. 4.6. Here, a 160,000-atom quad is investigated, which initially represents single crystalline austenite. At a constant temperature of 200 K, martensitic nucleation initiates and primary nuclei are again formed at the surface. From here, the transformation proceeds into the bulk, forming the needle-like martensitic plates of compatible twin variants discussed earlier. Figure 4.6a shows the product morphology, and (b) the associated potential energy field. Again, martensitic domains consist of finely twinned microstructures formed by compatible variants (see Fig. 3.3c). Once again, the twins are perfectly compatible and do not exhibit twin/twin interfacial energies. Location I in Fig. 4.6 shows the interface between variants having identical shear directions but opposite shuffle directions of the sublattices (anti-phase boundary).

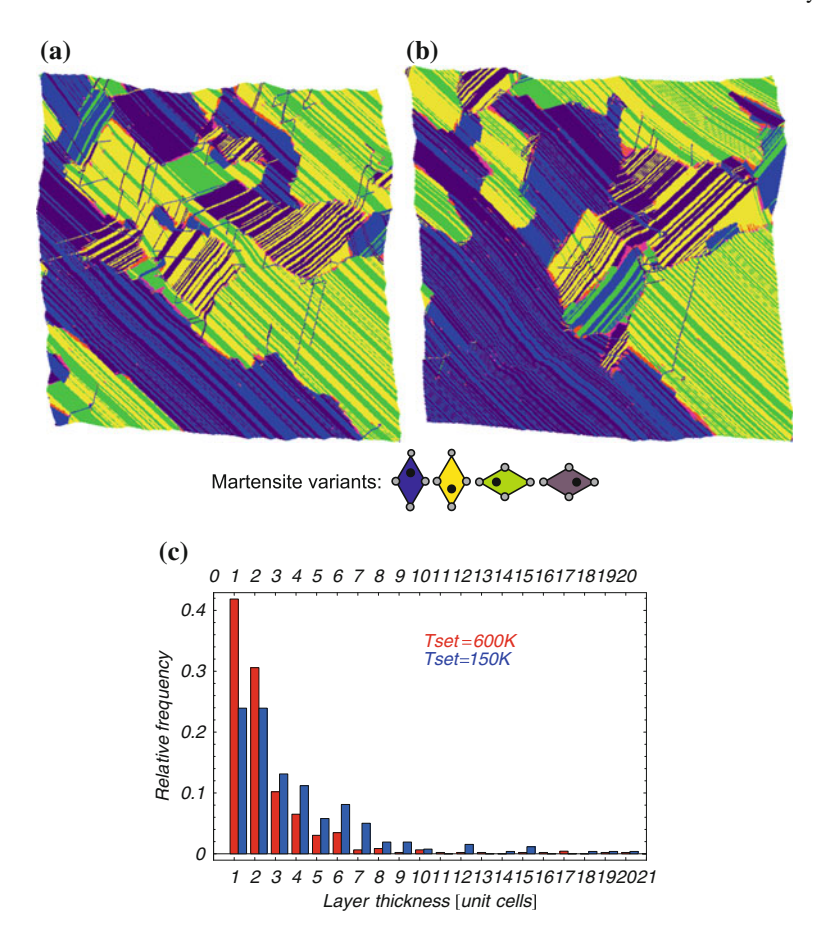


Fig. 4.5 Influence of the quenching rate on the transformation morphology. **a** and **b** Show two configurations of the 262,144-atom rectangle produced from identical nucleation situations but at different set-temperatures of the thermostat. **a** $T_{set} = 150 \text{ K}$, **b** $T_{set} = 600 \text{ K}$. A higher temperature affects a smaller thermodynamic driving force, thus the domain structure is slightly coarser while the twin laminates are on average finer. **c** Shows the corresponding frequencies of the layer thicknesses for both cases. (Colour online)

Such interfaces exhibit a substantial surplus of energy along the line where the shuffle changes direction (Fig. 4.6b). Interfaces of this type are typically straight, as indicated by the broken line in the magnification of location I. Location II in Fig. 4.6 shows the interface between the plates which nucleated on the two perpendicular axes [01] and [10] of the austenitic lattice. Variants within each individual plate are compatible, but different plates give rise to misfit at the boundary. The misfit produces strain energy, indicated in Fig. 4.6b, along boundaries which were dynamically created where the growing plates came into contact. These boundaries may thus assume an arbitrary shape. At some points along a domain boundary, the

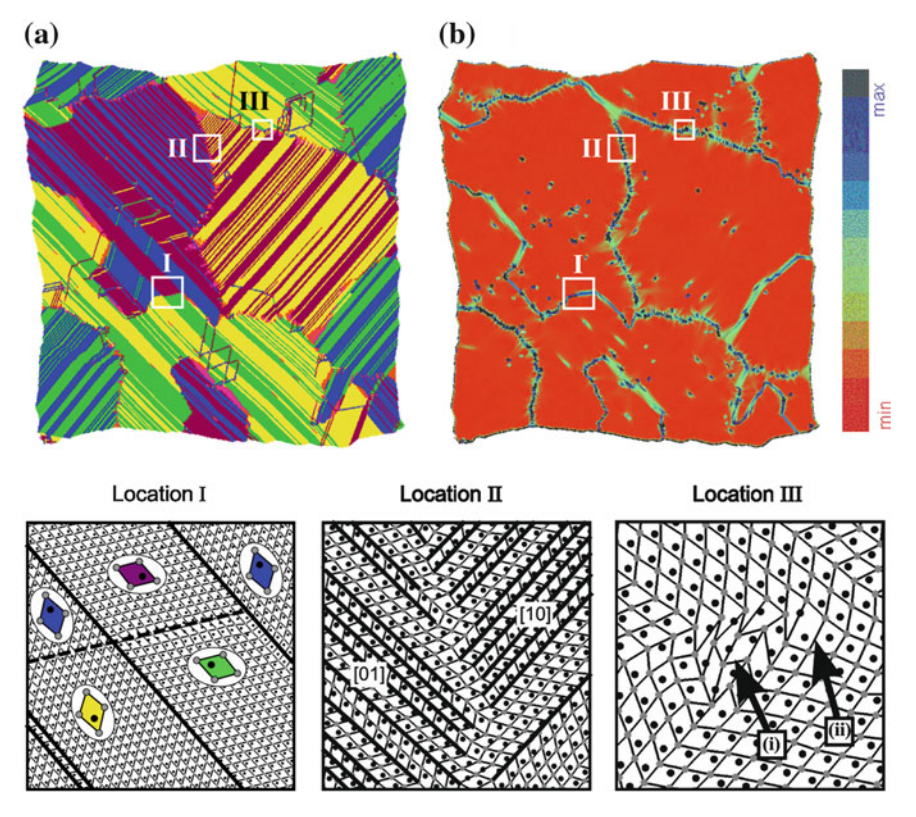


Fig. 4.6 Product of MT in an initial single crystal of a 160,000-atom quad. **a** Product morphology. Twins are colour coded according to the magnification of location I. **b** Potential energy field. Domain boundaries again possess higher surplus potential energies which significantly affect the colour contrast. However within a single domain, the twin structure visible in **a** is not represented in **b** (Video available online)

incompatibility gives rise to coordination defects. Location III in Fig. 4.6 shows such a situation: the two arrows indicate deformed unit cells at (i) and a vacancy at (ii).

We may conclude from these simulation results that MD simulations of MT in 2D Lennard-Jones solids capture the basic transformation mechanisms using atomistic resolutions. The sizes of our test ensemble (up to a quarter of a million atoms) appear to be sufficient to model a domain structure and its energetic implications. Although the model material is artificial, general ideas about MT should apply equally well to our simulations. The simulations exhibit heterogeneous nucleations of martensitic plates comprising of compatible twin variants. These plates grow as needles, with the tip moving perpendicular to the habit plane. When martensitic plates encounter one another, the variants are incompatible and the interfaces have high energy. All of this is observed in real MT. The needle tips and the connecting boundaries between the plates form point defects which may be identified as 2D analogues of vacancies

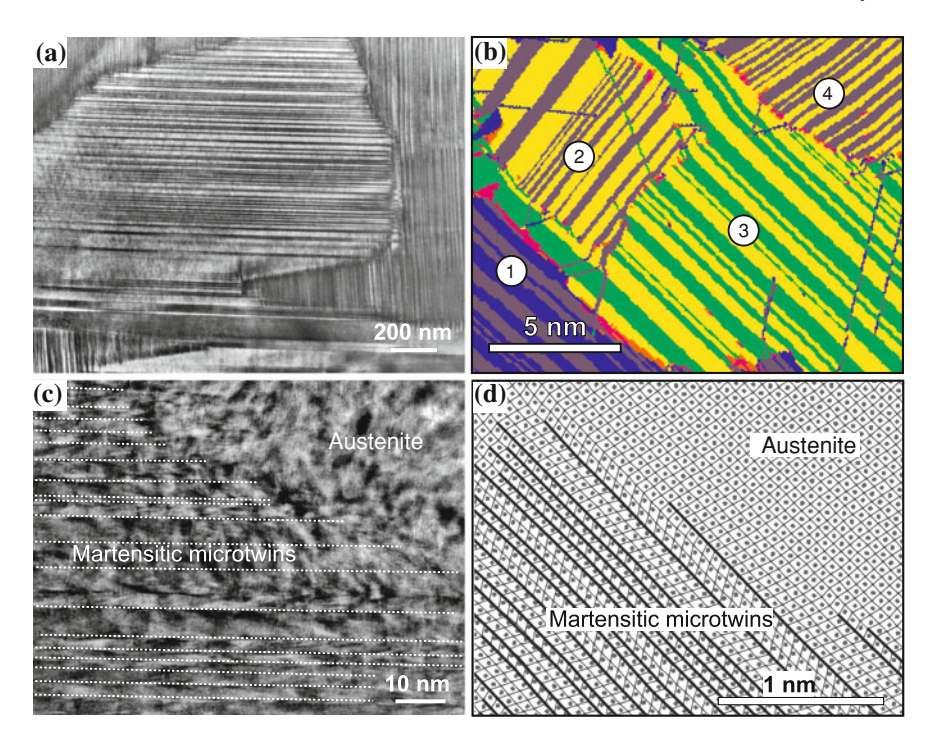


Fig. 4.7 HR-TEM images of NiAl and simulated microstructure in a 2D Lennard-Jones crystal. a HR-TEM image of martensitic morphology exhibiting various junctions between differently oriented martensite variants. b Simulated morphology obtained by temperature-induced MT of a large 2D test ensemble. Colours indicate 4 variants of martensite present in the model which may nucleate on two perpendicular axes. $\bf c$ and $\bf d$ show close-ups of the HR-TEM micrograph and the simulation result, respectively. HR-TEM images courtesy Schryvers [8]

or dislocations in 3D. The model exhibits variant diversity, as anticipated by the crystallographic theory, and produces a rich transformation morphology, as observed in real materials, e.g. NiAl: Fig. 4.7 shows a nanoscale HR-TEM image of martensitic domains in this alloy. Martensite plates are formed by compatible twin variants. Plates which nucleate independently (①—④) show incoherent, curved domain boundaries which come into contact and generate dislocations. The domain structure yielded by the 2D simulations looks remarkably realistic. Note that no effort was spent on parameterising the model with respect to a real material, thus the characteristic length scales deviate by approximately one order of magnitude. The HR-TEM image in subfigure (c) shows an irregular martensite-austenite boundary (broken white line). The martensite exhibits a fine microstructure of parallel layers of twin variants (dotted white lines) at thicknesses of up to a few dozen unit cell widths. Twins consist of energetically equivalent and crystallographically compatible variants of martensite. Subfigure (d): Growing martensite-austenite boundary during the transformation process that yields the morphology in (b).

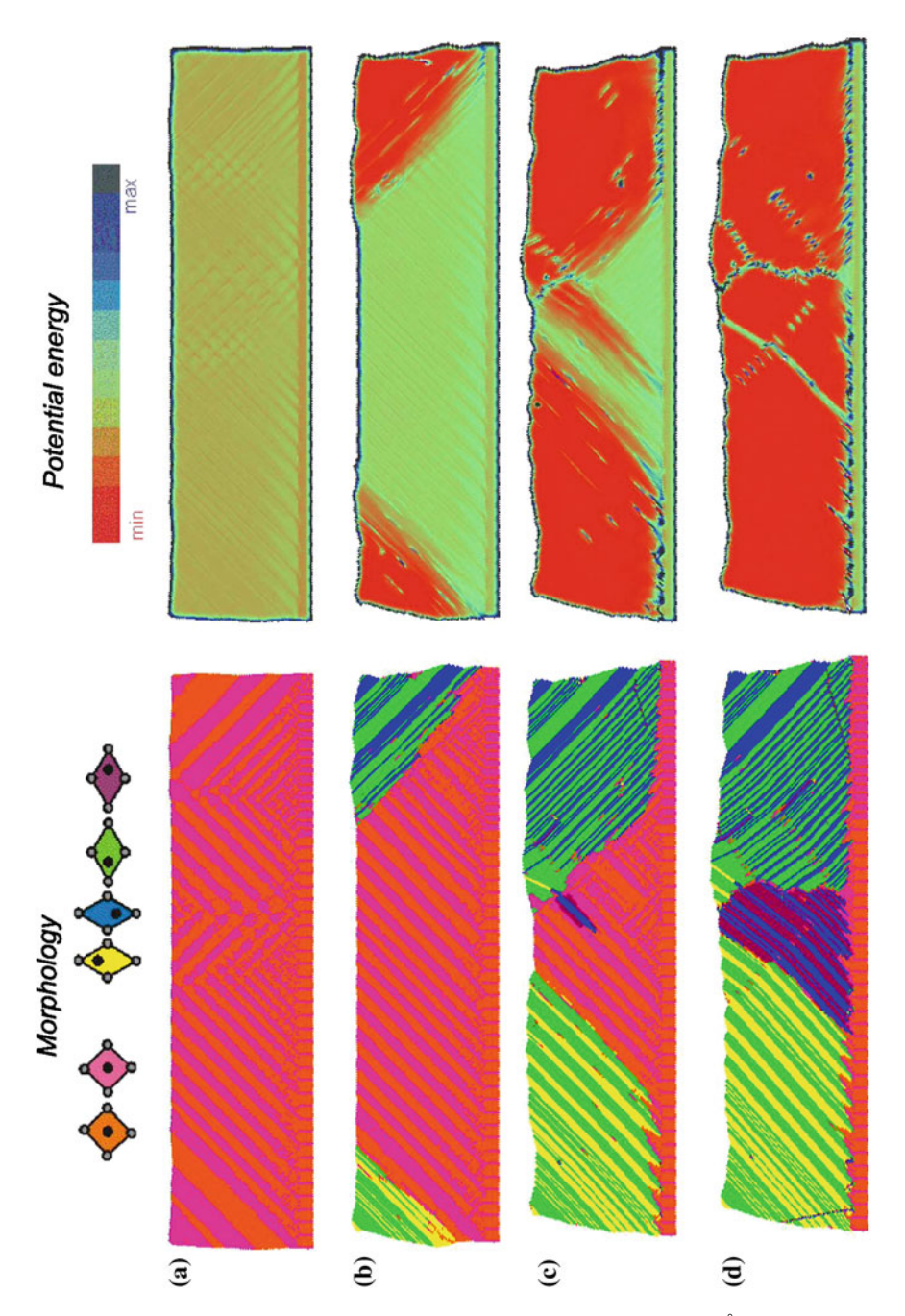


Fig. 4.8 MT in a substrate layer I. 65,536 atoms. Layer thickness approx. 90 Å. (8,4) Lennard-Jones potential, interaction cut-off approx. 6 Å, total simulation time 4 ps. **a–d** Four instants during MT. (Side-view intened, Colour online, Video available online)

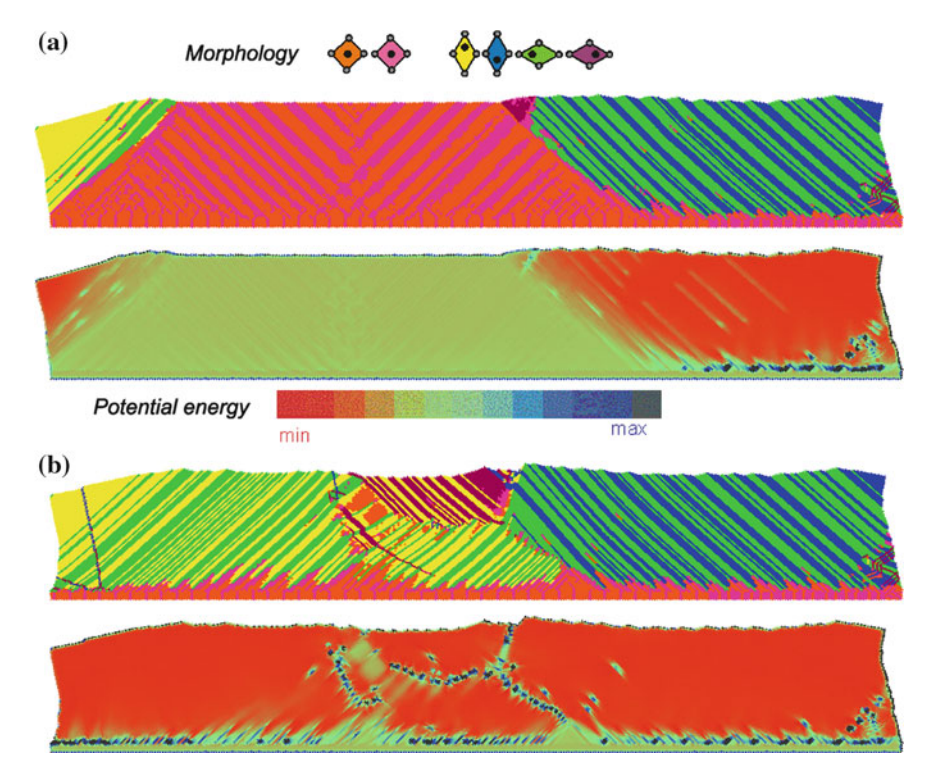


Fig. 4.9 MT in a substrate layer II. 61,440 atoms. Layer thickness approx. 70 Å. (12,6) Lennard-Jones potential. Interaction cut-off approx. Å. **a**, **b** Two instants during MT. Simulation time 4 ps. (Colour online, Video available online)

4.1.3 Substrate Layers

We briefly investigate the special situation of MT in a layer bound to some non-transforming substrate. In this case, the substrate is modelled by fixing the atoms in a surface layer such that they cannot transform into martensite during a temperature change. In such a model, temperature-induced transformation processes evolve by nucleation and growth is similar to the strip with free surfaces studied above, see Figs. 4.8, 4.9, 4.10. Martensite may nucleate at the free corners of the ensemble independently from where the transformation propagates along the substrate layer. The three cases presented in these figures basically differ in the ensemble's size. We partly employed (8, 4) Lennard-Jones potential in order to study the effect of the longer interaction ranges effected by this potential. For these cases, the cut-off radius was accordingly adjusted to $6\sigma_0$. These modifications were applied in order to investigate the interplay between the interaction range and the martensitic lamellae structure produced during MT. It appears that this effect is of minor significance.

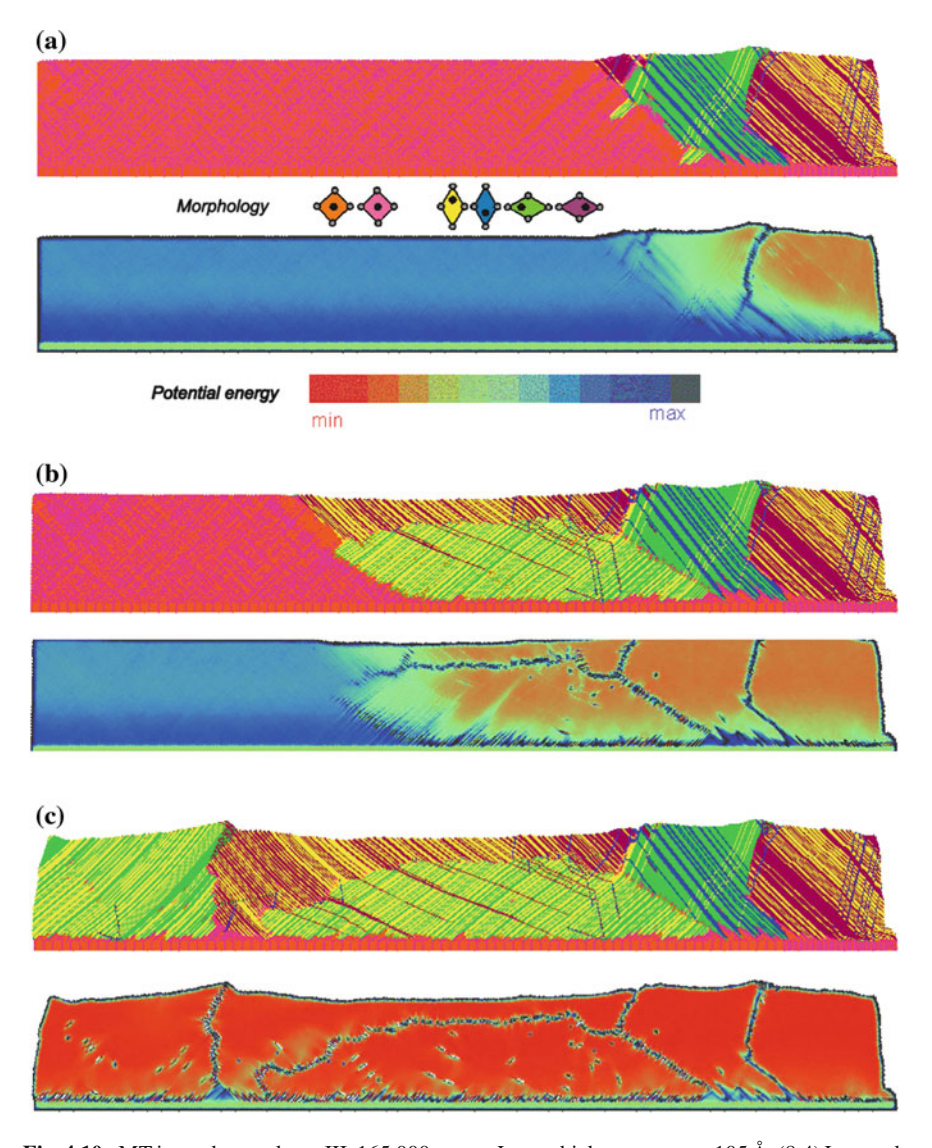


Fig. 4.10 MT in a substrate layer III. 165,000 atoms. Layer thickness approx. 105 Å. (8,4) Lennard-Jones potential. Interaction cut-off approx. 6 Å. \mathbf{a} - \mathbf{c} Three instants during MT. Total simulation time 2 ns. (Colour online, Video available online)

The resulting morphologies do not visibly differ from those produced with (12, 6) potentials.

In Fig. 4.8 the nucleations are stimulated such that the transformation waves propagate simultaneously from both ends of the layer. (a): Preceding the MT, a tweed pattern of pre-martensitic variants (orange and pink) is formed during cooling. (b):

The transformation nucleates simultaneously at the free corners and grows towards the mid-length forming twinned domains which extend through the thickness. A finite twin structure is formed within the moving transformation zone, as observed in the free strip. Once again, twins do not exhibit an interfacial-energy trace in the potential energy field. (c): Eventually, the two domains come into contact. The corresponding accommodation process produces an intermediary grain located between the two former grains. All domain boundaries produce distinct traces in the potential energy plot caused by incoherencies.

Figure 4.9 depicts a similar process using a slightly thinner layer. The progress of the transformation and the final morphology are similar to the former process. Again we observe two domains coming into contact and forming a granular contact zone. In Fig. 4.10, an even more extended ensemble was investigated. Here, the transformation proceeds from right to left. With an extended layer, the substrate loses control over the formation process, allowing inhomogeneous domains to form through the thickness. The resulting morphology thus becomes more diverse and tends to those observed in the simulations of bulky "quads" in Figs. 4.2, 4.3, 4.4, 4.5, 4.6, 4.7.

4.2 Transformation Dynamics and Microstructure

In 2D, twin variants are perfectly coherent without any misfit and consequently the martensite interfaces are free of interface energy. Despite the lack of twin-boundary energy, the model produces plausibly real microtwin structures. The microstructures are produced before the transformation wave has reached the edge of a test ensemble, and hence are due to a local rather than global energy minimisation.

In order to explain this, we define a small subset of $N_S = 54$ atoms which uniformly transforms into single variant martensite in $\Delta t_{\rm trans} \approx 0.28$ ps (700 time steps). This small subset defines a region which undergoes coordinated transformation motion as the transformation front passes this subset. This means that this layer can be reasonably treated as a single mesoscopic entity.

The total energy E_S is the sum of the potential and the kinetic energy of the subset's atoms. We define the potential energy V_S of the subset by

$$V_S(t) = \frac{1}{2} \sum_{\alpha=1}^{N_S} \sum_{\beta=1, \beta \neq \alpha, r_{\beta\alpha} \leq r_c}^{N} \Phi_{\alpha\beta}(r_{\beta\alpha}(t)). \tag{4.1}$$

Note this definition includes long-range interactions with the vicinity of the subset.

We apply the concept of separating mass centre velocities from the deviatoric fluctuations introduced on page 22. Accordingly, we define the velocity \mathbf{v}_S of the mass centre of the subset by

$$\mathbf{v}_S = \sum_{\alpha=1}^{N_S} \frac{m_\alpha}{m_S} \, \dot{\mathbf{x}}_\alpha \quad \text{with} \quad m_S = \sum_{\alpha=1}^{N_S} m_\alpha. \tag{4.2}$$

This velocity produces mesoscopic kinetic energy K_S of the subset, while the respective deviatoric fluctuations $\dot{\mathbf{x}}_{\alpha} - \mathbf{v}_S$ contribute to the caloric energy $N_S kT$,

$$K_S(t) = \frac{m_S}{2} \mathbf{v}_S^2(t) \tag{4.3}$$

$$N_S k T(t) = \sum_{\alpha=1}^{N_S} \frac{m_\alpha}{2} \left(\dot{\mathbf{x}}_\alpha(t) - \mathbf{v}_S(t) \right)^2. \tag{4.4}$$

Thus, the total energy of the subset may be represented as the sum of the internal energy $U_S = V_S + N_S kT$ and the mesoscopic kinetic energy of the centre of mass K_S . The energy balance for the subset reads

$$\frac{\mathrm{d}}{\mathrm{d}t}(U_S + K_S) = \dot{Q} + \dot{W}. \tag{4.5}$$

 \dot{Q} and \dot{W} represent the power of heating and the power of mechanical working exchanged with the environment, respectively.

During the MT, the potential energy changes from the higher austenitic to the lower martensitic level, see Fig. 4.11b. The potential energy is partly transformed into heat N_SkT and partly into kinetic energy K_S . During $\Delta t_{\rm trans}$, the temperature level slightly increases as a result of energy dissipation, but K_S is nonzero as the transformation wave passes. Integration of the energy balance (4.5) over $\Delta t_{\rm trans}$ suggests that in the local region only approx. 20% of the potential energy is transformed into heat. If we assume the heat flux is negligible during the short transformation time $\Delta t_{\rm trans}$, the majority of the released energy goes into work which is dissipated as heat over a longer timescale.

This result may be interpreted from the viewpoint of momentum. The transformation of a single crystallographic layer produces a mesoscopic momentum which is balanced by forces in the adjacent layers. The corresponding mechanical work—i.e., the flux of energy—can be identified from the energy balance as sketched above.

As a result of the hexagonal symmetry of the model martensite, microtwin interfaces have zero interfacial energy. This makes the model material convenient for comparing with crystallographic and energy-minimisation theories. Our simulations show that the martensite structure is rapidly formed in propagating transformation zones which are subject to local rotations and are not atomically sharp. The finite transformation zone allows variant rotation and the formation of crystallographically incompatible twins.

The formation of martensite layers introduces momentum at the mesoscopic level, which has to be locally compensated. It is the flux of this momentum—i.e.the local transformation stresses—that induces counter directional movement of the adjacent

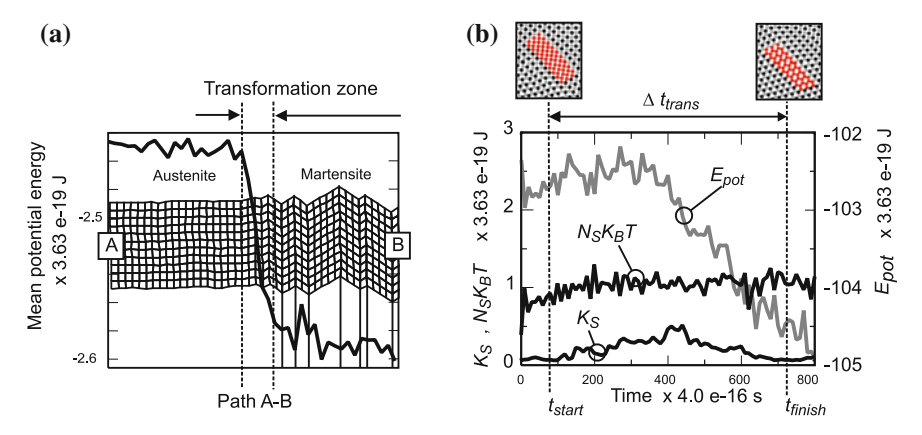


Fig. 4.11 Spatial and temporal energy graphs. **a** Mean potential energy along the path A–B across an austenite–martensite interface. The fluctuations visible on either side of the transformation zone are due to thermal and acoustic noise and do not, in general, coincide with interfaces. Most importantly, microtwin interfaces have zero interfacial energy. **b** Energy–time graphs during the transformation time of a subset of 54 atoms located in a crystallographic layer of martensite. Here, the initial and final shape of the subset is sketched. The energy functions are plotted according to the Eqs. (4.1), (4.3) and (4.4). (Colour online, Video available online)

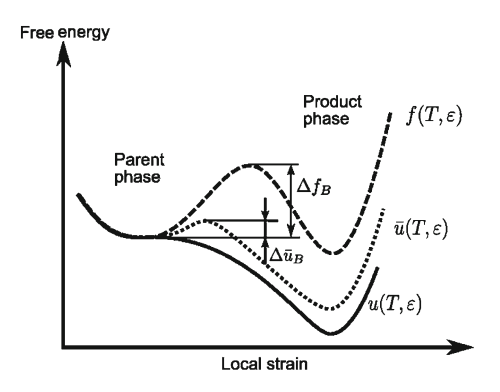
layer, which in turn nucleates a variant twin. Hence, by means of a type of bidirected domino effect, a microtwin patterned martensite plate can be formed. The impact of the mesoscopic transformation kinetics on the martensitic morphology is particularly augmented by the 2D Lennard-Jones model, but we could prove this effect be present during MT in 3D models as well. Therefore, it may reasonably be present in real materials too. In addition to this, 3D models and real materials exhibit twin–twin interfacial energies which also contribute to the local energy balance. Our simulations show, however, that the transformation kinetics indeed represent a fundamental mechanism for the formation of martensitic microstructure and must not be neglected.

The microstructure is immediately created by the transformation kinetics, and then fixed. It does not subsequently transform to minimise the energy of the entire system, rather it is the result of local dynamics and compatibility conditions. Consequently, the energetic condition determining the microstructure must also be a local condition.

4.3 Nucleation of Martensite

We have used the term "nucleation" in various places in this book in a deliberately naive manner so far, referring to incidents of martensite formation within the parent phase matrix. These incidents were judged by means of unit cell morphologies. We have seen, in MD simulations, it is not required to stimulate nucleation events by

Fig. 4.12 Sketch of two different nucleation scenarios. The *dashed line* illustrates the free energy of a macroscopic mass point as function of strain in a slightly undercooled state $T < T_E$



"seeds". Rather, nucleations are represented as specific solutions of the atomic trajectories determined by the Equations of Motion in a regime of global lattice instability. The model develops stable states similar to real materials: "natural" fluctuations of temperature or strains probe the energy landscape and eventually detect favourable loci where the transformation is initiated.

In unloaded samples nucleations are observed if the temperature is lowered below the theoretically derived equilibrium temperature T_E , as we have seen in the previous sections. For several reasons, an undercooling below T_E is always required: First, because the transformation is related to quick, volumetric latent heat release which for technical reasons cannot be compensated immediately by a thermostat, both in a laboratory and in a computer experiment. So without undercooling, the self-heating effect immediately inhibited the transformation. Second, because the free energy exhibits a nucleation barrier which the lattice has to overcome. The nucleation barrier Δf_B consists of an energetic barrier Δu_B and also an entropic barrier $T\Delta s_B$ in general, see Eq. (1.21) on p. 19. In lattices, nucleation barriers are often attributed to strain energies effected by lattice misfit of adjacent phases. Such nucleation barrier is entirely energetic and the entropic contribution is missing. However, for lattice transformations an entropic barrier must be expected.

In Fig. 4.12 two scenarios are illustrated: If the internal energy is represented by the dotted graph \bar{u} , then the free energy barrier Δf_B indicated has both an energetic contribution $\Delta \bar{u}_B$ and an entropic contribution $-T \Delta s_B$. In contrast, if the internal energy is represented by the solid graph u, then the energetic barrier is missing—as $\Delta u_B = 0$ —and hence the free energy barrier is solely entropic in this case.

MD simulations help to understand the nature of the entropic nucleation barrier. To see this we adjust the interaction parameters of our L-J model such that the energetic nucleation barrier between the parent and product phases is missing and analyse thermally stimulated nucleation events simulated with this specific model material. The simulation results are presented in the following. These were elaborated as joint work with Prof. R. Shneck, University of the Negey, Beer Sheva, Israel [9].

Table 4.2 Model parameters used with the nucleation experiment

Interaction parameters	
A–A interactions	$\varepsilon_{A-A} = 1.2 \varepsilon_0$
	$\sigma_{A-A} = 0.89 \sigma_0$
B–B interactions	$\varepsilon_{\rm B-B} = 0.61 \varepsilon_0$
	$\sigma_{\rm B-B} = 0.89\sigma_0$
A–B interactions	$\varepsilon_{A-B} = 0.17 \varepsilon_0$
	$\sigma_{A-B} = 0.6 \sigma_0$
Other parameter	S
A mass	$m_{\rm A} = 1.0 \mu_0$
B mass	$m_{\rm B} = 1.0 \mu_0$
Time step	$\Delta t = 0.0025 \tau_0$
Cut-off radius	$r_c = 3.5 \sigma_0$

4.3.1 Simulation Setup

The model crystal employed here consists of 38,016 atoms. The usual (12,6) L-J model was used to define the atomic interactions. The interaction parameters are set according to Table 4.2.

The initial lattice positions were defined with respect to the perfectly square lattice and dynamically relaxed to free surface conditions at a temperature of 150 K afterwards. The crystal is in an undercooled state at this target temperature according to the selected parameters.—cf. Fig. 3.11 on p. 69—therefore uncontrolled lattice transformations must be prevented during the preparative relaxation process. This can be achieved employing a trick: we have seen that lattice transformations require correlated atomic motions. Consequently, transformation events can be suppressed if these correlations are disabled. Technically, discorrelations of the atomic trajectories are effected by frequent randomisation of the atomic velocity vectors (preserving the atomic speeds). Provided the randomisation frequency is selected properly, this procedure allows for mechanical relaxations at the length scale of the crystal, while nucleations are inhibited on the microscale.

At the target temperature, the lattice produced by this method is pre-martensitic. Pre-martensite is represented by slightly sheared square unit cells as we have explained earlier. Here we refer to it as the parent phase. Typically, pre-martensite forms the tweed patterns observed prior to the martensitic transformation in earlier simulations, cf. Fig. 4.2 or Fig. 4.9, for example. The velocity randomisation procedure augments the natural tendency to reduce pre-martensite interfaces; therefore, the relaxed test crystal is eventually single crystalline. In this configuration, the crystal is fixed at two parallel surfaces, leaving the remaining two surfaces unconstrained, see Fig. 4.13. The thermostat and the velocity randomisation algorithm are switched off. With these preparations, martensitic nucleation events can be studied under mechanically equilibrated conditions. The results are recorded at high temporal resolution, employing a particularly short time step width of $\Delta t = 0.0025 \tau_0$.

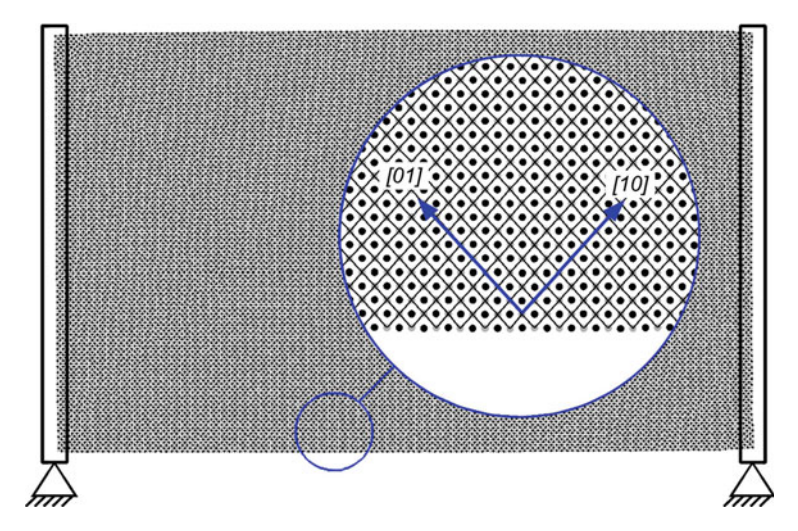


Fig. 4.13 Initial configuration prepared for the nucleation computer experiment. A relaxed single crystal is fixed on two sides in an undercooled state. Nucleations are allowed to evolve freely in absence of any further numerical manipulation (thermostat, seeds). The principle lattice directions are indicated by *arrows*

4.3.2 Simulation Result

We present the results of the computer experiment focusing attention to a time window of 10,000 time steps spanning the first two nucleation events observed in the crystal. We refer to these as the "primary" and the "secondary" nucleation, respectively. Figure 4.14 provides an overview of the process, showing four snapshots of the total crystal at 10, 5060, 6700 and 10000 time steps. The progress is visualised by four different representations, the morphology, the potential energy field, the temperature field and the mesoscopic kinetic energy field, respectively. The progress of these quantities is displayed by columns in Fig. 4.14. The morphology of the unit cells (first column) is analysed with reference to the deformation of square unit cells, defined in the parent phase. We employ the colour code depicted at the bottom to indicate their phase affiliation as usual. The potential energy field, the temperature and the mesoscopic kinetic energy are computed per atom by the MD program. In the representations, unit cells are coloured with reference to bi-atomic average values of these quantities. The atomic potential energy (second column) of an individual atom relies on its interaction neighbourhood set by the cut-off radius r_c . Neighbourhood atoms are enlisted in the Verlet list. The temperature (third column) and the mesoscopic kinetic energy (last column) are computed employing the concept of separating mean velocities from deviatoric fluctuations. This concept—introduced on pp. 21, 22—has also been used in the last section to compute the "mesoscopic" kinetic energy of a transforming subset of atoms. We have seen that transformation events are indicated by locally homogeneous displacements of atoms, causing a slight

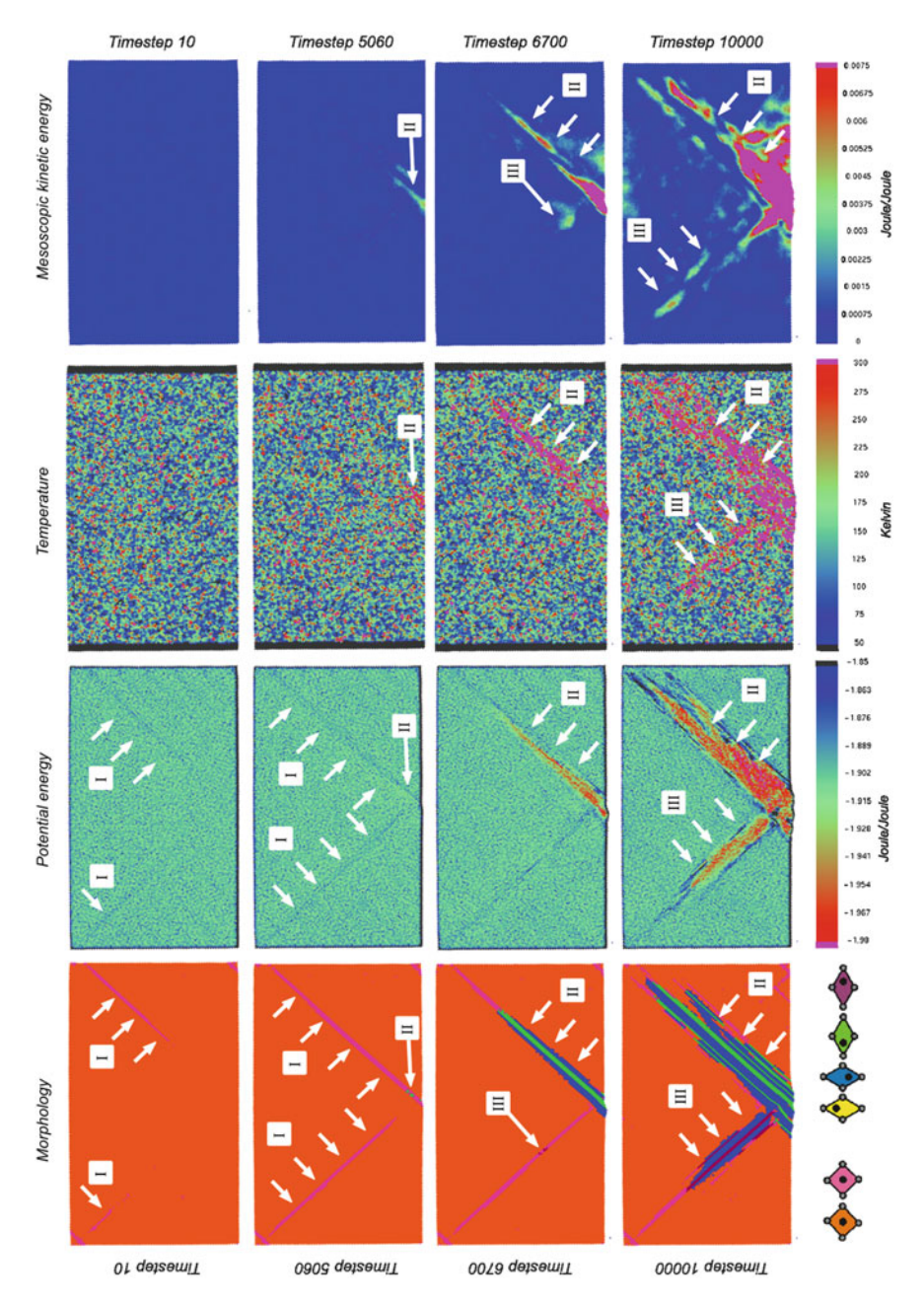


Fig. 4.14 Nucleation experiment with a rectangular 38,016 atomic crystal. Snapshots of four instants employing four representations each, the morphology, potential energy, temperature and mesoscopic kinetic energy, respectively. (Side-view is intended, Video available online)

drift of their common mass centres. Here we confine the argument in regard to the atomic interaction neighbourhoods and define the velocities of their respective mass centres by

$$\mathbf{v}_{S}^{\alpha}(t, \mathbf{x}_{\alpha}) = \sum_{\beta} \frac{m_{\beta}}{m_{S}^{\alpha}} \dot{\mathbf{x}}_{\beta} \quad \text{with} \quad m_{S}^{\alpha} = \sum_{\beta} m_{\beta}, \qquad (4.6)$$

$$r_{\beta\alpha} \leq r_{c} \qquad \qquad r_{\beta\alpha} \leq r_{c}$$

where m_S^{α} denote the masses of the interaction neighbourhoods of the individual atoms $\alpha=1...N$. Technically, these quantities are computed on the basis of the Verlet list which is maintained by the MD program for the calculation of the interaction forces. Accordingly, the mesoscopic kinetic energy of any interaction neighbourhood $\alpha=1...N$ may be defined by

$$K_S^{\alpha}(t, \mathbf{x}_{\alpha}) = \frac{m_S^{\alpha}}{2} \left(\mathbf{v}_S^{\alpha}(t) \right)^2. \tag{4.7}$$

This quantity represents a local measure for the homogeneity of atomic motions at the mesoscale. The index α refers to the position of atom α , while K_S^{α} is the property of all atoms belonging to its neighbourhood on average. This field quantity is visualised in the last column of Fig. 4.14. The temperature at the position of atom α hence reads

$$T(t, \mathbf{x}_{\alpha}) = \frac{1}{N_{S} k} \sum_{\beta} \frac{m_{\beta}}{2} \left(\dot{\mathbf{x}}_{\beta}(t) - \mathbf{v}_{S}^{\alpha}(t) \right)^{2}, \tag{4.8}$$
$$r_{\beta\alpha} \leq r_{c}$$

where N_S is the number of atoms located in the interaction neighbourhood. Temperature refers to the velocity fluctuations about the mesoscopic velocities \mathbf{v}_S^{α} .

The first row of Fig. 4.14—referring to 10 time steps—shows the total crystal in the pre-martensitic parent phase. Its morphology is indicated by orange colour. Two small strips of the pre-martensitic twin variant (pink colour at the arrow tips of "I") have formed. The potential energy field is homogeneous (green colour) with faint energy marks indicating the interfaces of the twin variant strip at "I". Respective signatures, however, are missing in the fields of temperature and mesoscopic kinetic energy. In the temperature field, the gripping zones are reflected to the left-and right-hand sides of the crystal, where the atoms are at rest. The second row of Fig. 4.14—referring to 5,060 time steps—shows the instant of first visual appearance of martensite at "II". Towards this time, the twin strips at "I" evolved along the principle lattice directions. The nucleus has a temperature signature, which indicates release of latent heat, and also a mesoscopic kinetic energy signature, indicating a localised martensitic transformation. The third row of Fig. 4.14—referring to 6,700 time steps—shows the instant of secondary nucleation at "III". Towards this instant, the primary nucleus has grown into a twin plate consisting of the two martensite

variants indicated by green and blue colour. This plate exhibits lower potential energy and elevated temperature owing to local release of latent heat during the ongoing transformation. The mesoscopic kinetic energy exhibits signatures at the plate interfaces, where the transformation is active. The last row of Fig. 4.14—referring to 10,000 time steps—shows the secondary nucleus extended at "III" and the extended primary nucleus extended. at "II". The ongoing transformations exhibit clear signatures in all four representations. Note to this time we first observe dark-blue the potential energy "halos" about the growing martensite plates. These represent elevated strain energy due to misfit between parent and product lattices.

4.3.3 Nucleation Centres

Figure 4.15 provides lattice enlargements of two areas containing the nucleations observed with the computer experiment. We identify two subsets of 28 atoms each representing the primary and the secondary nucleation centres, respectively, see Fig. 4.16. The primary martensite plate nucleates by shear along [10], while the secondary plate nucleates by shear along [01]. We denote the respective shear directions by s_i and the conjugate directions by \bar{s}_i , see Fig. 4.16c and d. Figure 4.18a visualises the atomic displacements located in subsets 1 and 2 for 2,000 time steps during the transformations. The displacements are represented by red-coloured line strips indicating the traces of past atom positions. We see the transformations evolve by lattice shear along invariant lines which are visualised by dashed lines. Atoms located along these lines keep their positions. All other atoms are displaced proportionally to their distances to the invariant lines. We see the primary nucleus is attached to an invariant [10] line to its right. The subset atoms are gradually sheared downwards. The secondary nucleus is intersected by an invariant [01] line. To the left, atoms are sheared upwards and downwards to the right.

Figure 4.18b and c show the components of the atomic trajectories of the subset atoms into the shear direction (b) and into the conjugate direction (c). These two diagrams confirm the shear components incorporate more significant information, than the conjugate direction. Hence we shall focus attention to the shear components. The transformation is initiated by correlated motions of a group of atoms for a short period of time. These correlations are required for finding and passing the transformation path which is connecting the two phases. We study the atomic trajectories in detail to understand this event.

Figure 4.17 shows the potential energy of the three subsets as function of time. Dropping potential energy curves indicate martensitic transformations; vertical dashed lines indicate the onset instants: for subset 1 this occurs after ca. 4,000 time steps and for subset 2 after ca. 6,000 time steps. Note that the progress of the potential energies of subsets 1 and 2 do not exhibit any significant potential energy barrier! We conclude the free energy nucleation barrier in fact is solely entropic in this material.

In the subsequent analysis we shall confine the information contained in the atomic trajectories delivered by the MD simulation program. We gradually restrict the vibra-

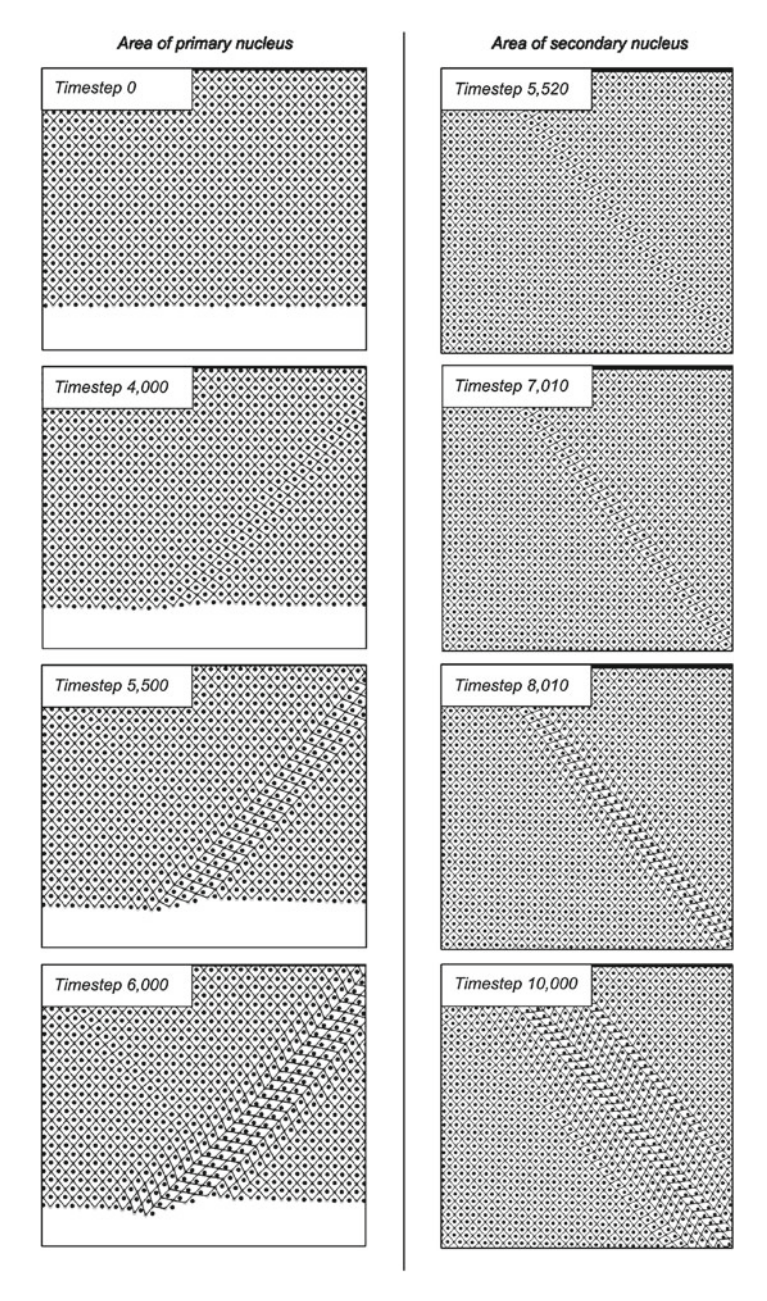


Fig. 4.15 Lattice representation of regions exhibiting nuceations. The parent phase is premartensite, indicated by slightly sheared squares but missing sublattice shuffle. In contrast, martensite exhibits a clear and distinctive shearing and sublattice shuffling

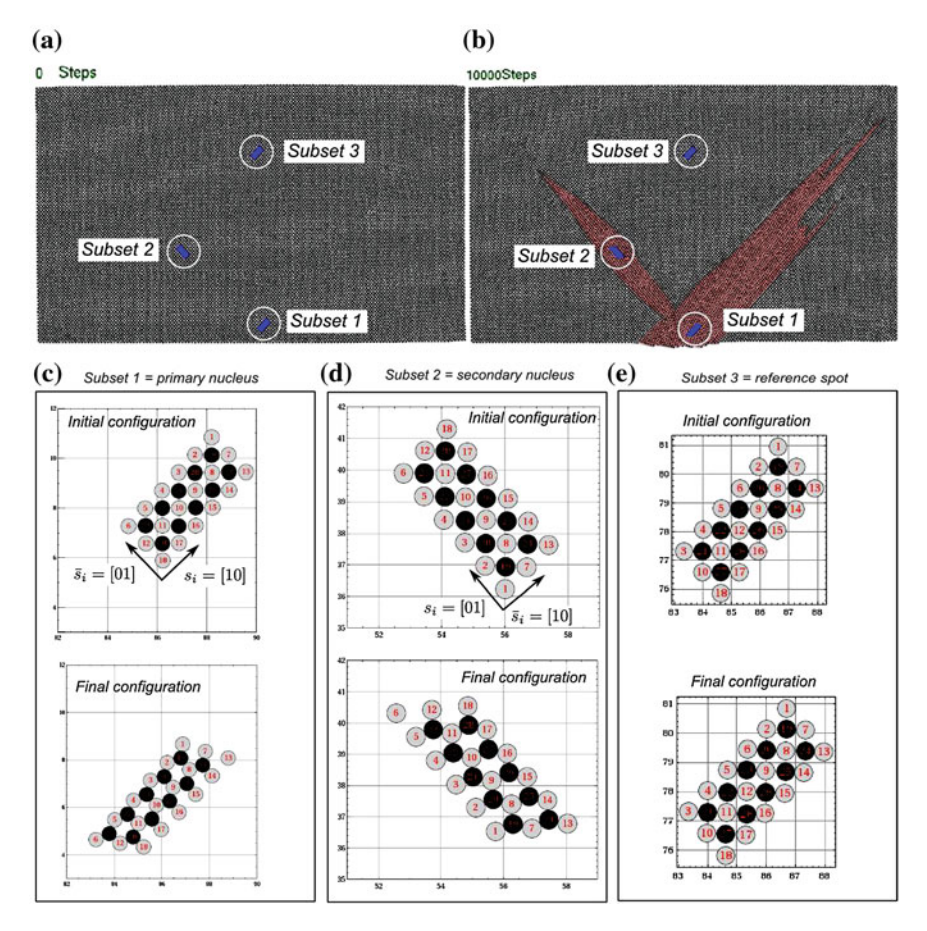


Fig. 4.16 Locations of the primary and secondary nucleation centre in the initial (a) and final (b) configuration of the crystal. A third subset (not undergoing the transformation) is defined for purpose of reference

tional modes by low-pass filtering and employ correlation methods for the sake of clear and instructive representations. Similar methods are known in the framework of nonlinear signal theories, see e.g. [10, 11].

4.3.4 Frequency Analysis

The frequency spectra of the vibrational atomic motions $\mathbf{x}_{\alpha}(t)$ are investigated using discrete Fourier transformations. For this purpose, we transform the periodically recorded trajectories into the frequency domain representation in the Fourier space. The trajectories are recorded for $T = 10,000 \tau_0$ seconds, equally discretised into

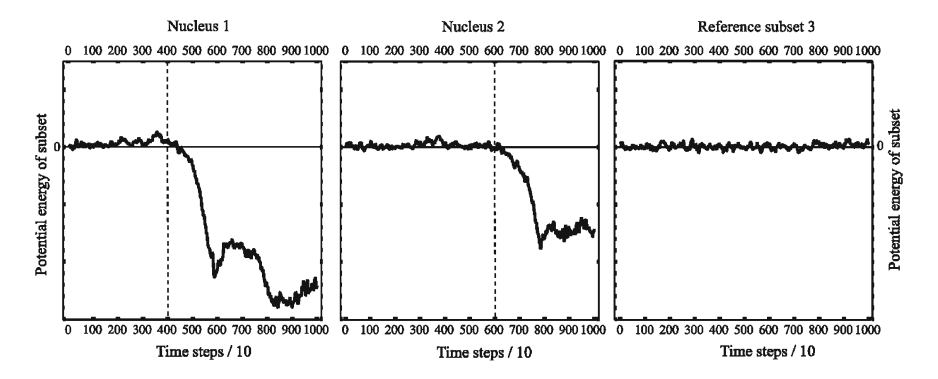


Fig. 4.17 Potential energies of the three subsets. Subset 1: Primary nucleation centre, subset 2: secondary nucleation centre, reference subset 3. Lattice transformations are indicated by dropping potential energies. There is no significant potential energy barrier visible with this model material. The nucleation is hindered entropically

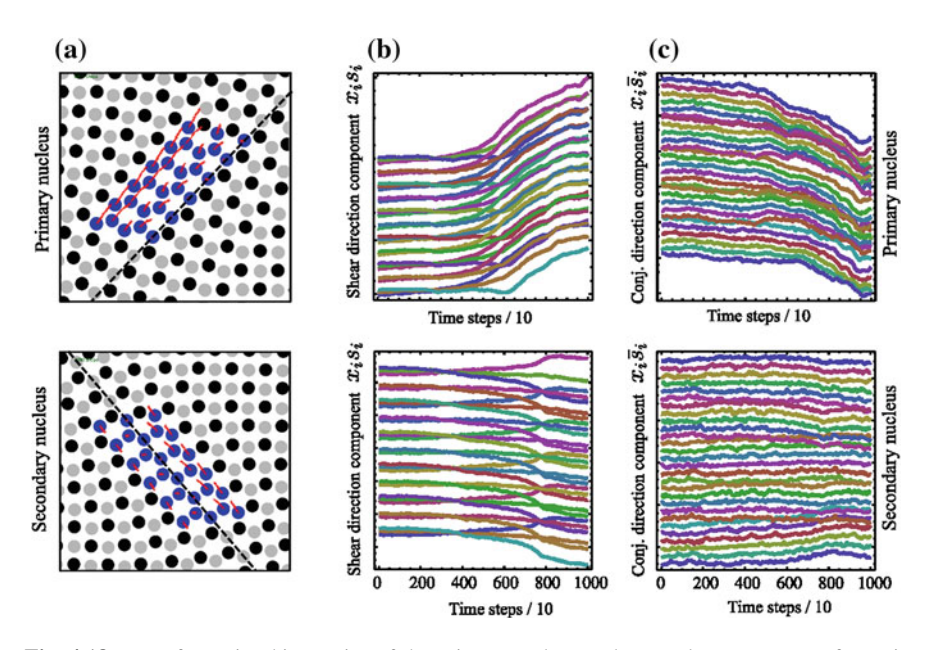


Fig. 4.18 Transformation kinematics of the primary and secondary nucleus. **a** Traces of atomic displacements during 2,000 time steps. Invariant shear lines are marked by *dashed lines*. **b** Shear direction components of motions, **c** conjugate direction components (Video available online)

v=1,000 intervals of width $\Delta t=10\,\tau_0$ seconds. We denote these discrete nodes by $\mathbf{x}_I^\alpha=\mathbf{x}_\alpha(I\,\Delta t)$ and calculate the spectral Fourier coefficients of atom α , denoted by \mathbf{X}_K^α ,

$$\mathbf{X}_{K}^{\alpha} = \sum_{I=0}^{\nu-1} \mathbf{x}_{I}^{\alpha} \exp(-\iota \ \omega_{I} K) \quad (K = 0, 1, \dots, \nu - 1) = \mathcal{F}(\mathbf{x}_{I}^{\alpha}), \tag{4.9}$$

where $\omega_I = I \, 2\pi / v$ denotes the *I*th discrete frequency of the Fourier spectrum. In the present case, this spectrum is resolved by intervals of $\Delta \omega = 0.157$ THz. The reverse transformation is given by

$$\mathbf{x}_{I}^{\alpha} = \frac{1}{\nu} \sum_{K=0}^{\nu-1} \mathbf{X}_{K}^{\alpha} \exp(\iota \ \omega_{K} I) \quad (I = 0, 1, \dots, \nu - 1) = \mathscr{F}^{-1}(\mathbf{X}_{K}^{\alpha}). \quad (4.10)$$

 $(\omega_K = K \, 2\pi/v)$. It is possible to restrict the Fourier transformation (4.9) to a selected time window $(t_{\rm end} - t_{\rm start})$, chosen sufficiently large to represent the oscillatory properties of the trajectories. Such window, moved along the time axis, may be used to screen the Fourier spectra as function of time, yielding time/frequency analyses. Alternatively, the reverse Fourier transformation (4.10) may be restricted to selected frequency ranges $(\omega_{\rm end} - \omega_{\rm start})$, which effectively models the application of frequency filters. In this case, the reverse transformation yields trajectories which exhibit the properties of the selected frequency modes only. We shall use both methods in the subsequent discussion.

Low-pass frequency filtering is applied to the trajectories of atomic positions and velocities in order to represent their tendencies. The zeroth frequencies representing the mean lattice sites—are always neglected in order to focus on the vibrational properties of the low-frequency band $\omega_2 \dots \omega_{10}$. Figure 4.19 shows the results for the primary nucleus and Fig. 4.20 for the secondary nucleus. In these two figures the shear-direction components of positions and velocities are shown in (a) and the conjugate components in (b). Squares of these quantities are plotted in order to augment the differences. Both figures exhibit distinct signatures in the shear directions, which are missing in the conjugate directions. We see within the selected frequency range, the atomic trajectories group according to their relative position to the invariant shear lines (Fig. 4.18a). The atom numbers indicated refer to their positions shown in Fig. 4.16 on p. 110. The onset of the transformations can be nicely recognised. The low-passed velocity signals indicate transformation-related drifts similar to the mesoscopic velocities of the interaction neighbourhoods discussed above. During the transformation we observe accentuated amplitudes; the onset of the transformations can be identified at the bases of these amplitudes, indicated by vertical dashed lines in the figures. No significant signal is visible for the components of the conjugate directions (b) except for some dispersion at the end of the graphs, which is due to latent-heat-related thermal activity of the atoms.

Cross-correlation representations of the low-pass filtered trajectories of Figs. 4.19 and 4.20 may be used to identify and accentuate the degree of correlated motions between the atoms. Here, we employ the correlation sum given in [11] as appropriate correlation measure,

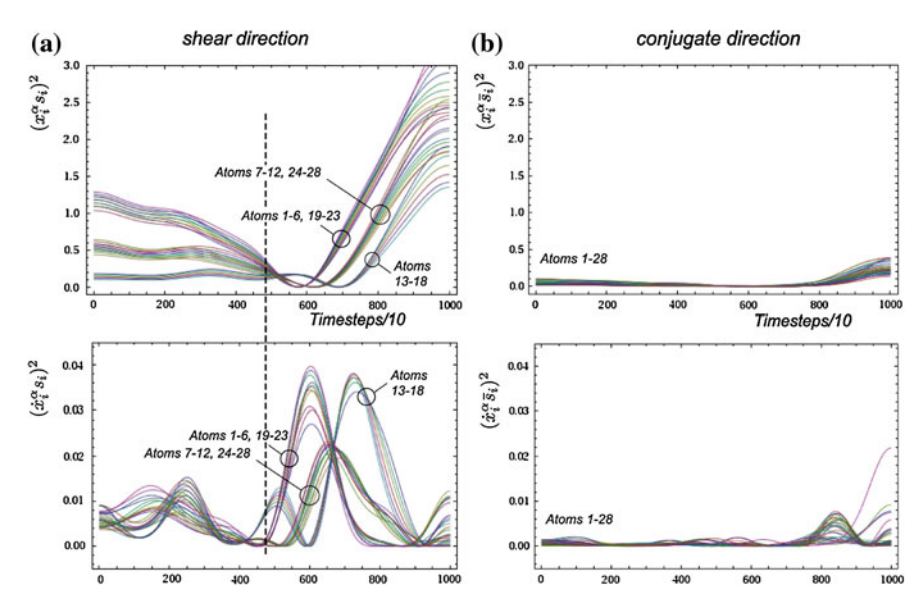


Fig. 4.19 Low-passed atomic trajectories (top) and velocities (bottom) of the primary nucleus. Frequency range $\omega_2 \dots \omega_{10}$. We plotted squares of these quantities in order to augment the details. a Shear direction components, **b** conjugate direction components. (Colour online)

$$\mathscr{C}(\varepsilon,t) = \frac{1}{N_S^2} \sum_{\alpha,\beta} \mathscr{H}\left(\varepsilon - \left| (\mathbf{x}_{\alpha}(t) - \mathbf{x}_{\beta}(t)).\mathbf{s} \right| \right). \tag{4.11}$$

 N_S denotes the number of atoms in the respective subsets and \mathscr{H} is the Heaviside step function. The sum counts the number of position pairs which are spaced no more than ε . Figure 4.21 shows the respective graphs for the two subsets as function of time for given parameter $\varepsilon=0.01$. The peaks indicate highly correlated atomic motions during the transformations. Their bases indicate the onsets of the transformation (vertical dashed lines). These define the instants of nucleation.

Next we investigate time/frequency representations of the atomic oscillations at the nucleation centres. For this purpose, we focus attention to four selected atoms located in the respective subsets 1, 2 and 3 and analyse the Fourier spectra during three consecutive time windows each. The widths of these windows span $\nu=333$ recorded time steps, see Figs. 4.22, 4.23, 4.24. In these figures, diagrams are arranged so as to display the respective time windows by columns. The first row (a) shows the shear-direction components of the atomic trajectories for frequencies above ω_{10} , representing the medium to high-frequency bands of the original data. These functions incorporate correlated oscillation modes during the transformations, which for the primary nucleus occur during 334–667 steps in Fig. 4.22 and for the secondary nucleus during 668–1,000 steps in Fig. 4.23. We do not expect such correlation signature for the non-transforming reference subset 3 in Fig. 4.24.

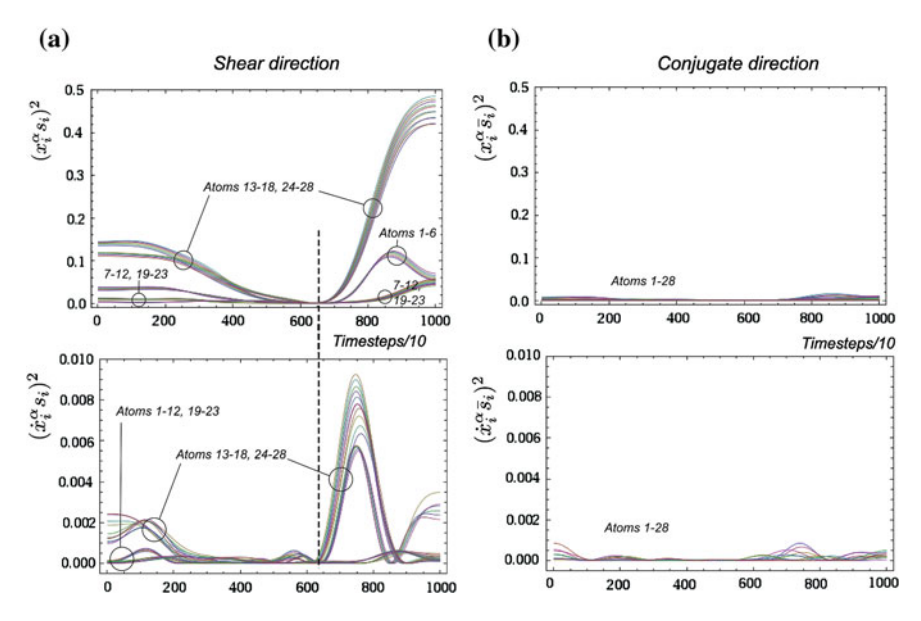


Fig. 4.20 Low-frequency range $(\omega_2 \dots \omega_{10})$ of positions (top) and velocities (bottom) of the secondary nucleus. Squares of these quantities are plotted in order to augment the details. a Shear direction components, **b** conjugate direction components. (Colour online)

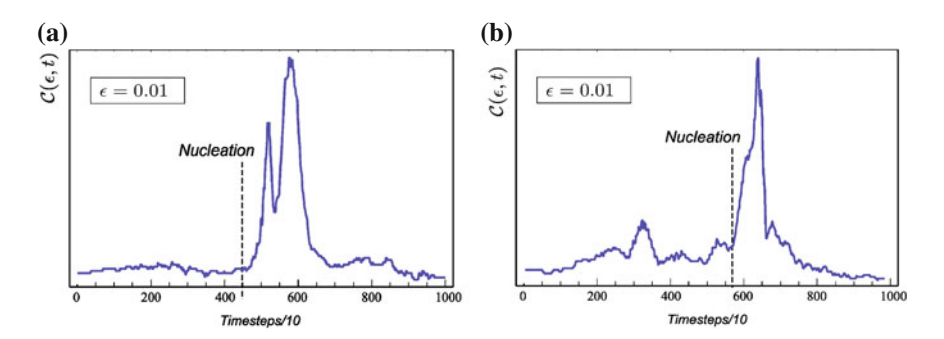


Fig. 4.21 Correlation sums of atomic motions at the nucleation centres of the primary (a) and the secondary (b) nucleation as calculated from Eq. (4.11). The peaks visible in the graphs indicate highly correlated atomic motions during the transformations. The onsets base of these peaks indicate the nucleations indicated by dashed lines. The plots are based on low-frequency filtered signals $(\omega_2 \dots \omega_{10})$

To detect correlated oscillation modes we employ a method similar to the autocorrelation integral used in signal theory for extracting low-frequency signals from high-frequency "noise". The cross-correlation function used here reads

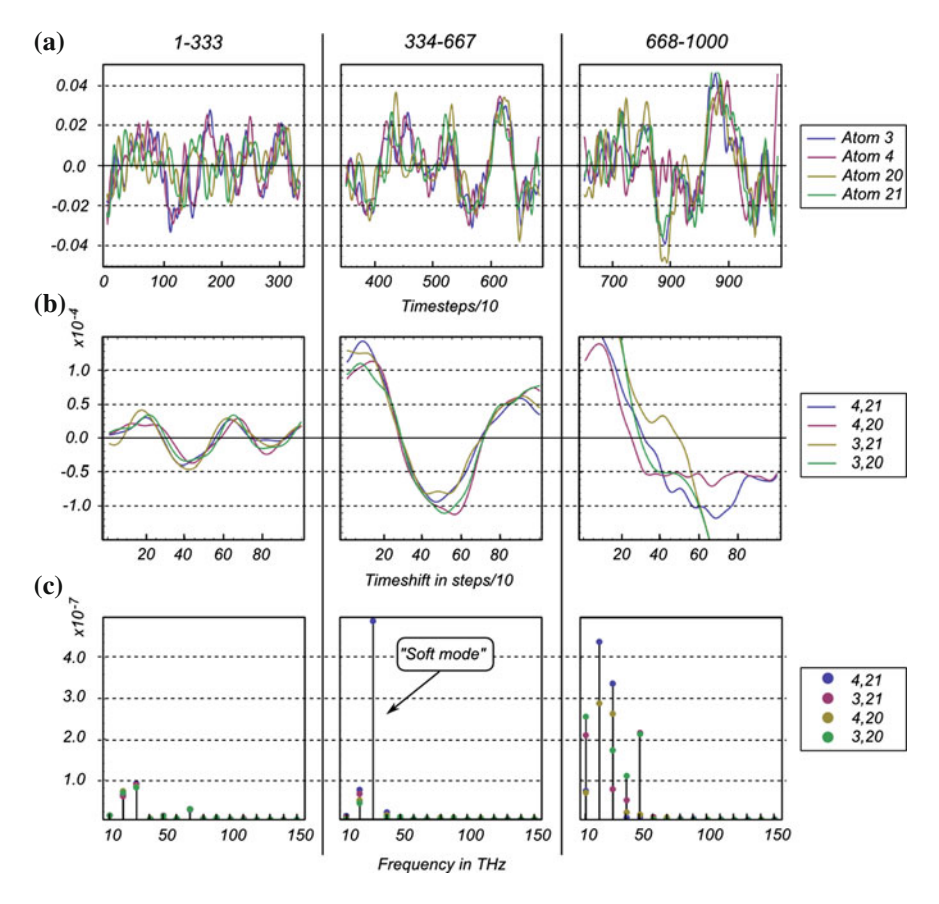


Fig. 4.22 Time/frequency analysis of selected atoms located in the primary nucleus. Columns indicate three subsequent time windows 1–333, 334–667 and 668–1,000 recorded time steps. Row **a** Shear-direction component of the trajectories of four selected atoms (numbers 3, 4, 20 and 21 of subset 1, cf. Fig. 4.16 on p. 110). Unfiltered signals, corrected mean lattice positions. Row **b** Four cross-correlation functions of the trajectories given in row **a** according to Eq. (4.12). Row **c** Frequency domain representations of the cross-correlated signal shown in row **b**. (Colour online)

$$\mathscr{R}_{\alpha\beta}(\tau) = \int_{t} x_i^{\alpha}(t) x_j^{\beta}(t+\tau) s_i s_j \, \mathrm{d}t. \tag{4.12}$$

Note only shear-direction components $(x_i^{\alpha}s_i)$ and $(x_j^{\beta}s_j)$ of the trajectories are considered, which incorporate the transformation-related signatures, as we have seen in Figs. 4.19 and 4.20. This integral in Eq. (4.12) correlates the trajectories of atom α at time t to the trajectories of atom β at time $t + \tau$. The results are shown for selected atom pairs in the rows (b) of Figs. 4.22, 4.23, 4.24, referring to the respective time windows. Inspection of these graphs shows that the cross-correlation has

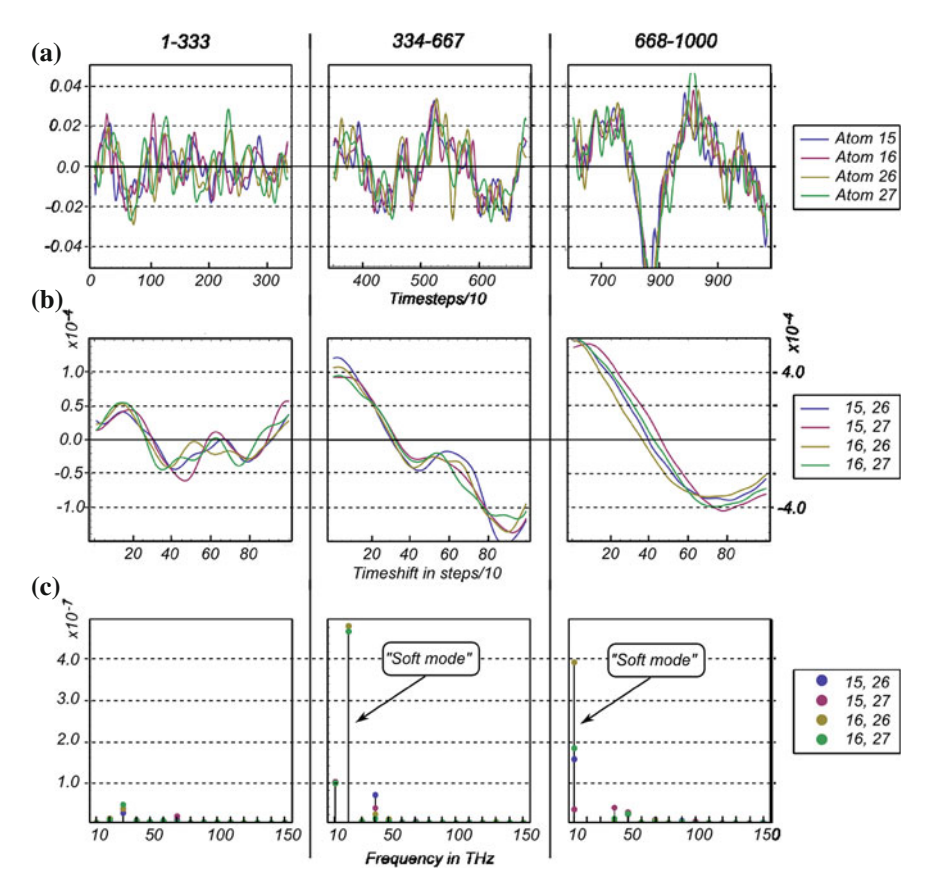


Fig. 4.23 Time/frequency analysis of selected atoms located in the secondary nucleus. Columns indicate three subsequent time windows 1–333, 334–667 and 668–1,000 recorded time steps. Row **a** Shear-direction component of the trajectories of four selected atoms (numbers 15, 16, 26 and 27 of subset 1, cf. Fig. 4.16 on p. 110). Unfiltered signals, corrected mean lattice positions. Row **b** Four cross-correlation functions of the trajectories given in row **a** according to Eq. (4.12). Row **c** Frequency domain representations of the cross-correlated signal shown in row **b**. (Colour online)

eliminated high-frequency fluctuations in order to augment the medium-frequency modes common the atom pair's trajectories.

The last rows (c) of Figs. 4.22, 4.23, 4.24 show the frequency spectra of the correlated signal plotted in the rows in (b). We see that for time windows spanning the transformation processes, the spectra exhibit significant, discrete amplitudes. This observation confirms that the transformation events are accompanied by specific, correlated oscillation modes, indicated by these large amplitudes. These modes induce the shear/shuffle motion of the atoms eventually producing martensite. Therefore, these modes are called the "soft modes". A soft mode is the property of a group of atoms, rather than of a single atom. In the figures, the soft modes of the primary nucleus (Fig. 4.22c, 334–667 steps) and the secondary nucleus (Fig. 4.23c, 334–1,000

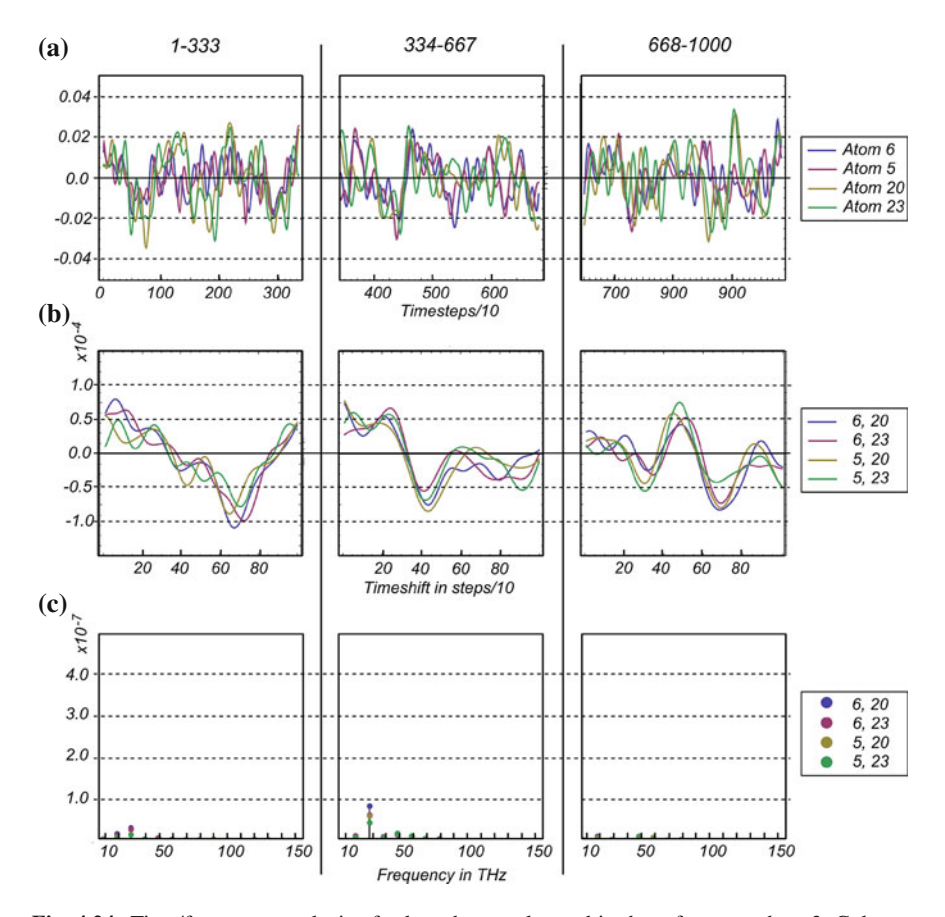


Fig. 4.24 Time/frequency analysis of selected atoms located in the reference subset 3. Columns indicate three subsequent time windows 1–333, 334–667 and 668–1,000 recorded time steps. Row **a** Shear-direction component of the trajectories of four selected atoms (numbers 5, 6, 20 and 23 of subset 3, cf. Fig. 4.16 on p. 110). Unfiltered signals, corrected mean lattice positions. Row **b** Four cross-correlation functions of the trajectories given in row **a** according to Eq. (4.12). Row **c** Frequency domain representations of the cross-correlated signal shown in row **b**. (Colour online)

steps) are indicated. Soft modes are missing in the reference subset 3 (Fig. 4.24c) and also in the time windows of subset 1 and 2 before the nucleation events, where the correlation of the atoms is too weak to induce a martensitic transformation. The last time window of subset 1 (Fig. 4.22c, 668–1,000 steps) indicates the dissipation process of the correlated motions into random thermal vibrations at larger amplitude after the transformation has finished locally. The atomic vibrations still exhibit decaying amplitudes and the spectrum is widening, meaning higher frequency modes are activated gradually during the dissipation process.

Figure 4.25 illustrates the normal mode spectra of the atoms in the subset 1 and 2 during the respective nucleation events by plotting the normal amplitude vectors

at the positions of the respective atoms. In these Figures, thermal fluctuations are represented by randomly directed arrow heads while the soft modes are indicated by aligned vector bundles pointing into the direction of the transformation path. Inspection shows these directions coincide with the shear/shuffle displacements of the atoms. We see the soft modes are indicated by large amplitudes and by significant correlation. Note that the normal mode bundles of type-A atoms (blue arrows) and of type-B atoms (red arrows) are slightly deviating, reflecting the shuffling of the respective sublattices during the transformation.

4.3.5 Phase Space Analysis

We have seen that the nucleation is indicated by local correlations of atomic trajectories. These correlations bring about soft modes, which can be represented by coherent, large-amplitude oscillation modes pointing into discrete directions, the directions of the transformation paths. These paths connect the parent and product configurations of the lattice. Different variants of martensite may be formed from the parent lattice and accordingly, there are as many transformation paths. We proceed to explore the phase space properties of those paths selected by the two nuclei. Because the phase space of the N_S atomic subsets is 2 N_S -dimensional, we have to confine the information to scalar quantities in order to visualise it. We suggest to employ the related potential and kinetic energies of the atoms for this purpose. We confine this information with respect to the low-frequency band $(\omega_2 \dots \omega_{10})$ of the shear-direction components of the atomic trajectories. Figures 4.26 and 4.27 show the results for the two nuclei. The phase curves are parametric in time as indicated in the diagrams. Since type-A and type-B atoms follow different energetic paths according to the L-J interaction parameters chosen, it is useful to plot their respective phase curves into separate diagrams. We see the potential energy is lower in the product phase for individual type-A atoms (a), while for individual type-B atoms (b), the potential energy is lower in the parent phase. The respective mean values are indicated by dashed lines. We see that the phase curves fluctuate about these mean values. The fluctuations are always larger in the product phase reflecting enhanced thermal activation due to release of the latent heat. The transformation is indicated by branches of the phase curves which connect the respective mean lattice positions in parent and product phase. For the primary nucleus, the respective branches fall into the time interval of ca. 450-600 steps (cf. Fig. 4.26) and for the secondary nucleus into the time interval of ca. 600-800 steps (cf. Fig. 4.27). Along these branches, the kinetic energy is drastically increasing, indicating accelerations of the atoms during the transformation. This energy is dissipated afterwards. During this transition branches, the lattice potential energies drop (cf. Fig. 4.17 on p. 111). In order to get this happening, the atomic trajectories must correlate in order to build up the soft mode. In the phase space, this correlation is indicated by converging phase curves within a narrow region indicated as "nucleation channels" in Figs. 4.26 and 4.27. These channels represent the transformation paths in phase space. We see them more

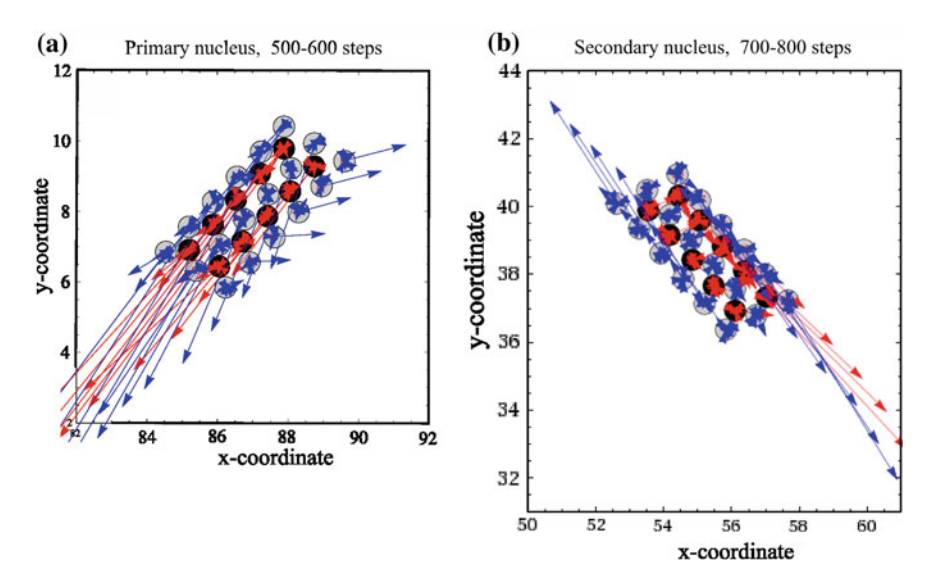


Fig. 4.25 Spectral analysis of the atomic motions in the primary (**a**) and the secondary (**b**) nucleus. *Arrows* represent normal amplitude vectors. Soft modes are indicated by large amplitudes and significant alignments of these vectors. Type A atoms: *grey points*, *blue arrows*; type B atoms: *black points*, *red arrows*. Compare to Fig. 4.18 on p. 111

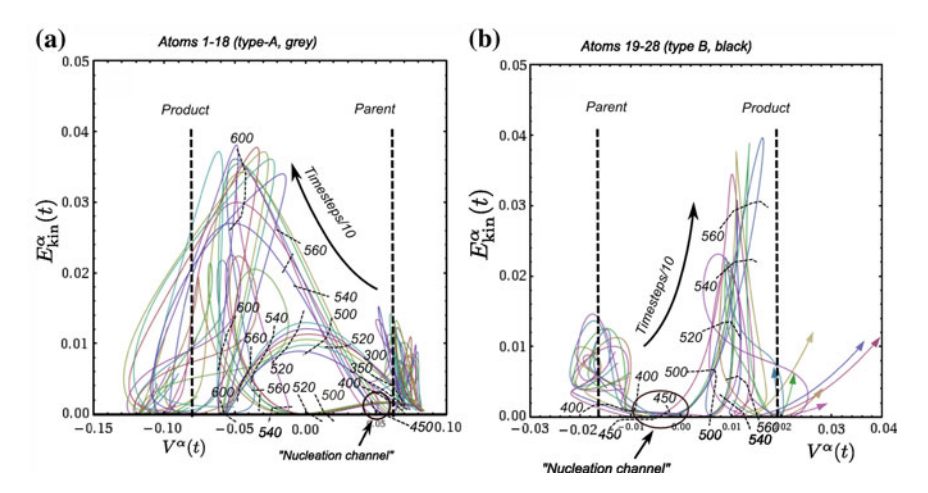


Fig. 4.26 Phase space representation of the primary nucleation process: kinetic energy versus potential energy of the subset atoms. **a** Type-A atoms; **b** type-B atoms. The potential energies V^{α} are due to Eq. (3.2) and $E^{\alpha}_{\rm kin} = m_{\alpha} \dot{\mathbf{x}}^{2}_{\alpha}/2$, both are low-pass filtered

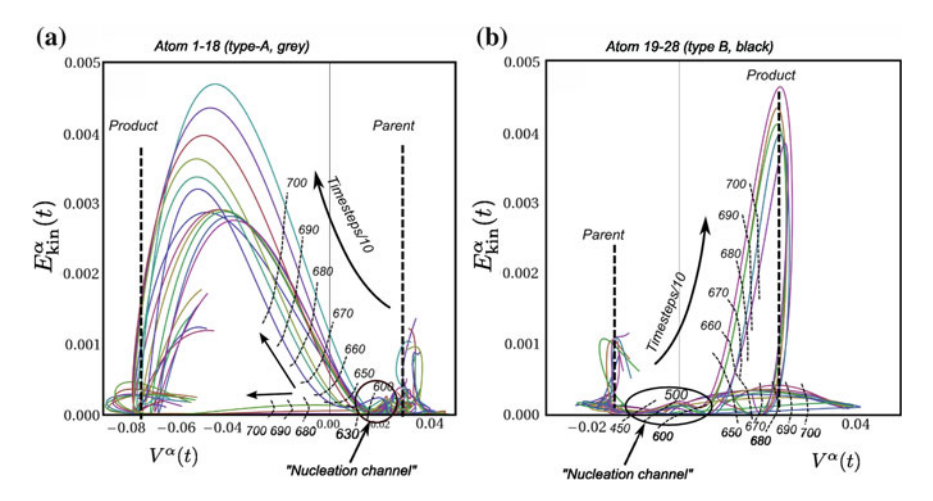


Fig. 4.27 Phase space representation of the secondary nucleation process: kinetic energy versus potential energy of the subset atoms. **a** Type-A atoms; **b** type-B atoms. The potential energies V^{α} are due to Eq. (3.2) and $E_{\rm kin}^{\alpha} = m_{\alpha} \dot{\mathbf{x}}_{\alpha}^2/2$, both are low-pass filtered. (Colour online)

distinct for the type-B atoms, cf. Figs. 4.26b and 4.27b, but they are also present for the type-A atoms. Inspection of these two type-B diagrams shows these channels are entered some time steps *before* the kinetic energy increases and the potential energy decreases. This indicates the atomic trajectories are already correlated, *before* the lattice transformation can be morphologically detected. We conclude that the correlation of the atomic oscillations is a necessary condition and, in fact, is the defining property of the nucleation process.

4.3.6 Entropic Nucleation Barrier

Based on a MD computer experiment we have investigated the nucleation processes in the 2D model material. The test crystal was established carefully in an undercooled and mechanically relaxed state. The interaction parameters were selected such that at this state, no potential energy barrier is hindering the lattice transformation and consequently the nucleation barrier is solely entropic by nature.

The nucleation processes evolve in absence of any exterior stimulation as "natural" solutions of the equations of motion. Two nucleation events are spotted which appear in temporal sequence, the first one close to the free surface of the crystal (primary nucleus) and the second one in the bulk (secondary nucleus). Atomic subsets at the nucleation centres are defined. Their trajectories are analysed in detail. We see that in both cases, the nucleation is indicated by spontaneous correlations of the trajectories, building up the soft modes. Soft modes therefore represent a collective property of

the atoms at the nucleation centre. In the phase space, this process is indicated by temporal convergence of the atomic phase curves into narrow nucleation channels.

We may interpret our findings in the framework of the probabilistic interpretation of entropy. We have shown on p. 70 that the parent phase provides higher configurational entropy and therefore, it is entropically preferred. At equilibrium it is possible to harmonically approximate the atomic oscillations (Einstein crystal) and this holds true for both phases, parent and product. This assumes the atomic trajectories are completely uncorrelated such that each atom may explore its individual subvolume in the phase space independently from the others. For the parent phase, this assumption holds true as long as temperature is sufficiently high and the atoms are thermally very active. In the high-T regime, thermal vibrations prevent atomic correlations on the microscale and consequently the narrow nucleation channel in phase space is not entered by a sufficiently large number of atoms at the same time. In an undercooled regime, however, the thermal fluctuations are diminished. In this setting, the atomic oscillations may gradually correlate to allow the atoms to test the potential energy landscape collectively, eventually discovering the nucleation channel connecting the phase space regions of parent and product lattice. Therefore, the entropic nature of the nucleation barrier may be interpreted as the probability for a group of adjacent atoms of finding the nucleation channel in the phase space. This must be regarded as a rare event and therefore, the nucleation is hindered even in situations where the potential energy does not effectively contribute to the nucleation barrier.

This explains why the crystal does not collapse spontaneously into martensite after the simulation is started. Also, we understand why the nucleation is preferably observed at interfaces: In such places, the respective interface energy restricts the atomic motions slightly such that parts of the phase space are inaccessible for the atoms a priori. Therefore, finding the nucleation channel is more probable for a group of atoms in these places, than in places where the atomic motions are unrestricted. Therefore, the probabilistic—entropic—nucleation barrier may be lowered by constraints affected by interfaces.

4.4 Tensile Testing in the Pseudo-Elastic Regime

4.4.1 Simulation Procedure

The model material may be investigated by simulated tensile tests subject to load and displacement control modes. We define two lateral gripping zones (sketched in Fig. 4.28) at which external forces are applied as a function of time and measure the resulting displacement of the gripping zones (load control mode). Alternatively, the atoms located in these zones may be designated positions which change in time in order to adjust the overall displacement. In this case, the average interaction forces which all the remaining atoms exert on the gripped atoms are measured (displacement control mode). No constraints are set with respect to the atoms located between the gripping zones; these may freely adjust their trajectories to the mechanical conditions

Thermostat: Temperature control

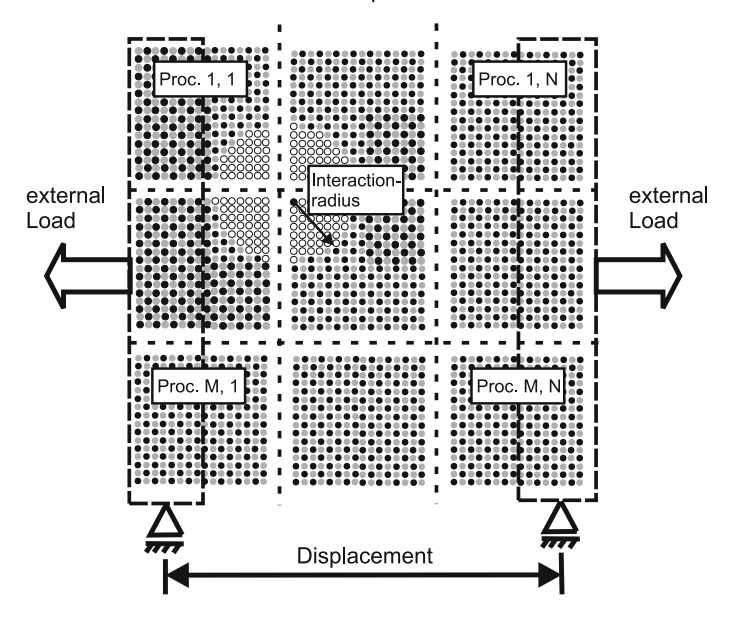


Fig. 4.28 Model set-up for numerical tensile tests

set by the grips and to the temperature, the latter being controlled by the method of velocity scaling and relaxation explained on p. 42.

Sometimes it is advantageous to stabilise the gripping zones by setting the cross-species interaction parameter ε_{AB} of the gripped atoms to a slightly higher value compared to those of the free atoms; thus stabilising the austenite at the grips. Also, we may restrict the translatory degree of freedom of the gripping zones. Under load control, vertical motions of the gripping zone may be suppressed, hence modelling a "horizontal sliding-bearing". Under displacement control, we control the atom's horizontal positions in the gripping zone but vertical motions may be allowed in order to reduce undesired bending moments that might build up during phase transformations ("vertical sliding-bearing").

Time- and length-scale issues place technical constraints for computer experiments of tensile testing. Any small load increment affects the fully dynamic response of the ensemble. The loading signal applied to the grips propagates as a stress wave into the bulk at the speed of sound. In a complex oscillatory process, the signal is dissipated and, after sufficient relaxation time, the atoms adjust their mean positions to the global constraints. Under adiabatic conditions, this process resulted in an increase in temperature since part of the mechanical energy introduced into the system by the grips is dissipated into heat. Isothermal conditions are maintained by the applied thermostat, which removes the dissipated component of the induced mechanical energy. An extensive investigation of the relaxation times as a function of the system size were provided by Dreyer, Herrmann et al. [12–14] for 1D atomic chains. For the 2D ensemble, we have to rely on heuristic analyses. In all cases,

Interaction parameters	
A–A interactions	$\varepsilon_{A-A} = 1.2 \varepsilon_0$
B–B interactions	$\sigma_{\mathrm{A-A}} = 0.89 \sigma_0$ $\varepsilon_{\mathrm{B-B}} = 0.61 \varepsilon_0$ $\sigma_{\mathrm{B-B}} = 0.89 \sigma_0$
A–B interactions	$\varepsilon_{A-B} = \begin{cases} 0.223 - 0.225 \varepsilon_0 & \text{(bulk atoms)} \\ 0.35 \varepsilon_0 & \text{(gripping zone)} \end{cases}$
	$\sigma_{A-B} = 0.6 \sigma_0$
Other parameters	
A mass	$m_{\rm A} = 1.0\mu_0$
B mass	$m_{\rm B}=1.0\mu_0$
Time step	$\Delta t = 0.01 \tau_0$
Cut-off radius	$r_c = 4.0 \sigma_0$

 Table 4.3 Common simulation parameters for simulations of tensile tests

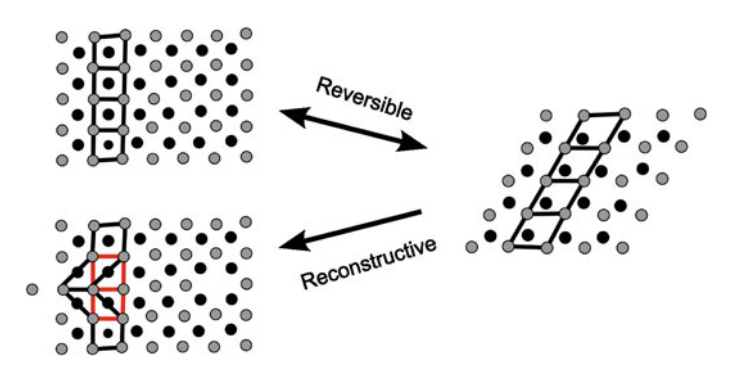


Fig. 4.29 Schematic drawing of two reverse transformation mechanisms. (Colour online)

we use small loading increments and allow sufficient relaxation times, at constant load, between two consecutive load increments in order to approximate quasi-static conditions as best as possible.

The model material is investigated in both the pseudo-elastic regime at high temperature and the pseudo-plastic regime at low temperature. The common model parameters are given in Table 4.3. More case-specific parameters are provided in the corresponding discussions below.

4.4.2 Load Control Mode

4.4.2.1 90,000-Atoms

We select the temperature of the thermostat to be 800 K in order to investigate large crystals in the pseudo-elastic regime, where the assembly is austenitic in the

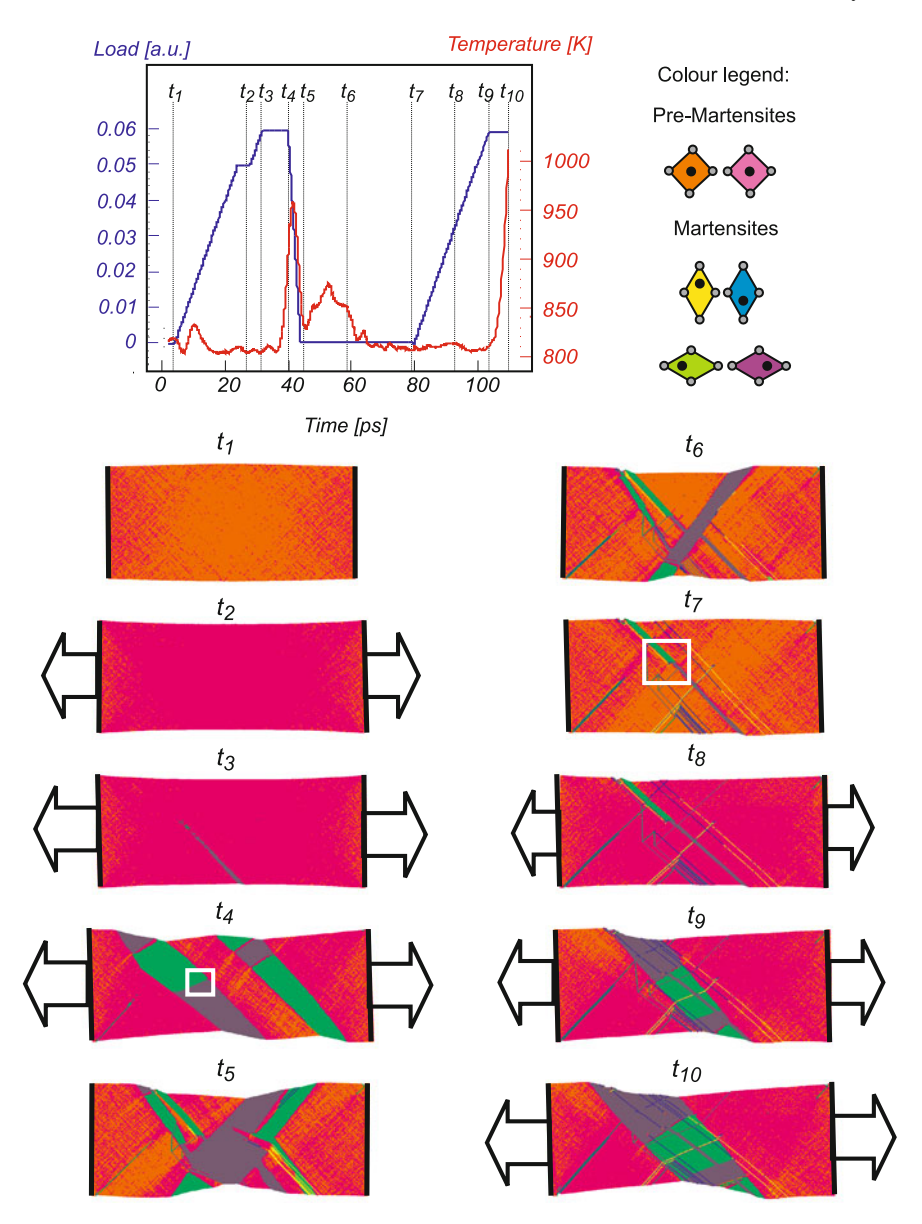


Fig. 4.30 Loading–unloading–loading cycle in a pseudo-elastic 90,000-atom assembly. Load control mode. The framed areas at times t_4 and t_7 are detailed in Fig. 4.31 (Video available online)

unloaded state. The first sample studied is a 90,000-atom rectangular-shaped strip. It is investigated subject to a cyclic tensile test under load control mode, see Fig. 4.30. The diagram in Fig. 4.30 shows the evolution of the external load and the temperature

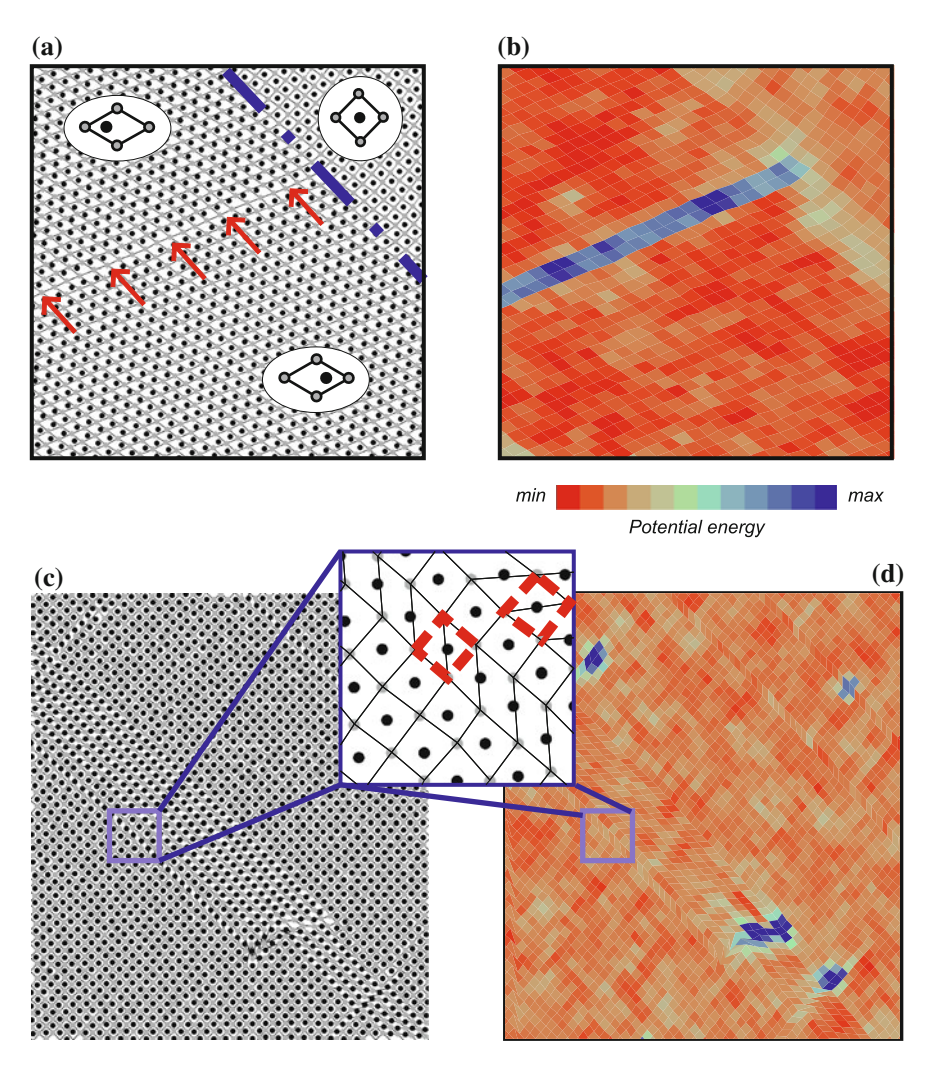


Fig. 4.31 Microstructural details and potential energies. Load control mode. **a**, **b** Refer to the framed area of Fig. 4.30(t_4) and **c**, **d** to the framed area of Fig. 4.30(t_7) (Video available online)

as function of time. Microstructural details are presented in Fig. 4.31. Below the diagram of Fig. 4.30, ten snapshots of the bar assembly are shown, referring to the times t_1 – t_{10} indicated in the diagram. We employ the same colour representation of the morphology introduced earlier, where orange and pink represent two variants of pre-martensite and yellow, blue, green and purple indicate the four generic variants of martensite. As before, the unit cells are defined and mapped to the lattice in the initial state where they form an ideal, nested square lattice. We refer to this state as

the reference lattice. The colour coding of the martensite is due to an analysis of the actual shapes of unit cells which are defined in the reference lattice.

Owing to the surface tension effects, the unloaded, austenitic strip exhibits a slight bulging visible at t_1 . This strain and thermal activation causes the unit cells to fluctuate about their square shapes, thus being identified with pre-martensite by the colouring algorithm. The application of a small load causes all the unit cells (with the exception of some near the grips) to shift into the favoured pre-martensite variant, pink coloured at t_2 . Accordingly, the overall strip is slightly elongated. Upon further loading, the MT load is reached at t_3 , when the first martensite nucleus is formed at the strip's mid-length on the lower surface. This nucleation event is immediately followed by a second one on the upper surface. The two nuclei spread as needles through the specimen and then proceed to grow laterally. These growth processes allow a significant macroscopic lengthening of the strip and a temporary increase in the temperature, owing to the release of latent heat, which is ultimately compensated by the thermostat.

Figure 4.31a exhibits the microstructural details within the framed area, indicated in t_4 , and Fig. 4.31b shows the corresponding potential energy field. Axial loading favours the formation of the martensite variants shearing in the direction of the load. Among the four generic martensite variants of Fig. 3.3c, two possibilities exist having the same shear; these are coloured green and purple in Fig. 4.30, which are distinguished by the shuffle directions of their sublattices. Both variants nucleate spontaneously and form homogeneous martensite domains. The interface between the domains is a single line of atoms, marked by red arrows in Fig. 4.31a. The interface with the parent phase is indicated by a blue broken-dotted line in this figure. The potential energy field in Fig. 4.31b shows that both the martensite/martensite and the martensite/parent interfaces exhibit interfacial energies. The potential energy of the martensite is lower than that of austenite, corresponding to the set interaction parameters. Again, the latter is not atomically sharp, rather it is represented by a narrow (3–4 unit cells width) transformation zone where the lattice is smoothly bent from one phase into the other. This observation coincides with the austenite/martensite transformation zone observed in the temperature-induced MT simulations discussed in Sect. 4.1 on p. 87 ff.

At t_4 , the loading is terminated and the strip is quickly unloaded. The load relaxation is accompanied by some further, momentary transformation processes (visible at t_6), after which the reverse transformation process starts (t_{5-7}). The reverse transformation is completed at time t_7 , when the strip has macroscopically returned to its reference shape and the thermostat has completely compensated the thermal effects. However, microscopically the lattice has changed.

Bhattacharya and co-workers [15] have pointed out that since the hexagonal lattice does not lie in the Ericksen–Pitteri neighbourhood of the square, square-to-hexagonal phase transformations incorporate two fundamental mechanisms for the reverse transformation: reversible and reconstructive. These are sketched in Fig. 4.29. In reversible transformations, nearest neighbouring atoms are maintained such that reference austenite unit cells (black lines) maintain their shape during the reverse transformation. In reconstructive transformations, the reference unit cells are dis-

torted, as indicated by black lines in the lower of Fig. 4.29. However, the perfect square lattice is locally reconstructed with the atoms having different neighbours (red /grey lines). In the literature the terminology "lattice invariant shear" is sometimes used to describe the reconstructive retransformation. We avoid this terminology here because the dislocations produce irreversible defects hence leaving a "varied" lattice rather than an "invariant" one. The reconstruction produces point defects which either glide to the surface, forming a kink, or pile up at obstacles in the bulk material.

Both mechanisms are observed in our simulations, with a preference for the reversible type. However, it is the reconstructive type that prohibits full microscopic recovery to the reference lattice: reconstructive martensite/austenite (m/a) transformations involve lattice slip caused by dislocation movements. These dislocations can be generated in the bulk during retransformation and they move along the principal lattice directions towards the surface, at which they terminate. Along these slip directions, the reference cells are degenerated: although there is no line defect in reference to the original austenite, we can easily visualise the slip lines. Figure 4.31c magnifies an area of the reversibly recovered bulk material containing a bundle of slip lines. Along the slip lines, the square lattice is reconstructed (dotted red cells) but the reference unit cells are degenerated (solid black cells). The slip lines terminate at the surface where they generate kinks; this is particularly emphasised for the bundle of slip lines visible in Fig. $4.30(t_7)$. The dislocations which generated these slip lines have produced a localised lattice defect with significant surplus potential energy in Fig. 4.31d.

Since the algorithm used to produce the colour code in Fig. 4.30 is based on the original shapes of the reference cells, the slip lines are misleadingly coloured as martensite; however, the lattice is in fact square, as can be seen in the magnifications of Fig. 4.31c and d.

The simulation experiment continues by repeatedly loading the strip, see Fig. $4.30(t_{7-10})$. Upon reloading, new transformation processes preferentially nucleate at the loci of the defects produced by the slip lines of the previous transformation cycle, presumably because of local stress at those sites. For this reason, the evolution of the second transformation significantly differs from the first because of pre-existing nucleation sites produced by the reconstructive aspects of the m/a transformation.

4.4.2.2 262,144-Atoms

We present a second tensile test under load control mode in the pseudo-elastic regime, using a larger assembly of 262,144 atoms, see Fig. 4.32. In the following discussion, we refer to the times t_{1-4} indicated in the diagram of Fig. 4.32a. The model material is the same as that used in the previous example.

With the 262,144-atom strip, the nucleation of martensite is observed at a normalised load of 0.0325, which is kept constant between t_1 and t_3 . In contrast to the 90,000-atom strip, two crossing nuclei simultaneously appear forming an "X" in the centre of the strip at t_1 . As with the smaller strip, the axial load induces the

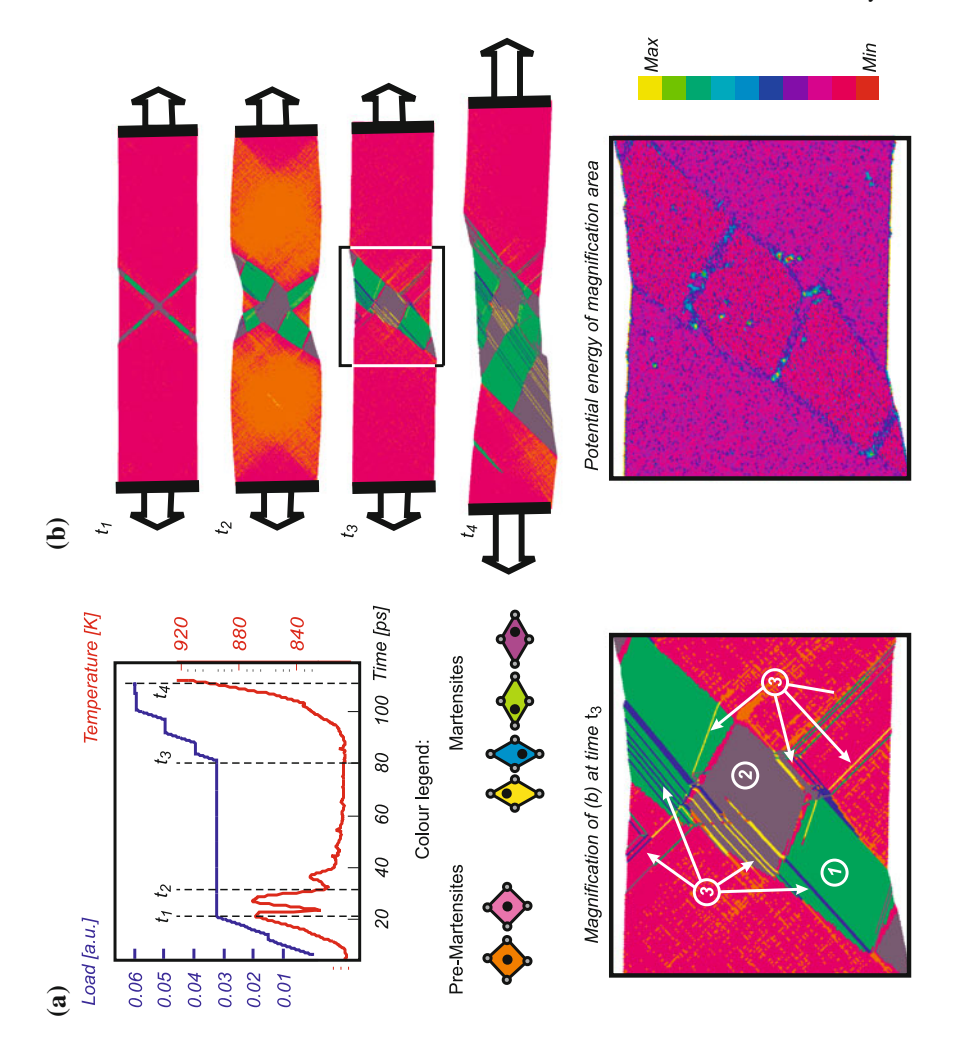


Fig. 4.32 Load-induced MT 262,144-atom strip. Load control mode. **a** Time evolutions of externally applied load and temperature. **b** Morphology at selected times. The two magnifications refer to time t_3 . (Side-view intended, Video available online)

nucleation of horizontally sheared martensite variants (green and purple coloured), which again form homogeneous domains. The nuclei grow laterally prior to one of the two becoming unstable and retransforming while the other nucleus continues to grow (t_2). This reorganisation forms the transformation morphology shown in Fig. 4.32(t_3). The reverse transformation is again dominated by the reversible transformation type which is accompanied by occasional reconstructive transformations producing lattice defects. These defects have higher potential energy than the surrounding parent phase and consequently they interfere with the ongoing trans-

formation process. Eventually, the growth decays in a region around the defects at the same normalised load of 0.0325. The magnification of the transformation region, presented in Fig. 4.32, shows the morphology of this region: The martensite consists of domains formed by the two variants at (1) and (2); it is penetrated by many previous dislocation slip lines (3). The potential energy field shows the domain structure and emphasises the surplus energy caused by the lattice defects which are generated by dislocations (blue spots). These may act as pinning sites for the transformation front: to drive the transformation beyond this area, a significantly higher load (0.06) is needed. Once the transformation zone has passed this region of defects, the MT grows towards the strip's ends without further obstacles (t_{3-4}).

In the tensile test, the lattice defects produced show two different interactions with subsequent transformations. First, they may serve as nucleation sites during consecutive loading, and second, they may act as obstacles during the growth process. We shall point out the consequences of these two generated lattice defects in the following subsection.

4.4.3 Displacement Control Mode

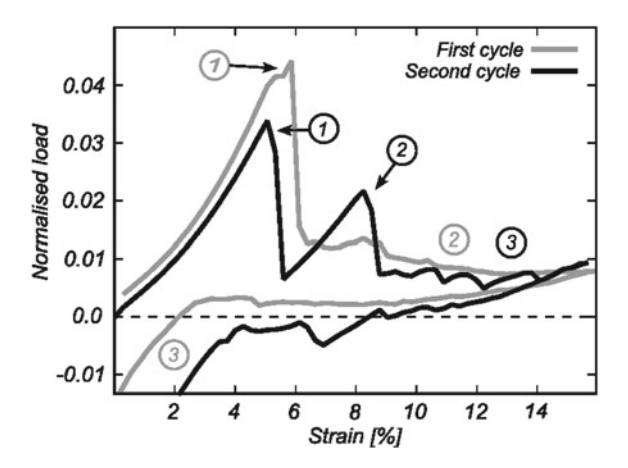
Displacement control mode provides the opportunity for controlling the growth rate of MT, whereas in load control mode, the transformation evolves freely once the critical load is exceeded. Therefore, it is much easier to approximate equilibrium conditions in simulations of tensile tests under displacement control. In this section we discuss two consecutive load cycles with a strip-shaped 165,000-atom assembly.

The cross-species interaction parameter is $\varepsilon_{AB}=0.225\,\varepsilon_0$ and the temperature is set to 1,000 K so the assembly is decidedly within the pseudo-elastic regime. The reference configuration is an austenitic rectangular single crystal (38.1 × 20.8 nm). Two gripping zones are defined at each end of the assembly. In the potential energy plots of Figs. 4.34 and 4.35, the gripping zones are indicated by zones of elevated potential energy owing to the increased cross-species interaction parameter ε_{AB} which is set to stabilise the grips. The left-hand grip is fixed and the opposite grip is displaced horizontally; however, the atoms in this gripping zone may move vertically to permit vertical transformation strains. Two consecutive loading/unloading cycles are simulated, in which the initial configuration of the second cycle was provided by the final configuration of the first.

In each load cycle, the strain is incremented by $2.62 \times 10^{-6}\%$ in every 100th time step, resulting in a comparatively slow global strain rate of 0.066/ns. The global strain is increased by approximately 16 % during 6 million time steps and decreased at the same rate. As an illustration of the computational effort: The simulation of a single load cycle on 66 contemporary 2.6 GHz CPUs requires 140 hours or ca. six days. With a workload of 2,500 atoms per node, a single time increment was calculated in 0.042 seconds using this computer.

The global load/strain diagram for the two cycles is shown in Fig. 4.33. We use red and blue colour codes to distinguish the first and the second load cycle, respec-

Fig. 4.33 Tensile testing in the pseudo-elastic regime in displacement control mode. 165,000 atoms. Load/strain diagram of two consecutive load cycles. The indicated numbers 1–3 refer to situations shown in Figs. 4.34 and 4.35



tively. For each case, the indicated numbers 1–3 refer to situations depicted in the illustrations of Figs. 4.34 and 4.35. We now proceed by discussing the details.

4.4.3.1 First Load Cycle

The simulation is initiated with a pristine single crystal configuration. An overall extension of this sample provokes a reaction force in the assembly through interactions between the free atoms and the gripped atoms. The slight extensions of the assembly affect the elastic loading of the reference lattice. At a critical strain, the first martensite nucleates. This instant is indicated by (1) in the grey load/strain curve of Fig. 4.33. The nucleation is accompanied by a single vacancy produced by a dislocation mechanism. This situation is detailed in the enlargement of Fig. 4.34(1). The locus of the vacancy is indicated by (i) and its energy mark is faintly visible in the potential energy plot. Along the dislocation line, visible in the morphology plot of Fig. 4.34(1), two martensite variants grow, similar to MT under load control mode. Once martensite has nucleated, the load signal of Fig. 4.33 drops significantly to the level of the yield load which, in the present case, is approx. 0.1. Further extension of the sample affects the growth of the martensite region by a shift of the habit line—more precisely, of the transformation zone—to the right. The growth occurs at almost constant load. Figure 4.34(2) depicts a single instant during this process. The austenite/martensite transformation zone exhibits the characteristic interfacial energy in the potential energy plot, which is already known from previous simulations. Moreover, as observed under load control mode, the load direction selects those martensite variants which offer a favourable shear direction. These are coloured in green and purple in the morphology representation of Fig. 4.34. We observe that these two variants are alternately produced along the habit line by an accumulation process, which is not investigated here further. We see that the martensite-martensite interfaces involve distinct interface energies. Also, we note that these interfaces are prone to produce lattice defects.

Subject to displacement reversal, the martensite transforms back into austenite. In this case, the habit line moves back to where it was originally produced by the loading. However, the corresponding recovery load level is lower than the yield load in the load strain diagram of Fig. 4.33; on average, 1/3 of the yield load. Thus, the unloading process gives rise to a distinct load/strain hysteresis. This behaviour is to be contrasted with the tensile test using the pseudo-elastic chain assembly investigated in Sect. 3.4.2 (shown in Fig. 3.19 on p. 80). This chain assembly did not exhibit hysteresis. The most important difference between the chain and the present assembly is that within the chain, all interface energies were artificially suppressed, while the present tensile specimen, its microstructure and all the energetic effects involved evolve freely. Therefore our conclusion in Sect. 3.4.2.5, which related hysteresis to interface energy, can be retrospectively confirmed.

A small fraction of the material was plastically deformed by dislocative processes during the loading/unloading process, producing a slight residual elongation of the assembly. Upon complete displacement reversal, the assembly is therefore slightly compressed. We have already pointed out (Fig. 4.31b) that the dislocation mechanism degenerates unit cells by slip along the principle lattice axes. Accordingly, the unit cells along these axes are misleadingly coloured as martensite by our colour algorithm in Fig. 4.34(3).

Some of the lattice defects produced during the process remain stable in the lattice. Owing to their higher potential energy, these defects show up as dark spots in the potential energy plot of Fig. 4.34(3). The enlargement shows the locus of an extended defect at (i). This defect and another, neighbouring defect (beyond the enlargement), provide a special energetic situation that allows for some small region of remanent martensite in the unloaded state, indicated by (ii) in the enlargement.

In sum, we see that a pristine sample exhibits a significant nucleation peak in the load/strain diagram. The nucleation is associated with the production of vacancies, and the transformation subsequently evolves by a moving transformation zone, where martensite domains are produced and distinguished by the shuffle-direction of sublattices. Both martensite/martensite and austenite/martensite interfaces involve interface energy and remanent lattice defects are produced. The global load/strain diagram is hysteretical.

4.4.3.2 Second Load Cycle

In the second load cycle, the simulation is initiated from the final configuration of the first cycle. The global load/strain curve is depicted by the black colour in Fig. 4.33. Black numbers 1–3 refer to situations shown in Fig. 4.35. The morphology of the initial state is shown in Fig. 4.35(1) with respect to a redefined reference lattice using next-neighbour analysis. Accordingly, the trace-lines of dislocations, misleadingly coloured as martensite in Fig. 4.34(3), vanish. All unit cells not identified as

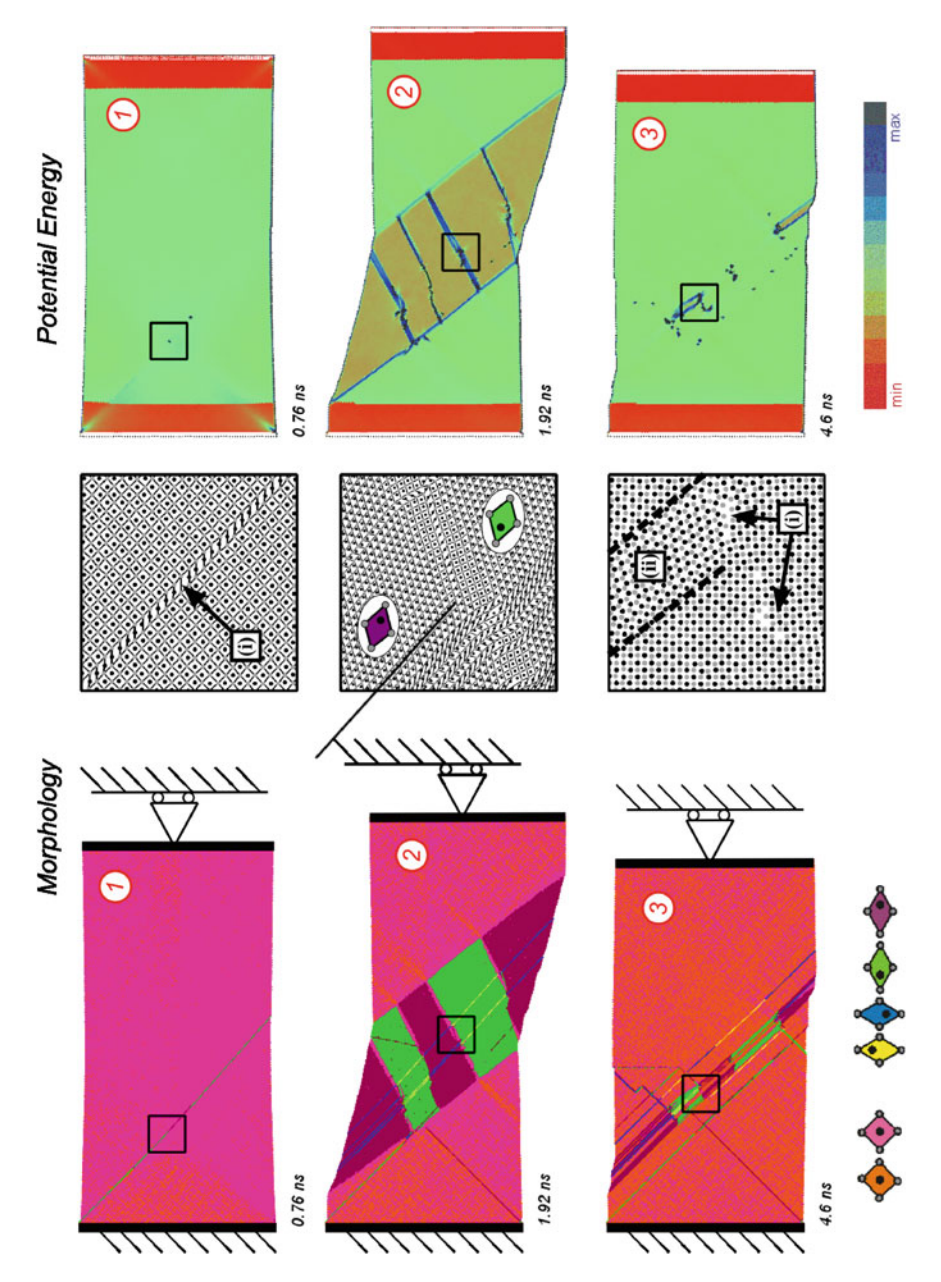
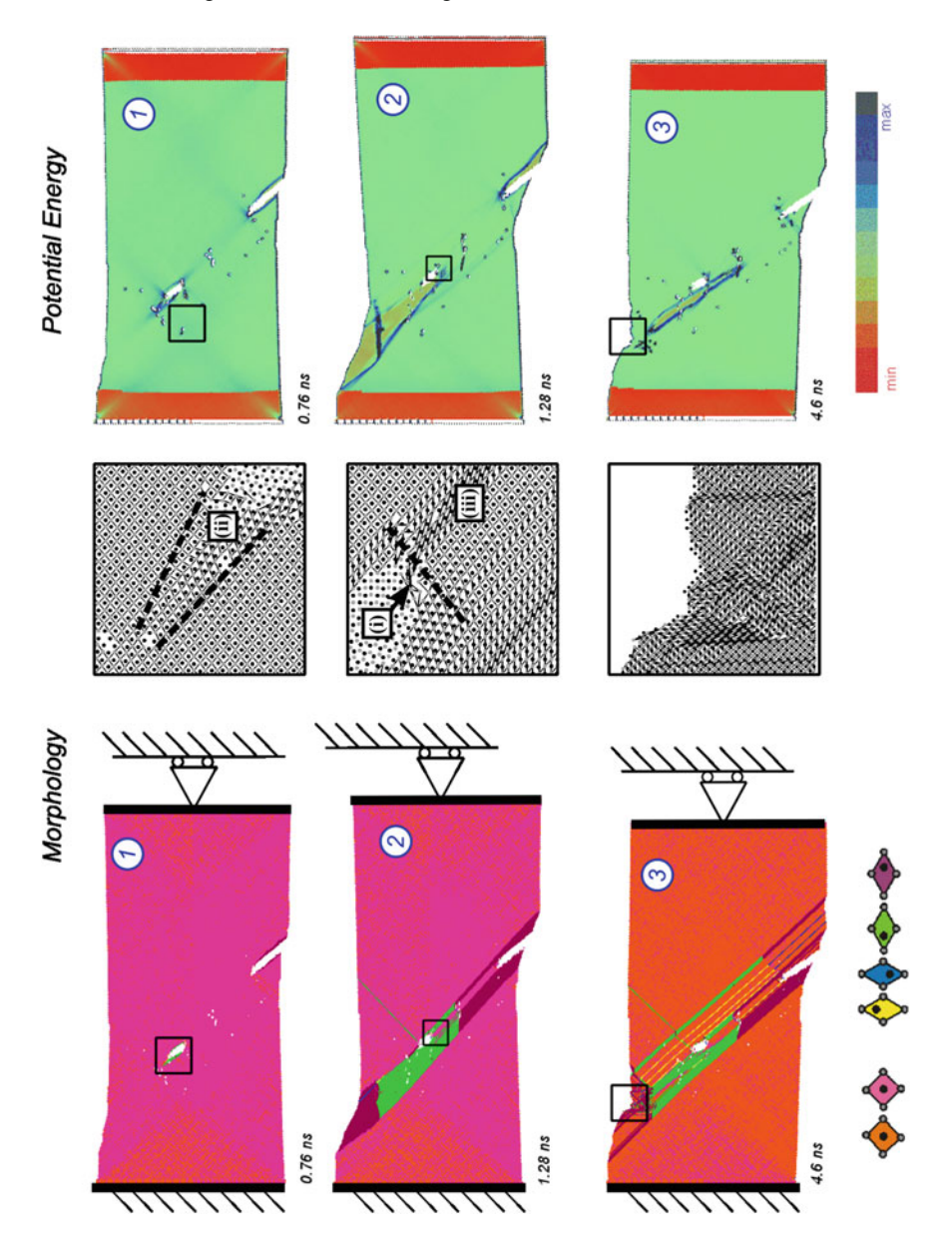


Fig. 4.34 Tensile testing in the pseudo-elastic regime. Displacement control, first cycle with a 165,000-atom assembly. Labels 1–3 indicate the situations in the load/strain diagram of Fig. 4.33. (Side-view intended)



 $\textbf{Fig. 4.35} \ \, \text{Second load cycle. Labels 1-3 indicate the situations in the load/strain diagram of Fig. 4.33.} \, \, (\text{Side-view intended, Colour online, Video available online})$

5-atomic square cells are ignored. These contain either defects, or represent remanent martensite. In the morphology plots of Fig. 4.35, these are blanked out (white spots).

Figure 4.35(1) shows the instant at which the martensite nucleates during loading. We observe a wedge-shaped nucleation occurring in the vicinity of a lattice defect, marked by (ii) in the enlargement of Fig. 4.35(1). The shape of this nucleus is augmented by broken lines. The respective nucleation load is smaller than that observed with the pristine assembly, Fig. 4.33. We may thus conclude that the nucleation barrier was reduced by the existing lattice defect. The nucleus quickly grows along the [01] lattice axis and the measured load signal drops to a lower level in a similar way to that observed in the first cycle. However, the transformation is obstructed in crossing other defects in this area of the assembly such that the growth process is disrupted. Similar to the 262,144-atom strip under load control discussed above, the internal load must be increased by further extension of the sample in order for the transformation to pass these obstacles. Consequently, the load/strain diagram exhibits a secondary nucleation peak at (2). Figure 4.35(2) depicts the morphological and the energetic situation. The enlargement shows in particular a band of austenite at (ii) which is prevented from transforming by a barrier of defects located along the broken line. Therefore, we see that defects may not only serve as nucleation spots but may also cause local stress fields that inhibit an ongoing transformation.

Once the transformation zone has passed the defected area, the measured load signal again drops to the yield load level which is slightly lower than that observed during the first load cycle. Therefore, the second cycle exhibits the tendency towards functional fatigue which is quantitatively similar to real materials [16].

As with the first load cycle, some amount of plastic deformation occurs during the loading/unloading cycle. This effect is clearly visible at the surface after full displacement reversal; see Fig. 4.35(3). Also, some small region of remanent martensite is indicated by the potential energy field at this time step.

To summarise, we conclude that the observed lattice defects generated by the loading process affect local stress fields which may promote the formation of martensite during nucleation. On the other hand, the defects may inhibit the growth process, depending on the specific situation in the travelling transformation zone.

4.5 Tensile Testing in the Pseudo-Plastic Regime

In the pseudo-plastic regime, we expect to observe martensitic de twinning in simulations of tensile experiments. Owing to the comparatively high martensite—martensite transformation loads (see Fig. 3.15 on p. 76), such processes are accompanied by significant plastic deformation, thus distinguishing pseudo-plastic (transformative) processes from true plastic (dislocative) processes. Here, we continue by describing the simulation of such a tensile experiment under load control mode using a 160,000-atom quad.

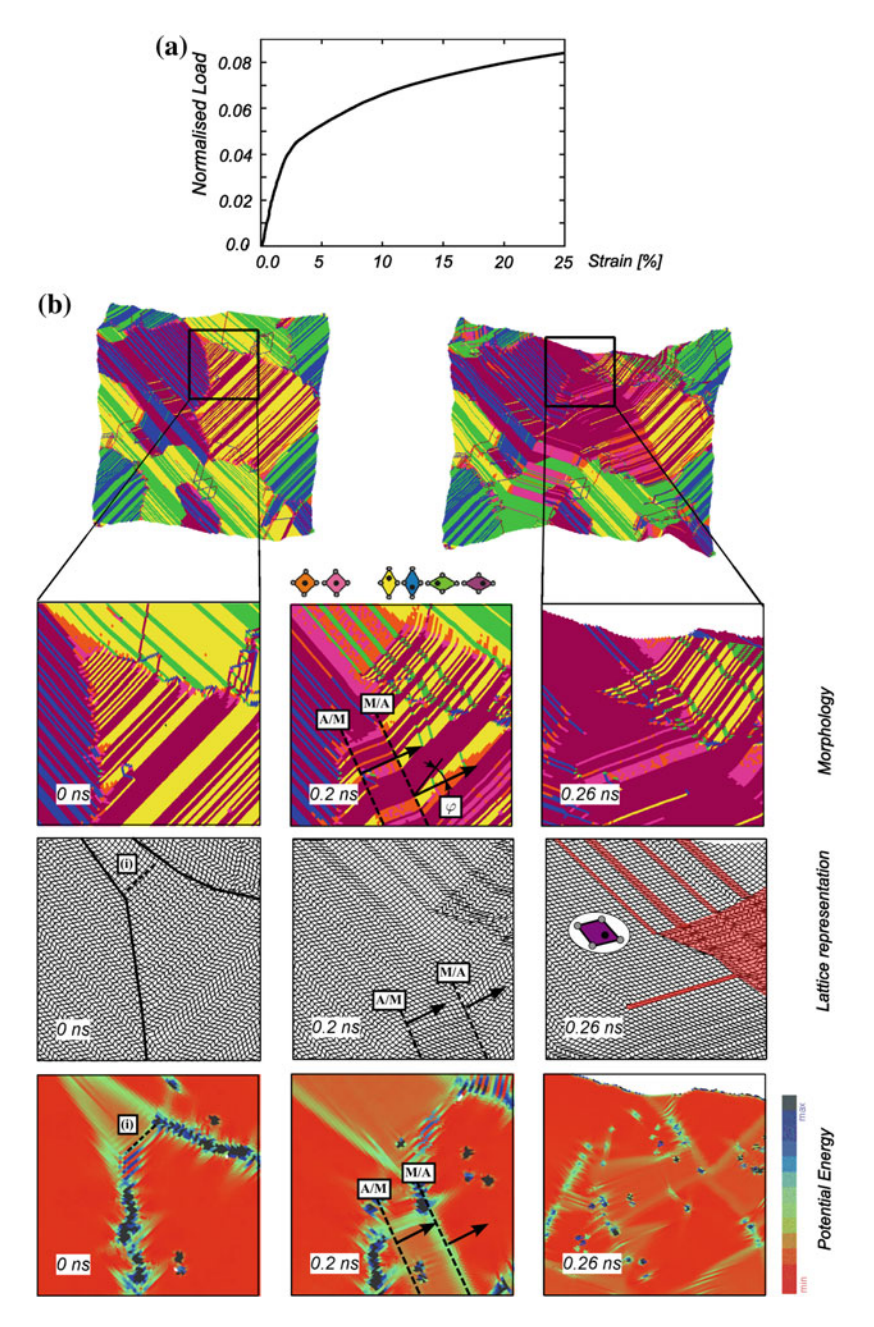
The initial configuration used for the simulation is a poly-domain crystal produced during a previous temperature-induced transformation process from an originally per-

fect single crystal. The corresponding formation process was described in Sect. 4.1.2 and Fig. 4.6 on p. 95 shows the product used here as the initial configuration. The cross-species interaction parameter is set to $\varepsilon_{AB}=0.225\,\varepsilon_0$ and the temperature is set to a low level of 300 K. We applied external loads to the atoms located in the gripping zones acting in opposite directions at each end of the sample. The load was increased by small increments of 5×10^{-4} in every 5,000th time step up to a normalised maximum load of 0.1, resulting in a loading rate of 0.43N/s. In total, one million time steps were calculated. The applied load eventually fractures the crystal. Here we shall restrict our discussion to the aspects of (pseudo-)plasticity observed prior the structural failure. The load/strain response is shown in Fig. 4.36a and the subfigure (b) illustrates the process at the three time instants 0.0, 0.2 and 0.26 ns indicated.

The fundamental difference of the present simulation with tensile tests in the austenite is that the domain structure is initially present in the martensite. The morphology of Fig. 4.6, which is used here as the initial configuration, exhibits a granular structure of twinned martensite plates which grew along the two principle lattice axes [01] and [10]. The incompatibility between the martensite variants involves incoherencies, indicated by distinct energy marks in the potential energy plot. Particularly the energetic situation at the triple domain junctions may stabilise remanent austenite, see Fig. 4.36(0 ns). In our tensile investigation of a small 2D crystallite, we saw that the transformation path from one martensite variant to the respective twin variant passes through the austenite; see Fig. 3.15 on p. 76. Therefore, we expect the triple-junction region in the larger sample to be prone to nucleation of the martensite—martensite transformation upon loading and focus our attention on it. Figure 4.36 shows enlargements of this area for the three instants.

The reference state of Fig. 4.36(0 ns) shows the remanent austenite island located in the triple domain junction at (i). The martensite domains are nicely twinned, which is obvious from the colouring, and also depicted in the lattice representation of Fig. 4.36(0 ns). The potential energy plot clearly exhibits the interfacial energy located at the domain boundaries. The austenite island is represented by green shading, indicating a slightly higher potential energy than the surrounding martensite.

Subject to a horizontal load, the green and purple variants in Fig. 4.36 are favourable and the yellow and blue variants are unfavourable. We have seen in Sect. 4.1.2 that each domain consists of alternating variants having opposite shear directions formed in the absence of loads. During loading, the unfavourable variants are transformed into the favoured variants once the load exceeds a critical threshold. This process proceeds via the intermediate formation of austenite. Figure 4.36(0.2 ns) shows an instant of this detwinning process. The process proceeds along moving interfaces intersecting the lamellae by some angle $\varphi \approx 30^{\circ}$ indicated in Fig. 4.36(0.2 ns). These interfaces are interpreted as a habit line. An individual habit line is indicated by a broken line labelled "M/A" in Fig. 4.36(0.2ns). The produced phase is immediately further transformed into a martensite variant favoured by the loading, forming a successive habit line parallel to the first, labelled "A/M" in Fig. 4.36(0.2ns). The distance between these two habit lines is small, approx. 10 lattice parameters in



 $\label{eq:Fig. 4.36} \textbf{ Tensile loading in the pseudo-plastic regime. a Load/strain diagram. b Situations during the loading process$

the present case. The intermediately formed phase and also the two habit lines are nicely recognisable in the potential energy plot of Fig. 4.36(0.2ns).

Once this process has passed through a domain, the martensite consists (almost) homogeneously of the variants favoured by the load. The initial domain structure is somewhat dissolved, Fig. 4.36(0.26ns), because the misfit between adjacent domains is reduced. The critical detwinning load is comparatively high, hence dislocations are activated, giving rise to significant (true) plastic deformation in parts of the material. In the lattice representation of Fig. 4.36(0.26ns), these parts are shaded by a pink colour. The overall view in the upper images of Fig. 4.36b show the sample a short time before structural failure. The plastic deformation is markedly augmented in the corners, where the failure starts.

In Sect. 3.4.2 we have described a tensile loading process with a chain of crystallites, see Fig. 3.18 on p. 80. The chain's load/strain curve exhibits an abrupt transition from the elastic into the transformed regime once the critical load is exceeded. In the simulation explained here, this transition is smooth. One reason for the difference is that in the chain, all crystallites are subject to the same load at an optimal angle and they are only free to adjust to this load governed by the weak inter-crystal interaction. In the quad assembly studied here, the martensite–martensite transformations, in contrast, occur subject to restrictive geometrical constraints which are determined by the domain structure, and the locally received loads are due to a complex stress field caused by this microstructure.

To summarise, we may state that load-induced detwinning processes can be locally resolved into domain structured martensite by the MD simulations. In this 2D model, the transformation process involves intermediate austenite formation produced along habit lines which cross the lamellar domains at an angle determined by the crystal-lographic requirements. The model material is subjected to significant true plastic deformation owing to the high level of the transformation load.

4.6 Transformation Cycles

4.6.1 Procedure

We now return to the temperature-induced transformation processes discussed in Sect. 4.1 and investigate the reverse m/a process and transformation cycles. In the Sect. 4.1 we have shown how MT evolves by nucleation and growth processes which form herringbone-shaped martensite plates comprising of compatible twin variants. Plates growing in perpendicular directions are incompatible, however, and distinct domain boundaries are produced where such plates come into contact. The incompatibility of the plates produces lattice defects which we identify by atoms with significantly higher potential energy than those within the martensite plates. Similar processes were also observed during load-induced transformations.

Here, we show under reverse transformation, these defects are partly eliminated and partly remain in the lattice. Mobile defects may migrate to the surface where they produce kinks, or they may pile up at obstacles, and similar effects were observed during load cycles. In any case, the potential energy landscape of the reconstructed austenite is irreversibly changed, and this change influences all the subsequent transformation processes.

A series of MD simulation experiments concerning transformation *cycles* was conducted to investigate this matter. Since austenite is stabilised entropically, the characteristic relaxation time of the reverse process is significantly longer than in its counterpart. Additionally, we have seen that the microstructure modulates the potential energy landscape of the assembly, provoking energetic obstacles which may delay an ongoing growth process. Both effects aggravate the assessment of phase equilibrium states in our simulations because long observation times are required.

One method of dealing with this problem is to slightly vary the cross-species interaction parameter ε_{AB} so that the target phase becomes energetically more favourable. From an orthodox point of view, this was an undesired "trick" since the interaction parameters determine a specific material and consequently, changing the parameters, results in changing the material. However, there is some theoretical justification for it: We have derived, within a certain range, a linear relation between ε_{AB} and the theoretical transformation temperature, see Fig. 3.11 (p. 69). This relation states that variations of the transformation temperature are proportional to variations in ε_{AB} . In addition to this, small variations of this interaction parameter do not affect the crystallography of the material. Therefore, transformation processes may be induced by temperature for fixed ε_{AB} . Alternatively, they may be induced by a slight variation in the interaction parameter ε_{AB} at constant temperature. We refer to the latter as energy-induced transformations. We have used both procedures in the investigation presented in this section. In temperature-induced processes, we set $\varepsilon_{AB} = 0.225 \,\varepsilon_0$ and vary the temperature within the interval of T = 200...1,500 K at rates of 2 K/fs (0.05 K/time-step). In energy-induced processes, the temperature was kept constant at either 200 K (for austenite/martensite transitions) or at 1,200 K (for m/a transitions) and the interaction parameter ε_{AB} then was varied at a rate of 6.25e-7 ε_0 /fs within an interval of $\varepsilon_{AB} = 0.19 \dots 0.27 \varepsilon_0$.

We have conducted three transformation cycles, each consisting of five transformation/retransformation processes. Although starting from slightly different initial conditions—the initial velocities were selected randomly with respect to the initial temperature—all three cycles show the same morphological and energetic trends, so the result can be regarded as reproducible. On the whole, the investigation discussed in Sect. 4.6 involved a total of approx. 30 million time steps.

All simulations explained in this section refer to the 160,000-atom crystal investigated in Sect. 4.1.2. The initial transformation process with this assembly was shown in Fig. 4.6 on p. 95.

4.6.2 Reverse Transformation of the 160,000-Atom Quad

We recall the two reverse transformation types introduced in Sect. 4.4, Fig. 4.29 (p. 123): reversible and reconstructive. Figure 4.37 illustrates that both mechanisms also occur during thermally induced reverse transformations with the 160,000-atom assembly. The top row of images in Fig. 4.37 depicts an austenitic nucleus at low T situated at a triple martensitic domain junction. The interface between the martensite variants contains defects visible at (ii) and these exhibit surplus potential energies marked by the colour contrast in (c). The nucleus mainly consists of reversibly transformed unit cells, but a localised point defect is also visible at (i).

The bottom row of images in Fig. 4.37 shows the same region after reverse m/a transformation at high T. The majority of the unit cells transformed reversibly into the austenite. Reconstructive transformations have occurred, e.g. in regions (iii) in Fig. 4.37. Colours in 4.37b are assigned with respect to the deformation of the reference unit cells defined in the austenite, and hence include historical information. Figure 4.37c shows that the 'reconstructed' region is still perfectly austenitic with no energy signature. Isolated energetic signatures are observed where the reconstructed region ends (i) and at former boundary junctions of the martensite plates (ii). These defects have both core energy and an associated strain field. For this reason, these spots have increased the potential energy dispersed in a strain field.

Figure 4.38 shows the 160,000-atom quad after completion of the reverse transformation. Frame (a) shows the morphology after redefinition of the reconstructed square unit cells as austenite. Following this redefinition, some atoms no longer have four nearest neighbours: these are shown as white spots in Fig. 4.38a. Inspection of the lattice (c) and the potential energy field (b) shows that these spots mostly represent vacancies with increased potential energy shown in (d). Remote from the spots, the potential energy fluctuates about the energy $e_{(\text{aust, mart})}^{0, \text{ id}}$ of the infinite lattice, as indicated by broken lines in Fig. 4.38d.

4.6.3 Cyclic Transformation Processes

Hitherto, a single transformation/reverse transformation process has been considered. We now consider cyclic transformations whereby the final configuration of the preceding transformation process is used as the initial configuration of the next cycle. The first transformation cycle with the 160,000-atom quad is initiated from a pristine austenite single crystal. The second cycle is initiated from the product of the first cycle shown in Fig. 4.38.

Figure 4.39a—c shows the MT in progress during the second cycle. Similar to the simulations of cyclic loading carried out in the pseudo-elastic regime, we observe martensite nucleating at defects which were produced during the previous transformation cycle. These defects are located along the broken line indicated in Fig. 4.39 and were preserved during the reverse transformation. Nuclei grow on either side

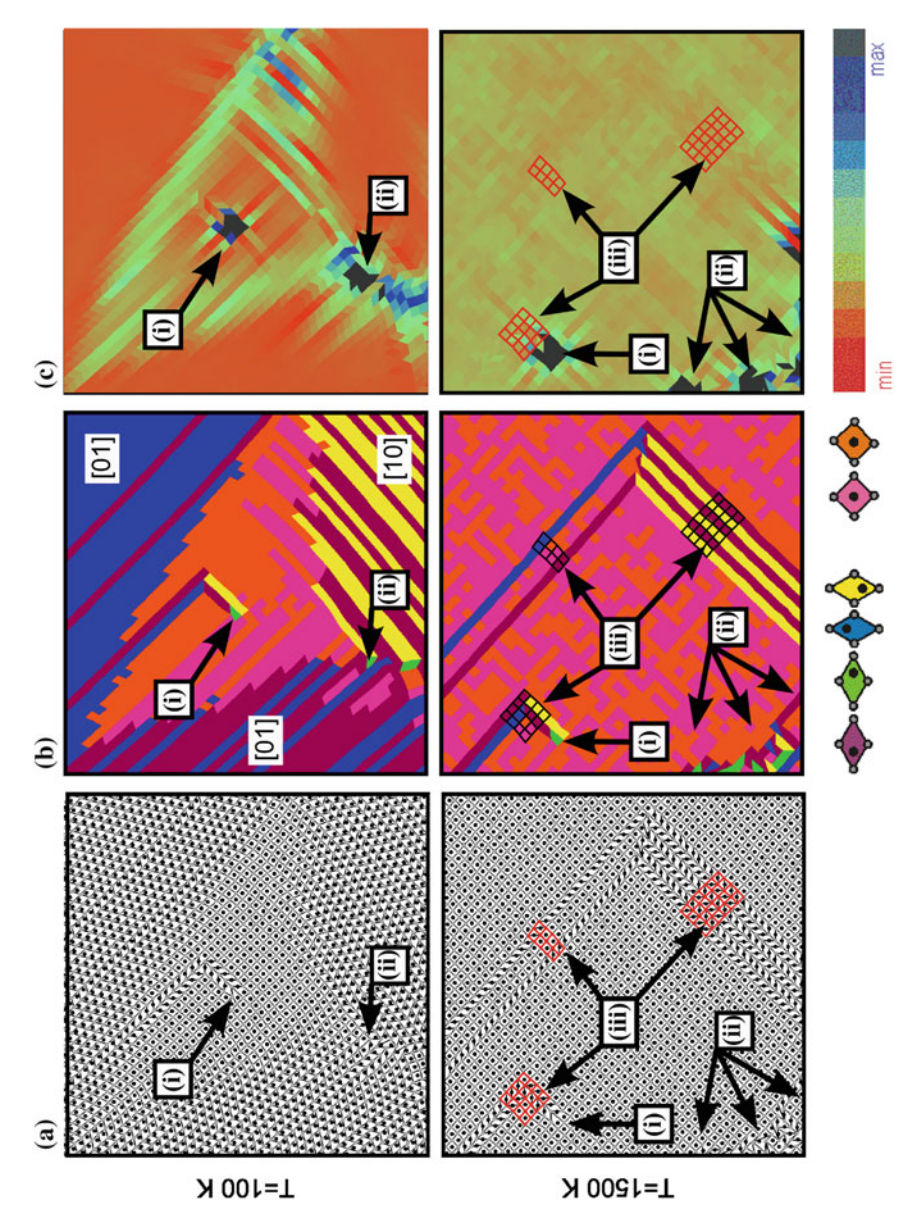


Fig. 4.37 Local detail of the reverse transformation in the 160,000-atom quad. Top row 100 K, bottom row 1,500 K. Columns: **a** lattice, **b** unit cell morphologies, with colours determined from the arrangement of the atoms which were nearest neighbours in the original austenite (**c**) potential energy field. (Side-view intended, Video available online)

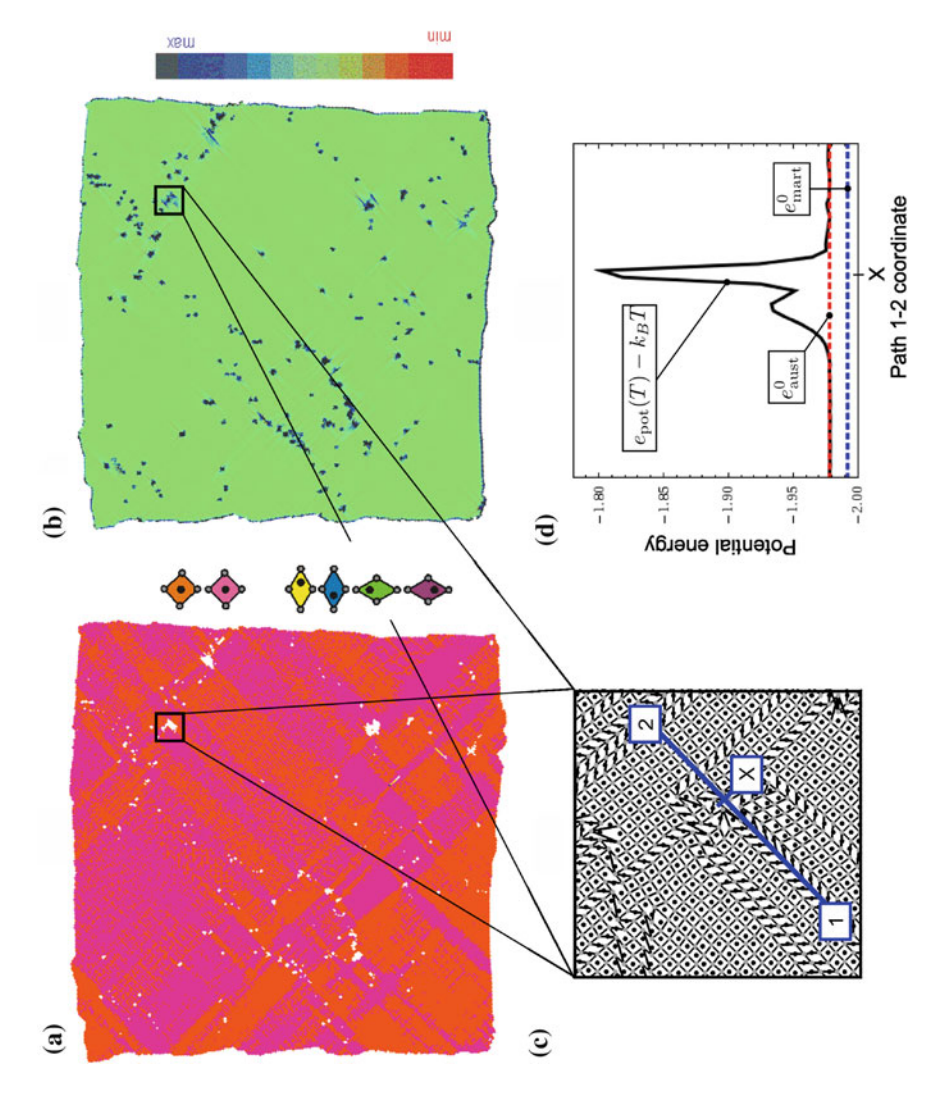


Fig. 4.38 Product of the reverse transformation. **a** Morphology, **b** potential energy, **c** magnification of defect region, **d** potential energy across defect along path 1–2. (Side-view intended, colour online, video available online)

of this defect line, forming new, differently oriented martensite plates. Also, new domain boundaries are formed where these new plates interact, indicated by (i) in Fig. 4.39c.

Thus the defect structure present in the austenite influences the nucleation and growth process of the subsequent martensite. This observation is confirmed by further transformation cycles; see Fig. 4.40 for a tableau of morphologies obtained by five subsequent forward/reverse transformation processes using the 160,000-atom quad.

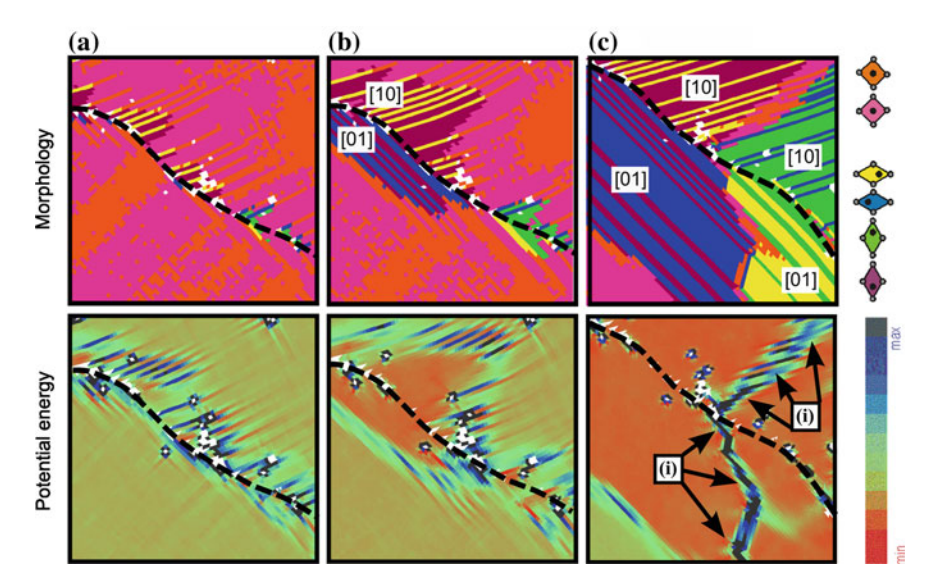


Fig. 4.39 Second transformation cycle: nucleation of martensite at T = 200 K, $\varepsilon_{AB} = 0.22$. The *broken line* indicates the previously formed martensitic domain boundary

The domain character of the martensite is clearly visible in the morphological representation and also by the surplus energy mark of the domain boundaries. Domains are produced during the first MT. Upon reverse transformation, some defects are eliminated, some migrate to the surface and still others remain immobile during the reverse transformation and serve as nucleation sites for subsequent MT, hence influencing the new domain structure. This mechanism accounts for an accumulation of defects along lines and eventually imprints a domain structure into the austenite which is reinforced by successive cycles.

The total potential energy of the specimen changes as defects accumulate. Table 4.4 gives the results of three independent cycle series. Each cycle started from a perfect, single crystalline quad. In two series, the transformations are induced by slowly changing the interaction parameter ε_{AB} at constant temperatures; 200 and 1,200 K for the MT and its reverse transformation, respectively. The third series was conducted completely in temperature control mode. To guarantee completion of all the transformation processes, the mean potential energy was normally measured for $\varepsilon_{AB}=0.25\ldots0.27$ and for $\varepsilon_{AB}=0.19$ during the reverse transformations and the converse process, respectively. Next, the energies were rescaled to a single, intermediate value of $\varepsilon_{AB}=0.225$ using the constant factors for ideal lattices from Fig. 3.10a. Finally Eq. (1.48) on p. 27 is used to calculate the ground state energy. In 2D this equation reads

$$e_{(\text{aust, mart})}^{0} = \frac{V_{(\text{aust, mart})}^{\text{int}}(\mathbf{x}_{\gamma}(t))}{N} - kT.$$
 (4.13)

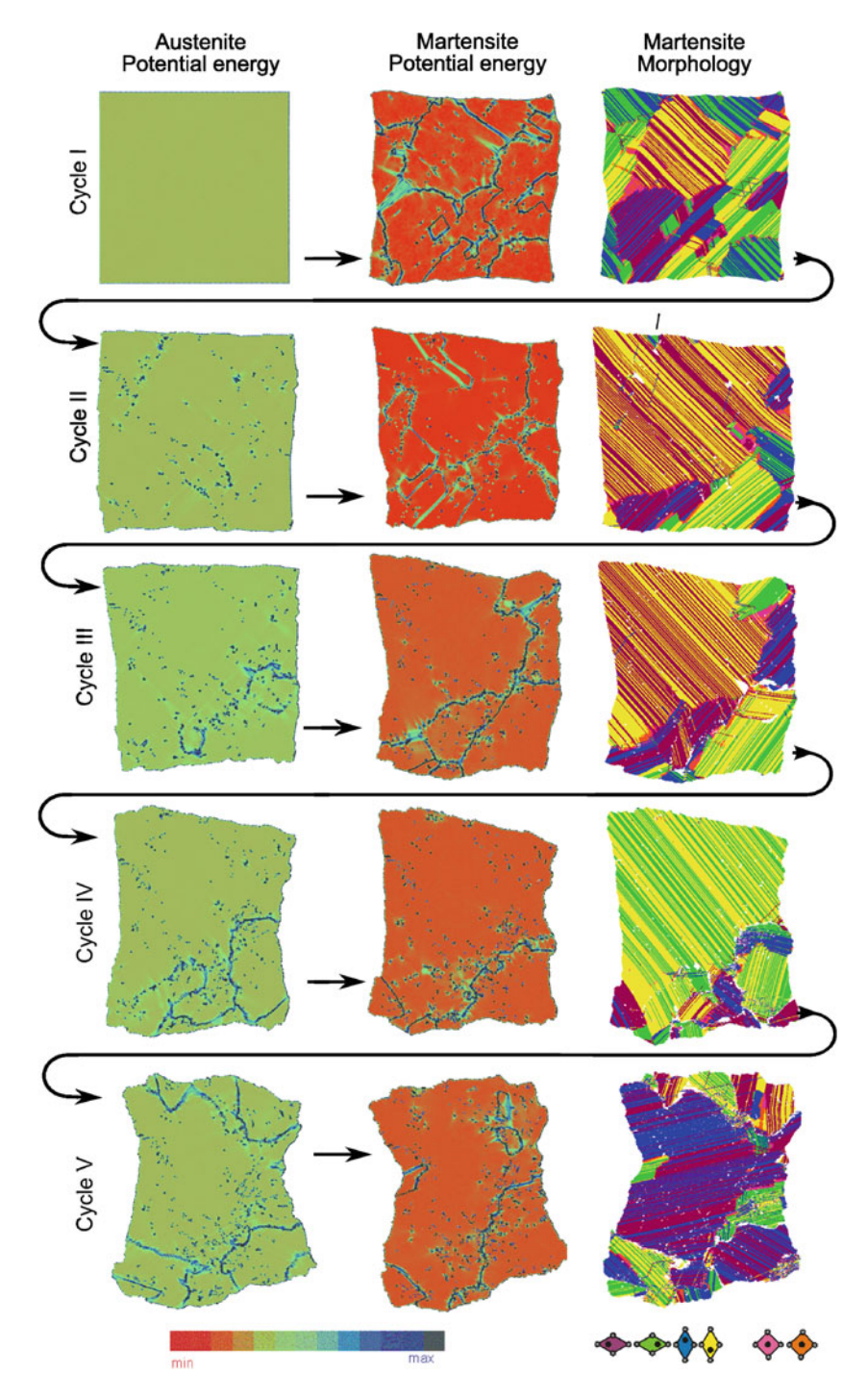


Fig. 4.40 Five cyclic martensitic/austenitic transformations. (Side-view intended)

	AB interaction-		e_0^0	aust, mart) #cy	cle	
Series	parameter	I	II	II	IV	V
		Aus	stenite, $\times \varepsilon_0$			
1	$\varepsilon_{AB} = 0.27$	-2.033	-2.031	-2.028	-2.020	-2.015
2	$\varepsilon_{AB} = 0.27$	-2.031	-2.025	-2.019	-2.024	-2.023
3	$\varepsilon_{AB} = 0.25$	-2.009	-1.999	-1.996	-1.997	-1.994
Trend	$\varepsilon_{AB} = 0.225$	-1.969	-1.963	-1.959	-1.958	-1.955
		Mar	tensite, $\times \varepsilon_0$			
1	$\varepsilon_{AB} = 0.19$	-1.970	-1.960	-1.964	-1.966	-1.962
2	$\varepsilon_{AB} = 0.19$	-1.959	-1.960	-1.964	-1.974	_
3	$\varepsilon_{AB} = 0.19$	-1.975	-1.976	-1.975	-1.977	-1.98
Trend	$\varepsilon_{AB} = 0.225$	-1.972	-1.969	-1.971	-1.976	-1.973

Table 4.4 Mean ground state energies measured in three cyclic transformation series with the 160,000-atom quad

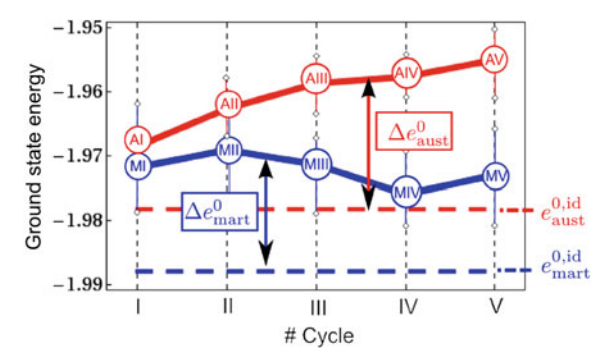


Fig. 4.41 Mean atomic potential energies of the 160,000-atom quad as a function of the cycle number calculated with $\varepsilon_{AB}=0.225$. The difference between AI and $e_{aust}^{0,id}$ shows the contribution from the surface. *Solid red* and *blue curves*: trend lines of austenite and martensite, respectively, according to Table 4.4. *Broken red* and *blue lines*: ground state energies of the respective perfect lattices

These specific energies are given in Table 4.4.

Each of the three cycle series produces a different defect morphology, but they exhibit a similar energy trend (Table 4.4 and Fig. 4.41). The respective specific ground state energies $e_{(\text{aust, mart})}^{0,\text{id}}$ of the infinite and perfect lattices of Sect. 3.2 are also included in Fig. 4.41 by the broken lines. These lines are lower because the MD simulation data include the defects and surfaces excluded in Sect. 3.2. The mean surplus energies due to defects and surfaces may hence be defined by

$$\Delta e_{(\text{aust, mart})}^0 = e_{(\text{aust, mart})}^0 - e_{(\text{aust, mart})}^{0, \text{id}}. \tag{4.14}$$

4.7 Hysteresis and Functional Fatigue

4.7.1 Thermodynamic Hysteresis

The results of Table 4.4 may be interpreted as the cause of hysteresis in the thermodynamic model. The guiding idea is that the surplus energies $\Delta e^0_{(\text{aust, mart})}$ shift the phase equilibrium condition (3.14), while we ignore the entropic effect of the lattice defects. For the transformation between imperfect structures, the ground state energies in Eq. (3.14) are replaced by the estimated ground state energies of the microstructured lattices, giving

$$T = \underbrace{\frac{e_{\text{aust}}^{0} - e_{\text{mart}}^{0}}{k_{B} \ln\left(\frac{\lambda_{\text{mart}}}{\lambda_{\text{aust}}}\right)}}_{T_{\text{id}}} + \underbrace{\frac{\Delta e_{\text{aust}}^{0} - \Delta e_{\text{mart}}^{0}}{k_{B} \ln\left(\frac{\lambda_{\text{mart}}}{\lambda_{\text{aust}}}\right)}}_{\Delta T}.$$
(4.15)

Here, ΔT denotes the shift of the transformation temperature due to the defect energies within the microstructure.

In the following, we consider a sequence of simulations where all transformations were entirely induced by temperature at a fixed interaction parameter $\varepsilon_{AB} = 0.225 \, \varepsilon_0$. For this case, the potential energies of the defective states are given in Fig. 4.41, indicated by AI...V and MI...V for austenite and martensite, respectively. In the pristine quad, the atoms have a mean potential energy of AI. Transformation causes a reduction in potential energy to that of the defective martensite. The thermodynamic transformation temperature of that process, $T_{\text{AI} \rightarrow \text{MI}}$, can be calculated from Eq. (4.15) as

$$T_{\text{AI} \to \text{MI}} = 59.8 \text{ K}.$$
 (4.16)

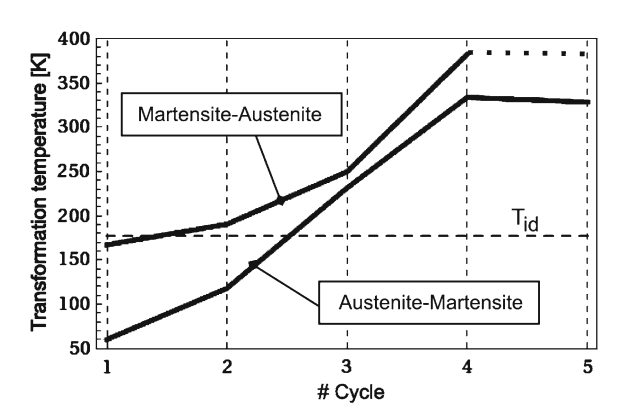
The reverse transformation generates the defective austenite state AII, which has a higher potential energy than the AI state. The reverse transformation temperature is then higher $T_{\text{MI} \to \text{AII}}$

$$T_{\text{MI}\to\text{AII}} = 166.8 \text{ K}.$$
 (4.17)

Hence, according to thermodynamics, the AI \rightarrow MI \rightarrow AII transformation cycle of the model has a temperature hysteresis of 107 K. Note that in the first cycle, the transformation temperature $T_{\rm id}$ of the infinite and perfect lattice is above both $T_{\rm AI \rightarrow MI}$ and $T_{\rm MI \rightarrow AII}$

$$T_{\rm id} = 177.0 \text{ K}.$$
 (4.18)

Fig. 4.42 Transformation temperatures of the 160,000-atom quad as a function of the cycle number. The hysteresis-free transformation temperature of infinite and perfect lattices (Sect. 3.2.2) is indicated by the *broken line*



4.7.2 Functional Fatigue

We need not stop here: going to the next MT of cycle II, the transformation temperature $T_{\rm AII \to MII}$ depends on the potential energies of states AII and MII and the subsequent reverse transformation by the states MII and AIII. Continuing to the last cycle, the respective transformation temperatures of MT and the reverse transformation are plotted in Fig. 4.42. Inspection shows that during the first four cycles, both transformation temperatures increase beyond the transformation temperature of the infinite lattice $T_{\rm id}$. The width of the hysteresis decreases during the first four cycles, with some evidence of defect saturation by the fifth cycle. Both transformation temperatures shift upward as a result of the evolution of the defect structure in austenite and martensite.

The cycling was continued beyond the fifth cycle; however, the quad hardens and begins to fracture: necking of the sample is already visible in the last cycle in Fig. 4.40. We regard this as a finite-size effect of the 160,000-atom quad but larger calculations would have to be compromised by shorter simulation times, i.e. unrealistically fast cooling rates. In this regard, the chosen assembly size is a compromise.

4.7.3 Predicted and Observed Hysteresis

The hysteresis predicted in Fig. 4.42 is based on an integral energy balance of the 160,000-atom crystal. This implies the idea of a homogeneous "mean field" defect energy. Figure 4.39 in Sect. 4.6.3 on the other hand has illustrated the impact of defects on nucleation, which shows that local conditions are important. The question is whether the local picture of the transformation evolution complies with the global prediction?

The answer is "almost". Figure 4.43 shows the evolution of the austenite fraction of the 160,000-atom quad as function of temperature upon heating and cooling within

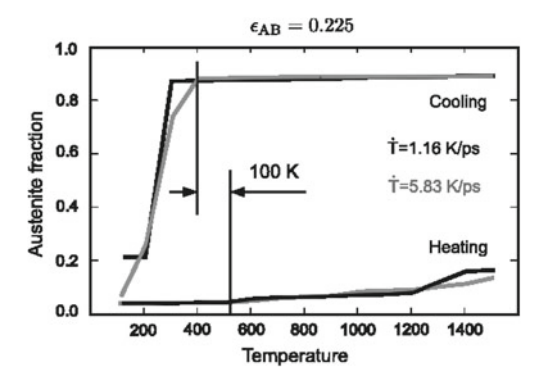


Fig. 4.43 Temperature controlled transformation process of a defect-infected crystal, austenite \rightarrow martensite upon cooling and martensite \rightarrow austenite at two distinct temperature rates. For these simulations the cross-species interaction parameter $\varepsilon_{AB}=0.225$ was set constant. Each atom is designated as austenite, martensite or defective according to how well its local coordination matches the reference structures (Fig. 3.3). As a consequence, the defects reduce the maximum austenite fraction below 100%. We associate the MA transition with the first appearance of austenite ("Austenite start")

the range 100...1,500 K. Cooling and heating processes were started from identical austenitic and martensitic initial configurations, respectively. These were chosen from previous second cycle simulations in order to provide defective lattices.

Two different cooling/heating rates were imposed, but the simulations show little difference between the respective curves. Figure 4.43 shows that the AM transformation occurs quickly upon cooling below 500 K. The MA transformation is sluggish in comparison and remains incomplete for the two chosen temperature rates. The reason for these distinct transformation behaviours is that AM transformations are driven by the potential energy while MA transformations are driven by the entropy. Entropically controlled transformations involve stochastic processes on the atomic scale and therefore exhibit comparatively long relaxation times.

If taken from the first appearance of the product phase (the so-called martensite start and austenite start temperatures), the temperature hysteresis for this particular transformation cycle is approx. 100 K. With this crystal, this hysteresis width appears to be consistent with the prediction of Fig. 4.42; however, the predicted transformation start-temperatures do not match.

The simulations show that the transformation produces distinct microstructures and generates lattice defects. These affect subsequent transformations and vary the potential energy landscape of the sample. If the sample is cycled through a series of forward/reverse transformations, the number of defects in each phase accumulates. Defects act as nucleation sources for the transition. Moreover, the location of the defects can be preserved through the cycling, providing a memory of previous structures. Eventually, sufficient damage accumulates the material fractures.

We have identified two possible retransformation mechanisms, a reversible and a reconstructive type. Reversible m/a transformations preserve reference unit cells,

while the reconstructive type involve dislocation movements and plastic deformation. Both types re-establish the square lattice structure. The simulations show that the model material has a preference for the reversible m/a transformations. However, the reconstructive type plays an important role because it generates lattice defects and surface roughening. These prevent the lattice from returning to its pristine state. We show that permanent damage accumulates from plate boundaries in the martensite, which persists through cycling and causes functional fatigue. This damage suggests a natural source of the "memory" and role of "training" in the reverse shape memory effect, and a thermodynamic contribution to hysteresis.

Similar behaviour was also observed for load-induced MT processes in the previous section. In the pseudo-elastic regime, axial loading selects the production of variants favoured by the load direction. Our 2D model provides two possible generic variants which are distinguishable by the shuffle directions of sublattices. Owing to these two possibilities, even load-induced MT produces domain structures during nucleation-and-growth processes. In the pseudo-elastic regime, unloading provokes reverse m/a transformations. Defects produced in a loading/unloading cycle can act as nucleation sites for subsequent loading. The nucleation barrier in pseudo-elastic load/strain curve is thereby lowered in subsequent cycles. In any case, the pseudo-elastic load/strain curve is hysteretic.

Our thermodynamic theory, developed for thermal hysteresis, is based on the expected defect state of the transformed material, and is broadly compatible with the simulation results. The thermodynamically predicted transition temperature increases with cycling, implying that the defect energy in the austenite increases faster than that in the martensite. Experiments with SMA show that upon thermal cycling, the transformation temperature may indeed increase, but the opposite effect is also observed, depending on the transformation history. However, the nature of the defects observed in 2D may bear little resemblance to those seen in 3D.

Our thermodynamic condition involves global energies, whereas the transformation is nucleated locally, typically at defects. Further study is required to define and measure the *local* thermodynamic transformation conditions which are similar to classical nucleation theory.

In conclusion, we have used MD to investigate some fundamental principles of cycling m/a transitions. We show that permanent damage accumulates from plate boundaries in the martensite, which persists through cycling and causes functional fatigue. This damage suggests a natural source for the "memory" and role of "training" in the reverse shape memory effect, and a thermodynamic contribution to hysteresis.

References

- O. Kastner, G. Eggeler, W. Weiss, G.J. Ackland, Molecular dynamics simulation study of microstructure evolution during cyclic martensitic transformations. JMPS 9, 1888–1908 (2011)
- O. Kastner, G.J. Ackland, Mesoscale kinetics produces martensitic microstructure. J. Mech. Phys. Solids 57(1), 109–121 (2009)

References 149

 O. Kastner, G.J. Ackland, Load-induced martensitic transformations in pseudo-elastic Lennard-Jones cyrstals. in *Proceedings of the SMASIS 2008, ASME*, Ellicott City, 28–30 Oct 2008

- O. Kastner, G.J. Ackland, Martensitic transformations in 2D Lennard-Jones crystals. in *Proceedings of ICOMAT 2008, International Conference on Martensitic Transformations*, Santa Fe, June 29–July 5 2008
- O. Kastner, G.J. Ackland, Atomistic Simulations of martensitic transformations in Lennard-Jones solids. Part I. in Science and Supercomputing in Europe, HPC-Europa, 2007, pp. 950–959
- O. Kastner, G.J. Ackland, Atomistic simulations of martensitic transformations in Lennard-Jones solids. Part II. In *Science and Supercomputing in Europe*, HPC-Europa, 2007, pp. 960– 962
- O. Kastner, G.J. Ackland, G. Eggeler, W. Weiss, Preprint Series Weierstrass Institut for Applied Analysis and Stochastics, 2010. Preprint 1497
- P.L. Potapov, P. Ochin, J. Pons, D. Schryvers, Nanoscale inhomogeneities in melt-spun Ni–Al. Acta Mater. 48, 3833–3845 (2000)
- O. Kastner, R. Shneck, Fundamental investigation of the nucleation of martensite in a lennardjones crystal. unpublished, 2012
- 10. K. Gröhenig. Foundations of time-frequency analysis. Birkhäuser, Boston Mass. (etc.), 2001
- 11. P.S. Landa, Regular and Chaotic Oscillations: Foundations of Engineering Mechanics (Springer, Heidelberg, 2001)
- 12. W. Dreyer, M. Herrmann, Numerical experiments on the modulation theory for the nonlinear atomic chain. Physica D **237**(2), 255–282 (2008)
- W. Dreyer, M. Herrmann, A. Mielke, Micro-macro transition in the atomic chain via Whitham's modulation equation. Nonlinearity 19(2), 471–500 (2006)
- W. Dreyer, M. Herrmann, M. Kunik, Kinetic solutions of the Boltzmann–Peierls equation and its moment systems. Continuum Mech. Therm. 16(5), 453–469 (2004)
- K. Bahattacharya, S. Conti, G. Zanzotto, J. Zimmer, Crystal symmetry and the reversibility of martensitic transformations. Nat. Mater. 428, 55–59 (2004)
- A. Condo, C. Somsen, J. Olbricht, G. Eggeler, A. Dlouhy, R-phase stabilization in ultra-fine grain NiTi wires after mechanical cycling. in *ESOMAT 2009—8th European Symposium on Martensitic Transformations*, Prague, 07–11 Sept 2009, ed. by P. Sittner, V. Paidar, L. Heller, H. Seiner

Chapter 5 Lattice Transformations in 3D Crystals

We discuss two simulation examples concerning transformations in 3D lattices, intended as appendix to the investigations of the 2D case presented in the previous chapter. The two examples concern a 3D Lennard–Jones material and an EAM model for zirconium. We follow this work's paradigm of not artificially constraining the model's surfaces in order to allow the transformation to freely evolve; including the resulting surface effects. Compared to the 2D case, a 3D model geometrically augments the impact of these surfaces: Assuming square and cubic assemblies in 2D and 3D with $N_{\rm 2D}$ and $N_{\rm 3D}$ atoms respectively, the fraction of surface atoms is approximately $4\sqrt{N_{\rm 2D}}/N_{\rm 2D}$ in the 2D and $6\sqrt[3]{N_{\rm 3D}}^2/N_{\rm 3D}$ in the 3D case. These fractions are equal for $N_{\rm 3D}=27/8N_{\rm 2D}^{3/2}$. Our 2D studies have revealed that with model sizes of 10^5 atoms, surfaces may influence the nucleation, but not the microstructure's formation in the bulk material. Using the above calculation, this figure translates into a 3D model size with 10^8 atoms. A five million 3D crystal therefore is "small" in regard to the surface influence, while in 2D, a quarter million atom crystal is "large". Computational resources limit our 3D models to sizes of a few million atoms, although the impact of the surface is still tangible with such sizes.

5.1 3D Lennard–Jones Crystals

5.1.1 Model Material

In a 3D Lennard–Jones crystal, we may employ the same (12, 6) Lennard–Jones potentials as with the 2D of Eq. (3.1) but with a different set of interaction parameters $\varepsilon_{\alpha\beta}$ and $\sigma_{\alpha\beta}$. We may adjust these order parameters with respect to the corresponding nearest-neighbour separations in a B2 unit cell¹ via the lattice parameter R

¹ B2 denotes nested cubic sublattices of two atom species, where the species mutually provide the interstitials for each other's cubic cells, hence producing a heterogeneous bcc structure.

Characteristic quantities	
	$\varepsilon_0 = 6.15 \times 10^{-19} \mathrm{J}$
	$\sigma_0 = 2.42 \times 10^{-10} \text{ m}$
	$\mu_0 = 58.69 \times 10^{-27} \mathrm{kg}$
Eq. (2.7)	$\tau_0 = 6.21 \times 10^{-14} \text{ s}$
Eq. (2.9)	$\Lambda = 0.69$
Interaction parameters	
A–A interactions	$\varepsilon_{\rm AA} = 1.0 \varepsilon_0$
	$\sigma_{\rm AA} = 0.89 \sigma_0$
B–B interactions	$\varepsilon_{\mathrm{BB}} = 1.14 \varepsilon_{\mathrm{0}}$
	$\sigma_{\mathrm{BB}} = 0.89 \sigma_0$
A–B interactions	$\varepsilon_{\mathrm{AB}} = 0.42 \varepsilon_{\mathrm{0}}$
	$\sigma_{\rm AB} = 0.7365 \sigma_0$
Other parameters	
B2 lattice parameter	$R = 0.96 \sigma_0$
A mass	$m_{\rm A} = 1.0 \mu_0$
B mass	$m_{\rm B} = 1.0 \mu_0$
Time step	$\Delta t = 0.01 \tau_0$
Cut-off radius	$r_c = 3.0 \sigma_0$

Table 5.1 Model parameters used with the 3D Lennard–Jones model

(see Fig. 5.1) and set $\sigma_{AB} \approx 2^{-\frac{1}{6}} \frac{\sqrt{3}}{2} R$ and $\sigma_{AA} = \sigma_{BB} \approx 2^{-\frac{1}{6}} R$. In this case, the B2 structure can be stabilised provided that the remaining parameters ε_{AA} , ε_{BB} and ε_{AB} are selected properly. Here, we arbitrarily select the pure-species parameters ε_{AA} and ε_{BB} and heuristically adjust the cross-species parameter ε_{AB} . In the 2D case we have rationalised the parameter identification using harmonic analysis and thermodynamic considerations. These arguments are not developed for the 3D case because they are based on the assumption of an infinite lattice, which is not appropriate for the 3D assemblies considered here. Table 5.1 provides the model settings used. Note that the characteristic time is selected with respect to the harmonic period of an atomic motion's oscillation in the characteristic pair potential, see page 42.

Figure 5.1 shows lattice representations of the parent (a) and the product lattice (b, d, e, f). The structures shown are taken from the simulations. During the transformation, the six square faces of the primitive B2 unit cells are deformed into diamonds in the product; shown in Fig. 5.1b. The lattice parameter R of the B2 structure is extended by $\approx 8\%$ into r in the product structure by the transformation. (c) shows the radial distribution function (RDF) of the product, where the three types of interactions are distinguished. The RDF exhibits peaks at $\frac{r}{\sqrt{2}}$ (for A–B), r (for A–A and B–B) and 1.55 r (for A–B), which indicates a nested fcc lattice. In fact, lattice inspection confirms that each atom species forms fcc unit cells, Fig. 5.1d. Accordingly, the stacking order of crystallographic layers along [111]_{fcc} is a-b-c for each species separately, see Fig. 5.1e.

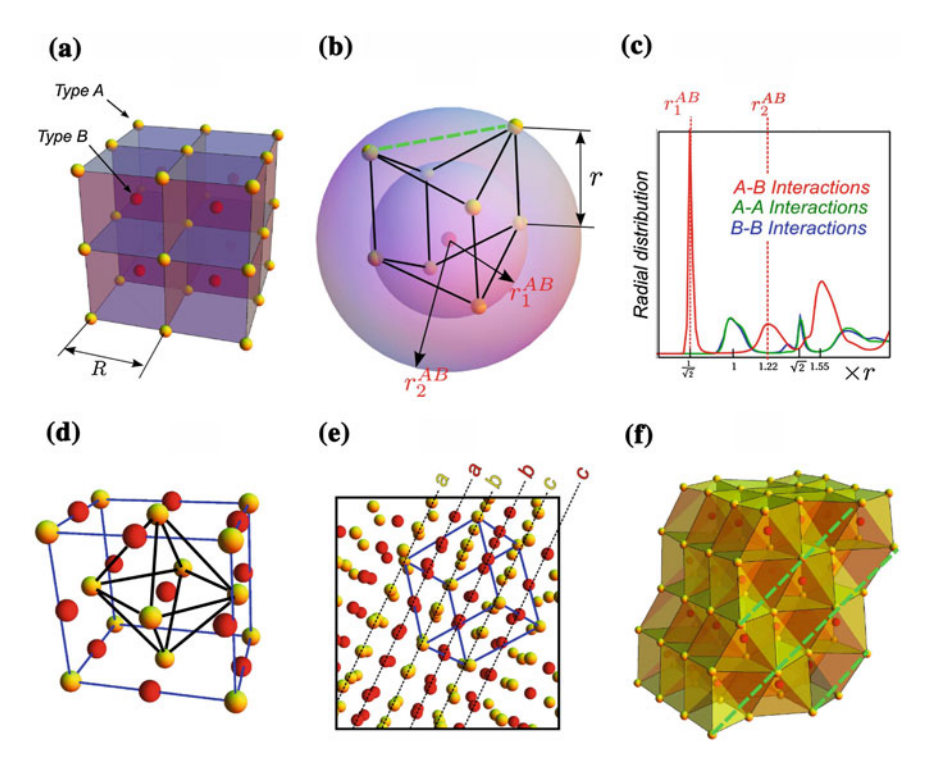


Fig. 5.1 3D Lennard–Jones model material. a B2 structure of the nested cubic sub-lattices with the lattice parameter R. MT deforms individual B2 unit cells into the product shown in (b). c Radial distribution function of the product. d Fcc unit cell isolated from the product lattice. e The product lattice exhibits an a-b-c stacking order for each atomic species, characteristic of fcc type of sublattices. f Perspective view showing the primitive unit cells. Simulation results are often represented using such a cell rendering mode, where the colour is selected by an analysis algorithm

Figure 5.1b shows that six of the former eight type-A corner atoms of a primitive B2 cell move symmetrically into positions on a spherical interaction shell of distance $\frac{r}{\sqrt{2}}$ about a type-B interstitial atom. The remaining two B2 corner atoms are shifted onto the next interaction shell. This shift breaks the symmetry of the B2 lattice. In the cubic phase, these two atoms are located at opposite positions of the B2 face diagonals, respectively. Hence, since 12 such pairs exist in the cubic phase, the transformation may produce 12 product variants. The orientation of a specific variant may be clearly visualised by the direction of a line connecting this atom pair, as indicated by the broken line in Fig. 5.1b. Such directions are also shown in (f).

5.1.2 Procedure

A spherical assembly of 5.5 million atoms (initial diameter approximately 40 nm) was simulated in parallel on a 125 processor grid. The initial configuration was

set up in the B2 phase using the lattice parameter R, listed in Table 5.1, as an initial estimate determined by a static relaxation of an infinite lattice. Prior to the simulation, the lattice was dynamically relaxed with respect to initial (high) temperature. The parameters employed are listed in Table 5.1. MT was induced upon constant cooling by means of a thermostat (velocity scaling method). The simulations were calculated on the HPC facility "JUMP" located at the Research Centre in Jülich / Germany (deployed in January 2010). JUMP consisted of 448 IBM Power6 processors with a comparatively fast clock rate of 4.7 GHz. An Infiniband network was used for the MPI communication and an additional 10 GB Ethernet for the I/O. In the simulations, the workload was distributed over a 5 × 5 = 125 processor grid. A single time step was calculated in $\tau_{\rm CPU,parallel}^{\rm tot}(\Delta t) = 1.12 \, {\rm s}$.

5.1.3 Results

Figure 5.2 depicts the progress of a simulated transformation process which uses the cell rendering mode. Figure 5.2a shows a snapshot at an intermediate time step. To provide a spatial representation, a composite of three planar sections along the main axes are shown in one image. Figure 5.2b shows six instants during the transformation as observed on the [111] section and Fig. 5.2c shows two views of the final product on both the [001] and [111] sections. Different filter modes are employed to depict the details: In both (a) and (b), the colours indicate the lattice structures hcp, fcc and bcc corresponding to the encoding shown in (a). These representations were obtained employing the Ball Viewer algorithm [1]. In (c), the colour visualises the potential energy field within the range indicated.

The free surface forces the unit cells located at the surface to spontaneously transform and produces product layers which are oriented along the main directions [110], [010] and [001]. For a short time period, these orientations also determine the growth directions from both sides before new nuclei are produced at the boundary between the product and the B2 phase. These secondary nuclei have different orientations and proceed into the bulk material forming wedge-shaped product regions. These structures are clearly visible on the [001] and [010] planes in Fig. 5.2a. The morphological analysis reveals that the wedges consist of fcc plates (green) which are separated by planar, interfacial mono-layers of hcp (red). A plan view of one such interfacial monolayer is visible in this figure on the [100] section image.

The wedge-shaped morphology of the secondary nuclei is also observed on the [111] sections shown in Fig. 5.2b. Wedge-like growths advance both axially, along the main direction of the wedge, and laterally forming a lamellar product structure. The final morphology has a distinct domain structure, clearly visible in the potential energy presentations of Fig. 5.2c. Domains consist of coplanar fcc lamellae, separated by interfaces. Entire domains are separated by distinct energy marks, coloured blue/grey in Fig. 5.2c: The domain interface energies are significantly higher than the interpose energies of individual fcc lamellae.

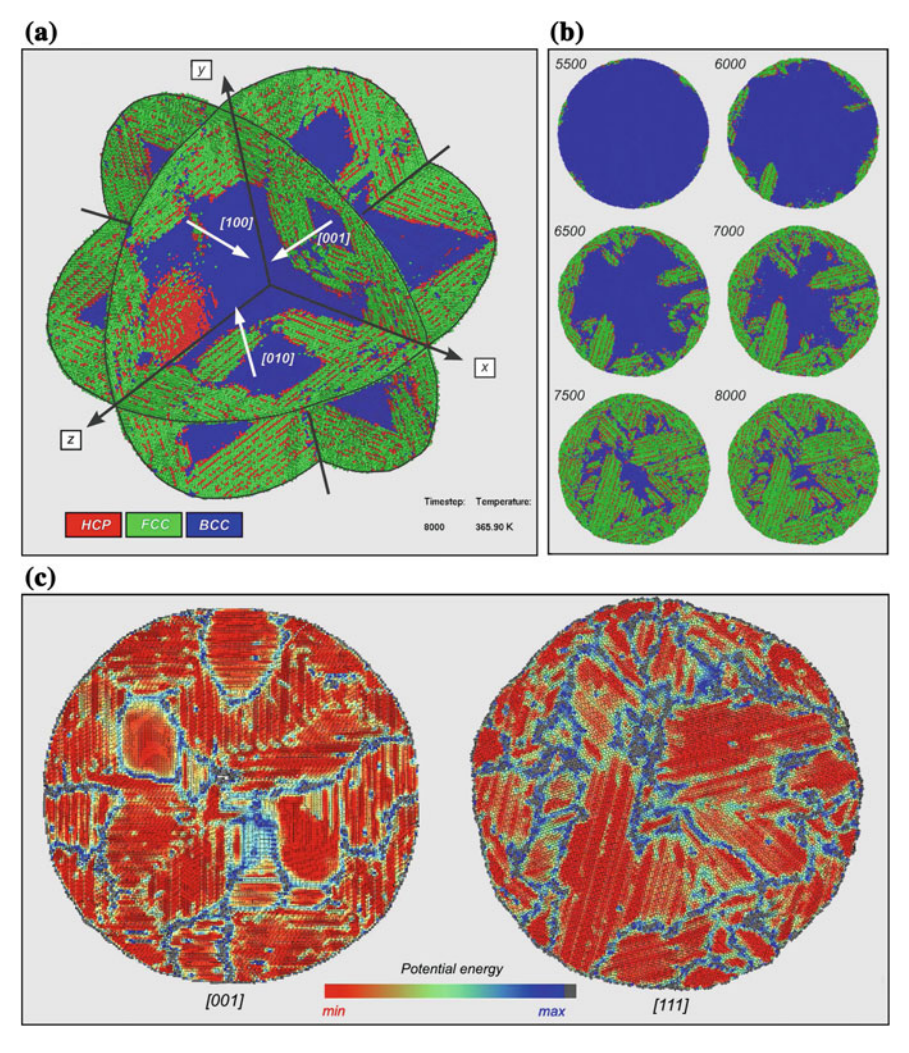


Fig. 5.2 MT in a sherical 5.5 million atom L–J crystal. a Overall view of three sections along the main axes at an intermediate time step. The section slices have thicknesses of 2 unit cells. b Transformation's progress observed on the [111] section. c Potential energy of the product (final state) on [001] and [111] (Video available online)

Figure 5.3 provides the energetic and morphological details of a wedge growth process. Figure 5.3a shows its morphology on the [001] section after 8,000 computed time steps. The enlargement shown in (b) confirms the lamellar character of fcc product plates. Individual lamellae are separated by hcp interface layers.

The crystallographic orientation of the product is depicted in Fig. 5.3c. As discussed with Fig. 5.1b, we use the separation vector between the off-centre atoms of the primitive unit cells as a measure of orientation. The solid lines visible in Fig. 5.3c

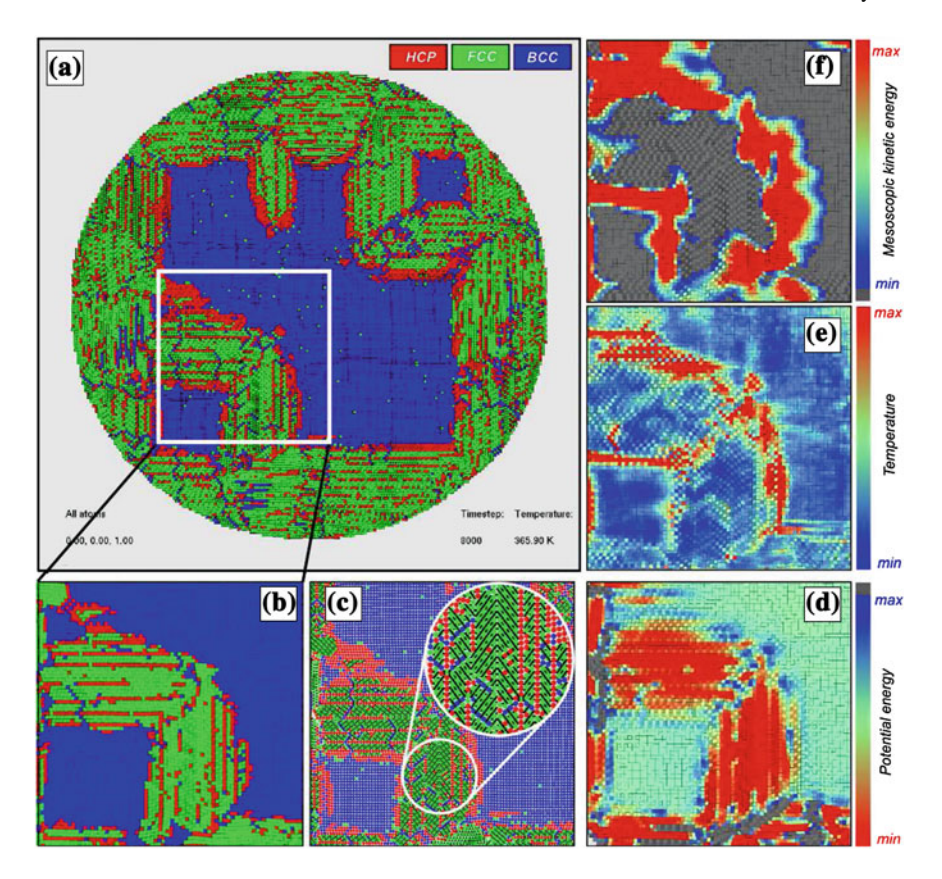


Fig. 5.3 Detail study of the transformation dynamics on the mesoscale. [001] Section through the sphere's centre. **a** Overall view. **b–f** Enlargements of the indicated region with different filter settings. **a**, **b** Crystal structure. **c** Orientation of martensite lamellae. **d–f** Energy and temperature as labelled (Video available online)

are produced by bundles of such vectors. We see that within an individual fcc lamella, the orientation is uniform. We conclude that such a lamella is produced by a single variant. Stacks of lamellae exhibit variants with alternating orientations. Therefore, this morphology has a striking similarity to martensitic twin structures observed in real materials and, because of this observation, we interpret the simulated product phase as *twinned martensite*.

This interpretation is confirmed by energetic arguments. Figure 5.3d shows the potential energy field of a martensitic wedge. We see that individual fcc lamella are energetically equivalent, since they exhibit the same potential energy. The colour-coding reveals fcc has a slightly lower potential energy (red) than the hcp interface layers (orange) separating the fcc twins. Therefore the product structure can be recognised in the potential energy field. Note that this was not so in 2D L–J lattices, where the martensite variants are perfectly compatible and therefore do not exhibit

interface energy. The potential energy of the parent B2 phase is higher than that of the martensite, thus making for clear signature in Fig. 5.3d. During the MT, the potential energy difference between parent and product phase is released as latent heat, hence increasing the temperature in the transformation zones, see Fig. 5.3e. The red colour signifies the warmer spots. We see that these spots are located on both sides of the pre-existing martensitic wedge, hence indicating zones of intense transformation activity. The presence of this latent heat signal is another indicator for an MT.

Figure 5.3f visualised the mesoscopic kinetic energy detected with the ongoing transformation. The mesoscopic kinetic energy is defined here as the kinetic energy of the mass centre of the interaction neighbourhoods of individual atoms according to Eq. 4 in Chap. 4) on page 101. In the MD simulation, these neighbourhoods are naturally defined by the chosen cut-off radius. In the present case, these neighbourhoods contain subsets of approximately 250 atoms. These are regarded as mesoscopic entities. Under equilibrium conditions, their mass centres are at rest and, accordingly, the kinetic energy of the mass centres are zero. We have seen with the 2D model that during the formation of martensite, correlated atomic motions cause slight dynamic shift of the mass centres, provoking increase of the mesoscopic kinetic energy locally (101 ff). Therefore, this field quantitiy provides another measure to spot ongoing transformation action, see Fig. 5.3f. Red colour signatures indicate indicate the transformation zones where the mesoscopic kinetic energy extends above some threshold value owing to the ongoing MT. We see these zones are slightly extended into the parent phase ahead of the transformation front, indicating gradual correlation of atomic trajectories, required to induce the tranformation locally.

The binary Lennard–Jones material investigated here exhibits a martensitic transformation between bcc austenite lattice and fcc martensite. The transformation evolves by nucleation and growth from the surface into the bulk. During the transformation, martensite plates are produced showing a lamellar twin structure. Twin variants are separated by planar twin–twin interfaces which can be identified with hcp monolayers, provoking twin–twin interface energy. Latent heat is released with the transformation since the bcc phase has a higher potential energy than the product. Thus, the transformation zones are locally heated and can be identified by the temperature signal. The formation of an individual martensite lamella is due to a short transient correlated motion of the atoms in that region. This motion increases the mesoscopic kinetic energy which can be detected during the simulation and then used to identify the transformation zones.

5.2 Zirconium Crystal

5.2.1 Model

Zirconium is a widely studied material on account of its importance in nuclear reactors. It exhibits temperature-induced martensitic bcc/hcp transformations but

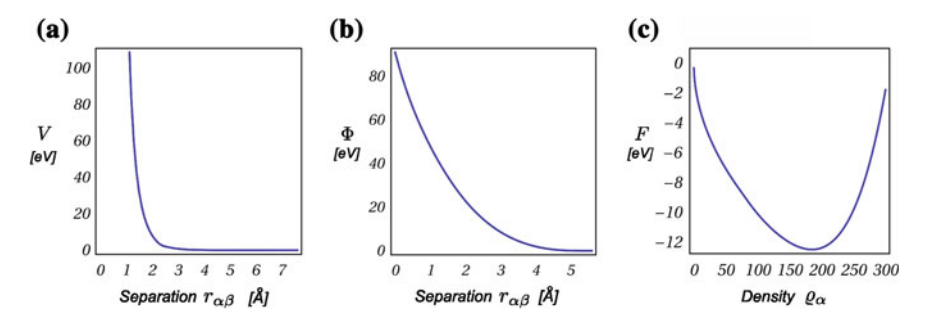


Fig. 5.4 EAM model functions for zirconium [2]

no shape memory effect since loading induces plastic deformation rather than de-twinning. Ackland has provided interaction potentials for this material and investigated such processes by MD simulations [2–5]. Here, we adopt a recently reported EAM potential and simulate T-induced transformation/reverse transformation processes in a 3.5 million atom sphere.

In the EAM, the total internal potential energy is given by

$$V^{\rm int} = V_{\rm rep}^{\rm int} + V_{\rm att}^{\rm int}, \tag{5.1}$$

where $V_{\text{rep}}^{\text{int}}$ and $V_{\text{att}}^{\text{int}}$ denote the repulsive and the attractive energy contributions. The former is represented by a repulsive pair potential V, whereas the latter is a many-body potential that depends on the positions of all the atoms within the interaction range,

$$V_{\text{rep}}^{\text{int}} = \sum_{\alpha=1}^{N-1} \sum_{\beta=\alpha+1}^{N} V(r_{\alpha\beta})$$

$$V_{\text{att}}^{\text{int}} = \sum_{\alpha=1}^{N} F(\rho_{\alpha}) \quad \text{with} \quad \rho_{\alpha} = \sum_{\beta=1}^{N} \frac{\Phi(r_{\alpha\beta})}{\rho_{\alpha\beta}}$$
(5.2)

Here, F is the embedding function and ρ_{α} is the local electron density which causes the cohesive interaction forces for individual atoms α in the lattice. It depends both on the position of the ionic core of that atom, via another pair potential Φ , and also on the positions of the atoms in its neighbourhood. The functions V, F and Φ need to be fitted to the thermo-mechanical properties of zirconium. The results used here were reported in [2]. Figure 5.4 shows the curve's trajectories for these functions.

EAM potentials are not capable of exactly satisfying the entire physical target properties, therefore the fitted curve must be a compromise. The model parameters used here are optimised with respect to the thermodynamic properties. The model predicts that the bcc/hcp phase transformation temperature occurs at 1233 K. Above this temperature, the model zirconium is in the bcc phase (A2 structure), which

Table 3.2 Would parameters used with the zheomum in	iouci
Characteristic quantities	
	$\varepsilon_0 = 1.6022 \times 10^{-19} \text{ J} = 1 \text{ eV}$
	$\sigma_0 = 10^{-10} \mathrm{m} = 1 \mathrm{\mathring{A}}$
	$\mu_0 = 91.224 \times 10^{-27} \mathrm{kg}$
(Eq. (2.8))	$\tau_0 = 7.55 \times 10^{-14} \mathrm{s}$
(Eq.(2.9))	$\Lambda = 1.0$
Other parameters	
A2 lattice parameter	$a = \begin{cases} 3.562 \sigma_0 & (Groundstate) \\ 3.814 \sigma_0 & (1,300 K) \end{cases}$
mass	$m = 1.0 \mu_0$
Time step	$\Delta t = 0.01 \tau_0$
Cut-off radius	$r_c = 7.6 \sigma_0$

Table 5.2 Model parameters used with the zirconium model

melts at 2109 K. The ground state lattice parameter of the model bcc is a=5.562 Å. The bcc-hcp transition occurs via the Nishiyama-Wassermann mechanism, in which the $\langle 110\rangle_{bcc}$ direction becomes the $\langle 0001\rangle_{hcp}$ direction. Since there are six nonequivalent $\langle 110\rangle_{bcc}$ directions, there are six possible orientations for the hcp lattice, referred to as variants [4]. The transformation induces a volume change of -0.8%. In the hexagonal phase, the ground state lattice parameters are a=5.22 Å and c=5.215 Å. The ground state energies of bcc and hcp are quite close and only differ by $0.03\,\text{eV}$ per atom.

5.2.2 Simulation Procedure

A spherical assembly of 3.5 million atoms (initial diameter approximately 53 nm) was simulated in parallel on 27 computation nodes. The model was set up in the bcc phase using an initial lattice parameter of $a=3.8\,\text{Å}$ which corresponded to an initial temperature of 1,300 K. At this temperature, the model was dynamically relaxed to the free surface before starting the actual simulation. To induce the transformation, the temperature was linearly quenched during 10,000 time steps from 1,300 K to the level of 800 K, at which it was maintained constant by means of the velocity-scaling method until the end of the simulation . A total of 70,000 time steps were calculated to simulate the bcc \rightarrow hcp transformation process. The final configuration of this simulation was then used as the initial configuration for simulating of the reverse hcp \rightarrow bcc transformation process. In this case, the temperature was rapidly increased from 800 K to the level of 1,300 K and maintained constant. The reverse transformation process was once again simulated for 70,000 time steps. Within this time, > 50% of the model material transformed back into bcc.

The simulations were calculated on the HPC facility "JUROPA-JSC" located at the Research Centre in Jülich / Germany. JUROPA-JSC is a new Linux cluster

consisting of 17,664 Intel Xeon cores with a (moderate) clock rate of 2.93 GHz. During the simulations, the workload was distributed over $3 \times 3 = 27$ processors, where a single time step required $\tau_{\text{CPU,parallel}}^{\text{tot}}(\Delta t) \approx 5.4 \,\text{s}$ of computation time.

5.2.3 Results

Once the temperature is lowered below the model's transformation temperature of 1,233 K, the transformation evolves in two stages. The first stage is characterised by rapid hcp nucleation symmetrically along the sphere's surface, Fig. 5.5 (after 5,000 time steps), from where it grows radially towards the sphere's centre. This produces a thickening hcp shell around a bcc core. Owing to the volume change accompanying the transformation, increasing stresses are induced in both the core and the shell. Eventually, these stresses initiate plastic deformation in parts of the shell, thereby releasing the stress and breaking the sphere's symmetry. This mechanical relaxation process is accompanied by transformation reversal, leaving some remanent hcp islands visible in Fig. 5.5a after 20,000 time steps. At this point, the second transformation stage starts, indicated by asymmetrical growth: See the three snapshots taken after 25,000, 40,000 and 60,000 time steps. This process produces a rich microstructure of hcp domains denoted by different orientations. BallViewer determines the orientation of the hcp basal planes by the direction of the hexagonal unit cells' c-axis. In the [001] section of Fig. 5.5c, these directions are depicted by bundles of black lines.

Our simulation confirms that bcc/hcp interfaces move along the $\{111\}_{bcc}$ directions [4]. Figure 5.6a provides a perspective representation. Three transparent $\{111\}_{bcc}$ planes are indicated, which illustrate the location of three such bcc/hcp interfaces visible along the three section slices shown. Two of the planes are oriented by $\langle 1\bar{1}1\rangle$ and one by $\langle \bar{1}1\bar{1}\rangle$. Figures 5.6b, c show the energetic representations as observed on the [001] section. Using sophisticated filter rules in the potential energy plot of Fig. 5.6b, the small energetic difference between hcp and bcc may be exploited to visualise the phase composition by colours. Figure 5.6c shows the mesoscopic kinetic energy. Transformation zones can be visualised by the method, however, the picture is not as clear as that using the Lennard–Jones crystal.

The hcp structure has a lower potential energy than that of bcc, but the latter can be stabilised by entropy at elevated temperatures. Therefore, the reversal hcp/bcc transformation can be simulated by a temperature increase, which is started after 70,000 time steps. The entropic stabilisation is governed by stochastic processes which involve longer relaxation times than the bcc/hcp transformation. After 127,000 time steps, the crystal exhibits the morphology shown in Fig. 5.7a. Although the reverse transformation is still not complete; approximately 50% of the material is already bcc, the simulation had to be terminated for technical reasons. From the result obtained so far, it is clear that the reverse process does not recover the initial shape since some plasticdeformation occurred during the bcc/hcp MT. This deformed

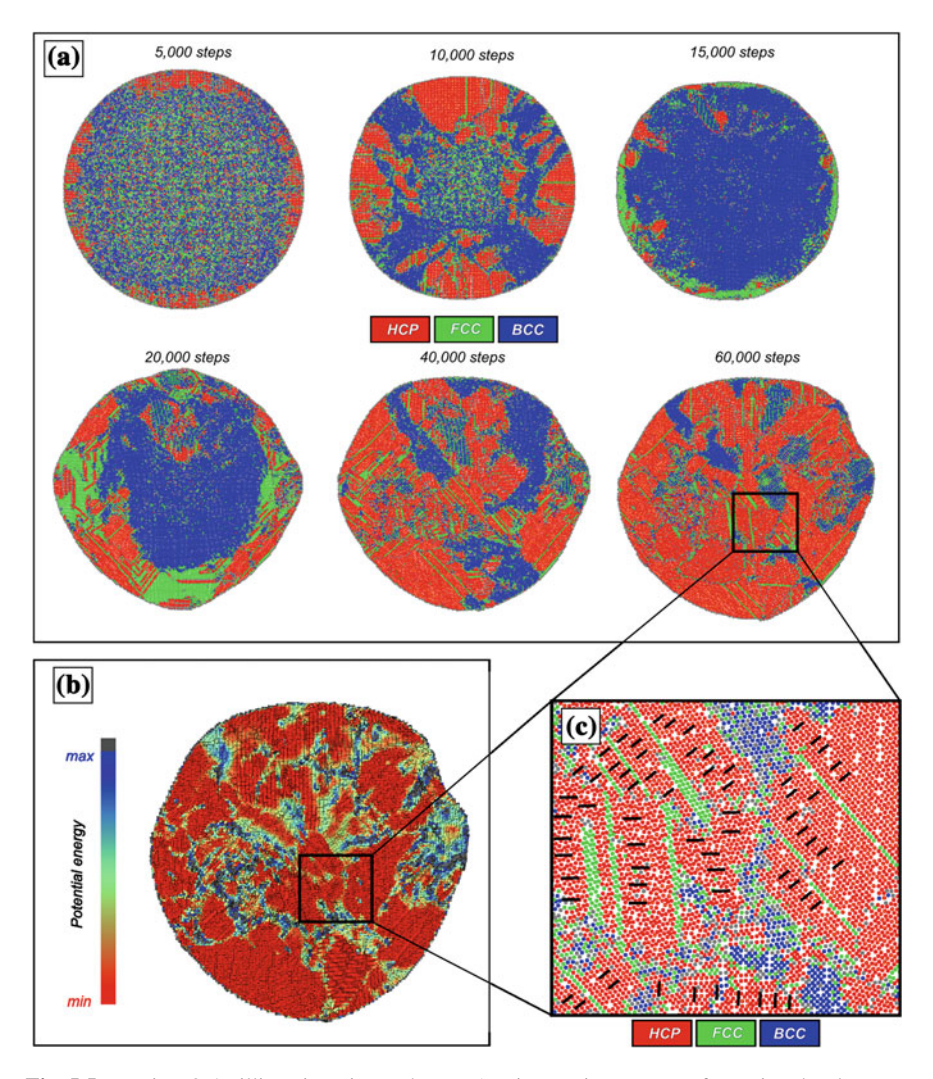


Fig. 5.5 MT in a 3.5 million zirconium sphere. EAM interactions. **a** Transformation development observed on a [001] section through the sphere's centre. **b** Potential energy distribution after 60,000 time steps. **c** Enlargement showing the domains' crystallographic orientations using bold lines [1] (Video available online)

the sphere into an asymmetric, potato-shaped assembly. The potential energy field in Fig. 5.7b reveals high-energy spots within bcc regions (grey-coloured) which indicate the existence of lattice artefacts.

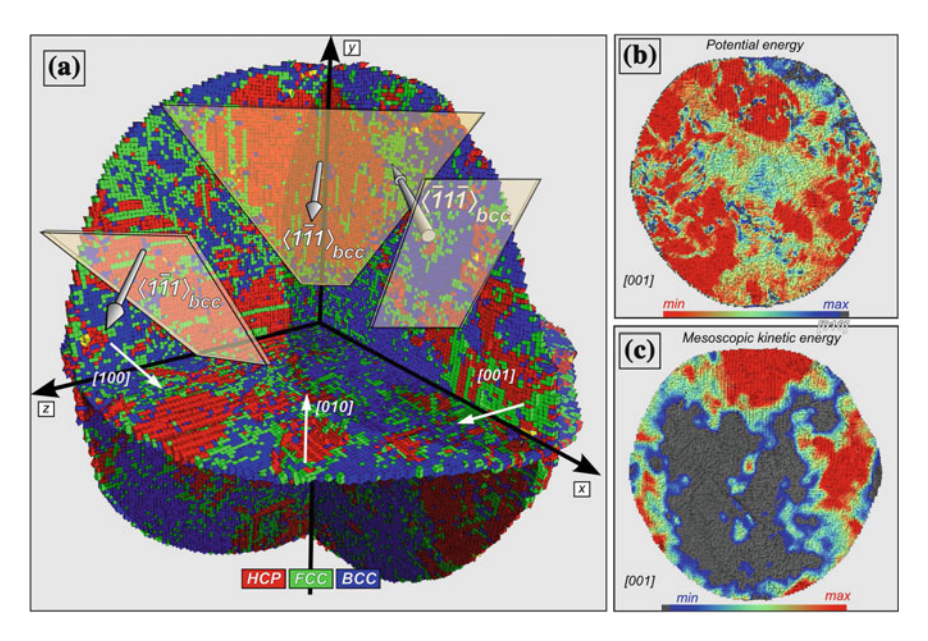


Fig. 5.6 Ongoing MT in a 3.5 million atom zirconium sphere after 30,000 time steps. a Perspective view ($[\overline{111}]$ direction) of the first octant bound by three section slices along the main axes. The bcc/hcp interface moves along $\{111\}_{bcc}$ directions; three such directions are indicated by the transparent planes. b, c Energy representations on the [001] section. (Side-view intented, colour online)

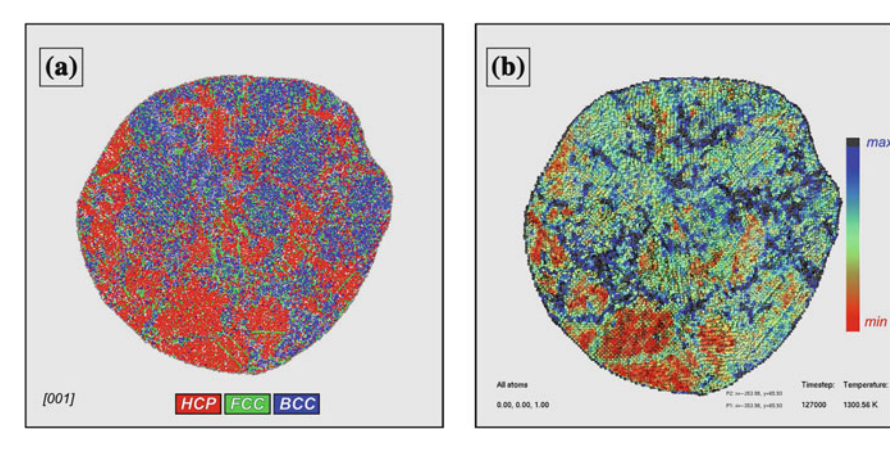


Fig. 5.7 T-induced reverse hcp/bcc transformation with the zirconium model after 127,000 time steps. a Morphology. b Potential energy, as observed on [001]. (Side-view intented)

5.3 Conclusions 163

5.3 Conclusions

Two different 3D interaction models were used to simulate MT in spherically shaped crystals. The Lennard–Jones model exhibits a bcc/fcc transformation which, despite its artificial character, shows all the characteristics of MT. We observed twinned, plate-shaped structures formed along planar interfaces. Martensite variants can be identified, which form coherent twins. Martensite plates nucleate in different crystallographic directions and form domains. Where domains come into contact with each other, incompatibilities produce distinct domain interfaces endowed with significant excess energy. The zirconium model exhibits the material-specific bcc/hcp transformations which also yield variants due to the differently oriented basal hcp planes. Once again, we observe domain formations.

Approximately 12% of the atoms are affected by the free surface which significantly influences the nucleation process. These respective parts of the simulations may therefore not be regarded as representative. The zirconium sphere even exhibits an extreme mechanical reaction caused by the transformation stresses that occur in the surface layer. Despite this, both simulation models show characteristic results in their core regions once the surface reactions have elapsed.

To reduce the surface effect, 3D model sizes must be at least two orders of magnitude larger than those investigated here. Larger model sizes could not be analysed within the framework of this project due to the lack of computing resources. For this reason, we have concentrated our investigates on the 2D model in the previous chapter, where the surface effect is geometrically reduced by an order of magnitude.

References

- G.J. Ackland, A.P. Jones. Applications of local crystal structure measures in experiment and simulation. Phys. Rev. B 73(5), 2006
- M.I. Mendelev, G.J. Ackland, Development of an interatomic potential appropriate for simulation of phase transformations in zirconium. Phil. Mag. Lett. 87, 349–359 (2007)
- 3. G.J. Ackland, S.J. Wooding, D.J. Bacon, Defect, surface and displacement-threshold properties of -zirconium simulated with a many-body potential. Phil. Mag. A 71, 553–565 (1995)
- U. Pinsook, G.J. Ackland. Atomistic simulation of shear in a martensitic twinned microstructure. Phys. Rev. B 62(9), 5427–5434 (2000)
- U. Pinsook, G.J. Ackland. Simulation of martensitic microstructural evolution in zirconium. Phys. Rev. B 58(17), 11252 (1998)

Chapter 6 Conclusions

The fascinating thermo-mechanical properties of shape memory alloys are determined by the structural phase transformations of their crystal lattice. These are functions of temperature and loading states. The phase stability is controlled by thermodynamics which states that a balance between energy and entropy decides the crystal structure. The method of molecular dynamics simulations is capable of naturally modelling this interplay. Here, the potential energy is set by the internal interaction potential used to model the cohesive forces between the atoms in the lattice, while the entropy, as well as temperature, enters the model dynamically as a statistical measure of the atomic fluctuations. These fluctuations evolve freely within the bounds set by the interaction potentials. The microstructures presented in this work all evolve as a consequence of this interplay of "determinacy and random walk" [1]. Therefore, our chosen method is not only based on the first principles of mechanics, but also incorporates first principles of thermodynamics.

In this work, we have studied in great detail the structures produced by the model system and how these evolve as a function of time in nucleation and growth processes. From the mathematical point of view, these structures are regarded as solutions of a system of coupled ordinary differential equations which are fully determined by the initial conditions. The structures formed in the simulations are always similar on the mesoscale, although the microscale details differ. The microstructures evolve "on their own", in a sense they are formed without any further assumptions or restrictions. Hence, these structures represent a fundamental property of the modelled system and are fully determined by the first principles of mechanics and thermodynamics. The results show an amazing resemblance to laboratory experiments, even in a simplified 2D setting. We conclude that the MD simulations method must indeed correctly incorporate these fundamental physical principles. The method therefore constitutes an appropriate theoretical "laboratory" which can be employed for principle material investigations.

Here, our paradigm was to preserve this natural model property as far as possible. We therefore employed as little additional numerical ballast as possible. Restricted to 2D, this paradigm can be realised. The 3D models studied here, however, turned

166 6 Conclusions

out to be too small, such that surface effects dominated the processes. Nevertheless, despite this, the 3D results hitherto obtained support, at least qualitatively, our 2D findings.

We can investigate model materials, as presented in this work, using this theoretical laboratory by means of thermo-mechanical tests. The results of the model's equations can be analysed in detail on different length scales. On the mesoscale, we observe evolutions of microstructures, can compare and assess these in regard to the thermo-mechanical conditions set. All this is possible without loss of the atomic detail: the method allows to reduce the observed processes down to the microscale of individual atomic trajectories at any time. In the context of growing computational capabilities, the MD simulations method therefore represents a powerful and comprehensive scientific tool.

Let us summarise the results. In 3D, we have studied bcc/fcc lattice transformations in artificial Lennard–Jones crystals and bcc/hcp transformations in a zirconium crystal. Despite reasonable surface reactions, we observed typical MT in the bulk material. The transformations evolve according to the material specificity, but MT characteristic morphologies are produced. These are indicated by twinned domain structures which are produced in travelling transformation zones indicated by both temperature signatures due to the release of latent heat, as well as mesoscopic kinetic energy signatures due to cooperative atomic rearrangements occurring during the transformation. All these characteristics are preserved by the 2D model.

Using the 2D case as appropriate model system, we have shown that temperature-dependent, non-convex free energy functions arise at the mesoscale from the atomic interaction dynamics. The phase stability of small crystallites obeys the predictions of the macroscopic equilibrium thermodynamics. If such elements are combined in a chain, their collective load/strain responses model pseudo-elasticity and pseudo-plasticity depending simply on the temperature level simulated. No modifications of the interaction parameters are needed to model these two completely different properties. Similarly, by combining thermo-mechanical processes with this chain, the shape memory effect is modelled. In the chain, twin/twin interfaces were artificially excluded and no domain boundaries occurred. In such a setting, the process diagrams do not exhibit hysteresis.

Microstructures are entailed in extended crystals. Although restricted to 2D, the model martensite bears variant diversity. Evaluation of the crystallographic compatibility conditions proves the existence of both compatible twin variants as well as incompatibilities between other variants. Twins are formed spontaneously in the travelling transformation zones and these processes produce perfectly coherent martensite domains. In regard to the formation of a finite-sized twin structure, we have pointed out the impact of the angular momentum produced during the formation of individual lamellae on the mesoscale. Domain boundaries, on the other hand, occur as the result of incompatibilities between the twin variants forming two adjacent domains. These incompatibilities incorporate interfacial energy signatures and may produce lattice defects.

In MD simulations, the nucleation processes of martensite are modelled as "natural" solutions of the equations of motion. Thermally induced nucleation events were 6 Conclusions 167

studied with teh 2D model material in detail. Nucleation is indicated by spontaneous correlations of the atomic trajectories, building up the soft modes. Soft modes therefore represent a collective property of the atoms at the nucleation centres. In the phase space, this process is indicated by temporal convergence of the atomic phase curves into narrow nucleation channels which connects parent and product structures. Therefore, the local correlation of atomic motions appears as a characteristic property of the nucleation event.

During martensitic growth, point defects may be produced at domain boundaries but they may also be generated during reverse martensite/austenite transformations. In 2D, we have identified two fundamental reverse transformation mechanisms; reversible and reconstructive. The latter incorporates vacancy production processes, which are shifted through the lattice by the dislocation mechanism. They may pile up at other immobile defects or migrate to the surface but they nevertheless irreversibly change the global energetic situation of the sample. These irreversibilities are shown to produce hysteresis and functional fatigue during cyclic transformation processes. Such processes have not previously been considered in 3D simulations because they involve time- and length scales not accessible by using contemporary computation facilities. The result obtained here highlights important energetic contributions to the microstructure regarding the thermodynamic phase stability condition. It shows that it is possible to identify these contributions on the mesoscale for sufficiently large crystals in 2D. Since computational resources are quickly growing, we are optimistic that similar studies will soon be possible using 3D crystals. Such studies may also reveal the interplay of dislocations and phase stability, which is not properly modelled in the 2D case.

One fundamental observation in our simulations is the fact that all observed transformations proceed by nucleation and growth processes. This is confirmed by laboratory experiments on real materials. The morphologies are produced in the transformation zones and subsequently barely change. We did not observe significant ripening processes which could have changed a produced domain structure in the 2D model within the time scales studied; not even under external loading of such morphologies. We conclude that the microstructure is primarily decided in these transformation zones and is therefore determined by local rather than by global thermodynamic conditions. Therefore, whatever structure was produced during the MT, it is unlikely that this structure represents a global energetic minimum. Consequently, it may be viewed thermodynamically as a metastable structure, which is stabilised by energy barriers produced by the microstructure.

MT proceeds as a travelling wave phenomenon. In continuum-scale theories, travelling waves are modelled by hyperbolic equations. MT, in contrast, is mostly modelled as a (pseudo-) stationary process, where rate equations are introduced in order to relax the local phase composition according to the thermo-mechanical boundary conditions set. Our results may help to introduce the physical origin of the necessary inertial term needed to set up a hyperbolic model equation for a transformation wave: During MT, inertia emerges on the mesoscopic length scale owing to cooperative transformation motions of the atoms. This effect can be energetically localised in MD simulations, whereas in laboratory experiments it gives rise to the

168 6 Conclusions

characteristic transformation *sound*. The identification of this effect may be regarded as an example of how MD simulations may aid and confine continuum-scale modelling.

At some future date, material scientists will be able to theoretically design materials on a computer. It will be possible to predict the atomic properties of alloys and their microstructural capacities in order to design their structural and functional properties prior to experimental testing. Currently, the theoretical work aims mostly at attempting to understand nature by means of properly modelling existing experimental data. In doing this, it is sometimes advantageous to idealise the matter and to consider simplified models in order to better understand the fundamental principles. In this situation, theory may occasionally identify a new physical aspect and guide the experiments to its verification. This work was conceived and structured within such a paradigm. On the other hand, reliable SMA model potentials for the technically relevant alloys such as nickel-titanium or magnetic SMAs are currently not available today. The aspect of modelling potentials therefore also establishes an important issue for the scientific agenda. Future MD simulations modelling of real SMAs rely on advances in modelling their potentials and also on the availability of the requisite computational resources.

Reference

1. I. Müller, W. Weiss, Entropy and energy (Springer, Berlin, 2005), pp. 169-178

A	Competing phase preferences, 17
Ab-initio, 8	Constitutive equantions, 11
Accomodation, 7	Convex hull, 16
Accuracy, 37	Correlation sum, 112
hardware, 37	Coupling, 1, 7
software, 37	CPU, 49
Ackland, 36, 55, 157	Cross-correlation, 112
Andersen, 44, 47	Crystal viewer, 54
Austenite, 3	Crystallographic theory, 9
	Cut-off radius, 50
	Cyclic thermal loading, 20
В	of L-J crystals, 59
B2, 151–154, 156	•
Bain, 9, 10, 72, 73	
parameters, 9	D
transformation, 9, 72	Daw and Baskes, 36
Balance laws, 11, 12	De-twinning, 78, 81
of energy, 12, 101	chain assembly, 131
of entropy, 13	quad assembly, 137
of mass, 12	Defect, 19, 20, 36, 63, 127, 131, 134
Ball Viewer, 55, 154, 160	accumulation, 139, 141, 142, 144-148
bcc, 160	energy, 89, 90, 92, 101, 118, 140
Bearing, 122	structure, 3, 4, 6–8, 10, 17–20, 35, 36, 43,
Bhattacharya, 126	48–50, 54, 91, 93, 94, 156, 167
Bloch basis, 64	Deformation gradient, 9
Bragg and Nye, 36	Descartes, 10, 11, 36
	DIC, 6
	Differential equations, 37
C	Discrete Fourier analysis, 110
Canonical distribution, 24, 25	Dislocation, 127
Cauchy, 8	movement, 127
Charactersistic quantities, 41	Displacement control, 75, 129
Clapp, 3, 36	Dissipation, 101, 117
Clausius-Clapeyron equation, 14	numerical, 38
Cohesive forces EAM, 158	Domain decomposition, 50
Common tangents, 14, 16, 77	Domain structure, 93, 134, 154
Compatibility, 90, 92	DSC device, 18

D (cont.)	FLOP, 49
Dynamic matrix, 64	Force, 7, 8, 12, 21, 22, 35, 37-40, 43, 45, 49,
	50, 53, 79, 130, 154, 158, 165
	in atomic assemblies, 21
E	in tensile experiments, 12
EAM see Embedded-atom method, 36	Frenkel and Smit, 38
Einstein crystal, 25	Frequency, 64
Electron density, 158	Frequency filtering, 112
Embedded-atom method, 36	Functional fatigue, 3, 18, 19, 134, 145, 167
Energy, 10-20, 22, 23-28, 35, 37-39, 42, 44,	in L-J crystals, 59
45, 53–55, 62–70, 76, 77, 84, 119, 120,	•
122, 127, 161, 163–168	
and entropy, 17	G
barrier, 16	Gibbs ensemble, 24
classical atom ensembles, 22	Gibbs Equation, 14
conservation, 37	Gibbs free enthalpy, 13
drift, 41	GLUI, 54
internal, 22, 26	Gripping, 107, 121
kinetic (of mass centre), 22, 26	Ground state, 17, 26, 27, 63, 64, 67–70, 142,
mesoscopic kinetic, 101, 157	158, 159
potential of atom, 60	energy, 17, 26, 67, 140
potential, total, 60	positions of atoms, 26
Engineering models, 27	Group/subgroup relationship, 62
empirical, 27	Growth process, 87, 92
energy-based, 28	-
plasticity theory related, 28	
Entropic phase stabilisation, 18	Н
of L-J lattices, 65	Habit plane, 9
Entropy, 8, 9, 11–14, 17–19, 24, 25, 27, 63, 67,	Halo, 51
71, 120, 146, 160, 165, 167	Hardware, 49
constant, 27	Harmonic, 26, 27, 41, 42, 63, 64, 74, 152
of ensembles, 27	wave, 64
principle, 11	Harmonic approximation, 25
EPCC, 53	HCP, 154, 160
Equal areas, 14, 16, 77	Helmholtz free energy, 14
Equations of Motion, 7, 22, 23, 39, 42, 43, 46,	non-convexity of, 15
48, 64, 103, 120, 166	of crystallite, 77
Lagrange, 23	of ensembles, 27
Newton, 21	Herringbone pattern, 91
Equations of motion	Hexagonal symmetry, 60
linearised, 64	HPC, 52
Equilibrium, 13, 37	HPCx, 53
Excess velocities atomic, 21	HR-TEM, 6
	Hysteresis, 2, 18
	and microstructure, 54, 100, 145
F	missing, 103
Fatigue, 3, 18, 19, 134, 145, 146, 148, 167 functional, 3, 18, 146	thermal, in L-J crystals, 59
structural, 135	
FCC, 55, 152–157, 163, 166	I
FEM, 28	Initial conditions, 39
Field variables, 11	Interaction, 19, 22, 25, 35, 37, 39, 40, 45, 51,
Finnis-Sinclair potentials, 36	105, 151, 165
Floating point number, 38	domains, 51

forces, 21 radius, 46 range, 45 Interface energy, 20, 121 Invariant line, 108 Isothermal conditions, 25 in MD simulations, 42 J James and Ball, 10	Martens, 3, 6 Martensite, 3 domains, 92 microstructure, 4 lamellae, 6, 156 twins, 6 of 2D model, 62 variants with 2D model, 62 wedge, 91, 154 Martensitic transformations (MT), 3, 4, 36, 37, 52, 55, 104, 108
JUMP, 53	CuNiAl, 5
JUROPA, 53	definition, 3, 4, 13, 19, 100, 138 literature, 4 NiAl, 7
K	Mass centre of assemblies, 21
Kelvin, 19	Mass-specific quantities, 13
Kinematic compatibility, 10	Maxwell line, 16
	Maxwellian distribution, 45
L	MD see Molecular dynamics simulations, 35
L-J see Lennard-Jones, 36	Mechanical equilibrium, 13
Lagrangian, 23	Melting line, 70
extended (Nosé-Hoover), 15, 29, 43,	Micro-mechanics, 8
47–49, 53, 62, 64, 97, 108, 131, 152,	Microcanonical ensemble, 23
157, 166	Military tranformation, 7
extended (Parrinello-Rahman), 48	Mobility of atoms, 27
Lamellar structure, 6	Molecular dynamics simulations, 8, 35, 148
Latent heat, 157	2D L–J, 62, 156
Lattice, 125	chain, 78
defect, 127, 131	crystallites, 74
invariant shear, 127	microstructure formation, 98
L-J, binary 2D, 61 L-J, binary 3D, 151	quads, 100 strip, 87
parameter, 46	substrate layers, 96
Zirconium, 160	3D L-J sphere, 151
Lennard-Jones, 84, 97	EAM Zr sphere, 159
crystal, bi-atomic, 61	method, 35
crystal, monatomic, 60	program, 52
parameters, 59	Momentum, 101
heterogeneous, 63	Morse potential, 36
Linux cluster, 53	MPI, 53
Load control, 75, 121–125, 128, 134	Multi-Scale, 8
Load/strain curve, 76–79, 82, 130, 132, 136, 148 chain, 77, 79, 80	definitions, 8
crystallite, 77	N
serrated shape, 81	Neighbourhood, 50, 53, 55, 105, 107, 112, 126, 158
	list, 50
M Muller-Achenbach-Seelecke <i>see</i> MAS model,	Newtonian mechanics, 21 NIC, 53
28	Non-dimensionalisation, 41
Many body problem, 35	Normal modes, 64

N (cont.) Nosé-Hoover, 43 Nucleation, 102 barrier, 19, 103 channel, 121	Pseudo-plasticity, 27, 59, 74, 79, 81–84 of chain assembly, 83 phenomenon, 2
entropic barrier, 103 event, 108 in fluids, 19 instant, 107	Q Quenching, 88, 90
trajectory correlation, 118 Numerical solutions, 37	R Rare event, 121 Reference state, 13
	Reverse transformation, 123
0	reversible and reconstructive, 126
Olson, 4	
OpenGL, 54	
	S
	Scales, 7
P	bridging, 8
Parallelisation, 49	Second cycle, 139
Parrinello and Rahman, 47	Second eigenvalue, 19
Partition function, 25	Shape memory alloy (SMA), 1, 7, 28, 77, 165
Periodic boundary conditions, 45	CuNiAl, 6
Phase, 65	NiTi, 1
curve, 119	scales, 7
equilibrium, 13, 14	thermo-mechanical properties, 1
fraction, 81	Shape memory effect, 2, 3, 83
mixture, 16	Shear/shuffle, 62
preference, 70	Shneck, 103
space, 23	Simulation videos, 49, 52
space analysis, 118	Singular surface, 20
Phonons, 2–7, 9, 11–17, 153, 154, 156,	Size, 16, 24, 47, 49, 50, 51, 53
157–159, 163, 164–167	domain, 50
optical and acoustic, 65	ensemble, 50
Pinning, 129	Small size effect, 74
Plastic deformation, 134	Smart material, 34
Plate group, 6	Snap springs, 79
Post processing, 53	Soft mode, 116
Potential, 67	Speed of sound, 8
curvature, 68	Stability, 49, 65
EAM for Zr, 158	mechanical of 2D lattices, 65
internal and external, 21	Thermodynamic, 13
Lennard-Jones, 59	thermodynamic of 2D lattices, 66 Strain, 154
Pro mortangita, 104	definition, 13
Pre-martensite, 104 Predictor-corrector method, 40	
Probability, 23	energy, 11 gradient, 154
of rare events, 121	Stress, 17
Product, 7, 19, 93, 95, 103, 141	Cauchy, 12
Pseudo-elasticity, 27, 29, 59, 74, 79, 82–85,	control (Parrinello-Rahman), 48
102, 121, 123, 124	definition, 15
of chain assembly, 81	Piola-Kirchhoff, 13
• ·	*

Surface energy, 20, 45, 74	strain, 14
Symmetry, 153	stress, 16
	temperature, 16, 68, 145
	wave, 88
T	zone, 101, 129, 157
TEM, 6	Twinning, 134
Temperature, 26	chain assembly, 131
Temperature-control, 82	Twinning condition, 9
in MD simulations, 82	
Tensile testing, 77, 80, 121, 130, 134	
chain assembly, 79	U
crystallite, 75	Undercooling, 103
cyclic, 123	Unloaded state, 17
pseudo-elasticity, 121	
pseudo-plasticity, 134	
rectangular strips, 124	V
Thermal, 79	VAMPIR, 53
equlibrium, 13	Variants, 108
expansion, 26	in 2D L-J lattices, 61
hysteresis, 145	incompatibility, 95, 134
Thermodynamics, 11	Velocity, 122
statistical, 23	computation, 39
Thermostat, 126	randomisation, 104
Andersen, 44	Velocity of mass centre, 100
Nośe-Hoover, 43	of assemblies, 21
velocity scaling, 44	of atomic subsets, 118
Time, 152	of interaction neighbourhoods, 105
CPU runtime, 49	Verlet algorithm, 105
physical, simulated, 49	coordinate, 39
reversibility, 37	velocity, 40
Time/frequency analysis, 110	Verlet list, 50
Transformation, 74	
bee-hep in Zr, 158	
critical load crystallite, 77	\mathbf{W}
cycles, 137, 141	Weak interaction, 82
dynamics, 10	
energy induced, 138	
front, 88	${f Z}$
kinetics, 102	Zirconium, 157
of unit cell, 62	
reverse, 137	